Towards Quantum Simulation of the Kondo-Lattice-Model

Dissertation
zur Erlangung des Doktorgrades
des Department Physik
der Universität Hamburg

vorgelegt von

André Kochanke

aus Bielefeld

Hamburg
2017

Gutachter der Dissertation: Prof. Dr. Klaus Sengstock
Prof. Dr. Andreas Hemmerich

Zusammensetzung der Prüfungskommission: Prof. Dr. Klaus Sengstock
Prof. Dr. Andreas Hemmerich
Prof. Dr. Henning Moritz
Prof. Dr. Peter Schmelcher
Prof. Dr. Günter Huber

Vorsitzender der Prüfungskommission: Prof. Dr. Peter Schmelcher

Datum der Disputation: 25. April 2017

Vorsitzender des Promotionsausschusses: Prof. Dr. Peter Schmelcher

Fachbereichsleiter Physik: Prof. Dr. Michael Potthoff

Dekan der Fakultät für Mathematik,
Informatik und Naturwissenschaften: Prof. Dr. Heinrich Graener

Abstract

Ultracold quantum gases of alkaline-earth-like metals are a versatile tool to investigate interacting many-body physics by realizing clean and controllable experimental model systems. Their intriguing properties range from energetically low-lying clock transitions, which allow for high-resolution spectroscopy, over meta-stable states, which can be regarded as a second species with orbital degree of freedom, to SU($\mathcal{N}$) symmetry, allowing novel magnetic phases. These open up new possibilities for quantum simulators. Using them in combination with optical lattices dissipative Fermi-Hubbard models and the Kondo-lattice-model can be realized, two promising examples for probing strongly correlated systems.

This thesis presents an experimental apparatus for producing ultracold samples of fermionic ^{173}Yb ($\mathcal{N} \leq 6$). A new bicolor dipole trap was implemented with a final, average trap frequency of $\bar{\omega} = 36\,\mathrm{Hz}$. Using optical, resonant pumping and an Optical-Stern-Gerlach scheme, the spin mixture can arbitrarily be changed from a six- to a one-component gas. Typically the degenerate Fermi gases consist of 87000 atoms at $17.5\%\,T_\mathrm{F}$ ($\mathcal{N} = 6$) and of 47000 atoms at $19.4\%\,T_\mathrm{F}$ ($\mathcal{N} = 1$).

The lowest lying meta-stable state $^3P_0$ ($578\,\mathrm{nm}$) is coherently controlled using a clock-laser setup with a linewidth of FWHM $= 1\,\mathrm{Hz}$ by means of Rabi oscillations or rapid adiabatic passage. By conducting spectroscopic measurements in a 3D magic lattice ($759\,\mathrm{nm}$) we demonstrate inter band transitions and observe the $^1S_0 \Leftrightarrow {}^3P_0$ excitation with a resolution of FWHM $= 50(2)\,\mathrm{Hz}$. Applying these techniques to a two-component spin mixture reveals a shift of the clock-transition caused by spin-exchange interaction between the orbital symmetric $|eg\rangle^+ |\uparrow\downarrow\rangle^-$ and the orbital antisymmetric $|eg\rangle^- |\uparrow\downarrow\rangle^+$ state.

Using the inelastic properties of the $^3P_0$ state a dissipative Fermi-Hubbard model is realized. The dynamics in this system can not be described by a simple two-body loss model. We identify two relevant time scales and observe a spin dependence of the $g^{(2)}$ correlation function.

The here presented apparatus and experimental results constitute an important step towards a profound understanding of strongly correlated many-body systems and for bridging the gap between quantum gases and condensed matter physics.

Zusammenfassung

Ultrakalte Quantengase mit erdalkali-ähnlichen Metallen stellen ein vielseitiges Werkzeug dar, um Vielteilchensysteme mit Wechselwirkung zu untersuchen. Dabei ist man in der Lage, diese experimentellen Modellsysteme in einer sauberen und kontrollierbaren Weise umzusetzen. Durch ihre faszinierenden Eigenschaften, z.B. energetisch niedrig liegende Uhrenübergänge, welche hochauflösende Spektroskopie ermöglichen, metastabile Zustände, die als unabhängige Teilchensorte mit orbitalem Freiheitsgrad betrachtet werden können oder SU($\mathcal{N}$)-Symmetrie, welche neuartige magnetische Phasen hervorbringen kann, können neue Arten von Quantensimulatoren ermöglicht werden. Im Zusammenspiel mit optischen Gittern können diese Metalle dissipative Fermi-Hubbard-Modelle und das Kondo-Gitter-Modell realisieren, zwei vielversprechende Beispiele für stark korrelierte Systeme.

Diese Abschlussarbeit präsentiert einen experimentellen Aufbau zur Herstellung von ultrakalten Gasen mit ^{173}Yb ($\mathcal{N} \leq 6$). Eine neue, zweifarbige Dipolfalle wurde aufgebaut und erreicht eine Endfallenfrequenz von $\bar{\omega} = 36\,\mathrm{Hz}$. Durch Benutzung von resonantem, optischem Pumpen und einem Optischen-Stern-Gerlach System kann eine beliebige Spinmischung zwischen einer und sechs Komponenten erzeugt werden. Typischerweise besteht ein entartetes Fermigas aus 87000 Atomen bei $17.5\%\,T_\mathrm{F}$ ($\mathcal{N} = 6$) und aus 47000 Atomen bei $19.4\%\,T_\mathrm{F}$ ($\mathcal{N} = 1$).

Der niedrigst liegende metastabile Zustande $^3P_0$ ($578\,\mathrm{nm}$) kann mithilfe eines Uhrenlasers, dieser hat eine Linienbreite von FWHM $= 1\,\mathrm{Hz}$, durch Rabioszillationen oder einer rapiden-adiabatischen-Passage populiert werden. Durch spektroskopische Messungen in einem magischen 3D Gitter ($759\,\mathrm{nm}$) demonstrieren wir Übergänge zwischen verschiedenen Bändern und beobachten die $^1S_0 \Leftrightarrow {}^3P_0$ Anregung mit einer Auflösung von FWHM $= 50(2)\,\mathrm{Hz}$. Unter Anwendung dieser Technik bei einer zweikomponentigen Mischung ergibt sich ein Frequenzversatz des Uhrenübergangs durch Spinwechselwirkung zwischen dem orbital symmetrischen $|eg\rangle^+ \, |\uparrow\downarrow\rangle^-$ und orbital antisymmetrischen $|eg\rangle^- \, |\uparrow\downarrow\rangle^+$ Zustand.

Unter Ausnutzung der inelastischen Wechselwirkung des $^3P_0$ Zustands wird ein dissipatives Fermi-Hubbard Modell realisiert. Die Dynamik in diesem System kann nicht mit einem einfachen Zweikörperverlust-Modell beschrieben werden. Wir identifizieren zwei relevante Zeitskalen und beobachten eine Spinabhängigkeit der $g^{(2)}$ Korrelationsfunktion.

Der hier vorgestelle Aufbau und die experimentellen Ergebnisse stellen einen wichtigen Schritt zum Verständnis von stark korrelierten Vielteilchensystemen dar und verbinden die Forschungsfelder von Quantengasen und kondensierter Materie.

Publikationen

Im Rahmen der vorliegenden Arbeit ist die folgende wissenschaftliche Veröffentlichung entstanden.

Publications

The following research article has been published in the course of this thesis.

[Dör13b] S. Dörscher, A. Thobe, B. Hundt, A. Kochanke, R. LeTargat, P. Windpassinger, C. Becker, and K. Sengstock, *Creation of quantum-degenerate gases of ytterbium in a compact 2D-/3D-magnetooptical trap setup*, Review of Scientific Instruments **84**, 043109 (2013)

Contents

List of Figures

Introduction

One of the biggest challenges in science is to understand and describe large systems consisting of many interacting, individual parts, solid state materials being a prime example. One of the main difficulties in describing such materials arises from the exponential growth of information with system size. Since the foundation of quantum mechanics by M. Planck [Pla01] and A. Einstein [Ein05], a successful approach was to reduce the complexity of such systems by only regarding sufficiently small subsystems which are actually manageable. In this context reduction does not only mean to handle fewer particles, e.g. atoms, photons or electrons, but also to find a model system that is sufficiently simplified compared to its natural counterpart while still being able to correctly describe the essential physics of the original system. Although it is very difficult to estimate the limitations of these approximations, ideally this bottom-up approach can reproduce the behavior of realistic materials and allows for direct comparison with experimental observation. A prime example during the last century was the description of specific heat in metals which could be explained by the Debye model [Deb12]. Another one was the discovery of conventional super conductivity and its description via the Bardeen-Cooper-Schrieffer theory [Coo56, Bar57].

Sometimes however the approach via an elementary model is not successful. The simplifications can render a model unable to capture the essence of the underlying physics and to reproduce experimental findings. Or it could be still too complex to be treated from a theoretical point of view. A third reason might be that an actual validation is not possible due to experimental difficulties. The Fermi-Hubbard model for example can describe the behavior of electrons in a lattice based on interaction and tunneling [Liu04]. It is however a simplified model and many years of research did not solve it in its entirety. Despite its great impact on the understanding of fermionic many-body systems, there are still many open questions, for example wether it can explain the formation of high temperature super conductors in cuprate materials [Lee06] or spin-liquid states in frustrated magnets [Bal10].

Alternatively the idea of complexity reduction can be applied to the experimental domain by the use of systems with very well understood components. In this way, they can be manipulated with a high degree of control and over a large parameter range, while still keeping most of the original system's properties. Consequently, they can be used to mimic physical systems found in nature and allow for verification of certain many-body models by circumventing the computational difficulties using its intrinsic quantum-mechanical behavior. As such they are referred to as quantum simulators [Fey82, Geo14]. These toy models can additionally be fascinating on their own producing even richer quantum behavior and enabling discoveries beyond naturally occurring physics.

Due to the development of new experimental techniques in the field of laser physics, atomic physics and photonics, experimentalists are now able to specifically tailor quantum systems based on ultracold atomic gases. These aim at treating difficulties arising in the field of con-

densed matter by strong interaction and correlations. Such quantum gases can reach temperatures in the nK regime, where the atoms occupy the lowest quantum mechanical states. Only then can the comparably weak interactions in dilute atomic gases dominate the equilibrium properties of the system. This field of research gained a lot of interest when by application of laser-cooling techniques [Let95] a Bose-Einstein condensate [And95, Dav95] and shortly afterwards also a degenerate Fermi gas [DeM99] were produced. Since quantum gas experiments benefit from environmental decoupling and have numerous tuning capabilities, rapid progress in this field was possible in showing fascinating experiments pushing the development from single-particle coherence to interacting systems. One example being the application of Feshbach resonances [Chi10], which can be used to directly modify atomic interactions. These enabled the community to directly observe the Bardeen-Cooper-Schrieffer to Bose-Einstein condensate crossover [Gio08] using a quantum gas [Reg04, Zwi04, Ran14].
Increasing effort was put into the development of further experimental techniques to enhance the complexity of realizable Hamiltonians. Especially the application of interfering laser beams to produce optical lattices paved the way for investigating the field of strongly correlated Hubbard models. This was demonstrated by the experimental realization of the superfluid to Mott insulator transition for bosons [Gre02] and for fermions [Jör08, Sch08]. Currently, optical lattice potentials represent a fundamental tool in the field of ultracold quantum gases [Blo05, Gre08]. Their versatility could be shown by revealing a multitude of physical phenomena, such as fermionic band insulators [Köh05], superexchange processes [Föl07, Gre13], artificial magnetic fields [Lin09, Str11], unconventional superfluid order [Öls13], topological non trivial bands, e.g. the Haldane model [Jot14] or the Harper-Hofstadter model [Stu15, Man15, Tai16], or measurement of the Berry curvature [Flä16]. Furthermore, they offer the possibility to implement novel lattice geometries like the honeycomb [Bec10, SP11], checkerboard [Öls12] or Kagome [Jo12] lattice and to engineer systems with reduced dimensionality [Gre01, Mor03, Wen13]. Other experimental advances are based on the significant increase of optical resolution to reach the capability of imaging and manipulate individual sites of an optical lattice [Bak09, She10], which recently lead to the in-situ observation of antiferromagnetic correlation [Bol16, Par16, Maz16].
Early experiments in the field of ultracold gases were based on Alkali metals, e.g. bosonic ^{87}Rb and fermionic ^{40}K. They posses strong cycling transitions in the near-infrared spectral range, which are well suited for laser cooling. The persistent demand for extending the tool box of quantum gases lead to new cooling and preparation schemes. Since particle interaction and lattice dynamics strongly depend on the atomic properties two other material classes received growing interest. On the one hand materials with long-range, dipolar interaction became a central subject. Single elements, which possess a strong magnetic moment, could be cooled to quantum degeneracy, e.g. Chromium [Gri05a], Dysprosium [Lu11] and Erbium [Aik12]. Other approaches to investigate these kind of long-range interactions involved cold, polar molecules [Pre16] or Rydberg atoms [Urb09, Gaë09]. On the other hand alkaline-earth-like atoms, e.g. Calcium [Kra09, Hal12], Ytterbium and Strontium [Ste09, dE09, DeS10], gained a lot of interest. Pioneering work in this field has been carried out by the research group surrounding Y. Takahashi producing the first Yb Bose-Einstein condensate [Tak03]. The electronic structure of alkaline-earth metals, consisting of two valence electrons, exhibits an energetically low-lying, ultra-narrow transition, which is insensitive to environmental perturbation and serves as excellent frequency reference. These elements were therefore used in the

field of frequency metrology [Tak05, Hin13, Blo14] until recently theoretical proposals showed how their properties can be used to engineer powerful tools for investigating quantum-many-body systems [Her09, Caz09, Gor10] and yield big advances towards quantum computation [Dal08, Gor09, Shi09].

Caused by the two-electron level structure alkaline-earth-like elements have a zero total angular momentum in the ground state ${}^1S_0$ and lowest meta-stable state ${}^3P_0$. Since the fermionic isotopes only carry nuclear spin, the orbital (electronic states) and spin degrees of freedom are decoupled. Hence atomic interaction is spin independent and these systems possess so called SU($\mathcal{N}$) symmetry [Caz14], $\mathcal{N}$ number of spins. Such systems are promising candidates for realizing exotic materials like spin liquids with topological order [Her11] and they can be used to prepare highly entangled states [FF12]. Furthermore, symmetry groups with $\mathcal{N} > 2$ are possible, e.g. in case of ^{173}Yb ($\mathcal{N} \leq 6$) and ^{87}Sr ($\mathcal{N} \leq 10$), which can possibly bridge the field of ultracold quantum gases with high energy physics [Rap07], where the strong force described by quantum-chromo-dynamics is based on a non-abelian gauge theory with symmetry group SU(3). Despite the possibility to use the emerging clock transition for frequency metrology, the ultra-narrow transition can also be regarded as a tool for precise spectroscopic investigation of many-body effects. Recent publications showed measurements of the spin-exchange interaction, which is caused by the interplay between spin and orbital degrees of freedom in a two-atomic state [Sca14, Cap14]. Orbital spin-exchange is connected to many quantum phenomena in the field of condensed matter, e.g. heavy-fermi materials and unconventional superconductors [Sig91, Mat98, Col06, FF10a, Zho16]. This new type of interaction could furthermore be exploited to realize Orbital-Feshbach resonances, which allow to efficiently tune the atomic interaction different to magnetic Feshbach resonances [Pag15, Höf15]. Beside the various applications of the clock transition the meta-stable state can be regarded independently as a second species with entirely different orbital properties. These can especially be exploited in state-dependent lattices. One option is the experimental realization of the Kondo-lattice-model [FF10b, Nak15, Zha16, Isa15], which is a promising candidate to answer open questions related to high-temperature superconductivity. Other possible applications are artificial gauge fields [Tho82, Ger10, Dal11, Che16], where light assisted tunneling can be used to create synthetic magnetism with neutral atoms.

This thesis aims at providing an experimental apparatus where some of the intriguing attributes of Yb can be exploited and an eventual realization of the Kondo-lattice-model is feasible. As a starting point for producing ultracold gases we analyze the MOT performance and demonstrate sufficient loading rates for the most abundant isotopes ^{171}Yb ($\mathcal{N} \leq 2$), ^{173}Yb ($\mathcal{N} \leq 6$) and ^{174}Yb. These measurements were carried out with emphasis on very few changes to the opto-mechanical MOT setup to examine possible two-isotope operation. This is a prerequisite for reaching quantum degeneracy in case of ^{171}Yb, because it needs to sympathetically be cooled due to its vanishing s-wave scattering length, and isotope mixtures. Furthermore, a new bicolor, optical dipole trap is used for efficient evaporative cooling of ^{173}Yb and ^{174}Yb to quantum degeneracy with a final trap frequency of $\bar{\omega} = 36\,\mathrm{Hz}$. A preferably low trap frequency is favorable to ensure clean preparation in an optical lattice. For the experimental realization of the Hubbard model the quantum gases can be transferred into a triangular optical lattice. Besides its application for many-body Hamiltonians the lattice confinement is required for high-resolution spectroscopy by operating with a magic wavelength ($759\,\mathrm{nm}$) and enabling excitation in the

Lamb-Dicke regime. To exploit the features of the meta-stable $^3P_0$ state we use a clock-laser setup with a linewidth of $1\,\mathrm{Hz}$. To demonstrate a sufficient resolution capability we show spectra of the clock transition $^1S_0 \Leftrightarrow {}^3P_0$ using ultracold, spin-polarized ^{173}Yb, which reach a width of FWHM $= 50\,\mathrm{Hz}$. Furthermore, a frequency shift of the clock-transition is visualized, which is caused by the spin-exchange interaction existing in two-atom states. The corresponding energy V_{ex} is a crucial parameter in the Kondo-lattice-model, because it determines the dominating quantum phases therein. In addition to using the clock transition as a spectroscopic tool, we exploit the inelastic properties of the $^3P_0$ state to experimentally realize a dissipative Fermi-Hubbard model. By analyzing the loss dynamics we draw conclusions about the correlation function in this system. Due to the atomic interactions in case of ^{173}Yb($^3P_0$), the emerging dynamics are dominated by Mott-like behavior. The ^{171}Yb isotope is a promising candidate to change the ratio between inelastic losses and on-site interaction significantly towards a loss-dominated system, which can possibly visualize the quantum Zeno effect [Ita90]. Lastly, a second lattice setup at a wavelength of $660\,\mathrm{nm}$ was implemented and characterized. At this wavelength the polarizablity of the meta-stable state is about a factor of five larger than for the ground state. In this way a state-dependent lattice can be realized, with mobile ground-state atoms and localized excited-state atoms, aiming at the investigation of the Kondo-lattice-model. The original model [Tsu97] assumes a vanishing ground state interaction. Therefore, the ^{171}Yb isotope would be the ideal candidate for this realization. However, ^{173}Yb could also be used for investigating an extended Kondo-lattice-model, which includes non-vanishing ground-state interaction.

Thesis outline

This thesis is structured in the following way:

- Chapter **one** describes the main cooling transitions of Yb and the overall experimental apparatus. Furthermore it presents changes to the cooling-laser systems to enable simultaneous trapping of different Yb isotopes. The performance of the magneto-optical-trap is characterized for the isotopes ^{171}Yb, ^{173}Yb and ^{174}Yb.

- Chapter **two** demonstrates the production of ultracold Fermi gases of ^{173}Yb by applying evaporative cooling in a new bicolor dipole trap ($\bar{\omega} = 36\,\mathrm{Hz}$). For preparing and detecting arbitrary spin mixtures resonant, optical pumping using the green Magneto-Optical-Trap transition and a spin-selective separation by means of an Optical-Stern-Gerlach scheme are applied. As an extension to imaging only the ground state atoms via absorption imaging a repump laser at $1388\,\mathrm{nm}$ using the $^3P_0 \Leftrightarrow {}^3D_1$ transition was implemented. Finally, the evaporation of a six- and two-component spin mixture is analyzed.

- Chapter **three** first presents the setup of a magic, triangular, optical lattice in which the metastable $^3P_0$ state of Yb is prepared. For the coherent control of this state a respective clock-laser setup is used with a short-term linewidth of $1\,\mathrm{Hz}$. Several changes of this setup lead to an increased long-term stability, which is highly desirable in terms of experimental reliability. The chapter furthermore shows ultra-narrow spectroscopy with spin-polarized and two-component ^{173}Yb. Using a single-spin gas and excitation via Rabi oscillations we reach a resolution of FWHM $= 50\,\mathrm{Hz}$. In case of a two-component mixture a frequency shift of the clock transition is observed, which is caused by the spin-exchange interaction present in two-particle states.

- Chapter **four** demonstrates an alternative approach to excite the meta-stable $^3P_0$ state by means of a rapid adiabatic passage. The inelastic properties of the $^3P_0$ state are exploited to induce particle loss in a lattice system for experimentally realizing a dissipative Fermi-Hubbard model. Using the decay behavior of the system the occupation of the lattice can be estimated.

- Chapter **five** shows the realization of a state-selective lattice at $660\,\mathrm{nm}$. The focus lies on the characterization of the beam quality and noise characteristics of the new laser source. First measurements with the state-dependent lattice show the first Brillouin zone using ^{173}Yb.

1. A 2D/3D-MOT Setup for Multiple Yb Isotopes

The temperature difference between a thermal, atomic cloud and the regime of quantum degeneracy is about ten orders of magnitude. Due to this enormous difference, individual cooling stages are used. As a first step the atoms need to be captured from a hot source and cooled to temperatures in the μK-regime. In our case this is carried out via a two stage magneto-optical-trap (MOT), which explicitly exploits the two-electron level structure intrinsic to Yb atoms. In contrary to loading atoms from background pressure, as it is possible for alkaline elements [Mon90, Wie95, Cat98], we capture Yb atoms directly from an atomic beam (several $100\,\mathrm{K}$) and cool them in a 2D-/3D-MOT. These setups have been well established in our group granting large optical access around the science cell and the possibility to cool different species simultaneously.

The main experimental apparatus was already build and used by my colleagues S. Dörscher [Dör13a] and A. Thobe [Tho14]. During this thesis the laser systems have been rebuild in large parts for more flexibility and reliability. Specifically, the new setup should enable us to simultaneously cool two different isotopes. This feature is crucial for reaching quantum degeneracy for the fermionic isotope ^{171}Yb, where the vanishing s-wave scattering length prohibits proper evaporative cooling. Furthermore, it generally enables us to conduct experiments involving isotope mixtures which for example exploit molecular scattering lengths or Bose-Fermi particle statistics.

The following chapter will give a brief overview about important properties of Yb and the main parts of the experiment. This is followed by a description of the rebuilt cooling laser setup and MOT characterization measurements concerning the isotopes ^{171}Yb, ^{173}Yb and ^{174}Yb. Planing and rebuilding as well as conducting the measurements were carried out by B. Abeln and the author.

1.1. Atomic properties for an Yb MOT

Natural abundance

Yb has seven stable isotopes. Two of them show fermionic behavior by carrying a nuclear spin I [Aud97]. The isotopic distribution is shown in Tab. 1.1. This variety alone offers many possibilities. Switching between different isotopes can be used to change the statistic behavior from bosons to fermions or the collisional properties [Kit08]. Furthermore isotopic mixtures can be produced. Most of them have been successfully cooled to quantum degeneracy by now [Sug11, Tak03, Fuk07, Fuk09] and also experiments involving Yb mixtures have been carried out [Hon02, Kit08, Tai10].

A	Abundance (%)	Spin (I)	Statistic
168	0.12	0	boson
170	2.98	0	boson
171	14.09	1/2	fermion
172	21.68	0	boson
173	16.10	5/2	fermion
174	32.03	0	boson
176	13.00	0	boson

Table 1.1.: Natural abundance of stable Yb isotopes. The table lists the Yb isotopes according to mass number A. The fermionic isotopes only carry a nuclear spin I. Data is taken from [Aud97].

Main atomic transitions

As Yb belongs to the class of alkaline-earth-like atoms, it carries two valence electrons. Hence, the term scheme shows a two-fold level structure, where Singlet and Triplet branch can be distinguished. As shown in Fig. 1.1 two transitions are used for laser cooling.

The *blue* transition connects the $^1\mathrm{S}_0$ ground state with the $^1\mathrm{P}_1$ excited state at a wavelength of $399\,\mathrm{nm}$. The *green* (inter-combination) transition connects the $^1\mathrm{S}_0$ ground state with the $^3\mathrm{P}_1$ excited state at a wavelength of $556\,\mathrm{nm}$. The main properties of these transitions are summarized in Tab. 1.2, where the Doppler temperature T_D and saturation intensity I_sat is given by [Met99]

$$\begin{aligned} k_\mathrm{B} T_\mathrm{D} &= \frac{\hbar}{2}\Gamma, \\ I_\mathrm{sat} &= \frac{\pi h c}{3\lambda^3}\Gamma, \end{aligned}$$

with λ and Γ being wavelength and decay rate of the excited state, respectively. As can be seen the values differ by two orders of magnitude, which can be used as an advantage for cooling Yb atoms. Since the vapor pressure of Yb is comparably low [Hay16], a MOT can not be sufficiently loaded from the background pressure. Therefore, we directly capture atoms from an atomic beam emerging from a dispenser with a 2D-MOT. Here, the broad linewidth is advantageous, because the capture velocity v_c is increased. As an upper bound the capture velocity can be estimated with $v_\mathrm{c} = \sqrt{\hbar k \Gamma d / m}$, k is the wave number, d the size of the MOT and m the atomic mass, which shows the dependence on the linewdith with $v_\mathrm{c} \propto \sqrt{\Gamma}$. However, simultaneously it is unfeasible for reaching low enough temperatures for subsequent evaporative cooling. Thus, a second cooling stage can be applied using the *green* transition. In this case the narrow linewidth enables us to reach sufficiently low temperatures for consecutive evaporative cooling.

Different isotopes possess distinct resonance frequencies [Das05, Pan09], which make it necessary that the laser sources can be adjusted accordingly. Especially in the case of cooling two isotopes simultaneously the laser setup has to be capable of providing the respective frequencies with sufficient power. Details about our present cooling laser setup, which fulfills these conditions, can be found in Sec. 1.3. As reference, the isotope shifts are shown in Tab. 1.3.

	λ (nm)	$\Gamma/2\pi$ (MHz)	I_{sat} (mW cm^{-2})	T_D (µK)
$^1S_0 \Leftrightarrow {}^1P_1$	398.9	29.13	59.97	699.0
$^1S_0 \Leftrightarrow {}^3P_1$	555.8	0.182	0.139	4.37

Table 1.2.: Cooling transitions of Yb. The table shows the most important properties of the two cooling transitions used in our 2D/3D-MOT setup. Listed are the wavelength λ, the linewidth Γ, the saturation intensity I_{sat} and the Doppler temperature T_{D}. Data is taken from [Kra16].

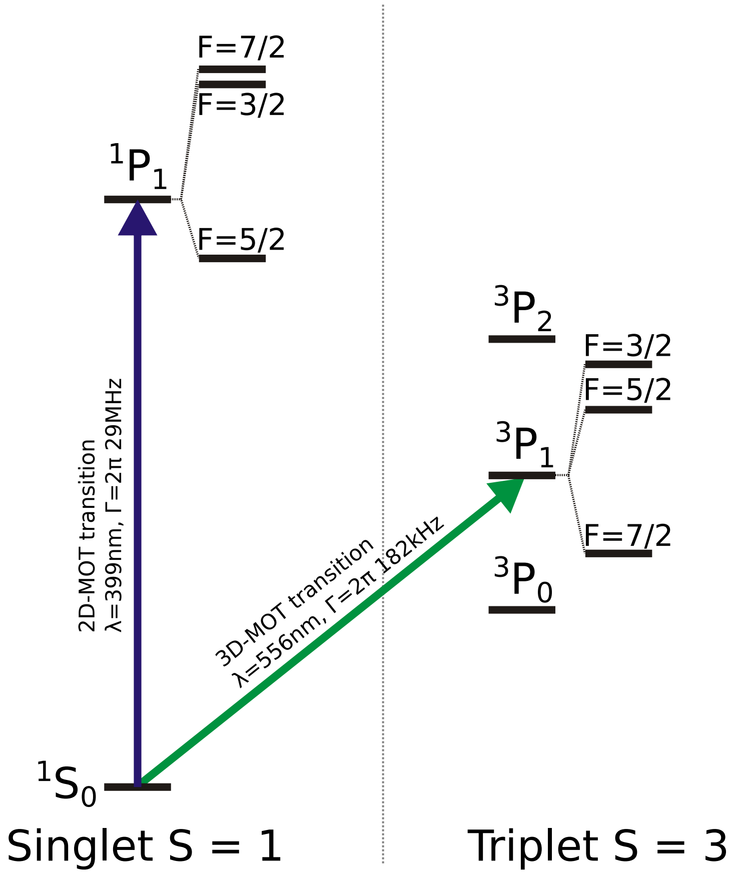

Figure 1.1.: Relevant atomic transitions for the Yb MOT. The sketch shows the lowest lying energy levels for the Singlet and Triplet branch of Yb. Hyperfine splittings are indicated for the ^{173}Yb ($I = 5/2$) isotope. Only the relevant MOT transitions are highlighted. The inter-combination transition is highly suppressed, which is indicated by the narrow linewidth for 556 nm. The sketch is not to scale.

$^1\mathrm{S}_0 \Leftrightarrow {}^3\mathrm{P}_1$		$^1\mathrm{S}_0 \Leftrightarrow {}^1\mathrm{P}_1$	
Isotope	Shift (MHz)	Isotope	Shift (MHz)
$^{173}\mathrm{Yb}\left(\frac{7}{2}\right)$	-2386.7	$^{176}\mathrm{Yb}$	-509.3
$^{171}\mathrm{Yb}\left(\frac{1}{2}\right)$	-2132.1	$^{173}\mathrm{Yb}\left(\frac{5}{2}\right)$	-253.4
$^{176}\mathrm{Yb}$	-954.8	$^{174}\mathrm{Yb}$	0.0
$^{174}\mathrm{Yb}$	0.0	$^{173}\mathrm{Yb}\left(\frac{3}{2}\right)$	516.0
$^{172}\mathrm{Yb}$	1000.0	$^{172}\mathrm{Yb}$	533.3
$^{170}\mathrm{Yb}$	2286.3	$^{173}\mathrm{Yb}\left(\frac{7}{2}\right)$	588.0
$^{173}\mathrm{Yb}\left(\frac{5}{2}\right)$	2311.4	$^{171}\mathrm{Yb}\left(\frac{3}{2}\right)$	832.4
$^{168}\mathrm{Yb}$	3655.2	$^{171}\mathrm{Yb}\left(\frac{1}{2}\right)$	1153.7
$^{171}\mathrm{Yb}\left(\frac{3}{2}\right)$	3804.6	$^{170}\mathrm{Yb}$	1192.4
$^{173}\mathrm{Yb}\left(\frac{3}{2}\right)$	3807.3	$^{168}\mathrm{Yb}$	1887.4

Table 1.3.: Isotope shifts of Yb. The table shows isotope shifts and hyperfine states of Yb for the transitions used in the 2D/3D-MOT setup. The values are given with respect to the ^{174}Yb frequencies.

1.2. The experimental apparatus

The schematics of the vacuum chamber are shown in Fig. 1.2. *Blue* (top) and *green* (bottom) MOT are located in individual glass cells, which are connected via a differential pumping stage. To both we applied a broadband, anti reflex coating from the outside. Each glass cell is connected to a $55\,\mathrm{l\,s^{-1}}$ ion pump and we typically observe pressures of $1.2 \times 10^{-9}\,\mathrm{mbar}$ in the 2D-MOT cell and $1.4 \times 10^{-10}\,\mathrm{mbar}$ in the 3D-MOT cell during standard sequences.

The Yb dispenser is located in the 2D-MOT cell, where the atomic beam is truncated using an aperture and directed towards the center of the glass cell, above the differential pumping stage. Here, two counter propagating laser beams at the *blue* transition intersect to cool them in the horizontal plane. Both beams are elliptically shaped to resemble the oval form of the atomic beam emitted by the dispenser. Since the atoms are not cooled in the vertical direction, they propagate through the differential pumping stage into the science cell. This process is enhanced via a near-resonant push beam from the top of the cell. The science cell is intersected by three counter propagating beams at the inter-combination transition to capture the 3D-MOT and shelve the atoms for further cooling processes.

Both MOT cells are surrounded by water-cooled coils for producing the magnetic field gradients. The 2D-MOT field is created by four rectangularly shaped coils with $4.6\,\mathrm{G\,cm^{-1}\,A^{-1}}$. With the presently implemented power supply we can reach gradients up to $56.5\,\mathrm{G\,cm^{-1}}$. The 3D-MOT field is created by two coils that can be switched between Helmholtz and Anti-Helmholtz configuration with $6\,\mathrm{G\,A^{-1}}$ and $1.3\,\mathrm{G\,cm^{-1}\,A^{-1}}$ respectively. Our power supply can deliver up to $140\,\mathrm{A}$ enabling us to produce offset fields up to $800\,\mathrm{G}$ and gradients up to $180\,\mathrm{G\,cm^{-1}}$.

In addition to the main coils, the science cell is surrounded by a cage of coils to generate offset fields for compensating stray magnetic fields and to produce quantization axes along different directions (cf. Chap. 3). For each axis three pairs of coils are available for various configurations [Dör13a]. The conversion can be as high as $1.79\,\mathrm{G\,A^{-1}}$, which results in an offset field of up to $10.7\,\mathrm{G}$ with our current power supply.

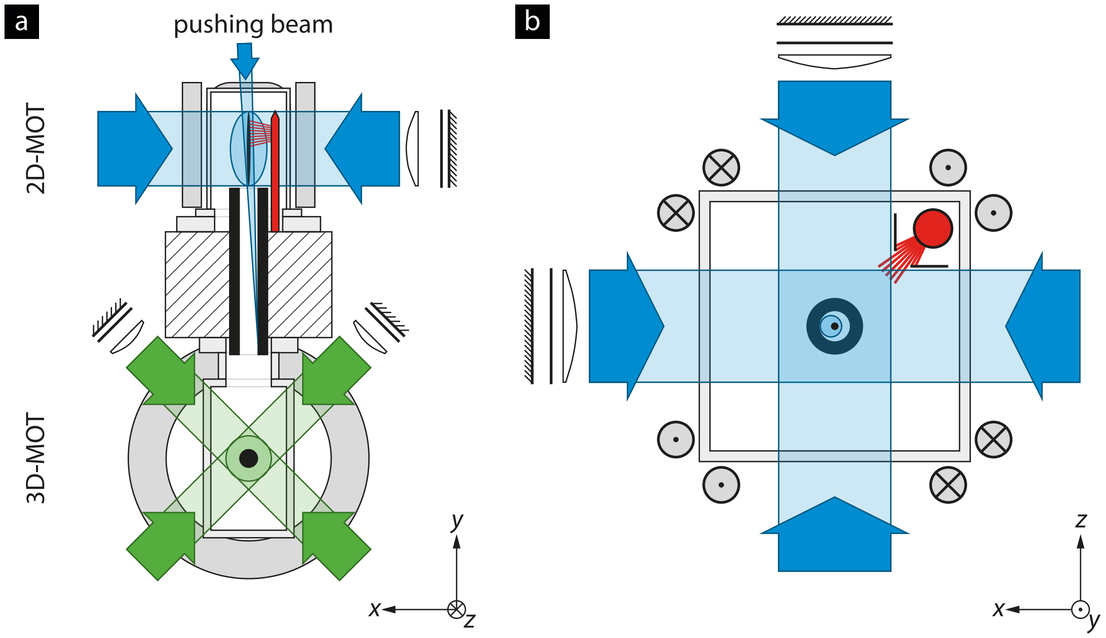

Figure 1.2.: Schematics of the 2D/3D-MOT setup. (a) The sketch shows a side view onto our vacuum apparatus. The 2D-MOT cell is located at the top illuminated with two counter propagating beams at the *blue* transition. The magnetic coils are next to the cell colored in gray. An atomic beam is generated via a dispenser (red), which points towards the crossed area of the 2D-MOT. The MOT loading rate is significantly increased using a push beam slightly red detuned to the resonance which is applied from the top and blocked by the differential pumping stage (black tube). The latter one connects both glass cells. The 3D-MOT cell is located at the bottom illuminated with three counter propagating laser beams at the *green* intercombination transition. The large, circular magnetic coils are colored in gray. **(b)** The drawing shows an enlarged view from above. The two counter propagating beams cross right above the pumping stage. They are intersected by the push beam. The aperture, which cuts off the atomic beam, in front of the dispenser is visible. The positioning of the magnetic coils is indicated including the current direction for generating a field gradient. The graphic was taken from [Dör13a].

1.3. Laser system for the $^1S_0 \Leftrightarrow {}^1P_1$ and $^1S_0 \Leftrightarrow {}^3P_1$ transition

The goal of the new laser setup was to increase its reliability concerning long-term lock stability. In addition, it should have the capability to provide two frequencies simultaneously for the preparation of isotope mixtures. The following chapter presents the crucial parts of this system. A detailed descriptions can be found in B. Abeln's Master thesis [Abe16].

1.3.1. *Blue* laser system

A sketch of the *blue* laser system is shown in Fig. 1.3. Two commercial laser sources[1], *Master Blue*[2] and *SHG Blue*, deliver an output power of $120\,\mathrm{mW}$ and $320\,\mathrm{mW}$ respectively.

---

[1] Toptica DL PRO, Toptica SHG PRO

[2] From our experience, the blue laser diodes tend to have a narrow current range in which they operate with a single longitudinal mode even though they are actively stabilized. Although this got improved a lot by using

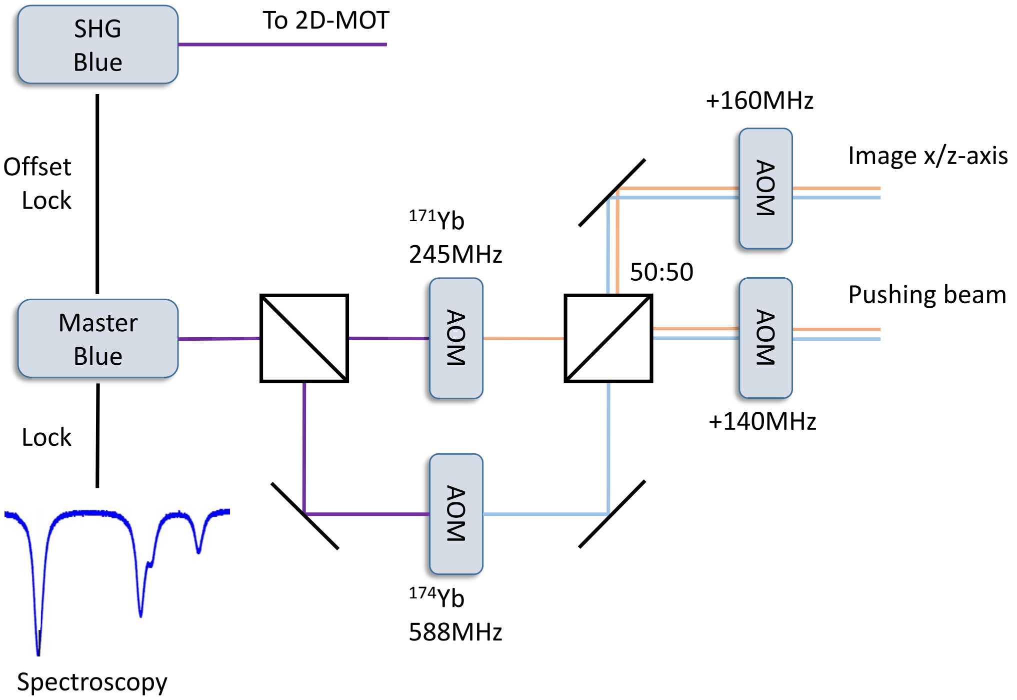

Figure 1.3.: Laser system for *blue* transition. The sketch shows a simplified version of the 399 nm laser setup in case of ^{171}Yb/^{174}Yb operation. The *Master Blue* laser is stabilized to a beam apparatus via absorption spectroscopy. Its light is used for imaging and the push beam. To simultaneously generate frequencies for two isotopes the beam is split to individually shift both branches with AOMs. The beams are then superimposed with a non-polarizing beam splitter. The *SHG Blue* laser is solely used for the 2D-MOT. It is stabilized with an offset lock, which can be tuned via a digital reference frequency. All AOMs, except for the 245 MHz one, are set into double pass configuration. The graphic taken from [Abe16].

The *Master Blue* laser provides light for absorption imaging[3], push beam (detuned by -20 MHz), spectroscopy using a beam apparatus and an offset lock between both lasers. The *SHG Blue* laser provides light for the 2D-MOT.

To ensure proper frequency stability, the *Master Blue* laser is locked to an atomic resonance via absorption spectroscopy [Bjo83]. Techniques involving the Doppler free signal are not necessary, because Doppler broadening is on the order of the linewidth. The error signal is generated via frequency modulation of an acousto-optic modulator (AOM) and a lock-in amplifier. The signal quality in case of the ^{174}Yb isotope is comparably better than for the other isotopes mainly due to the different abundances. To circumvent this issue we implemented an EOM[4] which allows bridging all isotope shifts. For instance, to lock the laser to ^{173}Yb the EOM frequency is

---

a commercial laser system instead of a home-build ECDL, we still keep a Fabry-Pérot interferometer in use to conveniently verify proper single-mode behavior of this laser.

[3] Details concerning the imaging setup can be found in [Sob14, Hun16].

[4] Qubig - EO-T990K3

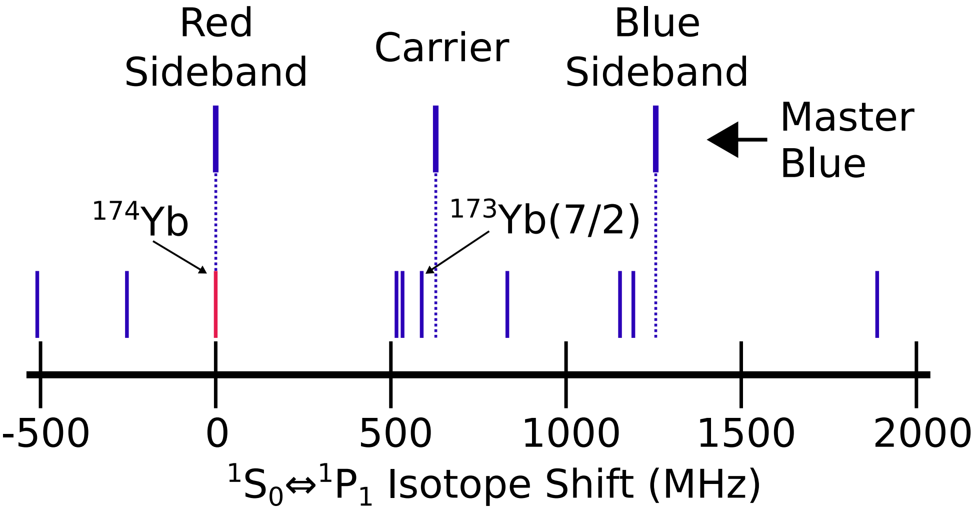

Figure 1.4.: Locking scheme for the *blue* transition using an EOM. The scheme shows the frequency relation between the *Master Blue* laser with respect to the isotopic shifts of the *blue* transition (cf. Tab. 1.3). The situation is exemplary depicted for ^{173}Yb operation. In this case the laser is $40\,\mathrm{MHz}$ blue detuned with respect to the $^1S_0 \Leftrightarrow {}^1P_1(F = 7/2)$ transition. Red and blue sidebands are generated via phase modulation using an EOM. The red sideband is resonant with the ^{174}Yb isotope and used for frequency stabilization. See the main text for more details.

set to $628\,\mathrm{MHz}$ to span the $^{174}\mathrm{Yb} \Leftrightarrow {}^{173}\mathrm{Yb}\left(\frac{7}{2}\right)$ frequency difference plus additional $40\,\mathrm{MHz}$. This situation is illustrated in Fig. 1.4. In this case we can use the red sideband to lock the laser to the ^{174}Yb isotope while the carrier and blue sidebands are not resonant with any other isotope. Finally, to implement resonant light for ^{173}Yb at the experiment the AOM used for locking is set to $100\,\mathrm{MHz}$ (double pass) and the AOMs directed towards the experiment are set to $-80\,\mathrm{MHz}$ (double pass). The EOM is equipped with an adjustable resonance circuitry which makes applying this procedure to other isotopes very convenient.

To generate blue light for two isotopes simultaneously, we split the beam of the *Master Blue* laser and shift the branches individually to cover the isotope shifts with respect to the lock point. Behind the AOMs, we superimpose the beams using a non-polarizing beam splitter. Further AOMs allow us to switch and adjust power and frequency of the superimposed beam.

The *SHG Blue* laser is located next to the main experiment with free space access to the 2D-MOT cell. Since the blue transition has a large saturation intensity, we decided to have as much power as possible available at the 2D-MOT and discarded earlier setups that involved fibers to transport light to the experiment. Thus we avoided power loss due to fiber-incoupling efficiency and long-term fiber degredation caused by facette bruning and solarization effects [Kle97]. The laser is switched via a shutter, because no special care needs to be taken for the timing due to long MOT loading times (typ. $30\,\mathrm{s}$). Frequency stabilization is carried out with a home build phase detector and PI regulation loop (offset lock) [App09]. The lock point can be changed to cool different isotopes via an external digital reference signal. In the case of two-isotope operation, the 2D-MOT will be loaded sequentially by changing the lock point during an experimental cycle via the external reference signal.

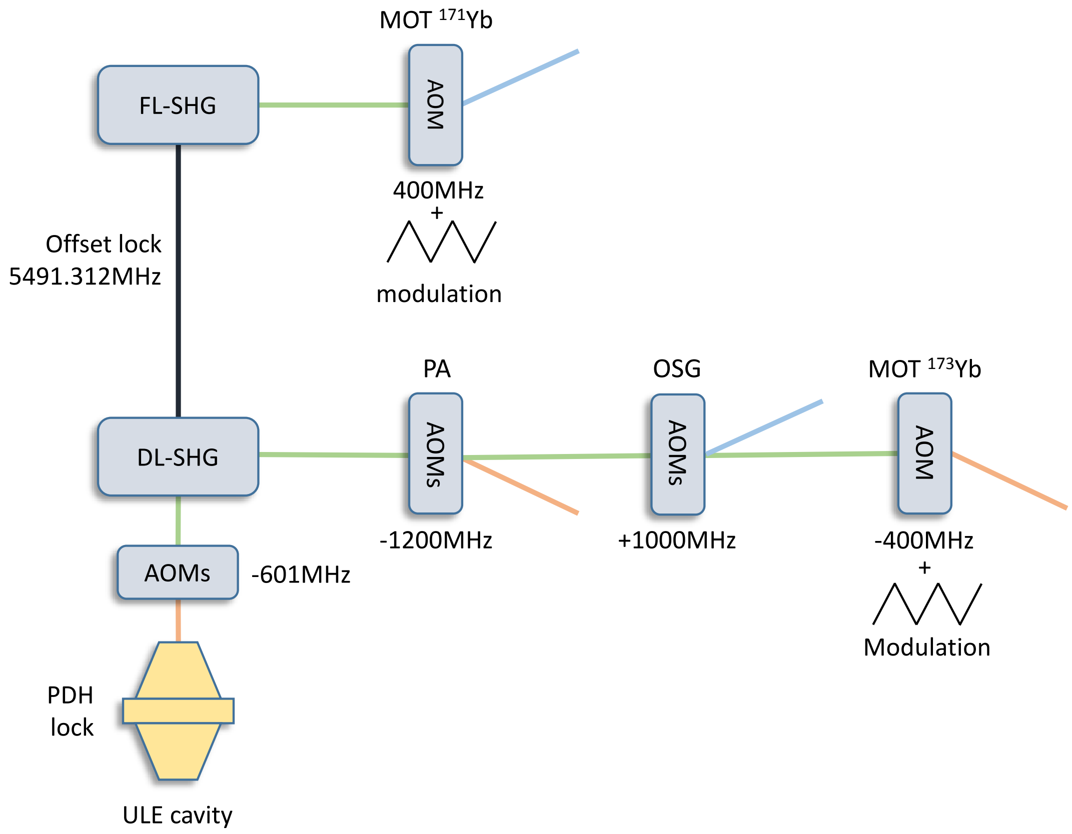

Figure 1.5.: Laser system for the *green* transition. The sketch shows a simplified layout of the *green* laser setup for ^{171}Yb/^{173}Yb operation. The *DL-SHG* laser is locked to an optical resonator via PDH technique. All of the laser power can be used for OSG, PA and MOT, because these frequencies are not used simultaneously. The other isotope can be cooled with the *FL-SHG* laser. Frequency stability is reach via an offset lock, which can be adjusted using a digital reference source. Both AOMs for the 3D-MOTs can be used to *FM* broaden the laser widths for improved atom capturing. “AOMs“ is representative for two and three units in a row. OSG: Optical-Stern-Gerlach, PA: Photo association, PDH: Pound-Drever-Hall, ULE: Ultra-Low-Expansion. The graphic was taken from [Abe16].

1.3.2. *Green* laser system

The setup for the *green* transition is shown in Fig. 1.5. The light is emitted by two commercial laser sources[5], *DL-SHG* and *FL-SHG*, with output powers of $350\,\mathrm{mW}$ and $250\,\mathrm{mW}$ respectively. Since both lasers have sufficient output power, we decided to plan a two-frequency 3D-MOT, where each laser provides light for one isotope. Further, the *DL-SHG* generates light for Optical-Stern-Gerlach- (OSG, cf. Chap. 2) and photo-association-like (PA) [Toj06] experiments. Since the last two applications involve a laser detuning on the order of $1\,\mathrm{GHz}$ with respect to the atomic resonance, we built two switchable beam paths, each including three AOMs in series. This way, we can use the full power of the *DL-SHG* for MOT, OSG and PA experiments.
Frequency stability for both lasers is achieved in the following way: Due to the narrow linewidth

---

[5] Toptica SHG PRO, Menlo Systems Orange one-SHG

of the *green* transition, the error signal amplitude received from Doppler-free absorption spectroscopy [Dem15] is rather small. To avoid poor locking performance we instead use an Ultra-Low-Expansion (ULE), high-finesse, optical resonator as a reference system on which we apply a Pound-Drever-Hall locking (PDH) technique [Bla01] to stabilize the *DL-SHG*. Since the tunability of the absolute frequency of the cavity modes (free spectral range about $2\,\mathrm{GHz}$) is very limited, we use two AOMs to cover eventual frequency differences between the cavity and the atomic resonance. The stability of the frequency chain including the cavity and all used AOMs is sufficient, such that we merely adjust it by some kHz per day. The *FA-SHG* is stabilized using an optical-phase-locked loop (OPLL) [Xu12] with a commercial frequency-phase detector and proportional-integral-derivative (PID) controller [6]. The frequency difference between both lasers can be adjusted using a digital radio-frequency (RF) source. The schematics are shown in Fig. 1.6.

As described in Sec. 1.1, the linewidth of the *green* transition is rather narrow ($\Gamma_{556} = 2\pi \times 182\,\mathrm{kHz}$). To circumvent the efficiency loss due to a reduced velocity capture range, we spectrally broaden the lasers. This is carried out by the switching AOMs onto which we apply a frequency modulation. During each MOT cycle the initial broadening and the detuning with respect to atomic resonance is linearly reduced towards final compression. This is used to optimize the loading efficiency of our dipole trap. The 3D-MOT stages are in detail:

- First stage: Atoms are being loaded at a large detuning -$6.7\,\mathrm{MHz}$, a spectral broadening of $7\,\mathrm{MHz}$ and a field gradient of $2\,\mathrm{G\,cm^{-1}}$. This stages lasts $10\,\mathrm{s}$ to $30\,\mathrm{s}$ depending on the desired number of atoms.

- Second stage: The detuning and spectral broadening are reduced to -$1.6\,\mathrm{MHz}$ and $2.3\,\mathrm{MHz}$ respectively and the field gradient increased to $10\,\mathrm{G\,cm^{-1}}$. The laser power is reduced by 30%. This stage lasts $200\,\mathrm{ms}$.

- Third stage: The detuning[7] is further decreased to -$0.74\,\mathrm{MHz}$ and the spectral broadening is switched off. The laser power is reduced to 4% of the initial value. The field gradient stays constant. This stage lasts $200\,\mathrm{ms}$.

The laser light is guided to the main experiment via optical fibers, overlapped on a rigidly-constructed, optical setup (cluster) and distributed towards the MOT telescopes. Each of these fibers is monitored with a PD before distribution to actively stabilize the fiber coupling.

1.4. MOT characterization for ^{171}Yb, ^{173}Yb and ^{174}Yb

As a prerequisite for a two-isotope MOT, we analyzed the performance for each isotope individually. As light source for the 3D-MOT we always used the *FL-SHG*, the *DL-SHG* merely ensured frequency stability via the OPLL. All measurements were taken at about the same time and with little changes to the opto-mechanical MOT alignment to have a certain comparability between different isotopes. Furthermore, in the case of ^{173}Yb it is crucial to set the 2D-MOT

---

[6] Menlo Systems, SYNCRO

[7] The rather large end detuning might be influenced by a laser linewidth on the order of $100\,\mathrm{kHz}$.

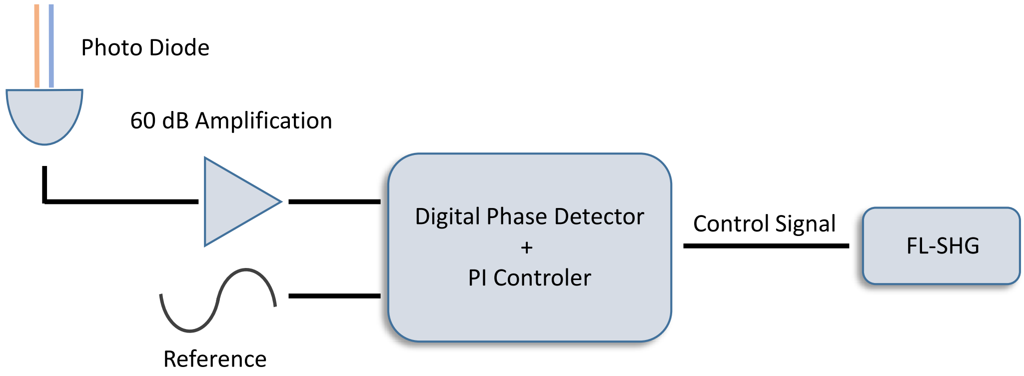

Figure 1.6.: Frequency stabilization of the *FL-SHG* laser. The sketch shows a simplified version of our locking setup. The *DL-SHG* laser is referenced to an optical resonator via *PDH* technique (omitted). Frequency stability for the *FL-SHG* laser is achieved via an *OPLL*. Both lasers are overlapped onto a fast photodiode. The resulting beat note is mixed with a digital RF source. A digital phase detector generates the error signal for a *PID* regulation loop, which acts on the piezo of the *FL-SHG* laser. The graphic was taken from [Abe16].

polarization to an empirical, elliptical setting different from pure circular. To our knowledge, only in this way we can reach sufficient MOT performance.
To change the experiment for cooling different isotopes we change the frequencies of all involved lasers. This means locking the *Master Blue* laser to a different isotope via the beam apparatus, change the cavity mode the *DL-SHG* is locked to and adjust the digital references in case of *SHG Blue* and *FL-SHG*.

1.4.1. Loading rate of the 3D MOT

To quantify the MOT performance for different isotopes we recorded loading curves for a maximum duration of $55\,\mathrm{s}$. The imaging beam was strongly detuned to avoid saturation effects during loading: $\Delta_{171} = 1.4\,\Gamma_{399}$, $\Delta_{173} = 1.6\,\Gamma_{399}$, $\Delta_{174} = 2.4\,\Gamma_{399}$. We calculated the actual amount of detected atoms using [Ste13]

$$R_{\mathrm{sc}} = \frac{\Gamma}{2}\frac{(I/I_{sat})}{1+4(\Delta/\Gamma)^2+(I/I_{sat})}. \tag{1.1}$$

In the case of low saturation $s = I/I_{sat} \ll 1$ the atom number can be extrapolated with

$$N_{\mathrm{act}} = N_{\mathrm{measured}} \times (1+4(\Delta/\Gamma)^2).$$

The result is shown in Fig. 1.4.1. The loading rates can be estimated via an exponential scaling law

$$N = N_{\mathrm{max}}(1-e^{-t/\tau}) \Rightarrow \dot{N}(t=0) = N_{\mathrm{max}}/\tau. \tag{1.2}$$

This gives initial loading rates of

$$\begin{aligned}
\dot{N}(t=0,{}^{171}\mathrm{Yb}) &= 1.59(2)\times 10^6\,\mathrm{s}^{-1},\\
\dot{N}(t=0,{}^{173}\mathrm{Yb}) &= 0.32(3)\times 10^6\,\mathrm{s}^{-1},\\
\dot{N}(t=0,{}^{174}\mathrm{Yb}) &= 2.24(1)\times 10^6\,\mathrm{s}^{-1}.
\end{aligned}$$

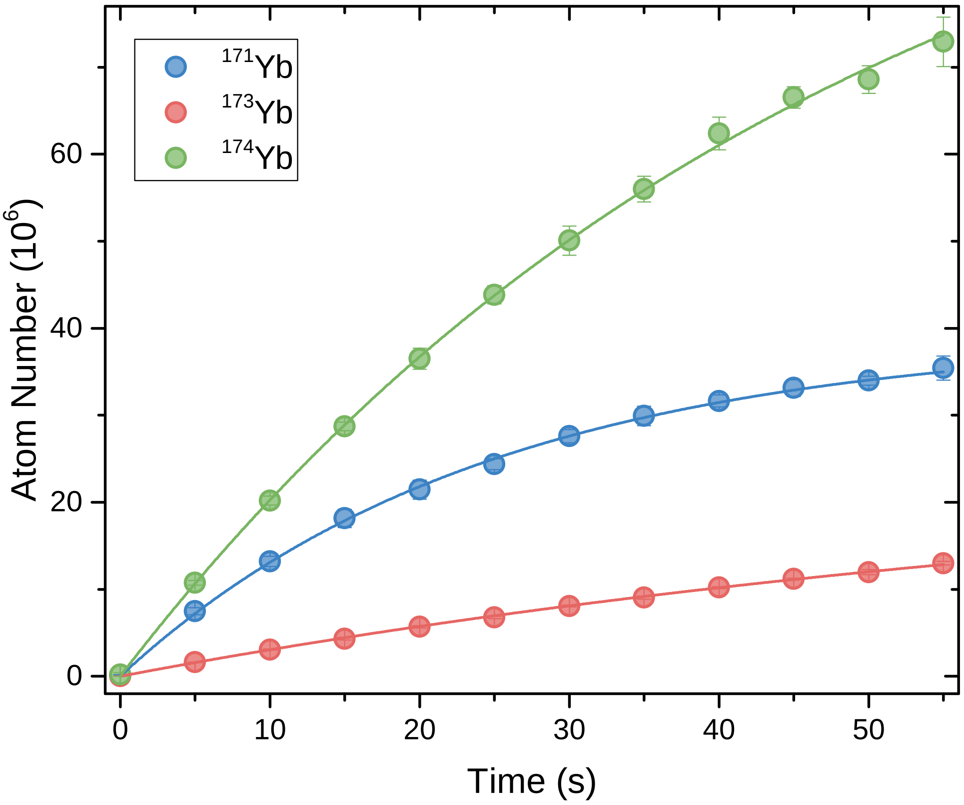

Figure 1.7.: MOT loading rates. The plot shows the loading curves for the isotopes ^{171}Yb, ^{173}Yb and ^{174}Yb for durations up to 55 s. Each isotope is loaded individually. Solid lines are fits according to Eq. (1.2). The fit results can be found in the main text.

Normalizing the loading rates according to the isotope abundance (Tab. 1.1) actually yields a MOT performance as $1.6 : 0.3 : 1$ for ^{171}Yb, ^{173}Yb and ^{174}Yb respectively. From previous works [Muk03] we expect the loading performance of ^{173}Yb to be greatly decreased due to the following reasons: 1. The g-factors of $^1S_0$ and $^1P_1$ are very different leading to a situation, where the Zeeman shift is dominated by the excited state. This configuration significantly deviates from the alkali-metal case, where the Zeeman shifts of ground and excited states are similar. This effectively reduces the capability to cool all m_F states equally well. 2. Due to the hyperfine splitting, the $F = 3/2$ state is located about $-2.5\,\Gamma_{399}$ with respect to the cooling transition $F = 7/2$. Thus, tuning the cooling-laser frequency too far red with respect to the $F = 7/2$ transition results in an anti-trapping force [Hon99, Rap04]. This sharp cut-off will be visible in the last part of this section. The MOT for ^{171}Yb shows even a better, normalized, loading rate compared to ^{174}Yb. A possible explanation is our 2D-MOT setup, which is optimized for best ^{173}Yb MOT performance. We experienced significant difference between the MOT beam geometry for optimal ^{173}Yb and ^{174}Yb loading rate. The herein shown value for ^{174}Yb is actuall about a factor of five lower compared to the highest observed value.

To possibly circumvent the unfavorable situation regarding the hyperfine splitting of ^{173}Yb, we tried to operate the MOT using the $^1P_1(F = 5/2)$ state, so effectively $F' = F$. For an idealized 1D MOT with $F = 1 \Rightarrow F' = 1$ it is not possible to effectively capture atoms due to the arising dark states. However, in case of larger F quantum numbers, as is the case for Yb, this argument is weakened due to the Clebsch-Gordon (CG) coefficients which favor states with a small $|m_F|$. In 2D, i.e. two counter-propagating beams, occurrence of dark states should be further suppressed because of pumping processes mediated by the perpendicularly arranged laser beams. These shift the mainly used $|m_F|$ transition to generate an effective slowing force [Tar15]. Still, these effects usually lead to a reduced MOT efficiency compared with the ideal case. So far we have not been able to demonstrate atom capture on the $F' = 5/2 \Rightarrow F = 5/2$ transition. Currently we pursue numerical analysis following a semi-classical approach, which includes our present 2D-MOT system and the level properties of Yb, to get a better idea on how to improve the performance. Details can be found in [Hil17].

Although this performance is surpassed by other Yb experiments [Sca15, Pag14] it is sufficient for reproducible production of ultracold quantum gases. Typically we load the MOT for $10\,\mathrm{s}$ in case of bosonic ^{174}Yb and for $30\,\mathrm{s}$ in case of fermionic ^{173}Yb. We have not yet produced ultracold ^{171}Yb gases, because this would involve sympathetic cooling with other Yb isotopes or Rb atoms due to the s-wave scattering length of this isotope. However regarding the MOT loading rate, we expect the same performance as in case of ^{174}Yb.

1.4.2. Dependence between MOT loading and push beam power

The push beam plays an important role because it helps to increase the MOT loading rate in a manageable manner. The geometry between 2D-MOT and push beam can be seen in Fig. 1.2. It has a diameter of a few mm within the 2D-MOT volume, is slightly tilted and focused inside the differential pumping stage to prevent *blue* photons to reach the 3D-MOT, which can reduce the loading rate due to their large radiation pressure ($\Gamma_{399} = 29.1\,\mathrm{MHz}$). Furthermore, the detuning is set to $-20\,\mathrm{MHz}$ with respect to atomic resonance. Combined with the beam focus this effectively applies an attractive channel for the atoms. Ideally, the 2D-MOT is first adjusted without the push beam, to find a well balanced alignment. Afterwards, it is switched on and the beam angle is adjusted for optimal loading.

Although for previous settings we could improve our loading rate by a factor of three for ^{174}Yb [Dör13a], this was not possible for the fermionic isotopes. Especially after adjusting the 2D-MOT for optimal ^{173}Yb performance the push beam can improve the loading rate by merely 50% for all three isotopes. The data showing the dependence between loading-rate improvement and push beam power is shown in Fig. 1.8.

The figure shows very similar, optimal powers for all three isotopes. For best performance we use around $250\,\mu\mathrm{W}$. The plot might suggest a marginal larger optimal power in case of ^{171}Yb, however this conclusion should be regarded carefully. The alignment of the 2D-MOT is very sensitive and it was possibly reproduced in the exact same manner.

From our experience we could not find any significant dependence of the push-beam polarization and the MOT loading rate. This seems reasonable because the beam hits the MOT under an angle such that beam and gradient field are not aligned in any specific way. Additionally, the continuous pumping processes during the MOT repopulate the ground state manifold continuously. Consequently, the push beam applies to all states equally and one specific polarization can not change its effective force.

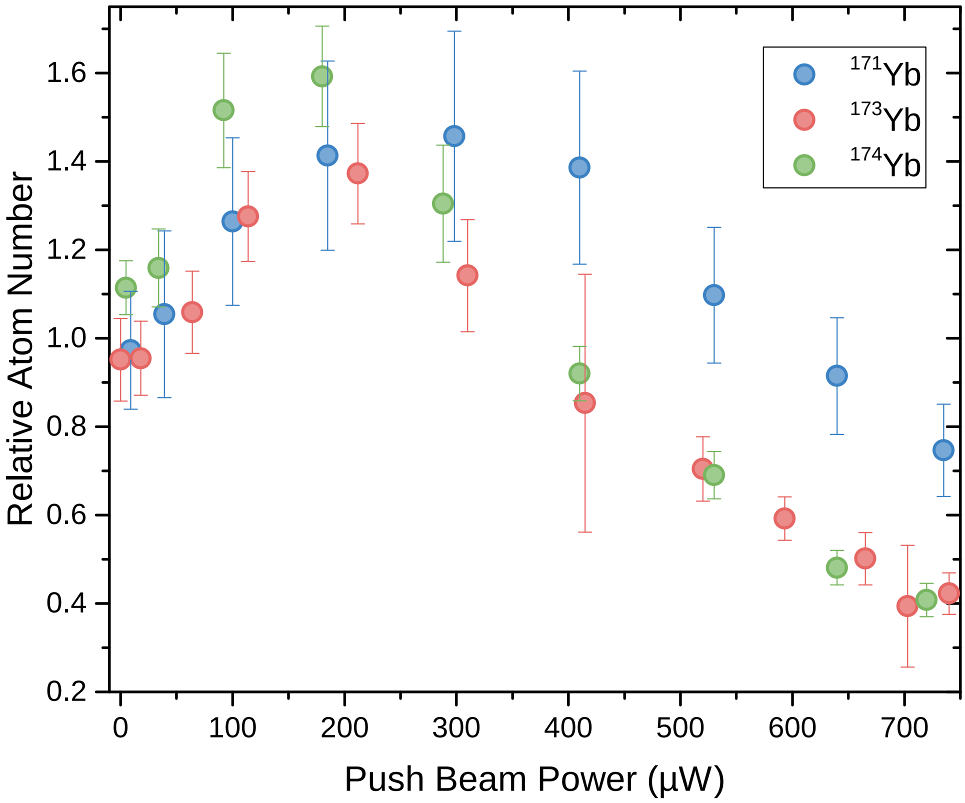

Figure 1.8.: Effect of the push beam. The plot shows the relative increase of loading performance for the isotopes ^{171}Yb, ^{173}Yb and ^{174}Yb depending on the push beam power. For optimal operation we use a power of $200\,\mu\mathrm{W} - 300\,\mu\mathrm{W}$. This improves our MOT performance up to 60%. More details can be found in the main text.

1.4.3. Dependence between MOT loading and 2D-MOT-laser power

Due to the saturation intensity of the *blue* MOT transition the requirements on laser power are more demanding as compared to alkaline-metal experiments. With the present laser setup we reach a peak saturation of about $s = I/I_{\mathrm{sat}} = 1.6$ at the center of the MOT beams with $150\,\mathrm{mW}$ of power in each beam and diameters of $1\,\mathrm{cm}$ and $4\,\mathrm{cm}$. Typically, Rb experiments can easily reach $s \geq 6$ [Erh04], which makes the setup more robust against missalignment of the beams. We analyzed the 2D-MOT performance depending on *blue* laser power by stepwise reducing the tampered amplifier power of the *SHG Blue* laser. The 2D-MOT was not realigned inbetween. The data is shown in Fig. 1.9. The loading times are $2.5\,\mathrm{s}$, $3\,\mathrm{s}$ and $2\,\mathrm{s}$ for ^{171}Yb, ^{173}Yb and ^{174}Yb respectively

The results show an increased MOT performance for higher 2D-MOT laser power which follows from an increased scattering rate. Furthermore, the graphs show a rather strong curvature, which might suggest that the MOT operates in a regime of high saturation. With our laser parameters we barely reach

$$R_{\mathrm{sc}}\frac{2}{\Gamma} \approx \frac{s}{s+5} = 0.24 \tag{1.3}$$

as estimation for the beam center (Eq. (1.1), $\Delta_{399} = \Gamma_{399}$). Comparing this with Fig. 1.10 this seeming saturation can hardly be explained by laser-power saturation effects. For our values

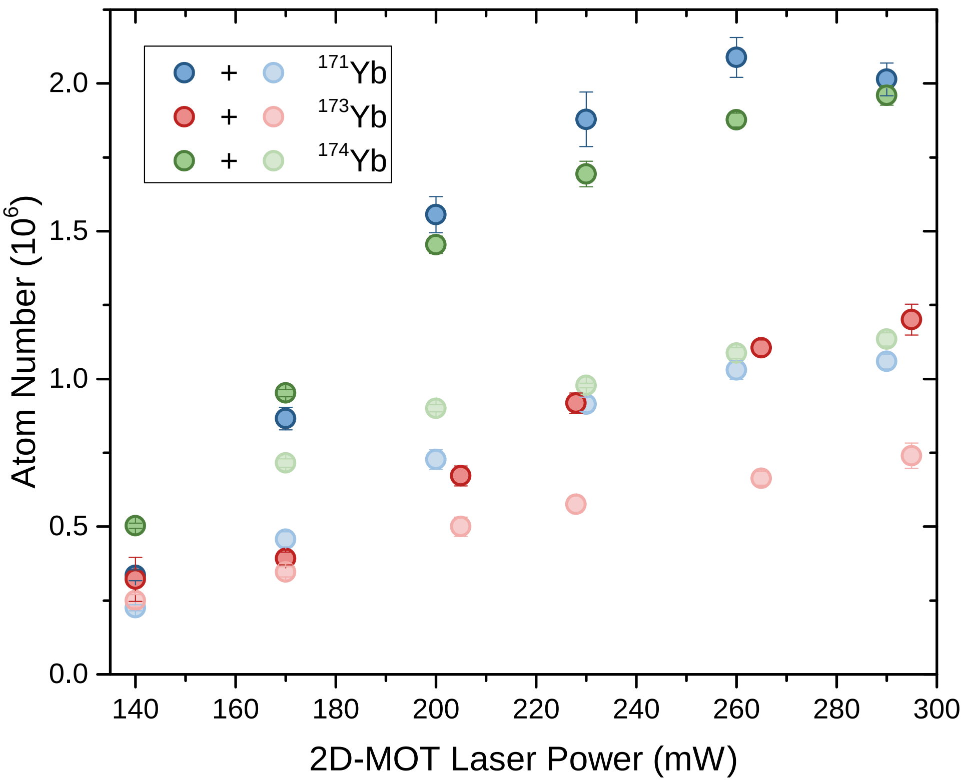

Figure 1.9.: Effect of 2D-MOT-laser power. The plot shows loading curves for the isotopes ^{171}Yb, ^{173}Yb and ^{174}Yb depending on the 2D-MOT laser power for 2.5 s, 3 s and 2 s loading time, respectively. Light colors indicate the push beam being switched off. In principle, the MOT performance increases with the laser power, which is still far from saturation of the transition. The data points seem to imply saturation effects of the loading, which cannot be attributed to the laser power. It is rather an effect of the sensitivity of MOT alignment. See the main text for more detail.

the dependence on bare laser power should be almost linear. We thus assume that the curvature is a result of a power dependent 2D-MOT alignment. Consequently, we expect our MOT to significantly benefit from a stronger laser source. In that case however, a realignment will be necessary.

Comparing the push beam performance in Fig. 1.9 to the previous section, it is noticeable that we reach higher loading-rate enhancement than before. For the highest 2D-MOT laser power we observe an improvement of about 2 (^{171}Yb), 1.5 (^{173}Yb) and 1.7 (^{174}Yb). As explained before, alignment of the 2D-MOT is very sensitive and this needs to be carried out regularly to reproduce sufficient MOT performance. Very likely the adjustment of the 2D-MOT laser beams with respect to the push beam and differential pumping stage causes this effect. Due to the low saturation, our setup might be more susceptible to these effects compared to experiments with high-power laser sources.

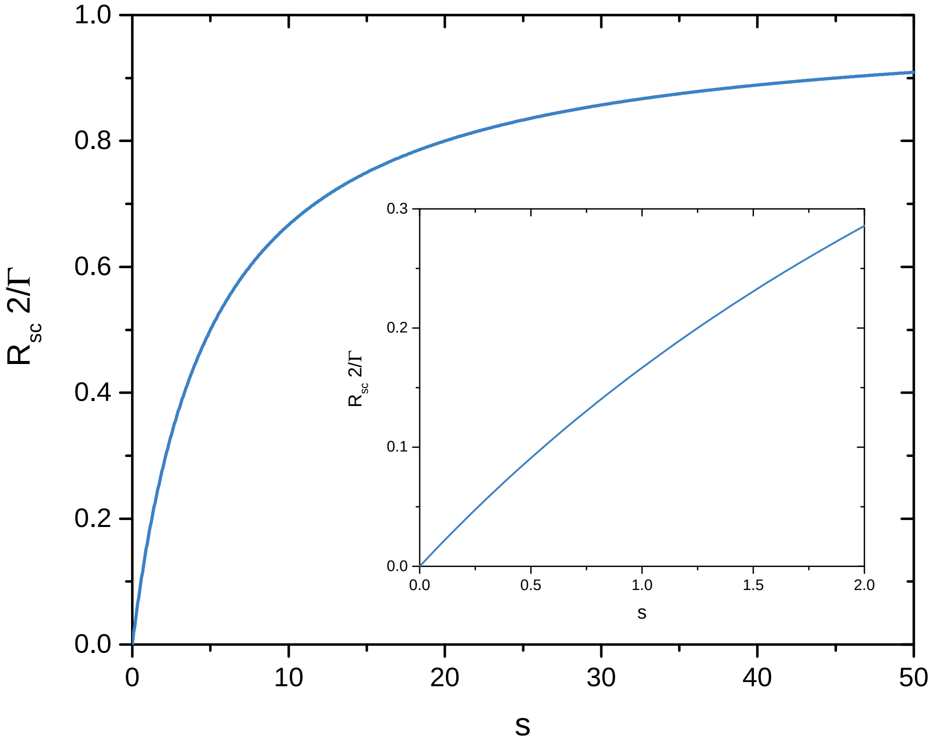

Figure 1.10.: Dependence between scattering rate and laser power. The scattering rate is normalized with $\Gamma/2$ and plotted with respect to the saturation $s = I/I_{\text{sat}}$ according to Eq. (1.3). For a parameter $s = 0.24$ the MOT performance is far from saturation limited and the scattering rate shows an almost linear dependence on s.

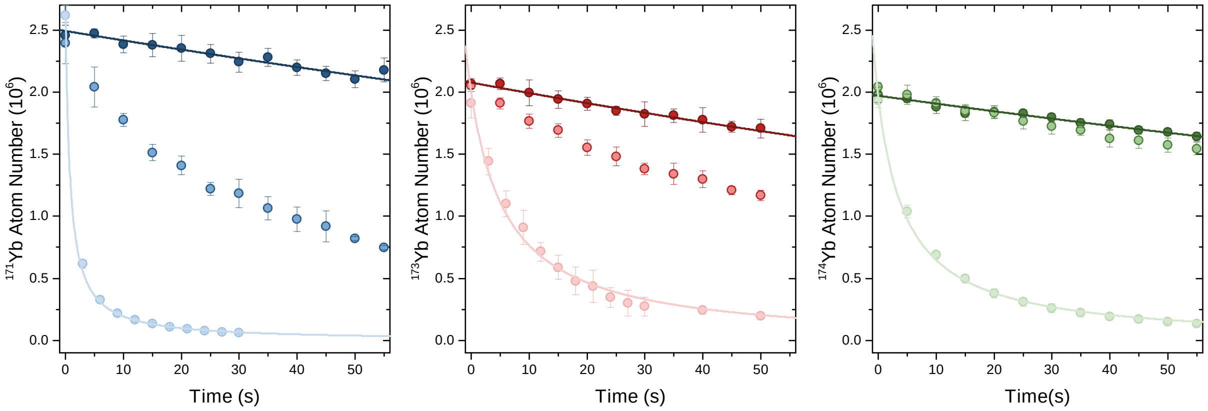

Figure 1.11.: MOT lifetime during different compression stages. The plots show the atom decay during different stages of the MOT for the isotopes ^{171}Yb, ^{173}Yb and ^{174}Yb. The colors illustrate different steps during MOT cycles. From dark to light colors: without compression, first and second compression. The dark solid lines give results according to Eq. (1.4), the light solid lines to Eq. (1.5). Fit results can be found in the main text. The lifetime after the first MOT stage is $\geq 240\,\mathrm{s}$ for all isotopes, making this part of the sequence ideal for two isotope operation. All data sets are averaged five times. Error bars are not always visible due to their size.

1.4.4. MOT lifetime during its different phases

For producing isotope mixtures the MOT needs to be operated with two different frequencies. The previous section demonstrated that the 2D-MOT performance is limited by the available laser power. Thus, operating the 2D-MOT sequentially is a power saving approach. Consequently, it is crucial to temporary shelf one isotope in the science cell. This can for instance be achieved by using the 3D-MOT. It is therefore important if and how the lifetime differs between the isotopes and the MOT stages (cf. Sec. 1.3.2). We measured the lifetimes of ^{171}Yb, ^{173}Yb and ^{174}Yb after each MOT stage. The 3D-MOT settings are kept unchanged between isotope switching. The results can be found in Fig. 1.11.

Evidently, the atomic lifetime depends severely on the different MOT phases and isotope choice. The results with the initial laser settings show very long lifetimes. We modeled this atom loss using a simple exponential decay law according to

$$\frac{\mathrm{d}N}{\mathrm{d}t} = -\gamma N \Rightarrow N = N_0\,\mathrm{e}^{-\gamma t}, \tag{1.4}$$

where $N(t)$, γ and N_0 denote the atom number depending on time, the decay constant and the initial atom number respectively. This is appropriate for a situation that is dominated by losses via the background gas. The fit results are:

	$\gamma\ (10^{-3}\,\mathrm{s}^{-1})$
^{171}Yb	$3.1(2)$
^{173}Yb	$4.2(2)$
^{174}Yb	$3.3(1)$

For all three isotopes the fits resemble the data very well and $\gamma^{-1} \geq 240\,\mathrm{s}$, which is an extremely long lifetime on all of our experimental time sales.

During the MOT phases with reduced broadening and detuning the results can not be described by a simple exponential decay law. These can rather be approximated with an additional term and respective two-body-loss parameter β [Ses89]:

$$\frac{\mathrm{d}N}{\mathrm{d}t} = -\gamma N - \beta N^2 \Rightarrow N = \frac{N_0\gamma}{N_0\beta(\mathrm{e}^{\gamma t}-1)+\gamma\mathrm{e}^{\gamma t}}. \tag{1.5}$$

The losses can be attributed to long-range ($\mathbf{r}^{-3}$) interaction between ground and excited-state atoms coexisting in the MOT [Mar93, Din99]. Two processes are involved: 1. The atoms can undergo state-changing collisions, leave on a lower molecular potential and gain sufficient kinetic energy for escaping the MOT. 2. Two excited atoms can undergo radiative escape by spontaneously decaying at a small internuclear distance. The released energy can be large enough for trap loss. Due to the larger laser saturation (reduction of broadening and detuning) and the increased density ($\approx 1.6 \times 10^{10}\,\mathrm{cm}^{-3}$), these loss mechanisms get more significant during the last phase of the MOT. The fit results for this phase are:

	$N_0\ (10^6)$	$\gamma\ (10^{-3}\,\mathrm{s}^{-1})$	$\beta\ (10^{-8}\mathrm{s}^{-1})$
^{171}Yb	$2.63(7)$	3.1	$47(1)$
^{173}Yb	$2.00(7)$	4.2	$7.7(3)$
^{174}Yb	$1.96(5)$	3.3	$10.0(3)$

γ was forced to the values of the first MOT phase. As the values of β indicate the two-body losses are most prominent for ^{171}Yb and get reduced for ^{174}Yb and ^{173}Yb. This scaling can possibly be related to their respective s-wave scattering lengths $a(^{173}\mathrm{Yb}) = 199\,a_0$, $a(^{174}\mathrm{Yb}) = 105\,a_0$, $a(^{171}\mathrm{Yb}) = -3\,a_0$, Bohr radius a_0. The strong repulsive interaction of ^{173}Yb reduces two-body losses and the very weak attractive interaction of ^{171}Yb leads to an increase of these processes. However, a comprehensive analysis would involve knowledge about the individual molecular potentials of the $^1P_1$ and $^3P_1$ states and their respective scattering properties. This could be further analyzed by investigating the dependence between two-body losses and different atomic densities / light intensities, which is beyond the scope of this thesis.
Despite the observed decay beyond single-particle losses, the analysis of all three MOT phases showed that the first one is favorable for simultaneously loading two isotopes. A lifetime of more then $200\,\mathrm{s}$ for all three isotopes should be more than sufficient.

1.4.5. MOT performance depending on 2D-MOT laser detuning and magnetic-field gradient

Two further properties of our MOT setup are highly important: The detuning with respect to the $^1S_0 \Leftrightarrow {}^1P_1$ transition and the magnetic field gradient of the 2D-MOT. We analyzed the dependence of these two parameters for the isotopes ^{171}Yb, ^{173}Yb and ^{174}Yb. The alignment of the MOT setup was initially optimized for ^{173}Yb. The results are shown in Fig. 1.12.
Fig. 1.12a to Fig. 1.12c roughly show a maximum loading rate at a gradient field of $49\,\mathrm{G\,cm^{-1}}$ and a detuning of $\Delta_{\text{2D-MOT}} = -1.2\,\Gamma_{399} = -2\pi \times 35\,\mathrm{MHz}$. Along the thesis of A. Thobe [Tho14] this can be explained for our MOT geometry in the following way. Assuming a transverse size of $1\,\mathrm{cm}$ an upper bound for the capture velocity can be estimated: $v_\mathrm{c} = 102\,\mathrm{m\,s^{-1}}$. According to Eq. (1.1) a finite saturation of $s = 1.6$ reduces the maximum possible scattering rate to $s/(s+1) = 62\%$. Due to the Gaussian shape of MOT beams the effective scattering rate gets further reduced and the actual capture velocity might be estimated to be $v_\mathrm{c} \approx 40\,\mathrm{m\,s^{-1}}$. This corresponds to a Doppler shift of $v_\mathrm{D} = 100\,\mathrm{MHz}$. The optimal field gradient produces a Zeeman shift across the MOT of $69\,\mathrm{MHz}$. The remaining frequency difference is covered by the power broadened linewidth of $\sqrt{1+s}\,\Gamma = 2\pi \cdot 47\,\mathrm{MHz}$. The 2D-MOT detuning corresponds to the atoms at rest near the edge of the captured volume.
The result for ^{173}Yb shows a rather sharp cutoff at a detuning of $-1.4\,\Gamma_{399}$ with respect to the $F = 7/2$ state. This can be attributed to the hyperfine splitting of the $^1P_1$ state. Due to a frequency difference of only $72\,\mathrm{MHz}$ $(2.5\,\Gamma_{399})$ between $F = 7/2$ and $F = 3/2$ the effective cooling performance of the 2D-MOT is strongly reduced. The blue detuning to $F = 3/2$ of the MOT laser leads to Doppler heating.
The result in Fig. 1.12c shows a significantly different behavior than the measurement involving the fermionic isotopes. For gradients smaller than $45\,\mathrm{G\,cm^{-1}}$ the loading rate drops notably. Unfortunately, this has to be attributed to technical issues during the measurement. There is no particular physical reason that the bosonic MOT should have a hard cutoff at this point and the measurements from the previous sections indicate that the MOT performance of ^{171}Yb and ^{174}Yb should be very similar. As can be seen in Fig. 1.12d, a previous measurement using ^{174}Yb shows MOT loading for magnetic field gradients as low as $25\,\mathrm{G\,cm^{-1}}$. Furthermore, the

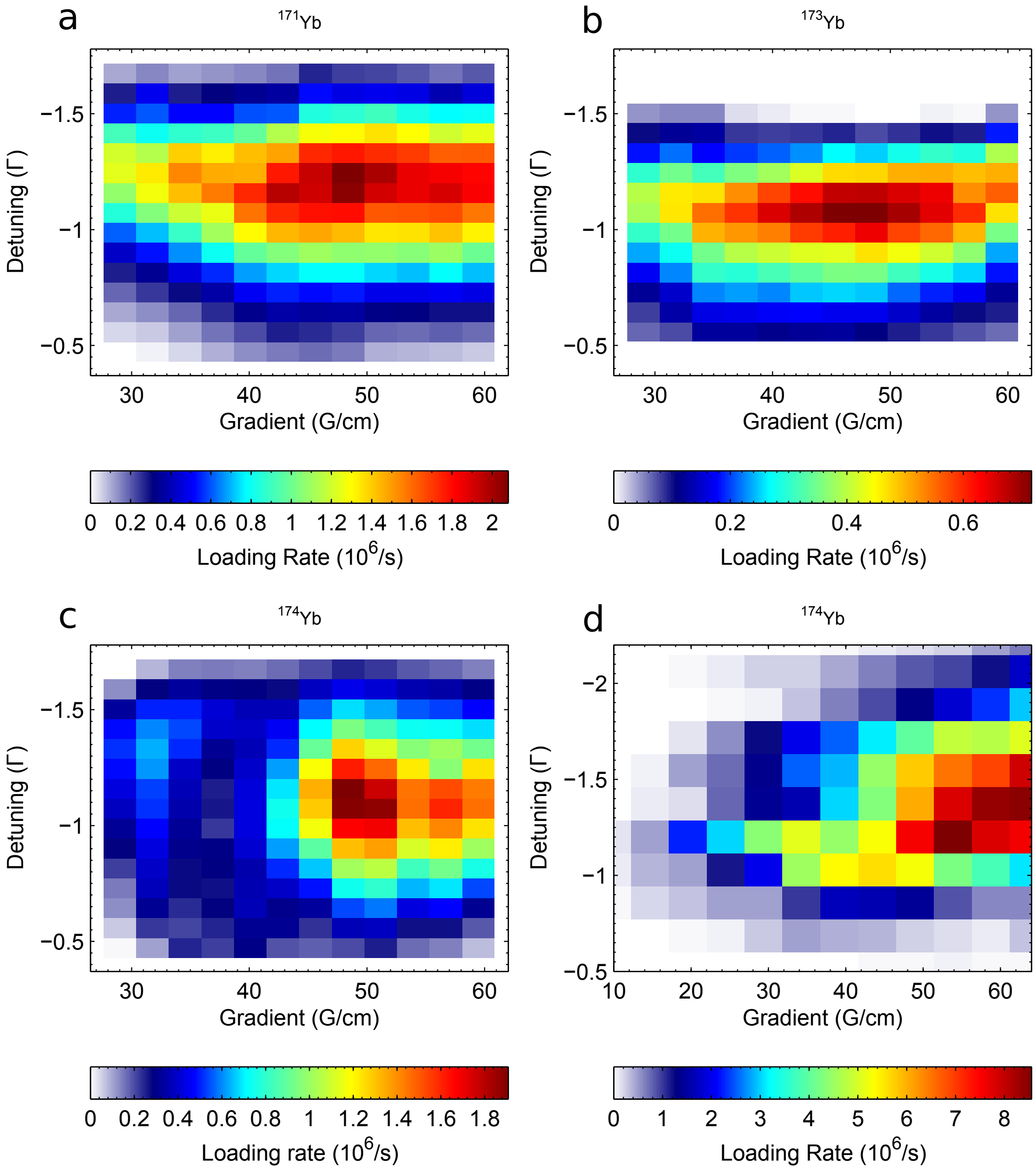

Figure 1.12.: MOT performance depending on 2D-MOT-laser power and magnetic-field gradient. All surface plots show the dependence between 2D-MOT laser detuning and the magnetic field gradient for isotopes ^{171}Yb, ^{173}Yb and ^{174}Yb. Images **(a)** to **(c)** were produced during this thesis, while image **(d)** is taken from [Dör13a]. The optimal parameters for **(a)** to **(c)** are similar: $\Delta_{\text{2D-MOT}} \approx -1.2\,\Gamma_{399}$, magnetic gradient $\approx 49\,\mathrm{G\,cm^{-1}}$. The data in **(b)** shows a sharp cut-off at $\Delta_{\text{2D-MOT}} \approx -1.4\Gamma$ due to the unfavorable hyperfine splitting of the $^1P_1$ state. The data in **(c)** has to be regarded carefully, because the left half of the plot is a result of technical issues during the measurement. The optimal paramters in **(d)** are $\Delta_{\text{2D-MOT}} \approx -1.2\,\Gamma_{399}$, magnetic gradient $\approx 54\,\mathrm{G\,cm^{-1}}$. See main text for details.

optimal field gradient is slightly higher, which is probably caused by a higher 2D-MOT laser power. Also, for ^{174}Yb we conducted numerical analysis of our MOT setup by integrating atom trajectories with a semi-classical model [Dör13a] and this shows good agreement with the data in Fig. 1.12d.

Conclusion

This chapter presented two versatile laser systems at $399\,\mathrm{nm}$ and $556\,\mathrm{nm}$, which are used to address the MOT cooling transitions of Yb. The layout of both systems is design in a way that a two-isotope operation will be possible. We characterized the MOT performance individually for ^{171}Yb, ^{173}Yb and ^{174}Yb with few changes to the opto-mechanical part of the setup, because this can not be changed during one experimental cycle. The loading rate for ^{173}Yb with $0.32 \times 10^6\,\mathrm{s}^{-1}$ is comparably low, which we attribute to atomic properties reducing the MOT performance, i.e. unfavorable hyperfine splitting and large differential Zeeman shift. Still, the performance is sufficient for the production of degenerate Fermi gases. Since the loading rates for ^{171}Yb and ^{174}Yb are significantly higher, we estimate the overall performance to be good enough for cooling isotope mixtures, which among others will be an essential step towards sympathetic cooling of ^{171}Yb to quantum degeneracy.

To technically realize a multi-isotope MOT we are currently working on the ability to dynamically change the lock-point of our 2D-MOT cooling laser. A sequential loading of the 2D-MOT will be necessary, due to the limited laser power at $399\,\mathrm{nm}$. First measurements concerning the sweep speed of this dynamic lock can be found in B. Abeln's thesis [Abe16].

Possible ways to improve the overall MOT performance mainly rely on the 2D-MOT. The loading rate would certainly profit from a stronger laser source to produce higher saturation factors. Another point is the sensitivity of proper beam alignment. The stability could be increased by changing the free-space setup back to a fiber coupled version, although this would reduce a significant part of usable laser power due to typical fiber-coupling efficiencies and long-term fiber degradation, e.g. ultraviolet solarization. New techniques in doping single-mode fibers with Hydrogen to increase the long term usability for short wavelengths will certainly make this change more favorable [Col14]. Other experiments could significantly increase the performance of their MOT system by using the *blue* and *green* transition simultaneously [Lee15, Kaw15]. This is achieved by superimposing both colors onto the 3D-MOT to use the advantages of both transitions. Numerical simulations suggest that a similar approach for two frequencies using the *blue* transition can also improve the loading rate of the 2D-MOT [Hil17].

2. Preparation and Detection of Degenerate ^{173}Yb Gases

The MOT setup presented in the previous chapter is capable of capturing and cooling Yb atoms to the µK regime. In this state, the ensemble can still be described as a thermal gas. Further cooling methods are necessary to reach quantum degeneracy, i.e. Bose-Einstein condensate (BEC) or degenerate Fermi gas (DFG). These typically rely on cooling via evaporation, either by one isotope alone (^{173}Yb, ^{174}Yb) or sympathetic with other isotopes (^{171}Yb), if the scattering length is unfavorable. Since the ground state of Yb does not carry an electronic angular momentum, techniques involving magnetic trapping [Pri83] can not be applied, but instead one has to rely on an all optical setup [Gri00]. Typically this is realized by transferring atoms from the MOT into a crossed dipole trap and subsequent evaporative cooling.

During evaporative cooling the dipole-trap laser intensity is gradually reduced. Ideally, the resulting potential shows large, initial trapping frequencies to enhance elastic collisions and low, final trapping frequencies. These are favorable to suppress excitation into higher lattice bands (cp. Sec. 3.3.1). Both conditions can be contradictory because of limited laser power. The first section explains how we implemented a bicolor dipole trap to circumvent this contradiction and engineer a potential which has both advantages.

Although we previously worked with the bosonic isotope ^{174}Yb, mainly for benchmarking the experimental apparatus, the fermionic isotopes are our main research interest. Therefore, it is essential to manipulate and measure the spin distribution, e.g. for realizing different SU($\mathcal{N}$) symmetric systems [Gor10]. The population of certain m_F spin states can be changed by resonant pumping using the green MOT transition, but spin detection via a magnetic Stern-Gerlach [Ger22] experiment is unfeasible due to the missing angular momentum of the ground state. Similar to the trapping of atoms by using dipole forces, the spacial separation of different spin states can instead be obtained via a spin-selective optical potential. This detection scheme is referred to as optical-Stern-Gerlach (OSG) [Sle92]. The second section explains the related properties of Yb and how we implemented an OSG beam at our experiment.

For all experiments involving the $^3P_0$ state, simultaneous knowledge about ground- and excited-state atoms is a big advantage. The main reason is the large increase in signal-to-noise-ratio (SNR), which suffers from atom-number fluctuations between each experimental cycle. Although depopulating the meta-stable state using the clock laser is possible, it is technically less demanding to use the $^3P_0 \Leftrightarrow {}^3D_1$ transition to transfer the atoms to the ground state [Bar07]. The theoretical efficiency and implementation at our experiment are discussed in the third section.

Finally, the last section shows measurements to characterize the dipole-trap setup using different spin mixtures of ^{173}Yb.

The new dipole trap setup was planned by A. Thobe and the author and build by A. Thobe, B.

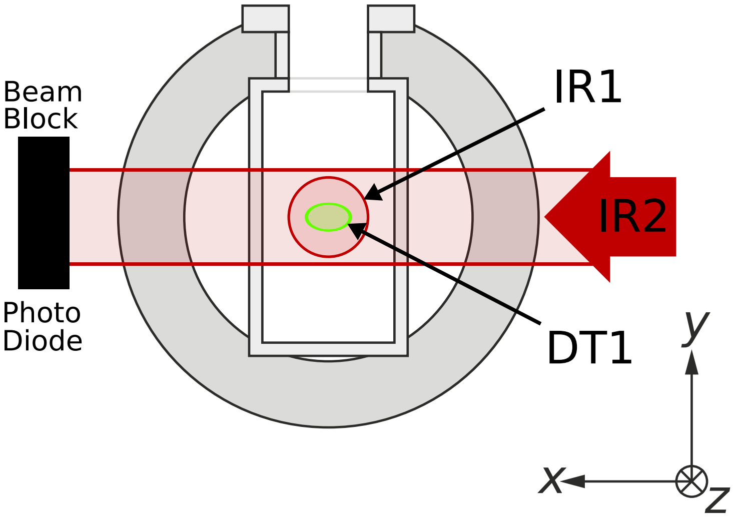

Figure 2.1.: Optical-dipole-trap geometry. The image shows only a front view of the science cell. Indicated are the three dipole traps DT1 ($532\,\mathrm{nm}$) in z-direction, IR1 ($1064\,\mathrm{nm}$) in z-direction and IR2 ($1064\,\mathrm{nm}$) in x-direction. All beams are in the horizontal plane. The dipole traps are pointed onto beam blocks, where we measure the power of diffuse light with photo diodes for power regulation. The relative beam sizes are to scale. The actual alignment differs slightly. See the main text for details.

Hundt, T. Ponath and the author. Spin selective detection was planned by the author and implemented by A. Thobe and the author. Detection of the excited state was planned by A. Thobe and the author and implemented by the author. The data was evaluated by the author.

2.1. A bicolor, optical dipole trap

We use two different laser sources for producing our dipole trap. First, a commercial, frequency doubled Nd:YAG laser[1] emits $18\,\mathrm{W}$ at $532\,\mathrm{nm}$ (DT1). Second, a commercial MOPA system[2] provides $25\,\mathrm{W}$ at $1064\,\mathrm{nm}$ for the final, crossed dipole trap (IR1 and IR2). A sketch showing the beam geometry can be seen in Fig. 2.1.
The green dipole trap was previously implemented by my colleague S. Dörscher. The full laser power is transmitted using one elliptical, free-space telescope. We have about $14\,\mathrm{W}$ power available at the science cell and the beam has a waist of $18\,\mu\mathrm{m} \times 29\,\mu\mathrm{m}$. Details and characterization can be found in [Dör13a].

2.1.1. 1064 nm laser system

Schematics of the laser system can be found in Fig. 2.2. The setup was planned in a very compact way and all components were selected for high-power application. The laser source is additionally isolated using a Faraday isolator[3]. The power between both beam paths can be

---

[1] Coherent VERDI V18
[2] Coherent Mephisto
[3] Soliton HP-04-I-1064

set using a polarizing beam splitter[4] (PBS). Each arm is equipped with a high-power AOM[5] located on top of a massive, rotatable aluminum block for enhanced thermal stability. We reach a diffraction efficiency of about 90% at center frequencies of $\pm 110\,\mathrm{MHz}$. Both AOM orders are used to avoiding interferences. The AOMs are implemented for switching and power regulation. Light for power regulation is picked up[6] behind the science cell by using the diffuse light scattered by beam blocks. We implemented shutters based on movable mirrors for each branch serving two purposes:

1. If the dipole trap is not used during an experimental cycle, we need to safely dump $25\,\mathrm{W}$ of power. The shutters can reflect the laser light onto large beam blocks.
2. We observed degrading fiber coupling efficiency due to the thermal load of the RF source. During a typical experimental cycle the AOMs are set to full power while the shutters are still closed. To switch the dipole traps on the AOMs are disabled shortly while the shutters open. Right afterwards the AOMs are enabled again.

The laser is located on a different optical table as the science cell. We transfer the light using Large-Mode-Area (LMA) fibers[7]. From our experience, the fibers show superb thermal stability on a daily basis and allow high coupling efficiencies of around 80%. Note that these fibers are polarization maintaining and thus have a specific orientation. We set the light polarization with a $\lambda/2$ plate in front of the fiber coupler. It is hermetically sealed[8] to prevent dust deposition on the fiber facet.
Typically we have about $1.5\,\mathrm{W}$ for IR1 and $11.5\,\mathrm{W}$ for IR2 available after the telescopes. This leaves enough laser power as buffer.

2.1.2. Dipole trap geometry

Neutral atoms can be trapped into a beam focus due to the polarizability α of the electronic shell [Gri00]:

$$U_{\text{dip}} = -\frac{1}{2\epsilon_0 c}\Re(\alpha) I, \ \mathbf{F}_{\text{dip}} = \partial_{\mathbf{r}} U_{\text{dip}} \tag{2.1}$$

with dipole potential U_{dip}, vacuum permittivity ϵ_0, speed of light c and intensity I, dipole force $\mathbf{F}_{\text{dip}}$ and gradient $\partial_{\mathbf{r}}$. Eq. (2.1) can be simplified for practical use to

$$U_{\text{dip}}(\mathbf{r}) = \frac{3\pi c^2}{2\omega_0^3}\frac{\Gamma}{\Delta} I(\mathbf{r}) \text{ and} \tag{2.2}$$

$$\Gamma_{\text{sc}}(\mathbf{r}) = \frac{3\pi c^2}{2\hbar\omega_0^3}\left(\frac{\Gamma}{\Delta}\right)^2 I(\mathbf{r}). \tag{2.3}$$

ω_0, Γ, Δ indicate resonance frequency, linewidth and detuning of the most significant transition, i.e. ${}^1S_0 \Leftrightarrow {}^1P_1$ in case of Yb. The choice of the waist had to be decided from the following

---

[4] Thorlabs PBS25-1064-HP

[5] Crystal Technology 3110-197

[6] Thorlabs PDA36

[7] NKT Photonics LMA-PM-15; note the unusual low NA of 0.06 at $1064\,\mathrm{nm}$

[8] Schäfter und Kirchhoff 60FC-SMA-T-23-A15-03; EFL $15.13\,\mathrm{mm}$ at $1064\,\mathrm{nm}$

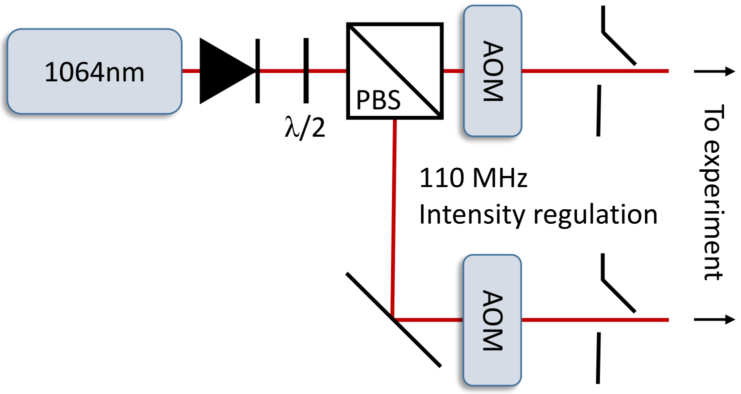

Figure 2.2.: Laser setup for the 1064 nm dipole trap. The graphic illustrates a simplified version of our dipole-trap laser setup. It is specifically designed for high power application. Each laser arm is individually switchable and power regulated. Light is lead to the science cell via two Large-Mode-Area fibers. The AOMs are located on top of massive aluminum blocks for better thermal stability. Beam shaping optics are omitted. PBS: polarizing beam splitter.

arguments. Ideally, a dipole trap has preferably low trapping frequencies at the end of evaporation. When superimposed with an optical lattice, this suppresses excitations into higher bands, because occupation of the lowest band scales with $\propto \bar{\omega}^{-3}$ [Viv04], $\bar{\omega} = \sqrt[3]{\omega_x \omega_y \omega_z}$ being the mean trapping frequency. However, the trapping frequency can not be arbitrarily small, because gravity leads to a sag, i.e. the atoms are not located at the center of the beam. Approximating the gaussian-beam profile with a harmonic potential the sag can be calculated:

$$\frac{1}{2}\omega_y^2 y^2 = gy \Rightarrow y = \frac{2g}{\omega_y^2},$$

with position y and vertical trap frequency ω_y. The theoretically maximum sag is $y = w_y/2$, because the force is the strongest at this position. Eventually, this reasoning leads to the maximally possible waist, which still can hold the atoms against gravity with a given laser power. Note that this equation is not a valid approximation for shallow traps, because the harmonic oscillator model is not applicable. We therefore base the following estimations on a calculation, which involves the Gaussian beam profiles. As a compromise, we decided for a weak circular beam with $50\,\mu\text{m} \times 50\,\mu\text{m}$ and a strong, elliptical beam with $65\,\mu\text{m} \times 220\,\mu\text{m}$, which is perpendicular to the first one. Broadly speaking, the elliptical shape ensures enough force at minimum power and the weaker perpendicular beam applies confinement along the axis of the strong beam.
The depth and trapping frequencies can be calculated with Eq. (2.2) for an ideal geometry, where IR1 is centered at half of IR2's waist. The results can be found in Tab. 2.1.

2.1.3. Characterization of the IR-dipole-trap telescopes

The requirements on optical performance are less strict compared to optical lattices, because no interference pattern is created. Still, a preferably clean Gaussian mode with a waist as close as

IR1 IR2	$50\,\mu\text{m} \times 50\,\mu\text{m}$ $65\,\mu\text{m} \times 220\,\mu\text{m}$	$52\,\mu\text{m} \times 51\,\mu\text{m}$ $67\,\mu\text{m} \times 227\,\mu\text{m}$
ω_x (2π Hz)	29	32
ω_y (2π Hz)	63	62
ω_z (2π Hz)	28	28
$\bar{\omega}$ (2π Hz)	38	39
Depth (nK)	133	144

Table 2.1.: Calculated dipole-trap parameters. The table shows the corresponding trap parameters for a crossed dipole trap using IR1 and IR2. The values are calculated using $P_{\text{IR1}} = 50\,\text{mW}$, $P_{\text{IR2}} = 7.3\,\text{W}$ (left column) and $P_{\text{IR1}} = 70\,\text{mW}$, $P_{\text{IR2}} = 8\,\text{W}$ (right column). Intersection geometry: IR1's mode center is located on top of IR2's half-waist (largest force). The left column shows the situation for the planned geometry, the right one indicates values for the measured waists (Sec. 2.1.3) and powers from actual experimental cycles. The average trap frequency is rather robust against minor changes of the beam geometries and the trap depth can easily be compensated by power adjustments.

possible to the design geometry is favorable.

The boundary conditions for the telescopes are the waists given in the previous section and the working distance, which is limited by other optical elements and has a value of about $500\,\text{mm}$. Additionally, we wanted to use the sealed fiber couplers, which were already applied for coupling into the LMA fibers. These can only be delivered with a limited selection of lenses. Eventually, we decided for the $15\,\text{mm}$ version of fiber coupler.

In case of IR1 this made an expanding telescope of $1:4$ necessary. The lenses are manually aligned in a tube system and located on a two-axis translation stage. In case of IR2 beam expansion was not necessary, because the beam diameter after the fiber coupler was just suitable to fit the conditions above. However, to engineer an elliptical waist we used a pair of anamorphic prisms[9]. The resulting aspect ratio is about $1:3.5$. Unlike cylindrical lenses they do not need to be properly rotated around the optical axis, because they are mounted on top of a plane aluminum block. But, adjustment of the angle with respect to each other is extremely sensitive. We found it efficient to align the prisms, while we simultaneously monitored the beam mode on a camera. They were initially fixed with UV-curing glue[10] and additionally with two-component epoxy afterwards. Due to the lateral beam shift we glued the prism and lens mount individually onto a base plate, which is translatable into two directions. Sketches of both telescopes can be seen in Fig. 2.3.

Both telescopes were analyzed using optical design software[11]. Since the fiber NA is rather small, the geometric errors are only marginal and the telescopes should theoretically work diffraction limited. Since real optical components often deviate within their tolerances and can not be aligned perfectly, it is crucial to further analyze the final optical setup as it is used at the experiment. One possibility, besides mere qualitative evaluation of the transversal beam profiles, to quantify a beam quality relies on the divergence along propagation. It can be shown

---

[9] Thorlabs PS872-C; note that the 0° and 60° coatings are not ideal

[10] Thorlabs NOA61

[11] Oslo 6 Premium

that for higher order Gaussian modes the half angle Θ is modified via

$$\Theta = M^2 \frac{\lambda}{\pi w_0},$$

with the propagation factor M [Joh98]. The beam radius w can then be calculated via

$$w = w_0 \sqrt{1 + \left((z - z_0) \frac{\lambda M^2}{\pi w_0^2} \right)^2}. \tag{2.4}$$

In this model an ideal Gaussian mode (TEM$_{00}$) yields a propagation factor $M^2 = 1$. Any deviation is possibly caused by geometric errors, called abberations, of the light source, e.g. shape of the laser diode, or other optical components along the beam path [Ruf94, Luo10].
For this purpose we measured the transveral beam profiles of both telescopes using a CCD camera[12]. The results can be found in Fig. 2.4 and Fig. 2.5. Both axes of IR1 show rather large values for M^2 around 1.12. Here, the data range is certainly problematic, because the measurement does not cover several Rayleigh ranges, which leaves out the part of linear beam divergence. Furthermore, the beam shows slight astigmatism, because the waist positions differ by about $2\,\mathrm{mm}$. However, essentially the waists at an intermediate position are sufficiently close to the design goal. Although the exact working distance was not measured, it is sufficiently well within $50(5)\,\mathrm{cm}$. In case of IR2 the M^2 values could only be properly estimated for the vertical direction. The data set for the horizontal radius was too limited due to the large Rayleigh range. For the vertical direction however we measure a quite low value with 1.08 and the model resembles the data very well. Both indicate good optical performance of the telescope. Since the prisms cause an elliptical beam shape, the waists can not overlap [Sal91]. However, for the purpose of atom trapping only the intensity of the beam is relevant. Thus, the working point is at the position of the vertical waist. Here, both values fit very well with the design goals and also the working distance is very close to the planned setup.
As can be expected from the waist sizes of all dipole traps, aligning all of them simultaneously is very difficult. Adjusting them from scratch involved a step wise approach, i.e. optimizing atom transport first from the MOT into DT1 and then into the IR traps. On a daily basis we try to change the beam positions as little as possible. Here, especially IR1's focus serves as a fix point in the science cell. Since the final atom position is particularly depending on the alignment of IR2, we finely need to correct the vertical position every other day. Usually, this recovers the optimal trap geometry.

2.1.4. Evaporation sequence

We evaporate ^{173}Yb using the following procedure. During the MOT phase all three dipole traps are set to full power: DT1 $14.75\,\mathrm{W}$, IR1 $1.08\,\mathrm{W}$ and IR2 $10.5\,\mathrm{W}$. First, DT1 is exponentially ramped to its lowest value of $25\,\mathrm{mW}$ during $5\,\mathrm{s}$ and switched off afterwards. Power control is based on the signal of a logarithmic photo diode. Second, the IR intensities are simultaneously

---

[12] Coherent LaserCam-HR

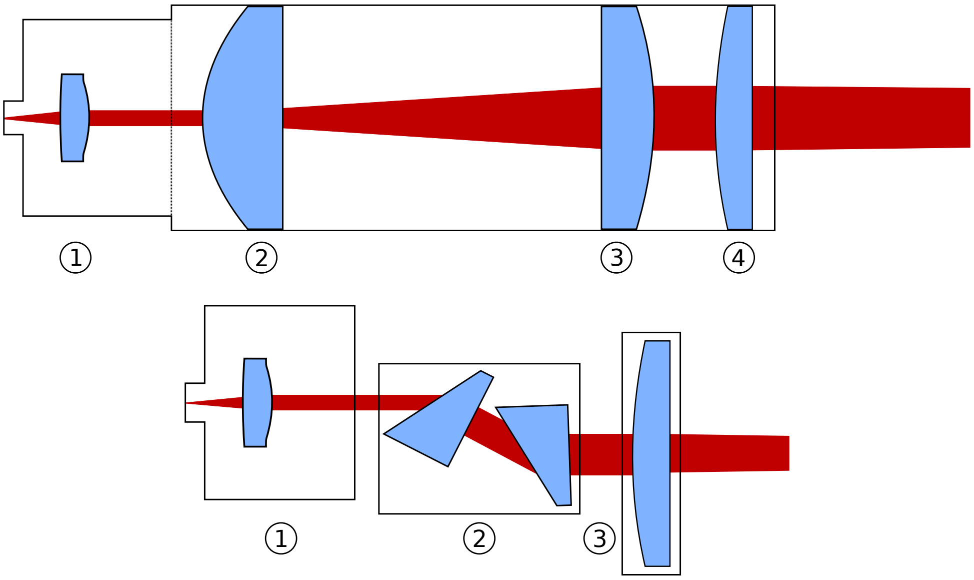

Figure 2.3.: Telescopes of the IR dipole traps. Top: The IR1 telescope consists of four lenses: **1.** Aspheric lens $f = 15\,\mathrm{mm}$ **2.** Plano-convex lens $f = 25\,\mathrm{mm}$ **3.** Plano-convex lens $f = 100\,\mathrm{mm}$ **4.** Plano-convex lens $f = 500\,\mathrm{mm}$. The $1:4$ expanding telescope is necessary to fit the working distance/waist. The lenses are aligned manually inside a tube system. The aspheric lens is part of a hermetically-sealed fiber coupler to prevent dust deposition. **Bottom:** The telescope uses the following parts: **1.** Aspheric lens $f = 15\,\mathrm{mm}$ **2.** Anamorphic prism pair with magnification of 3.5 **3.** Plano-convex lens $f = 500\,\mathrm{mm}$. The same fiber coupler as for IR1 is used for positioning of the aspheric lens. The prism pair causes a transversal beam shift. Hence, prisms and focusing lens are located within individual mounts, which are glued to a base plate. The top view shows the larger beam axis which generates the smaller waist at the focus position.

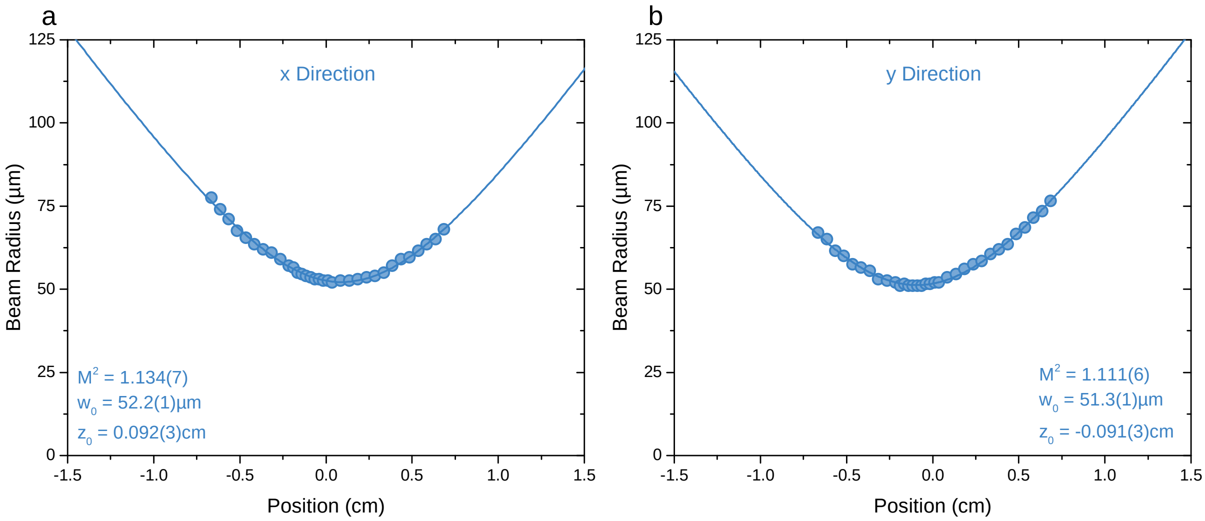

Figure 2.4.: Transverse mode profile of IR1. Both plots show measured beam radii for different positions along the optical axis. The M^2 values are slightly increased, which is possibly related to the limited data range. The data points can be well approximated using the M^2 model. The telescope shows slight astigmatism which is negligible. The intermediate position between both waists is close to the design goal. Although the exact working distance is not measured it is well within $50(5)\,\mathrm{cm}$.

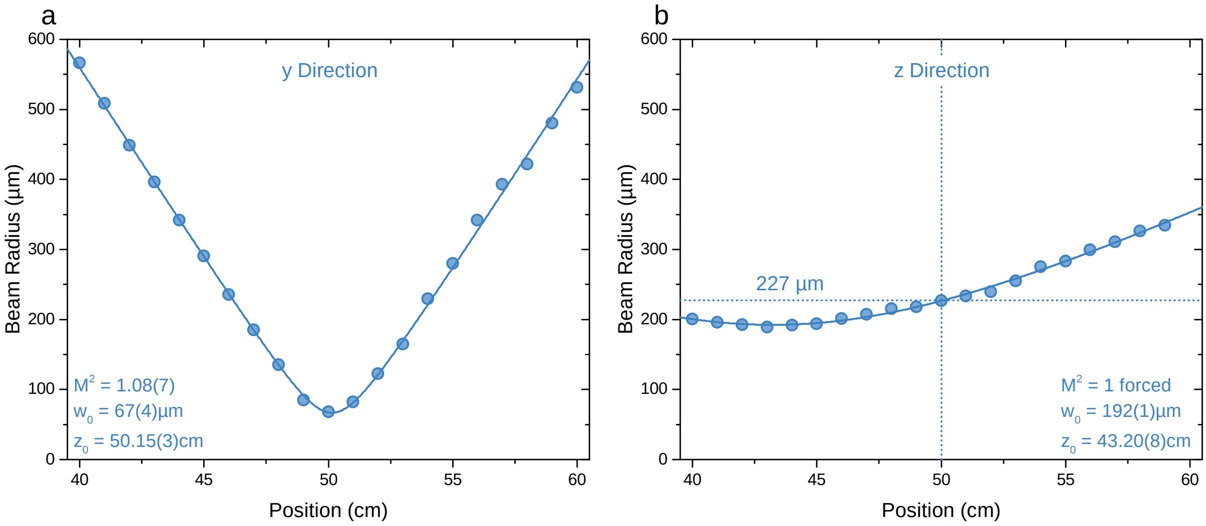

Figure 2.5.: Transverse mode profile of IR2. Both plots show measured beam radii for different positions along the optical axis. The M^2 value for the vertical direction shows a low value of 1.08 and the data points basically lie on top of the fit, which indicates very good optical performance. Due to the elliptical beam profile, both waists can not overlap. For trapping purposes only the intensity is relevant. Thus the operating point lies at the waist of the vertical axis. Here, both waists are very close to the planned values. The working distance is suitable considering the overall optical setup.

decreased using an exponentially changed[13] set value (linear photo diode) for $10\,\mathrm{s}$ to reach their final values of $70\,\mathrm{mW}$ (IR1) and $8\,\mathrm{W}$ (IR2). Subsequently, we increase the IR powers by 5% to avoid further particle loss after evaporation. The specifics of the sequence were experimentally determined to optimize the final amount of atoms and their temperature. A sketch of the evaporation sequence can be found in Fig. 2.6.

2.1.5. Dipole trap characterization using ^{173}Yb

Trap frequencies

To verify the design plan from above we measured the center of mass oscillations using a ^{174}Yb BEC in a dipole trap with IR1 and IR2. The atom cloud was deflected using a short pulse of misaligned lattice beams ($759\,\mathrm{nm}$). The position was successively recorded for all direction x, y and z. The results can be seen in Fig. 2.7.

The oscillations are clearly visible and also the Sine fits are in good accordance with the data. We determined the following frequencies:

$$\omega_{\text{x,y,z}} = 2\pi \times \{26.6(5), 70.5(3), 24.0(1)\}\,\mathrm{Hz}. \tag{2.5}$$

This means that the new dipole trap has an average frequency of $\bar{\omega} = 2\pi \times 35.6(3)\,\mathrm{Hz}$. Comparing these values with Tab. 2.1, we find quite good agreement between the theoretically calculated potential and the actual trap frequencies. Small deviations can be attributed to slight

---

[13] Exponential ramps controlled via the experiment software have variable time constants, i.e. independent of the duration all exponential ramps look self similar.

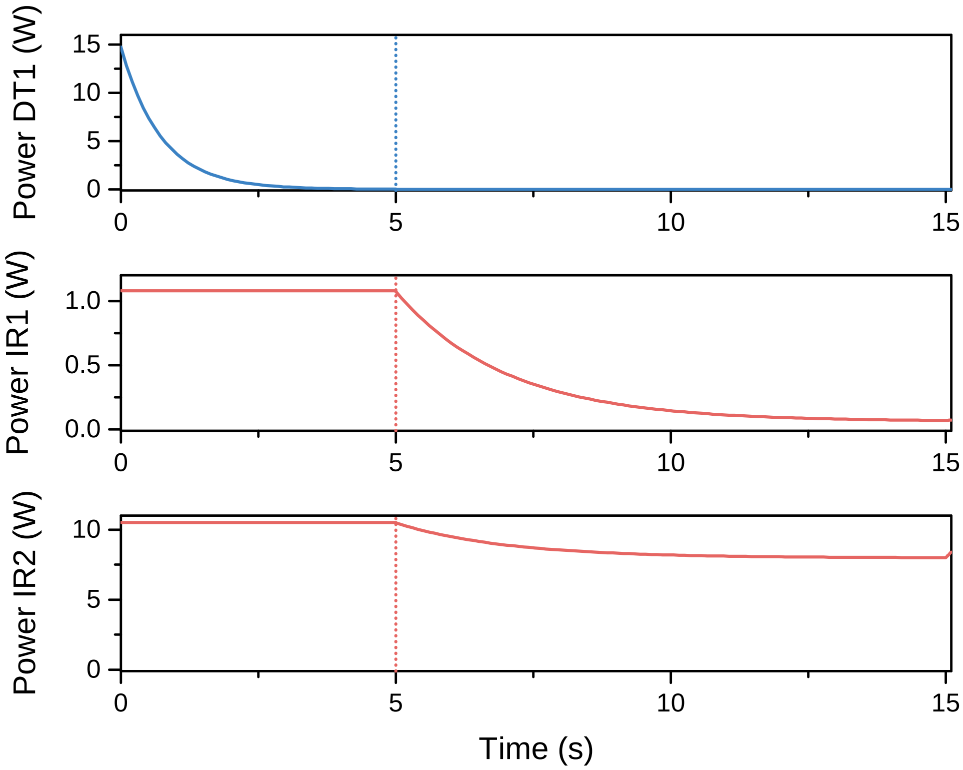

Figure 2.6.: Evapoaration sequence. The plots show the powers evolution of all dipole traps for a sequence to evaporate ^{173}Yb. It consists of two phases: First, DT1 is ramped exponentially while the IR traps stay at their maximum power. DT1 is then switched off. Second, the IR powers are exponentially ramped to their minimum value. Finally, the intensity of both IR traps is increased by 5% to avoid further particle loss.

misalignment between both beams.
Summarizing, the new optical dipole trap has a low mean trapping frequency, which is about a factor of 3 lower compared to the previous dipole-trap setup [Dör13a]. This should enable us to significantly reduce population of higher bands, when transferring the atoms into the optical lattice.

Lifetime of ^{173}Yb

In addition to the trap frequencies the atomic lifetime is important for all following experiments, because it defines a limiting timescale. We measured the remaining amount of ^{173}Yb atoms after different waiting times in the final dipole trap. The results can be seen in Fig. 2.8. From a simple exponential fit we determine a lifetime of about $30\,\mathrm{s}$. Since this is a lot longer than typical experimental sequences it should not constitute a limiting timescale. The theoretical off-resonant scattering rate can be calculated to be $\approx 119\,\mathrm{s}$. We concluded that the atomic lifetime is not limited by photonic scattering but rather by collisional losses due to the background gas $(p = 1.3 \times 10^{-11}\,\mathrm{mbar})$.

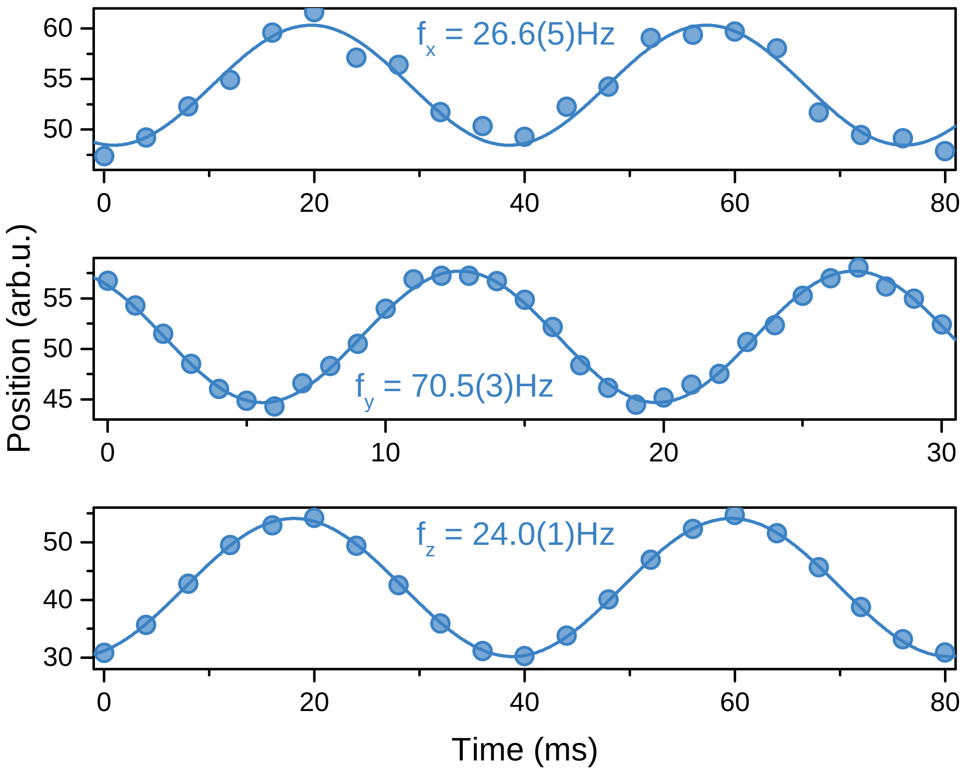

Figure 2.7.: IR-dipole-trap frequencies. The plots show the center of mass motion of a ^{174}Yb BEC, which we initiated using misaligned lattice beams ($759\,\mathrm{nm}$). We measured the oscillations in all spacial directions. The solid lines indicate fits using Sine functions. The fit results and -errors are indicated in each plot. We averaged the sequences three times for the x-axis and five times for the y- and z-axis.

Conclusion

This section presented our new bicolor dipole trap setup. We planned a laser setup optimized for high-power application using LMA fibers. The fiber coupled telescopes show very good thermal stability, i.e. coupling efficiency and beam pointing. The experimentally determined waists are very close to the design goals and the telescopes' optical performance is sufficient. Measuring trap frequencies and lifetime with ultra-cold gases, we found a threefold reduction of final trapping frequencies and an extensive lifetime of about $30\,\mathrm{s}$, which should not limit typical experimental time scales.

An alternative approach to a dipole trap which enhances initial evaporation and shows low, final trap frequencies uses time averaged potentials [Bai12]. These can be engineered using AOMs. The beam geometry relies on a rather tight focus, which is preferred at the beginning of evaporation. During intensity reduction frequency modulation of the AOM is used to widen the focus and thus create an averaged potential with low trapping frequencies. Such modulation schemes can also be used for the generation of arbitrary potentials [Zim11].

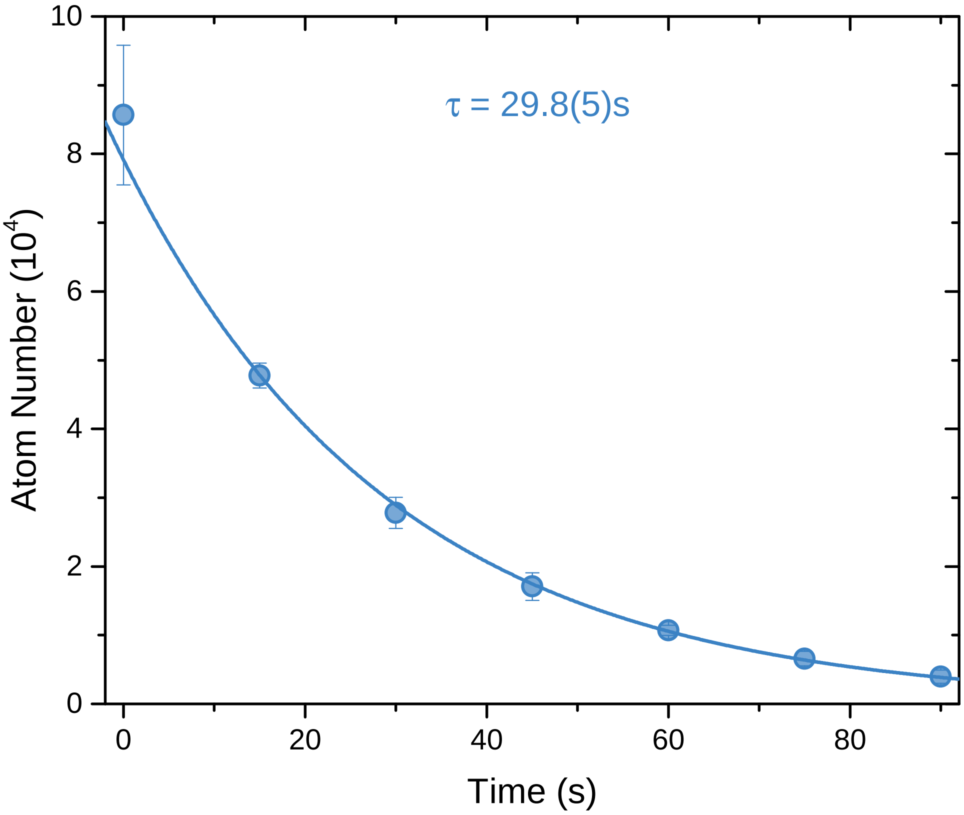

Figure 2.8.: Lifetime of degenerate ^{173}Yb. The plot shows the amount of ^{173}Yb atoms in the final IR dipole trap for different holding times. The data was six times averaged. The solid line shows an exponential fit without offset with corresponding $1/\mathrm{e}$ time constant τ. The lifetime of the DFG is very long compared to typical experimental timescales and should not constitute any limitations.

2.2. Spin selective detection

Producing ultra cold samples of the fermionic Yb isotopes opens a vast tool box for possible experiments. Since these rely on the spin degree of freedom, knowledge about the spin composition is essential. Therefore, a scheme for detecting m_F state occupation is necessary. The missing electronic angular momentum of the Yb ground state prohibits efficient spin separation using magnetic fields. Relevant is only the nuclear magneton μ_I which is about a factor of 2000 smaller than μ_B. Hence, the Zeeman splitting in case of ^{173}Yb is merely $m_F \times 112\,\mathrm{Hz\,G}^{-1}$ [Sca15]. More efficiently, a spin depending potential can be generated using a near resonant, focused laser beam. This section explains the theoretical background and our experimental results.

2.2.1. Optical setup

The laser setup was already briefly described in Sec. 1.3.2. A sketch of the respective level scheme and the laser-setup part close to the science cell can be seen in Fig. 2.9. Since the SHG source is locked to a high-finesse cavity at about $400\,\mathrm{MHz}$ blue detuning with respect to the

^{173}Yb: $^3P_1(F = 7/2)$ state, we shift the frequency using an AOM cascade of two double passes, each shifts with $400\,\mathrm{MHz}$, and one single pass with a shift of $200\,\mathrm{MHz}$. Details about why this particular frequency was chosen can be found in the following section. We simultaneously use the last AOM in front of the fiber link for switching the beam. To keep the optical setup after the fiber as simple as possible we use fiber-polarization control to set the beam to a circular polarization ($\sigma^{\pm}$) and avoid further polarizing optics. Since we can use almost all the light of the laser, we reach a power of about $45\,\mathrm{mW}$ behind the telescope despite the limited efficiency of the AOMs.

Different to the magnetic potentials that can usually be engineered for spin separation, the spatial extension of typical OSG beams is very limited. According to Eq. (2.1) the potential is directly connected to the intensity profile of the beam. For typical polarizabilities and available laser powers the waists range from several tens of $\mu\mathrm{m}$ to few hundreds of $\mu\mathrm{m}$. These small foci are essential to reach sufficient forces at the slope of the Gaussian beam profiles [Sie86]. Due to the relative size between atomic cloud and OSG beam the spatial dependence on the dipole force can lead to strong deformation of the atomic cloud [Ste11]. For this reason ideally the waist is as large as possible. An upper limit is given by the available laser power, because the maximum force is given by

$$F^{\mathrm{max}}\left(\frac{w_0}{2}\right) \propto \frac{I_0}{w_0},$$

and the Intensity scales with

$$I_0 \propto \frac{P_0}{w_0^2},$$

with intensity I_0, power P_0 and waist w_0. As a compromise we decided for a waist of $100\,\mu\mathrm{m}$, which showed good separation for pulses on the order of $100\,\mu\mathrm{s}$ duration.

The telescope for producing the respective waist inside the science cell was put on top of a rigid aluminum post with an angle of incidence of $11°$. It was manually assembled using a lens tube. For collimation we used an achromatic lens[14] with a focal length of $f = 15\,\mathrm{mm}$ and for focusing a singlet lens[15] with $f = 750\,\mathrm{mm}$ to cover a large distance towards the atoms. Due to the big lever of the beam we use differential-$\mu\mathrm{m}$ screws to position the focus slightly above the atomic cloud. In addition, the post can be translated along the optical axis.

2.2.2. Polarizability of the $^3P_1$ state for the isotopes ^{171}Yb and ^{173}Yb

Essential for the separation of different m_F states are the individual polarizabilities, because $F_{m_F} \propto \alpha_{m_F}$ according to Eq. (2.1). Therefore, we calculated the actual values for ^{171}Yb and ^{173}Yb using atomic parameters from [Pan09]. The results can be found in Fig. 2.10. Both plots show the behavior exemplary for σ^+ light. Regarding the polarizability differences in case of ^{173}Yb, a situation slightly blue detuned with respect to the $F = 7/2$ transition seems optimal. A balance has to be found between the smallest potential difference $U_{\text{dip}}(m_F = -3/2) - U_{\text{dip}}(m_F = -5/2)$ and the overall scattering rate. In case of ^{171}Yb, the situation is more relaxed, because of the overall large polarizability difference between both

---

[14] Thorlabs AC064-015 ML

[15] Thorlabs LA1978-A-ML

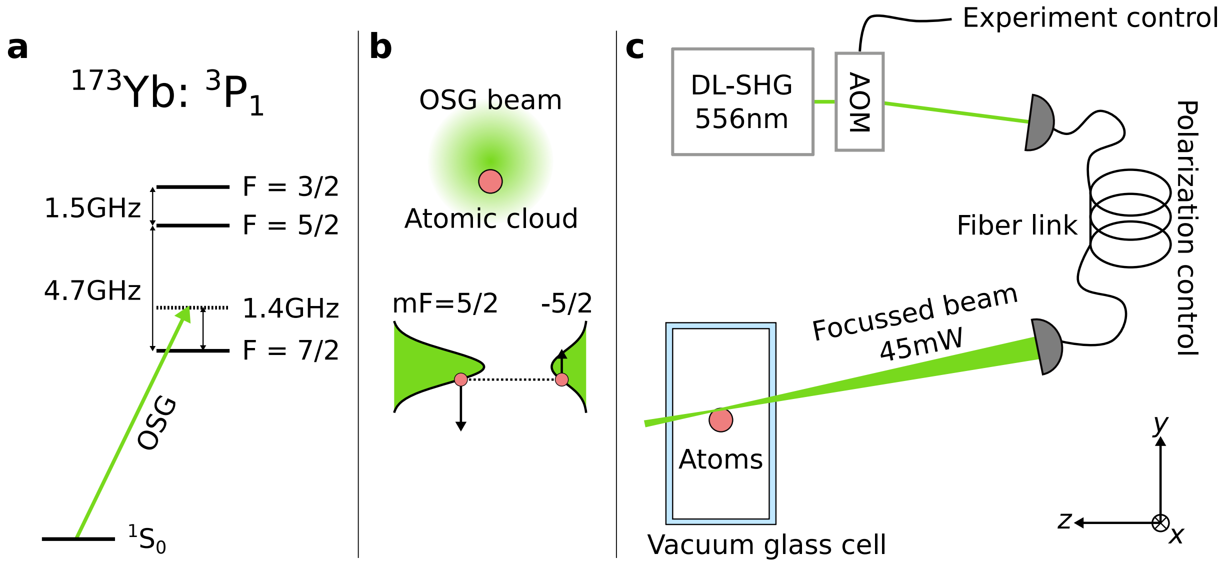

Figure 2.9.: OSG level scheme for ^{173}Yb and laser setup. (a) The illustration shows the level scheme relevant for OSG application with ^{173}Yb. Indicated is the laser frequency about $1.4\,\mathrm{GHz}$ blue detuned with respect to the $^3P_1(F = 7/2)$ state. Level distances are not to scale. **(b)** Both images illustrate the geometry between OSG beam and atomic cloud. Depending on the m_F state the beam focus can act repulsive or attractive. Sizes are not to scale. **(c)** The graphic shows a simplified version of the OSG laser setup. We use a SHG system as source for $556\,\mathrm{nm}$ light. The single AOM is representative for an AOM cascade of three units. We set the proper light polarization ($\sigma^{\pm}$) using fiber-polarization control. The OSG-beam focus is slightly adjusted above the atomic cloud, has a waist of $100\,\mu\mathrm{m} \times 100\,\mu\mathrm{m}$ and an incident angle of about $11°$.

m_F states.

For quantifying the efficiency of the separation we calculated the potential differences ΔU_{dip} between adjacent m_F states and normalized them with the mean scattering rate $\bar{\Gamma}_{\text{sc}}$. The result can be found in Fig. 2.11a. It can be seen that this measure confirms the frequency range between hyperfine states $F = 7/2$ and $F = 5/2$ to be optimal. Similar values can be found to the far left (red detuning). However, these frequencies are technically hard to reach. As Fig. 2.10 already indicated, the critical part is the separation of the least affected m_F state. In this case these are $m_F = -5/2$ and $m_F = -3/2$. Fig. 2.11 even suggests to increase the detuning a little to reach the maximum value of the blue solid line. All other pairs are better separated than these two.

Finally, Fig. 2.11b shows the scattering rate γ_{sc} along a trajectory for different m_F states. The calculation was carried out exemplary for an OSG duration of $250\,\mu\mathrm{s}$, beam waist $100\,\mu\mathrm{m}$ and a power of $45\,\mathrm{mW}$ using a Runge-Kutta method for ordinary, differential equations [Sha97]. The initial position of the particles was set to the $w/2$. Here, the initial force is maximized by the largest gradient. The plot indicates that scattering is relatively constant during illumination. The values for both lowest m_F states actually increases a little, which is expected, because these states are attracted towards the beam focus. Integrating each graph results in the total amount of scattered photons:

$$m_{-5/2} : 0.03,\ m_{-3/2} : 0.04,\ m_{-1/2} : 0.06,\ m_{1/2} : 0.08,\ m_{3/2} : 0.11,\ m_{5/2} : 0.14. \qquad (2.6)$$

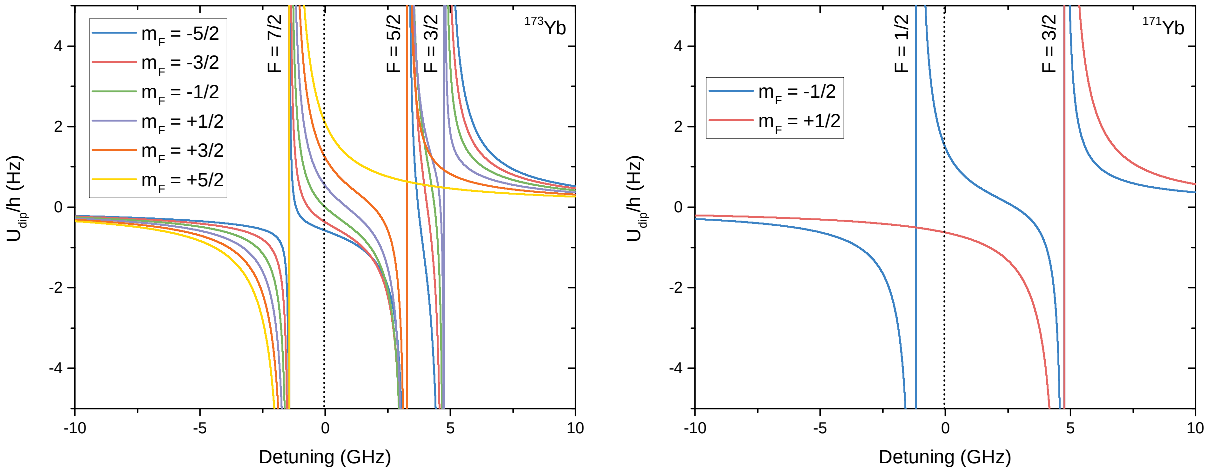

Figure 2.10.: Polarizability of the $^3P_1$ state for ^{171}Yb and ^{173}Yb. Both plots show the dipole potential of different m_F states for an intensity $I = 1\,\mathrm{W\,m^{-2}}$. The light is purely circular (σ^+) polarized. The center ($0\,\mathrm{GHz}$) is set to the resonance of ^{176}Yb. Atomic properties for the calculation are taken from [Pan09]. The black dotted line indicates the frequency position of our OSG laser. Here, the polarizability differences show large values. For further discussion see main text.

These numbers indicate that up to a portion of 14% atoms a subject to off-resonant scattering. This can be observed in the following section.

2.2.3. OSG imaging

For determining the spin distribution we initially apply an OSG sequence before commencing actual measurements. An exemplary image of a six-component gas of ^{173}Yb can be found in Fig. 2.12. In this case the OSG beam was switched on for $250\,\mu\mathrm{s}$ at a power of $45\,\mathrm{mW}$ and the picture was taken after a time-of-flight (TOF) of $13.5\,\mathrm{ms}$.

The image shows very good separation for the higher m_F states, while the lowest ones can barely be distinguished. This behavior is in agreement to the polarizabilities shown in Fig. 2.10. The total separation between $|m_F| = 5/2$ is about $650\,\mu\mathrm{m}$. This value is in very good agreement with the numerically determined trajectory.

Furthermore, scattered atoms are visible in between and below the different m_F states. Recapturing the numbers from 2.6 it is apparent that during illumination off-resonant photons are scattered. Based on the estimation, in case of $m_F = 5/2$ about 14% of the atoms scatter a photon. The visible atoms next to the main peaks can be attributed to this process. For instance the cloud below the $m_F = 5/2$ peak is located within a distance of $94\,\mu\mathrm{m}$. The direction of separation coincides with the optical axis of the OSG beam. The displacement can therefore be explained by the absorption of $556\,\mathrm{nm}$ photons. The velocity change due to one photon in case of Yb is $4.1\,\mathrm{mm\,s^{-1}}$ which is not sufficient to explain this distance by mere propagation during TOF ($55\,\mu\mathrm{m}$). Instead, the scattering event happens during illumination, which additionally changes the actual trajectory in the potential of the OSG beam. The atoms in between the peaks can be likewise explained by scattering processes during illumination. Thus they are subject to differently applied forces. In addition, each m_F state needs to propagate through all other states

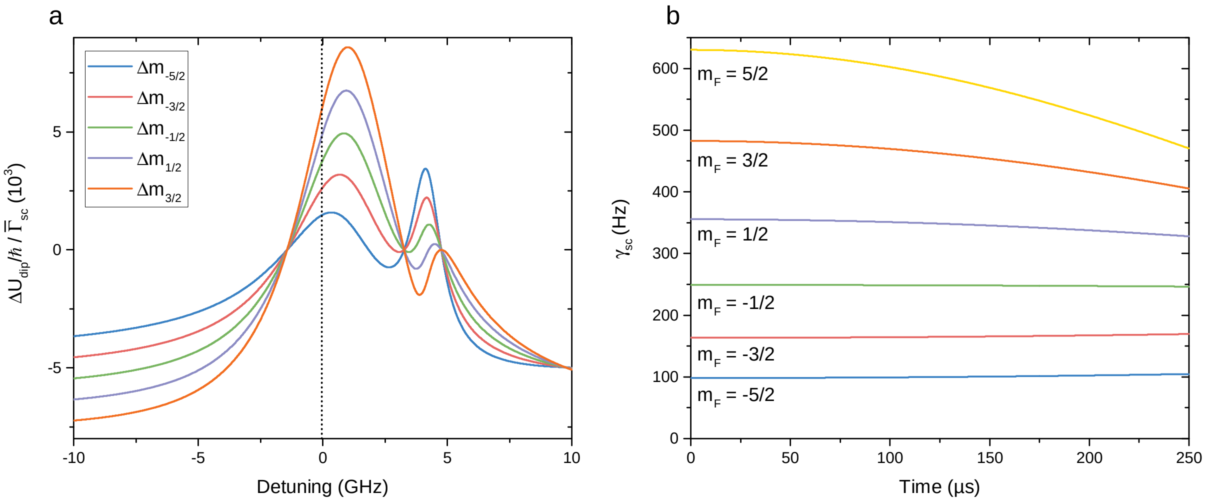

Figure 2.11.: OSG efficiency and scattering rate. **(a)** The plot shows a measure for the efficiency of the OSG scheme by comparing the potential differences ΔU_{dip} with the mean scattering rate $\bar{\Gamma}_{\text{sc}}$. Extrema can be found between the hyperfine states $F = 7/2$ and $F = 5/2$. Most crucial is the separation of the lowest m_F states, because their difference is the smallest one. The black dotted line points out our present setting. The values to the far left show large values too. However, these frequencies are technically difficult to engineer. **(b)** The diagram shows the scattering rate for each m_F state on a numerically determined trajectory. For the exact parameters see main text. The scattering rate stays rather constant along the trajectory. A slight increase is visible for the lowest m_F states, because these are attracted to the center for the OSG beam. The total amount of scattered photons can be determined by integrating each graph. The results can be found in Eq. (2.6).

initially, because the preparation starts from an equal spin distribution. This possibly results in dragging of atoms.

The effect of photon scattering and the small separation between the lowest m_F states limit the accuracy of precise atom counting per spin state. If an accurate mixture is needed, state transfers according to the values in 2.6 need to be considered. These drawbacks can possibly be reduced by application of a second beam with opposite polarization. This was already successfully demonstrated in case of Sr [Ste11]. Our calculations demonstrated a significant reduction of scattered photons and an increased separation of the spin states using two beams, which are horizontally separated with the atomic cloud being located in between. Both are set to the same frequency. In this way, the small polarizability difference between the lowest m_F states can be significantly increased. Crucial for this technique is a strong external quantization axis to avoid any polarization mixing at the overlap region of both beams.

2.3. Detection of the $^3P_0$ state

In the following chapters excitation of the $^3P_0$ state is an essential tool for ultra-narrow spectroscopy and initiating dynamics in optical-lattice systems. Thus, individual counting of ground and excited state atoms is highly preferable. However, since it is a clock state with a lifetime $\geq 10\,\text{s}$, waiting for the atoms to spontaneously decay to the ground state is not an option. There are basically three ways to depopulate the clock state and measuring the atom number using

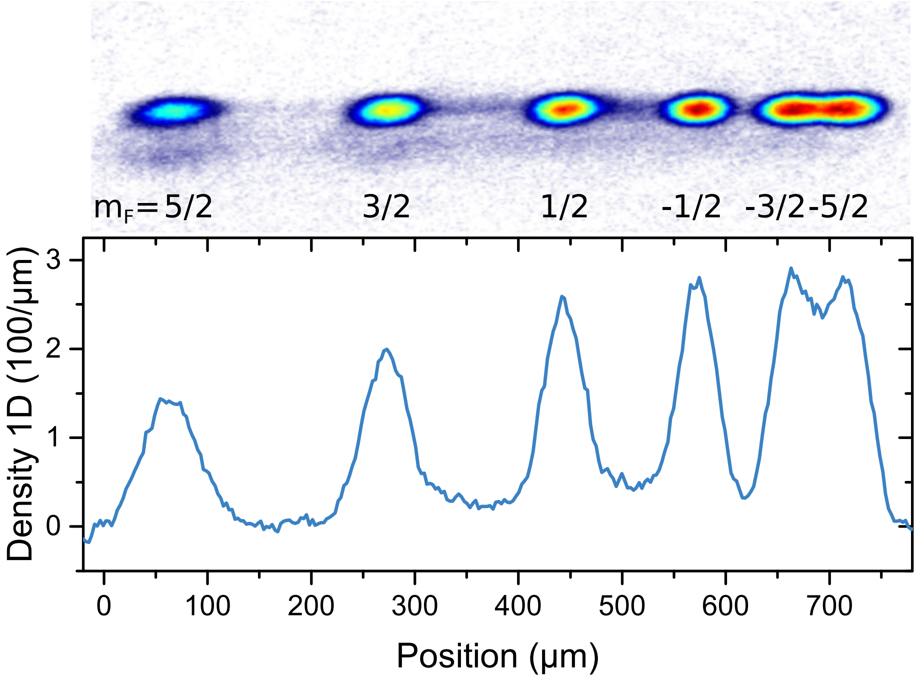

Figure 2.12.: Spin separation of a six-component ^{173}Yb mixture using OSG. The image shows spin separation caused by the OSG beam for $250\,\mu\mathrm{s}$ and a TOF of $13.5\,\mathrm{ms}$. The distance between different m_F states varies significantly according to the individual polarizabilities. A low amount of atoms is visible between and below the main peaks. These are caused by off-resonant scattering with the OSG beam. The image was three times averaged.

absorption imaging:

1. The clock laser can be used for depopulating the $^3P_0$ state.
2. A Raman-laser pair [Una98] can be applied to coherently transfer atoms to the $^3P_1$ state. These atoms would decay to the ground state.
3. A repump laser can cycle atoms on the $^3P_0 \Leftrightarrow {}^3D_1$ transition until all of them decay to the $^1S_0$ state via the $^3P_1$ state.

Although the first option seems to be straight forward, one has to keep in mind that for this approach the same frequency stability as for excitation of the clock state is needed (cp. Chap. 3). To ensure depopulation of all spin states the laser possibly needs to be saturation broadened depending on an external magnetic field or the stability of the laser. Furthermore, addressing the clock transition is preferably done in a magic, optical lattice to suppress frequency broadening and shifts. Thus this approach is undesirable when working with a different wavelength, as is for example needed in case of a state depending lattice. Using other coherent methods, like a rapid adiabatic passage (RAP), to reduce the frequency sensitivity brings other drawbacks, which are described in Chap. 4.

The second approach is less demanding regarding frequency stability due to the larger linewidth of an intermediate state. However, this method involves two additional lasers at $649\,\mathrm{nm}$ and $680\,\mathrm{nm}$ to couple the states $^3P_0$ and $^3P_1$ via $^3S_0$ in a Lambda scheme [Vit16]. These need to be

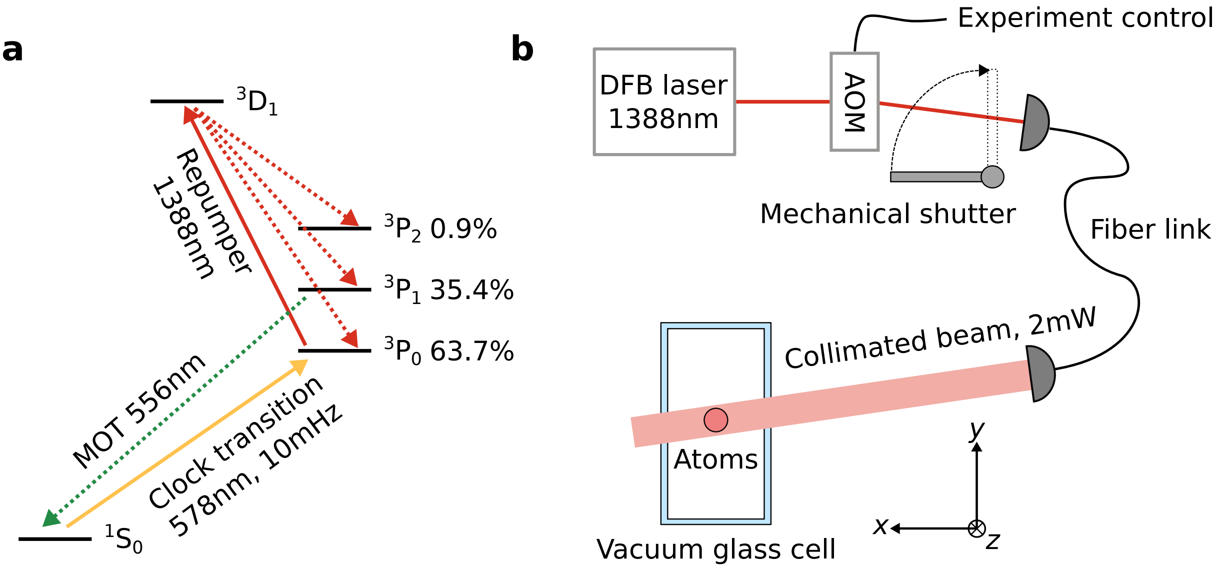

Figure 2.13.: Level scheme and laser setup of repumper transition. **(a)** The sketch shows the atomic states involved during repumping. The clock state is initially populated using Rabi oscillations (π-pulse) or RAP. Laser light at $1388\,\mathrm{nm}$ can cycle atoms between the $^3P_0$ and $^3D_1$ state. The respective branching ratios for the three decay channels are indicated. Atoms reaching the other meta-stable state $^3P_2$ are considered as lost. From the MOT state $^3P_1$ the atoms can decay to the ground state by emitting a photon at $556\,\mathrm{nm}$. These atoms can be imaged using regular absorption imaging at $399\,\mathrm{nm}$. **(b)** The drawing shows a simplified version of the repump-laser setup. We use a DFB laser which is actively temperature stabilized. Due to the diode type the frequency is highly tunable by its temperature. We do not apply any locking scheme to this laser. The beam is switched using an AOM and it is lead to the science cell using a fiber link. A large beam diameter of $2\,\mathrm{mm}$ makes the setup robust against misalignment. The graphic was taken in parts from [Hun16].

phase stabilized with respect to each other which brings new technical challenges[16].
We decided to implement the third option, because it only involves a single laser at $1388\,\mathrm{nm}$. The demands on frequency stability are significantly lower compared to a clock transition. On the one hand the natural linewidth with $267\,\mathrm{kHz}$ [Bow96] is at least comparable to the frequency stability of temperature stabilized laser diodes. On the other hand we apply frequency modulation to increase the spectral width of the laser to $\approx 10\,\mathrm{GHz}$ to ensure enough power spectral density in case of small drifts. A sketch of the level scheme with the involved states and the $1388\,\mathrm{nm}$ laser setup can be seen in Fig. 2.13.

2.3.1. 1388 nm laser setup

As laser source we use a commercial distributed-feedback laser diode[17] with $10\,\mathrm{mW}$ output power. The diode is conveniently delivered in a butterfly package with connected fiber and Peltier element. The frequency can easily be adjusted by changing the temperature. We switch the laser power using an AOM and implemented an additional shutter to avoid any leakage

---

[16] For an absolute frequency reference a galvatron can be used for preparing atoms in the $^3P_0$ state without the need of a clock-laser setup.

[17] NTT Electronics NLK1E5AAA

of resonant light. Laser light is lead to the atoms using a fiber link. A large waist of about $1\,\mathrm{mm} \times 1\,\mathrm{mm}$ is used to keep the beam pointing insensitive against misalignment. We use about $2\,\mathrm{mW}$ of power during imaging. No specific polarization was set.
For monitoring purposes we implemented an optical resonator to confirm single-mode operation of the laser. Furthermore, to measure the actual wavelength we use an optical spectrum analyzer[18] (OSA). The resolution at $1388\,\mathrm{nm}$ is roughly $10\,\mathrm{GHz}$, which is just sufficient to visualize the frequency modulation we apply onto the laser-current driver. We initially aligned the beam using resonant light for the $^1S_0 \Leftrightarrow {}^3P_1$ transition. The absolute accuracy of the OSA is sufficient to find a spectroscopic signal with ultracold ^{173}Yb.

2.3.2. Theoretical efficiency of repumper transition

The efficiency of the repumper scheme can be estimated by comparing the different decay channels originating from the $^3D_1$ state. Due to selection rules the decay only happens into the ^3P manifold [Har89]. The branching ratios between the respective states $J = \{1, 2, 3\}$ can be calculated using the 6J-symbols [Mes81, Ste13]:

$$\tau^{-1} \propto \omega_0^3 \frac{2J+1}{2J'+1} |\langle J||e\mathbf{r}||J'\rangle|^2, \; \langle J||e\mathbf{r}||J'\rangle \propto \begin{bmatrix} L & L' & 1 \\ J' & J & S \end{bmatrix}.$$

The variables are lifetime τ, angular momentum L, spin S, total angular momentum J, the transition frequency ω_0 and dipole operator $e\mathbf{r}$. Bare symbols indicate initial states and primed ones final states. As result we calculate the following values:

$$^3D_1 \Leftrightarrow \{^3P_0 : 63.7\%, {}^3P_1 : 35.4\%, {}^3P_2 : 0.9\%\}.$$

Using these values together with the decay rate of the $^3D_1$ state $\Gamma = 2\pi \times 419\,\mathrm{kHz}$ [Bow96] the coupling strengths can be calculated:

$$\begin{aligned} \Gamma(^3P_0 \Rightarrow {}^3D_1) &= 2\pi \times 267\,\mathrm{kHz}, \\ \Gamma(^3P_1 \Rightarrow {}^3D_1) &= 2\pi \times 148\,\mathrm{kHz}, \\ \Gamma(^3P_2 \Rightarrow {}^3D_1) &= 2\pi \times 4\,\mathrm{kHz}. \end{aligned}$$

As indicated in Fig. 2.13 the only way to reach the state $^1S_0$ involves the $^3P_1$ state. If instead an atom decays to the $^3P_0$ state it can be excited once again. Atoms which decay to the $^3P_2$ state are lost. Since this state is meta stable with a lifetime of $\approx 15\,\mathrm{s}$ [Por99], an additional laser would be needed to get these atoms back into the pumping cycle.
At this point the efficiency can already be estimated by directly comparing the branching ratios. However, a more reliable model makes use of the coupled rate equations [Cho12], which describe all involved pumping processes:

$$\begin{aligned} \dot{N}_{^3P_0} &= -g_0\Gamma_{\mathrm{sc}}N_{^3P_0} + g_0\Gamma N_{^3D_1} \\ \dot{N}_{^3P_1} &= g_1\Gamma N_{^3D_1} \\ \dot{N}_{^3P_2} &= g_2\Gamma N_{^3D_1} \\ \dot{N}_{^3D_1} &= g_0\Gamma_{\mathrm{sc}}N_{^3P_0} - \Gamma N_{^3D_1} \end{aligned} \tag{2.7}$$

---

[18] Yokogawa AQ6370

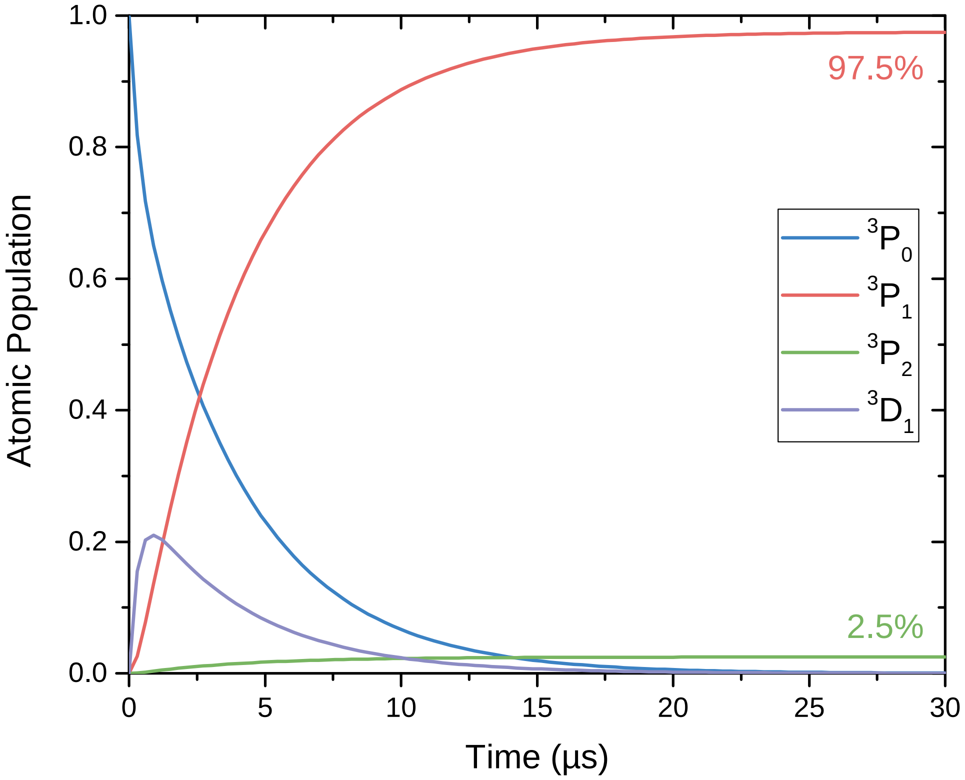

Figure 2.14.: Time evolution of repumping scheme. The graphic shows a simulation of the population according to the coupled differential equations in 2.7. Atoms initially located in the clock state $^3P_0$ are excited to an intermediate state $^3D_1$. These atoms can decay to the ^3P manifold with branching ratio 63.7% ($^3P_0$), 35.4% ($^3P_1$) and 0.9% ($^3P_2$). Any occupation of the other meta-stable state $^3P_2$ is considered as lost. Atoms reaching the MOT state $^3P_1$ decay to the ground state and can be imaged using $399\,\mathrm{nm}$ light. According to the calculation the theoretical efficiency is 97.5%. For an intensity $I = 10000 \times I_{\mathrm{sat}}$ the system becomes stationary after $30\,\mu\mathrm{s}$.

Here, N_{x} indicates the respective amount of atoms, $g_{0,1,2}$ describe the branching ratios, and Γ_{sc} is the photonic scattering rate. Since we reach a very high intensity on the order of $10000 \times I_{\mathrm{sat}}$[19] we set $\Gamma_{\mathrm{sc}} = \Gamma/2$. The solution of the coupled differential equations can be seen in Fig. 2.14. The time evolution suggests that we can depopulate the $^3P_0$ state within $30\,\mu\mathrm{s}$. Merely 2.5% of the atoms are lost in the second meta stable state $^3P_2$. The population distribution in the first few µs shows up to 20% occupation of the $^3D_1$ state. In a typical experimental cycle the repump laser is switched on for $1\,\mathrm{ms}$ to ensure full depopulation of the $^3P_0$ state.

2.3.3. Experimental sequence

The following section describes the full imaging sequence applied to detect ground- and excited-state atoms simultaneously. This procedure is divided into the following three steps:

1. We image the ground state atoms $^1S_0$ using absorption imaging at $399\,\mathrm{nm}$.
2. The repump laser is switched on for $1\,\mathrm{ms}$ to transfer the $^3P_0$ states into the ground state.

---

[19] $I_{\mathrm{sat}} \approx 13\,\mu\mathrm{W\,cm^{-2}}$, $I_{\mathrm{peak}} \approx 127\,\mathrm{mW\,cm^{-2}}$

Isotope	Shift (MHz)
^{171}Yb$(F=\frac{1}{2})$	4082
^{170}Yb	2551
^{173}Yb$(F=\frac{7}{2})$	2115
^{172}Yb	1110
^{171}Yb$(F=\frac{3}{2})$	1019
^{174}Yb	0
^{173}Yb$(F=\frac{5}{2})$	-209
^{176}Yb	-1061
^{173}Yb$(F=\frac{3}{2})$	-1110

Table 2.2.: Hyperfine splitting of the $^3D_1$ state. The hyperfine splitting was measured by directly exciting the $^3D_1$ state and detecting fluorescence at $556\,\mathrm{nm}$. Data was taken from [Bow99].

3. We take a second image at $399\,\mathrm{nm}$, which was originally intended as reference for the initial picture.

Due to the double imaging and the spacial separation between ground- and excited-state atoms the second image can be used as normalization for the initial image and the other way round. This approach is only possible, if the TOF between both pictures is long enough to clearly separate both clouds. We usually wait for $2\,\mathrm{ms}$. An exemplary picture, where we prepared a $50:50$ mixture of ground- and excited-state atoms in the magic lattice, can be seen in Fig. 2.15.

All atoms we detect scattered on average 2.8 photons at $1388\,\mathrm{nm}$. Due to the directed photon absorption and an intermediate TOF of $2\,\mathrm{ms}$ each repumped atom is displaced by about $9.5\,\mu\mathrm{m}$. This effect should be negligible considering the total TOF and our large field of view.

We experimentally analyzed the efficiency of repumping by measuring the ground and excited states simultaneously during a sequence of Rabi oscillations. If the sum of both states shows any oscillation coinciding with the Rabi frequency, it would indicate an efficiency loss for the repumping process. We prepared a spin-polarized sample of ^{173}Yb $(m_F = 5/2)$ in a magic lattice $(V_{\mathrm{1D}} = 50\,E_{\mathrm{r}})$ and applied a Rabi frequency of $\Omega = 2\pi \times 2.7\,\mathrm{kHz}$. The result is shown in Fig. 2.16. The solid lines indicate fits using a damped sine function with frequencies $2.78\,\mathrm{kHz}$ and $2.72\,\mathrm{kHz}$. In addition, the sum of ground and excited states is shown and the respective Fourier transform (FFT) is plotted. Considering the atom sum in Fig. 2.16a no apparent oscillation is visible. This is confirmed by looking at the respective frequencies in the Fourier spectrum. We thus concluded that within our atom-counting sensitivity no additional efficiency loss occurred due to the repumper scheme.

The repump scheme as described here is not sensitive to detect individual m_F states but was rather set up in a way to maximize robustness against frequency instability. The spectral broadening we apply to the laser diode covers not only the Zeeman splitting but also the hyperfine manifold as can be seen from Tab. 2.2. However, there is no principal reason that prevents repumping at $1388\,\mathrm{nm}$ to be spin selective. For this to work, a magnetic field needs to be applied to sufficiently split the Zeeman states of $^3D_1$. Furthermore, one needs to actively stabilize the laser to an absolute reference for precise frequency tuning.

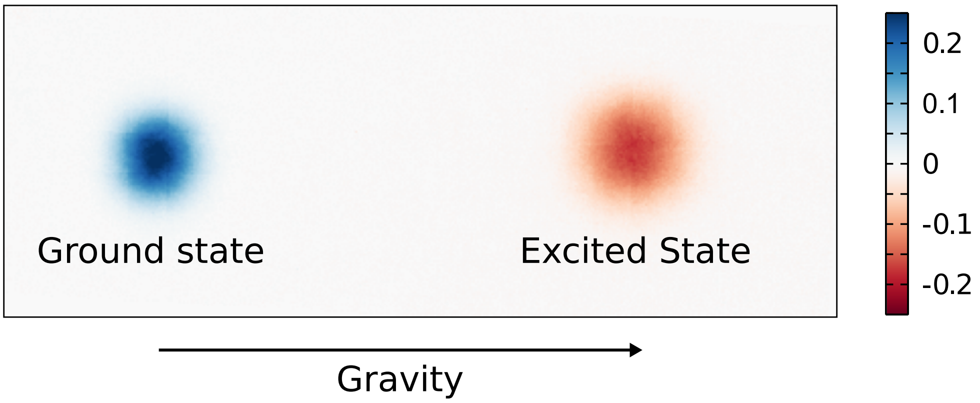

Figure 2.15.: Double image of $50:50$ mixture of $^1S_0$ and $^3P_0$. The picture is taken during a Rabi cycle for a spin-polarized gas of ^{173}Yb in a deep, magic lattice, which are excited via the clock transition at $578\,\mathrm{nm}$. The ground-state atoms are first detected using absorption imaging at $399\,\mathrm{nm}$. Afterwards, the excited states are transferred to the ground state using the $1388\,\mathrm{nm}$ repump laser for $1\,\mathrm{ms}$. A second absorption image is taken after $2\,\mathrm{ms}$. Each picture can be used as a reference for the other one, because both atomic clouds do not overlap. The Graphic was taken from [Hun16].

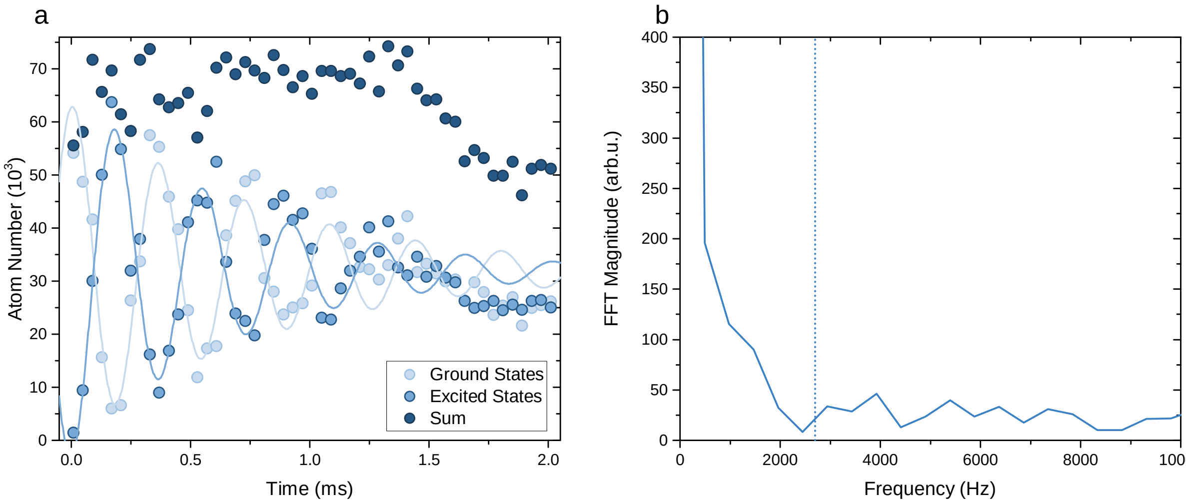

Figure 2.16.: Repumper efficiency. (a) The plot shows simultaneous measurement of ground- and excited-state atoms undergoing Rabi oscillations. We used a spin polarized sample of ^{173}Yb ($m_F = 5/2$) in a deep, magic lattice ($V_{1D} = 50\,E_r$). Solid lines indicate fits with a damped Sine function. The frequency results of $2.78\,\mathrm{kHz}$ and $2.72\,\mathrm{kHz}$ are in very good accordance to the expected $2.7\,\mathrm{kHz}$ deduced from the beam intensity. The sum of both atoms indicates a drop of the total atom number at the end of the sequence which can be attributed to technical issues during the measurement sequence. **(b)** The graph shows the Fourier transform of the atom-number sum. No significant amplitude in the vicinity of $2.7\,\mathrm{kHz}$ is visible. Thus, we do not measure an efficiency loss of the repumper scheme within our atom-counting sensitivity.

2.4. Evaporation of different spin mixtures

The last section shows the performance of our experimental apparatus considering the production of a DFG with different spin mixtures. In addition, the evaporation process in case of six and two spin components is compared.

2.4.1. Ultracold ^{173}Yb gases with different spins

DFGs were produced by the scheme already explained in Sec. 2.1. The amount of atoms and the corresponding temperature for a six-component gas during evaporation can be seen in Fig. 2.17. Particle numbers were determined using absorption imaging. The temperature was measured using the rate of expansion after TOF for the first $5\,\mathrm{s}$ [Brz02]. During evaporation in the IR trap, $5\,\mathrm{s}$ to $15\,\mathrm{s}$, we approximated the atomic distribution with a Thomas-Fermi fit [DeM01a] to determine the fugacity. The temperature can be calculated in units of the Fermi temperature T_F using

$$Li(3, -\xi) = -\frac{1}{6(T/T_F)^3}, \tag{2.8}$$

with polylogarithm *Li* and fugacity ξ. The absolute temperature can be deduced by interpolating the trapping frequency for all intermediate steps of evaporation by [Ket08]

$$\frac{T}{T_F} = \hbar\bar{\omega}(6\,N_{\mathrm{comp}})^{1/3},$$

with the mean trap frequency $\bar{\omega}$ and the amount of atoms per spin component N_{comp}. Note that the Thomas-Fermi fit results for $5\,\mathrm{s}$ and $6\,\mathrm{s}$ have a bad fidelity due to a cloud size that is comparable to our field of view. We observe a rather smooth transition between bicolor and IR dipole trap. We attribute this to a well engineered transfer between DT1 and the IR traps. After transfer into the crossed IR trap the cloud has a temperature of about $1\,T_F$. The slopes at the end of evaporation suggest that the process of cooling can be continued at the cost of more particles. This we could observe at our experiment by reaching temperatures as low as $10\%\,T_F$ with about 10^4 atoms. Fig. 2.18 demonstrates the DFGs for three different spin mixtures at the end of evaporation. We typically produce a six-component gas with 87×10^4 atoms at a temperature of $17.5\,T_F$.

For the preparation of other spin mixtures we applied a high magnetic field of $64\,\mathrm{G}$ to significantly split the m_F substates of $^3P_1$. Individual states were depopulated using resonant light with circular polarization to redistribute the population and only leave the desired states occupied. The pumping procedure took place right before evaporation while the atoms were already loaded into the dipole trap. Principally we can produce arbitrary spin mixtures between $\mathcal{N} = 6$ and $\mathcal{N} = 1$. Fig. 2.18a to 2.18c only demonstrate the six-, two- and one-component Fermi gases, because these are of main interest for this thesis. The polarized DFG was generated by mostly redistribute the population to one state and use the remaining other spin states for evaporation. The images indicate that evaporation with fewer spin states tends to produce higher temperatures and smaller amounts of atoms. Here, the pumping process is at least partially

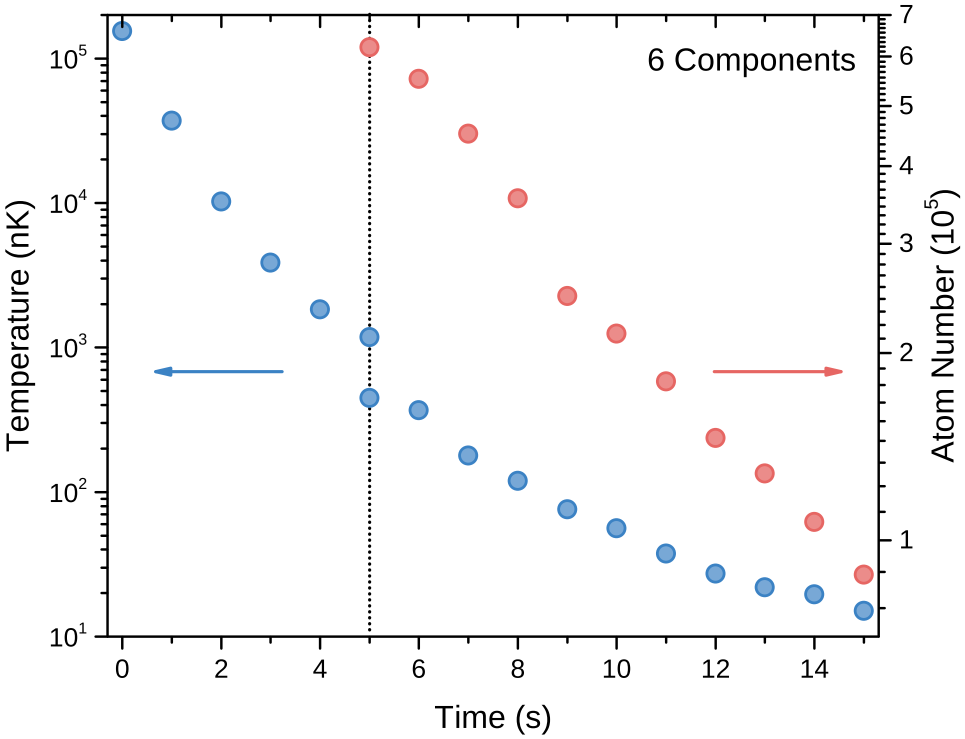

Figure 2.17.: Atom number and temperature during evaporation of ^{173}Yb. The plot shows characteristics of evaporation in the bicolor dipole trap using an equally distributed mixture of ^{173}Yb. The black dotted line indicates the time when DT1 is switched off. The amount of atoms was determined using absorption imaging. The temperature was measured by analyzing the cloud expansion during TOF for the first 5 s. The temperature during IR trap evaporation was deduced using the fugacity from a Thomas-Fermi fit and calculated trap geometry. The slopes at the end of evaporation suggest that further cooling is possible. The atom number during the first 5 s could not be determined due to the limited field of view. The measurement was three times averaged.

causing this effect due to heating of the sample. In addition, a polarized gas is subject to Pauli-Blocking and hence elastic scattering is suppressed at low temperatures. The following section specifically analyzes the evaporation process for a spin-depending efficiency.

2.4.2. Spin-dependent evaporation

To compare the evaporation for different spin mixtures we applied the preparation method mentioned above. Here, the results for a six- and two-component gas are shown, where the latter one has about 8% residual atoms of the other four states. To characterize the efficiency of the evaporation process Fig. 2.19 shows how the temperature T depends on particle number N. Both plots are limited to the phase in the IR trap, because the atom number in DT1 can not be determined due to the extension of the cloud. The temperature was determined using Eq. (2.8). The fit reliability is shown in Fig. 2.20 for a six-component gas.

Both graphs in Fig. 2.19 show a decreasing slope towards lower temperatures. This is expected because of Fermi-Dirac statistics and Fermi pressure [Koe87, DeM99]. Both effectively reduce the scattering rate at temperatures approaching $0\,\mathrm{K}$ [Hol00, DeM01b]. In this sense it

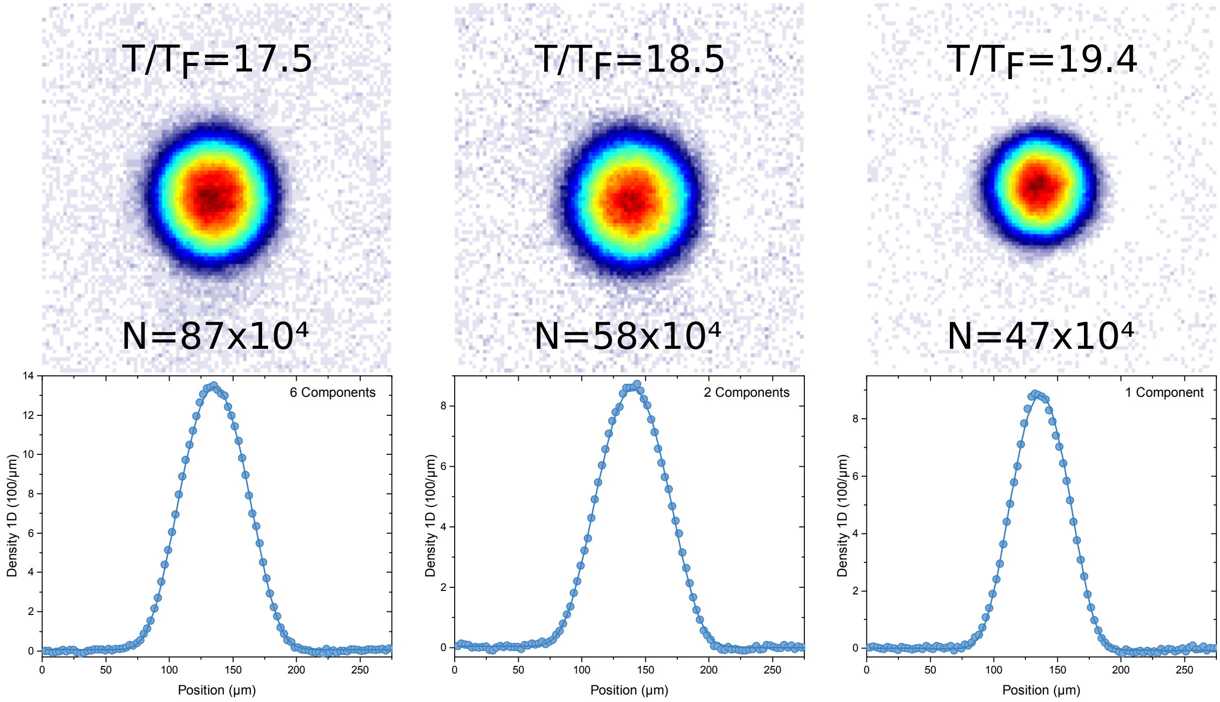

Figure 2.18.: Ultracold quantum gases of ^{173}Yb with different spin compositions. The three columns demonstrate our capability to produce ultracold gases with six, two and one spin component. The upper row shows absorption images with $399\,\mathrm{nm}$. The lower row shows the respective column sums with Thomas-Fermi fits (solid line). Spin states are eliminated by using spin-selective pumping via the green MOT transition. The Reduction of spin components leads to a slight increase of temperature and reduction of atom number. The first two images were taken with a TOF of $20\,\mathrm{ms}$, the last one with $13.7\,\mathrm{ms}$. The images are not averaged.

is not surprising that the suppression of cooling for the two-component gas is more severe. Fig. 2.19b further suggests that in the two-spin mixture the cooling comes to a stop, where in the six-spin case further cooling seems to be possible. Comparing both overall performances the six-component gas shows a steeper slope indicating a better efficiency, which is reasonable due to the larger amount of scattering partners.

These measurements constitute only a starting point for a comprehensive understanding of the underlying processes during evaporation. The next step would involve a respective measurement with a spin-polarized gas to specifically compare the low temperature behavior to the cases of two and six spins.

Conclusion

This chapter presented our scheme to produce, manipulate and detect ultracold ^{173}Yb gases. The new bicolor dipole trap improved the old setup in two ways: The initially large trapping volume can capture more atoms and the high trapping frequencies favor fast evaporation. Furthermore, the crossed IR trap reaches a low mean frequency $\bar{\omega} = 2\pi \times 36\,\mathrm{Hz}$, which is about a factor of three lower than the previous setup. In the following chapter we show that this is sufficient to prepare a DFG in the lowest band of an optical lattice. Efficient evaporation enables us to

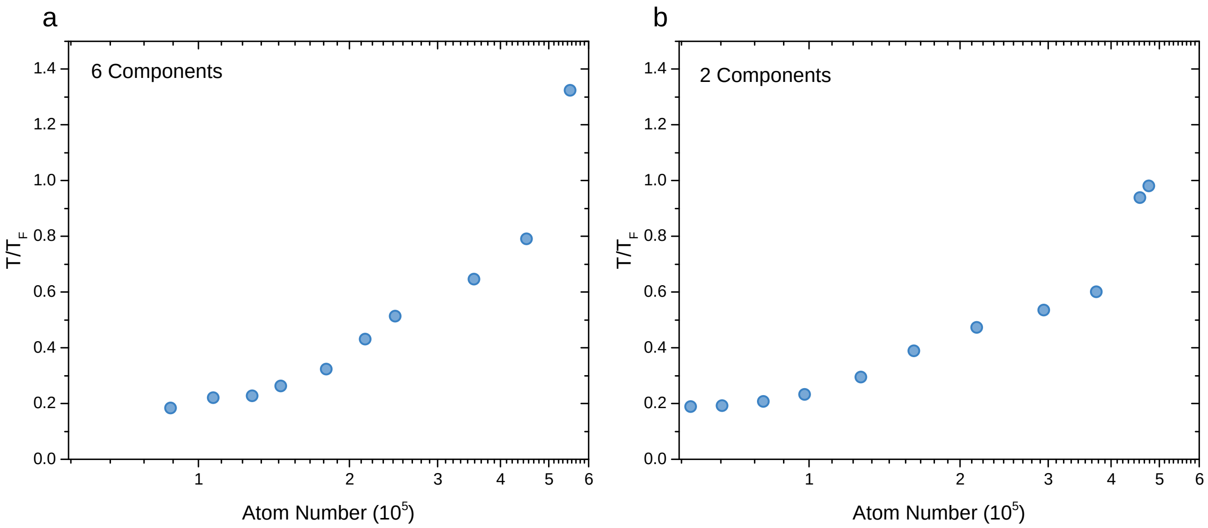

Figure 2.19.: Evaporation of a six- and two-component mixture of ^{173}Yb. Both graphs show how the temperature depends on atom number while evaporating a six- **(a)** and two-component **(b)** mixture. The amount of atoms was determined using absorption imaging after $20\,\mathrm{ms}$ TOF. The temperature was measured using the fugacity as result of a 2D Thomas-Fermi fit. While in **(a)** a slight slope persists at the end of evaporation, the data in **(b)** seems to settle. This is possibly caused by Pauli blocking and Fermi pressure. In addition, the overall slope of **(b)** is lower compared to the one in **(a)** indicating a worse evaporation efficiency in case of a two-component gas. The measurement was three times averaged.

typically reach six-component DFGs with 87×10^3 atoms at $17.5\% \, T_F$. We can individually manipulate the spin composition by resonant pumping using the $^1S_0 \Leftrightarrow {}^3P_1$ transition and detect the resulting state occupancy by applying an OSG scheme via the same transition. In the following chapters we make use of the clock state $^3P_0$. It is therefore essential to also detect these atoms. This is done by utilizing a repump transition coupling the $^3P_0$ and $^3D_1$ state ($1388\,\mathrm{nm}$). This enables us to conveniently measure the amount of atoms using absorption imaging at $399\,\mathrm{nm}$. Finally, we characterized the evaporation using the bicolor dipole trap and compared the efficiency between a six- and two-component gas of ^{173}Yb. We find a reduced evaporation efficiency in the case of a two-spin mixture.

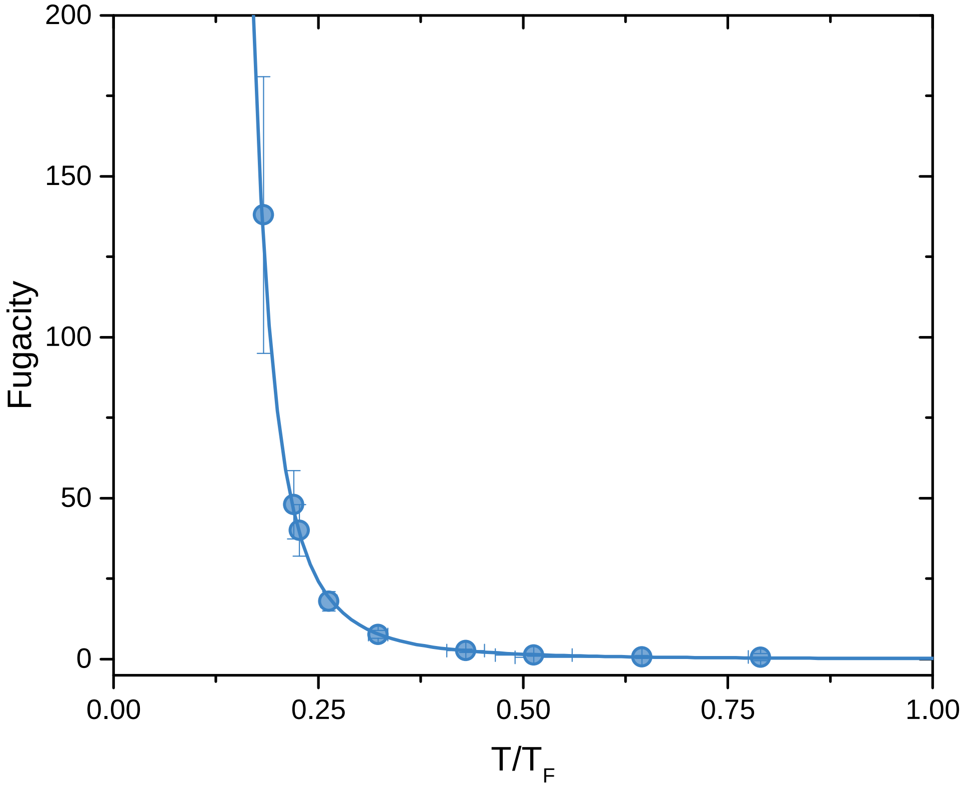

Figure 2.20.: Dependence between fugacity and temperature. The plot demonstrates the fit fidelity with which we determine the temperature of a DFG. The fugacity is deduced using a 2D Thomas-Fermi distribution. Data was averaged three times. Measurements with $T \geq 1 \times T_F$ are left out due to the cloud size being comparable with the field of view.

3. Probing ^{173}Yb Atoms via an Ultra-Narrow Transition

The clock transition in Yb at $578\,\mathrm{nm}$ is an example for ultra-narrow transitions in the visible range. It is very well suited for operating atomic lattice clocks [Hin13]. In addition to measuring time with an unprecedented precision, atomic clocks find application in the field of gravitational wave detectors [Kol16]. In the context of ultracold quantum gases such a transition can be a versatile tool for various applications. Due to its high resolution, interaction effects which lead to slight energy shifts on the order of kHz can easily be resolved. An example being the exchange-interaction energy persistent for two fermions on the same lattice site [Sca14, Cap14]. Due to the long lifetime of the clock state it can be regarded as an additional particle type. This orbital degree of freedom can be used to simulate solid-state models as the Kondo-Lattice-Model (KLM) [FF10b] or initiate two-body losses to realize dissipative systems [Gri05b, Bar13a]. Furthermore, the clock transition can be used to engineer artificial gauge fields with neutral atoms to mimic the behavior of charged particles in a magnetic field [Dal11, Man15].

Three prerequisites are necessary to exploit all features of the $^1S_0 \Leftrightarrow {}^3P_0$ transition. First, measurements have to be carried out in a magic optical lattice, i.e. at a wavelength that causes equal polarizability for both states. This is essential to avoid a frequency shift and broadening of the transition due to the AC-Stark shift. Second, the light source for interrogating the atomic transition needs to have a very narrow linewidth itself to generate sufficient power spectral density and avoid power broadening. Third, the laser has to be locked to a very stable reference, because already a drift of several $10\,\mathrm{Hz}$ corrupts the measurement. Fortunately, these tools are available at the experiment and will be described in the following.

The chapter is organized as follows: First, the setup for a magic optical lattice is presented. This is the same setup which is applied in the following chapter. Next, the clock-laser setup is presented and its performance characterized. Finally, the last section describes the use of the clock transition to observe inter band transitions and the exchange interaction with ^{173}Yb.

The lattice setup was planed and build by B. Hundt [Hun16] and N. Petersen [Pet14]. The clock-laser system was originally build by A. Thobe [Tho14]. A redesign was planned by T. Ponath and the author and the modifications were implemented by T. Ponath [Pon17] to improve the performance in several ways. The spectroscopy measurements were done by T. Ponath and the author. Data was analyzed by T. Ponath and the author.

3.1. A magic optical lattice for Yb

Optical lattices are a well established tool in the field of ultracold quantum gases [Jak98, Blo05]. The periodic potentials generated by interfering laser beams enable the experimentalist to hold

a large amount of control over amplitude, phase and geometry. This paved the way for step stones like observation of the Mott insulator transition [Gre02, Wei11], simulation of classical magnetism using neutral atoms [Str11], first observation of an antiferromagnet phase in the Hubbard model [Par16, Bol16] or the first measurement of the Berry curvature [Flä16].
Besides these applications the use of an optical lattice in connection with clock spectroscopy serves two technical reasons: 1. The lattice laser emits light at the magic wavelength of $759\,\mathrm{nm}$ [Bar08, Par13, Sca15] to suppress shifting and broadening of the atomic transition. 2. Due to large lattice depths the excitation of motional degrees of freedom is reduced and excitation of the clock state can be carried out recoil free [Esc03].

3.1.1. 759 nm laser setup

As laser source for the magic optical lattice we use a commercial Ti:Sa[1] system emitting about $4.5\,\mathrm{W}$ at the desired wavelength of $759\,\mathrm{nm}$. The frequency is actively stabilized using a fiber link to a wavelength meter[2]. The beam is split into four individual branches, one for the 1D lattice and three for the 2D lattice, which are switchable and power regulated using AOMs. We choose a detuning of $160\,\mathrm{MHz}$ between 1D and 2D lattice to avoid any interference between them. Light pickups for stabilization are located before the science cell in case of the 1D lattice and after transmission of the science cell in case of the 2D lattice. In addition to power regulation the AOMs can also be used for shaking of the lattice by phase modulation of the RF sources [Str12].
For the stability of the lattice position it is necessary to maintain phase stability between different beams. In case of the 1D lattice this plays only a marginal role due to the boundary condition of the retro reflecting mirror. In case of the 2D lattice however phase noise can significantly alter or modulate the position of potential wells. Although we previously used active fiber-noise-canceling (FNC) [Ma94] to avoid these effects, our observation indicated that AOM drivers depending on digital RF sources[3] without FNC possess even better performance.
Each beam is guided to the science cell via optical fibers. These are directly connected to the beam shaping optics defining the geometry of the optical lattice.

3.1.2. Implementation at the science cell

An overview of the beam geometry around the atomic cloud can be found in Fig. 3.1. The telescopes of the 2D lattice are directly pointed onto the science cell with an angle of $120°$. The polarization of each beam can be set using $\lambda/4$ plates right behind the telescopes to switch between a triangular or honeycomb lattice. Using a combination of $\lambda/2$ and $\lambda/4$ plates arbitrary superpositions of these lattice types can be engineered. Throughout this thesis only the triangular structure is used (linear polarization pointing into z-direction). Perpendicular to the 2D lattice and pointing into the z-direction, the 1D lattice is build using a single retro reflected beam.

---

[1] Coherent Verdi V18 & MBR 110

[2] Angstrom WS/U-10U

[3] DDS sources stabilized to a GPS based $10\,\mathrm{MHz}$ OCXO

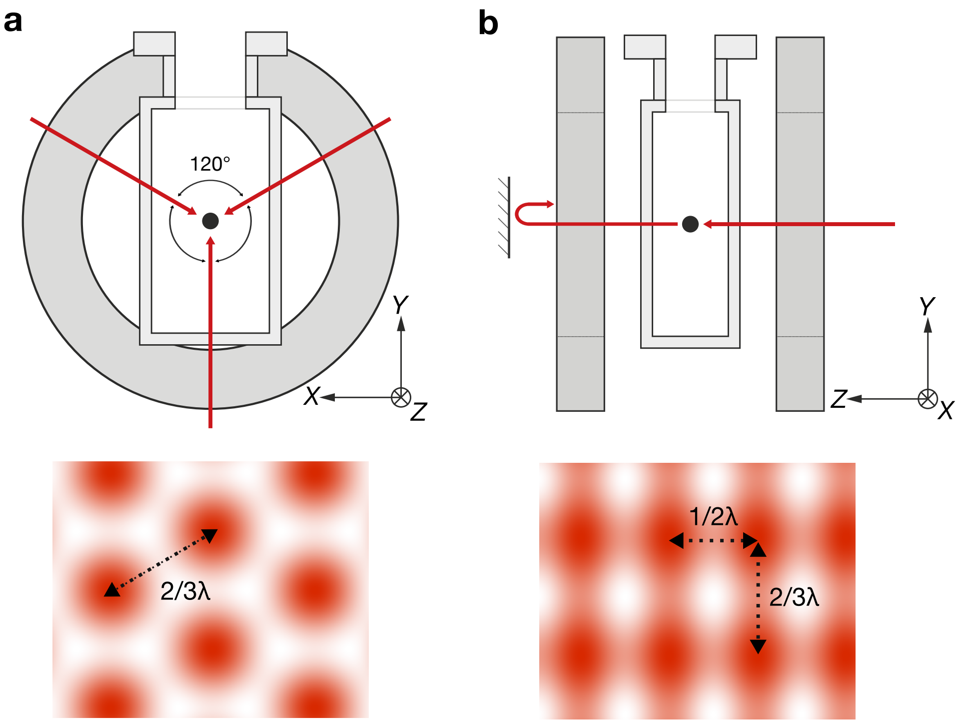

Figure 3.1.: Optical lattice geometry surrounding the science cell. **(a)** The sketch shows the geometry of the 2D lattice (x-y plane). All three beams are phase coherent with respect to each other. They intersect with an angle of 120° to each other. The geometry of the lattice can be tuned via the beam polarization. **(b)** The 1D lattice is generated using one retro reflected beam. The polarization points into the y-direction. Graphic was taken from [Hun16].

We use manually assembled telescopes with very high optical performance producing clean Gaussian modes. Each one carries a PBS to suppress polarization drifts of the fibers. A detailed description and analysis of them can be found in [Pet14, Hun16]. As a compromise between available laser power and versatility we chose waists of $84\,\mu\mathrm{m}$ for the 1D-lattice telescope and $93\,\mu\mathrm{m}$ for the 2D-lattice telescopes. We have a power of about $1\,\mathrm{W}$ for the 1D lattice and about $400\,\mathrm{mW}$ for each 2D-lattice beam available. The power can be redistributed to reach even higher intensities for the 1D lattice if necessary.

3.1.3. Characterization of the optical lattice

For the atom transfer between dipole trap and optical lattice and for producing an optimal lattice geometry the alignment of all four beams with respect to the dipole trap and with respect to each other is essential. We optimized the beam adjustment in two steps. First, all four lattice beams were individually pointed at the DFG in the dipole trap. This was done by analyzing possible oscillations induced by the additional attractive beam and eliminating this effect. This technique was used for bosonic as well as for fermionic isotopes. Second, The polarization for the triangular lattice needs to point perpendicular to the 2D-lattice plane. Since the 1D-lattice polarization lies within the 2D-lattice plane no interference should be visible between those beams. We verified this by employing Kapitza-Dirac diffraction [Gad09] and minimized this effect.

Close to the waists of the lattice beams their wavefronts can be approximated by plane waves. In this case the optical lattice can be idealized [Bec08] by

$$\begin{aligned} V_{1\mathrm{D}}(z) &= V_0\,\cos^2(k_L\,z), \\ V_{2\mathrm{D}}^{\triangle}(\mathbf{r}) &= V_0\left(\frac{3}{4}+\frac{1}{2}(\cos(\mathbf{b}_1\,\mathbf{r})+\cos(\mathbf{b}_2\,\mathbf{r})+\cos((\mathbf{b}_1-\mathbf{b}_2)\,\mathbf{r}))\right), \end{aligned} \tag{3.1}$$

with $k_\mathrm{L} = 2\pi/\lambda_\mathrm{L}$, lattice laser wavelength λ_L, reciprocal lattice vectors $\mathbf{b}_1$ and $\mathbf{b}_2$. V_0 denotes the lattice depth with $V_0 = 4\,U_\text{dip,max}$ (cp. Eq. (2.1)). Conveniently, the lattice depth can be measured in units of the recoil energy

$$E_\mathrm{r} = \frac{(\hbar k_\mathrm{L})^2}{2m} \approx h \times 1.99\,\mathrm{kHz}.$$

Summarizing the values of waists and beam powers with the just stated potential model we are able to reach a 1D-lattice depth of $V_{1\mathrm{D}} \approx 150\,E_\mathrm{r}$ and a 2D-lattice depth of $V_{2\mathrm{D}}^{\triangle} \approx 50\,E_\mathrm{r}$.

One of the main reasons for the use of a magic lattice is the possibility of recoil-free spectroscopy. The excitation of a free particle leads to absorption of the photon momentum, because every motional state is allowed. The situation is drastically changed in the environment of an optical lattice, because kinetic energy is quantized in form of lattice bands. In this way the change in kinetic energy while changing the internal, electronic state can be suppressed, if the recoil energy of the photon is a lot smaller than the bandgap energy:

$$\hbar\omega_\text{r,spec} \ll \hbar\omega_{nn'},$$

with the recoil energy of the spectroscopy laser $\hbar\omega_\text{r,spec}$ and frequency gap $\omega_{nn'}$ between bands n and n'. From this equation it is apparent that the suppression can be increased for larger lattice depths. This inequality is typically quantified using the Lamb-Dicke parameter [Win98] with

$$\eta = \sqrt{\frac{\omega_\text{r,spec}}{\omega_{nn'}}},\ \eta^2 \ll 1. \tag{3.2}$$

η^2 is proportional to the transition probability. Fig. 3.2 indicates how the Lamb-Dicke parameter depends on the lattice depth. For the properties of our 1D-lattice we can reach a Lamb-Dicke parameter as low as $\eta^2 \approx 0.07$. This enables us to significantly decouple the excitation of internal and external degrees of freedom.

A typical absorption image of ultracold Yb is shown in Fig. 3.3. Here, the momentum distribution of a ^{174}Yb BEC and ^{173}Yb DFG after TOF in the plane of the 2D-lattice is visible. In case of the BEC the image visualizes the quasimomenta of the triangular lattice and indicates a superfluid state. In case of the DFG, consisting of six spin components, the particles fill up the first Brillouin zone. The image demonstrates the hexagonal shape after band mapping [Köh05].

Since the lattice depth plays an important role for clock spectroscopy, good calibration of the regulation electronics is essential. A typical approach uses intensity modulation [Sav97, Kol06], where the energy gaps between different lattice bands can spectroscopically be determined. This technique is applicable for BECs as well as for DFGs. The difference is mainly an occupation of quasi momentum $q = 0$ in case of bosons, where fermions rather occupy the full lowest lying band depending on particle number. On on hand, this washes out a clear resonance frequency due to the curvature of lattice bands, on the other hand it can be used to measure the full band structure [Hei11]. For the following parts of this thesis we conducted calibration only with fermionic ^{173}Yb.

Since the perturbation via amplitude modulation has even parity, uneven inter-band transitions are suppressed. We typically prepare atomic samples in the lowest lying band. Hence, the strongest signal can be observed by tuning the modulation frequency to the second excited band. Higher bands can also be used but the transition amplitudes are reduced proportional to the Franck-Condon factor.

An exemplary image of a DFG subject to amplitude modulation can be found in Fig. 3.4. A sample of ^{173}Yb was loaded into the 1D lattice with $V_{\mathrm{1D}} = 7\,E_{\mathrm{r}}$ and a shallow dipole trap. We afterwards modulated the 1D-lattice power and took an absorption image after TOF with a band-mapping time of $500\,\mu\mathrm{s}$.

For the calibration of the lattice depths we did not analyze the full bandstructure. Instead we applied strong amplitude modulation and counted the loss of atoms due to parametric heating in the first Brillouin zone. Empirically this method produces clearer, spectroscopic features for deep lattices. Our FWHM resolution is about $3\,\mathrm{kHz}$. For deep lattices the bandwidth of the lowest lying band can be neglected and only the second excited band needs to be taken into account. The bandwidth for $n = 2$ is $\approx 1.5\,\mathrm{kHz}$ at a depth of $30\,E_{\mathrm{r}}$. Hence, the bandwidth can be neglected within our spectroscopic resolution.

The Results for $30\,E_{\mathrm{r}}$, $40\,E_{\mathrm{r}}$ and $50\,E_{\mathrm{r}}$ can be found in Fig. 3.5 with a modulation duration of $20\,\mathrm{ms}$ and band-mapping time of $2\,\mathrm{ms}$. Exemplary spectra can be seen in the insets. The respective lattice depths were determined by calculating the band gap $n = 0 \Rightarrow n' = 2$ at $q = 0$ with a 1D-band-structure. The solid line indicates a linear fit to the data points with a forced origin at $(0, 0)$. In a similar manner we analyzed the 2D-lattice beams. Here, the three 1D lattices produced by a pair of 2D-lattice beams were calibrated to yield the same lattice depths with equal power.

Modulation spectroscopy has distinct features to visualize the underlying band structure but relies on a quite narrow set of parameters and further depends on band mapping. An alternative approach uses the $^3P_0$ clock transition. By applying a laser frequency, which not only covers the internal-energy change but additionally the motional-energy change, atoms can be excited to sidebands [Lei03]. In this way the band spacings can be resolved with high resolution. This will be visualized in Sec. 3.3.1.

3.2. Laser system for high-resolution spectroscopy

To exploit all features that are associated with a clock transition it is essential to have a laser system with enough power and coherence time available. Sufficient Laser power is important to maximize the beam waist for suppression of dephasing due to inhomogeneous illumination. At the same time though, the Rabi frequency should be sufficiently high for the ability of power broadening. Taking the Rabi frequency as $77\,\mathrm{Hz}/\sqrt{I}$, $[I] = \mathrm{mW\,cm^{-2}}$ [Bar07] and our beam

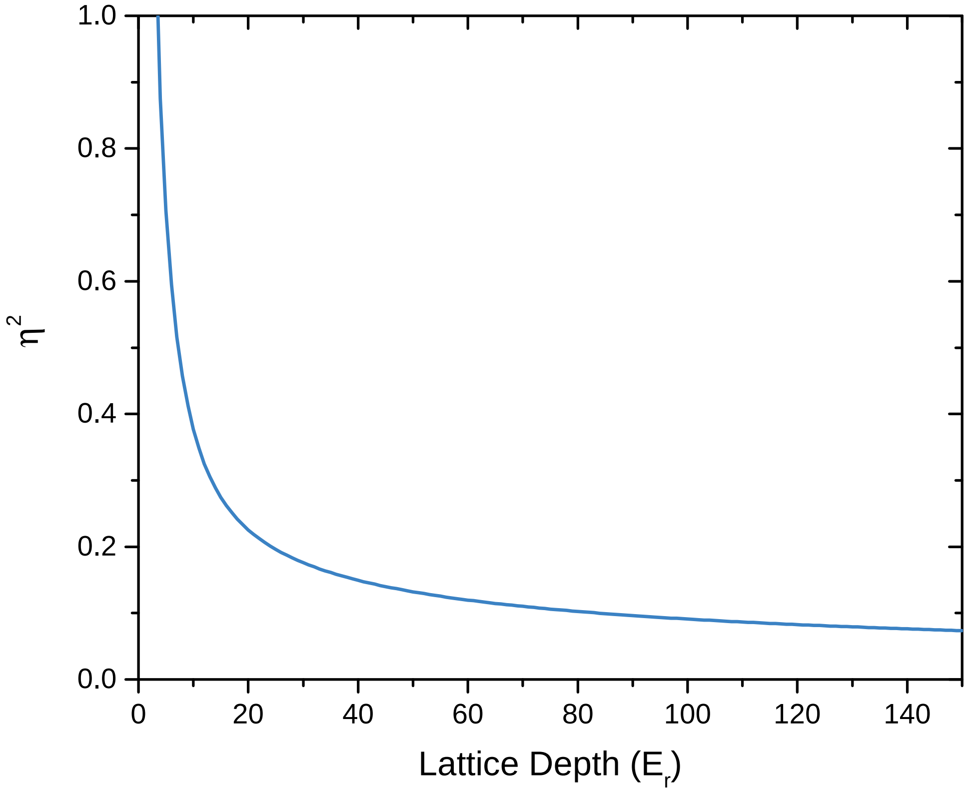

Figure 3.2.: Dependence between Lamb-Dicke parameter and lattice depth. The plot illustrates the relation in Eq. (3.2). In the case of Yb the photon recoil is $\omega_{\mathrm{r}}(578\,\mathrm{nm}) = 2\pi \times 3.4\,\mathrm{kHz}$. $\omega_{nn'}$ denotes the bandgap between $n = 0$ and $n' = 1$. It is determined with a 1D-bandstructure calculation.

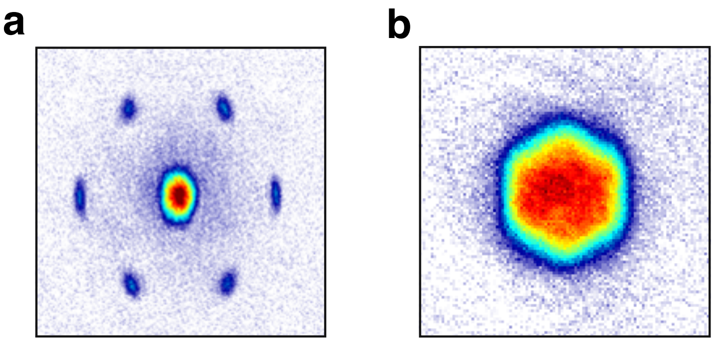

Figure 3.3.: Absorption images of BEC (^{174}Yb) and DFG (^{173}Yb) in the 2D lattice. Both images show typical measurements of a ^{174}Yb BEC **(a)** and a ^{173}Yb DFG **(b)** in a triangular lattice after TOF. The BEC shows strong diffraction peaks indicating a superfluid state. The atoms subject to fermionic statistics fill up the first Brillouin zone and indicate the hexagonal shape. **(b)** was taken for a six-component mixture and 2 ms bandmapping duration.

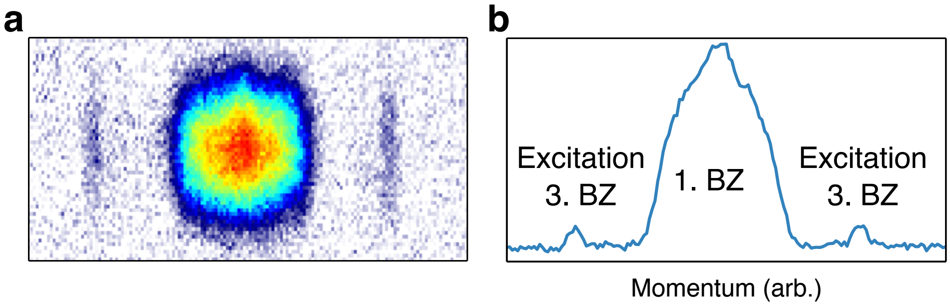

Figure 3.4.: Modulation spectroscopy in the 1D lattice. The graphic shows the absorption image **(a)** of a spin polarized gas of ^{173}Ybsubject to amplitude modulation in a 1D lattice $(7\,E_\mathrm{r})$ after band mapping $(500\,\mu\mathrm{s})$. For compensating gravity an additional shallow dipole trap was switched on. **(b)** shows the respective column sum indicating the excitation into the third Brillouin zone. Note the narrow excitation width compared to the size of the Brillouin zone.

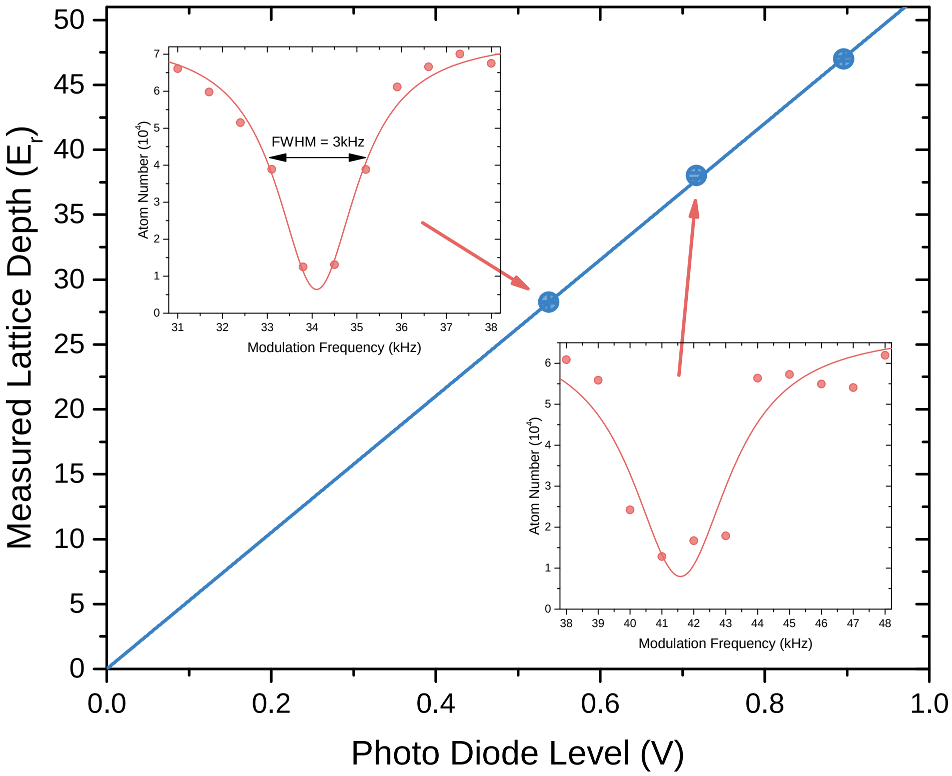

Figure 3.5.: Calibration of the 1D lattice. The plot shows the modulation spectroscopy results for $30\,E_\mathrm{r}$, $40\,E_\mathrm{r}$ and $50\,E_\mathrm{r}$ in a 1D lattice with a six component gas of ^{173}Yb. A shallow dipole trap was switched on to compensate the gravitational sag. The beam power is measured with a photo diode and related to the lattice depth. It is determined by comparing the resonance frequency with a 1D-bandstructure calculation. Insets indicate exemplary spectra with Lorentz fits to determine the center of the spectroscopic feature. The solid line shows a linear regression with origin forced to $(0, 0)$.

waist with $w_0 = 100\,\mu\mathrm{m}$ at least some mW of power are needed at the atom position to reach Rabi frequencies in the kHz range. Other applications like artificial gauge fields [Dal11] are possibly even more demanding. On the other hand the laser coherence needs to be significantly higher than the aimed interrogation time. Typical energy shifts due to interaction lie in the kHz regime leading to a favored resolution of better than $100\,\mathrm{Hz}$. This kind of coherence demands a laser linewidth on the order of $10\,\mathrm{Hz}$ for high-contrast spectra.

These kinds of laser systems are well established within the atomic-clock community [Not05, Sto06, Lud07]. Due to the narrow linewidth of the clock transition an error signal generated with a gas cell or beam apparatus using the atomic resonance is not feasible. Instead, stabilization is achieved using a PDH [Dre83] lock to a stable Fabry-Pérot resonator usually consisting of Ultra-Low-Expansion (ULE) glass. Due to the fast feedback the stability of the reference resonator gets transferred onto the laser such that linewidths below $1\,\mathrm{Hz}$ can be achieved [Aln08]. A detailed analysis about the necessary gain, bandwidth and detector attributes can be found in [Tho14] and a comprehensive description and characterization of our present setup is given in [Pon17].

3.2.1. Clock-laser setup

A sketch of the clock system is illustrated in Fig. 3.6. As light source we use a commercial SHG laser[4] at $578\,\mathrm{nm}$ with an output power of $300\,\mathrm{mW}$. Ideally the electronic feedback is directed to the laser diode, e.g. Sr lattice clocks with commercially available laser diodes at $698\,\mathrm{nm}$ [Lud07]. To actually reach a feedback that is capable of reducing the linewidth of a laser it is essential to achieve enough gain at low frequencies. Figuratively speaking this reduces the noise close to the carrier. Equivalently, the in-loop bandwidth needs to be sufficiently high, because every realistic regulation loop shows low-pass behavior. A possible measure of the bandwidth is the $0\,\mathrm{dB}$ point, where the electronics cannot suppress noise anymore. We analyzed two different laser diodes at $1156\,\mathrm{nm}$ with respect to their low-pass behavior (phase roll-off). Due to their large phase roll-off in the kHz regime, they were unsuitable for sufficiently high regulation bandwidths. We instead decided to avoid fast feedback to the laser diode and use an AOM for this task. The applied regulation electronics[5] provides two outputs with different bandwidths $45\,\mathrm{MHz}$ and $10\,\mathrm{kHz}$. We apply the fast branch directly to the AOM for linewidth narrowing and the slow one to the laser piezo for drift compensation. We reach in-loop regulation bandwidths up to $950\,\mathrm{kHz}$. Note that is is crucial to focus the laser beam close to the AOM transducer due to the modulation bandwidth limitation by the speed of sound in the crystal (typ. $4200\,\mathrm{m\,s^{-1}}$).

The design of our reference resonator is based on [Not05, Rüt10] consisting of plane and concave mirror substrate (radius of curvature $50\,\mathrm{cm}$) with a distance of $7.75\,\mathrm{cm}$. The spacer and both mirror substrates are made from ULE glass to ensure a CTE zero crossing close to room temperature. We determined the finesse [Rem92] to be $\mathcal{F} = 216900(400)$ corresponding to a cavity linewidth of $\Delta\nu_{\text{cav}} = 8.92(1)\mathrm{kHz}$ using a ring-down measurement [Ber00]. To decouple the cavity from its environment it is located within a vacuum chamber ($5 \times 10^{-8}\,\mathrm{mbar}$) and

---

[4] Toptica SHG PRO

[5] Toptica FALC

two heat shields, which are actively temperature stabilized[6]. In addition, the full vacuum setup is positioned onto a vibration-isolation platform[7]. All parts are set up on an optical table and shielded by an acoustic-isolation box.

For the generation of the PDH error signal we use phase modulation via a fiber EOM[8]. The change from the free-space alternative had two main reasons: First, the π-voltage in fiber EOMs is significantly lower. Thus, reaching the optimal modulation depth[9] for the best detector sensitivity does not involve high-power, low-noise amplification. Second, in addition to the RF signal for phase modulation a direct-current (DC) signal can be applied for active residual-amplitude modulation (RAM) reduction [Li12, Zha14]. Furthermore, the EOM is located into a closed box to be actively temperature stabilized to reduce long-term RAM effects.

The specific layout of the fiber EOM consists of polarization-maintaining fibers bonded to a waveguide crystal. This construction leads to a drastic reduction of the RAM amplitude. Consequently, high-gain amplification is necessary to reach signal levels on the order of $1\,\mathrm{V}$, which is necessary for our regulation electronics. Due to the technical limitations of our detector, i.e. noise and gain, we estimated that the bandwidth of this amplifier should be on the order of $\mathcal{O}(10\,\mathrm{kHz})$ to reach a signal to noise ratio of $\mathcal{O}(10)$. Considering typical modulation frequencies of $20\,\mathrm{MHz}$, filters with very high quality factors $Q \geq 2000$ are necessary. Reaching such narrow bandwidths with discrete components is a challenging task. Fortunately, so called crystal[10] filters are commercially available with quality factors $Q \geq 3000$.

Note further that due to the enormous bandwidth of fiber EOMs of $\mathcal{O}(1\,\mathrm{GHz})$ they can possibly be used for shifting the clock laser with respect to the cavity [Sca15]. Two frequencies are applied to the EOM. One is used for shifting the laser frequency with respect to the optical resonator. The other one is applied for generating the PDH error signal. This feature would make a shifting AOM obsolete.

The PDH error-signal slope sensitively depends on the power inside the cavity. The intra-cavity power can be reduced due to several effects, e.g. drifts of the fiber link onto the optical platform, RAM or drifts of the beam alignment in front of the cavity. A good measure for the intra-cavity power is the transmitted light. We thus realized an active power regulation using a photo diode positioned directly behind the cavity. The feedback is lead to the AOM in front of the fiber link. We simultaneously use this AOM for changing the frequency of the laser. This is necessary due to two reasons: 1. The frequency difference between the optical resonator and the atomic transition needs to be covered, because they do not necessarily coincide. The atomic transition might also be shifted based on the applied experimental sequence, e.g. by an external magnetic field. 2. Frequency drifts of the clock laser need to be compensated. Therefore, we apply a linear feed forward to the RF source of this AOM. We control the drift compensation by an application running on the experimental-control computer.

Due to the high demand on coherence time, special care has to be taken for the fiber link to the science cell. Since the fiber covers a distance of roughly $5\,\mathrm{m}$ it is subject to environmental stress. Vibrations and thermal drift can possibly broaden the linewidth of the clock laser. We

---

[6] Wavelength Electronics WTC3243

[7] MinusK 150BM-1

[8] Jenoptik PM594

[9] Carrier and first sideband powers have the relation $P_1 = 0.41\,P_0$

[10] E.g. Vectron MQF 20.0-0600/03

thus apply a FNC scheme to reduce phase noise. Instead of using the reflected light of the fiber tip, we use a rigidly constructed aluminum block which holds the retro-reflex mirror of the 1D lattice and a mirror for FNC. In this way we could extend the regulated optical path as far as possible and simultaneously stabilize the phase of the clock laser to the reference frame of the atoms. Originally, motion of the lattice mirror could result in a Doppler shift altering the atomic resonance. Although it is difficult to estimate the vibrational characteristics of a mirror substrate, the Doppler shift caused by a motion of $0.1\,\mu\mathrm{m}$ with $1\,\mathrm{kHz}$ is $\Delta f \approx 170\,\mathrm{Hz}$. The AOM applied for FNC is at the same time used for switching the clock laser. A sketch of the setup close to the science cell can be found in Fig. 3.7.

To guarantee high stability of frequency-shifting elements all involved RF sources or RF references are based on digital circuitry that are stabilized via a GPS based oscillator[11].

3.2.2. A 1 Hz linewidth laser source

Coefficient of thermal expansion zero crossing

The great advantage of using ULE glass does not lie in a particular low coefficient of thermal expansion (CTE), e.g. the CTE of Zerodur lies within the same order of magnitude. It is rather the fact that the CTE zero crossing is close to room temperature and thus technically easier to reach. Assuming a linear dependence of the CTE on temperature by

$$\mathrm{CTE} = \alpha_{\mathrm{CTE}} \times \Delta T,$$

with material parameter α_{CTE}, the frequency shift due to a change in temperature can be written as

$$\frac{\Delta L(t)}{L_0} = \frac{\Delta \nu(t)}{\nu_0} = \alpha_{\mathrm{CTE}} \times (\Delta T)^2(t), \tag{3.3}$$

with the length L, and time t. As is apparent a CTE zero crossing leads to an extremal behavior of the length and frequency change. Small temperature fluctuations at this point can be neglected up to first order leading to stable long-term behavior.

To estimate the point of CTE zero crossing we set the temperature regulation to different set values. Simultaneously the frequency change is measured. This is done by analyzing the beat note with a frequency comb[12]. Due to long equilibration times of the cavity system on the order of days (time constant $\tau \approx 22\,\mathrm{h}$) we assumed an exponential temperature dependence on time and extrapolated the final frequency for each temperature step. Fig. 3.8 shows exemplary one temperature step. The result concerning the CTE zero crossing is presented in Fig. 3.9. The solid line is a parabolic fit with a maximum at $32.32(9)\,°\mathrm{C}$, which is well within the range of specification and our regulation electronics. Ideally the temperature of the cavity is as close as possible to the CTE zero crossing. Since the laser setup was needed for spectroscopy we stopped further extensive measurements and estimated the actual temperature to be at the CTE zero crossing. Retrospective analysis however suggests that the current set value is rather $32.0(2)\,°\mathrm{C}$. Combining the determined CTE zero crossing and the current temperature the sensitivity can be estimated to lie between $74.4\,\mathrm{kHz\,K^{-1}}$ and $322\,\mathrm{kHz\,K^{-1}}$.

---

[11] Menlo Systems GPS

[12] Menlo Systems FC1500

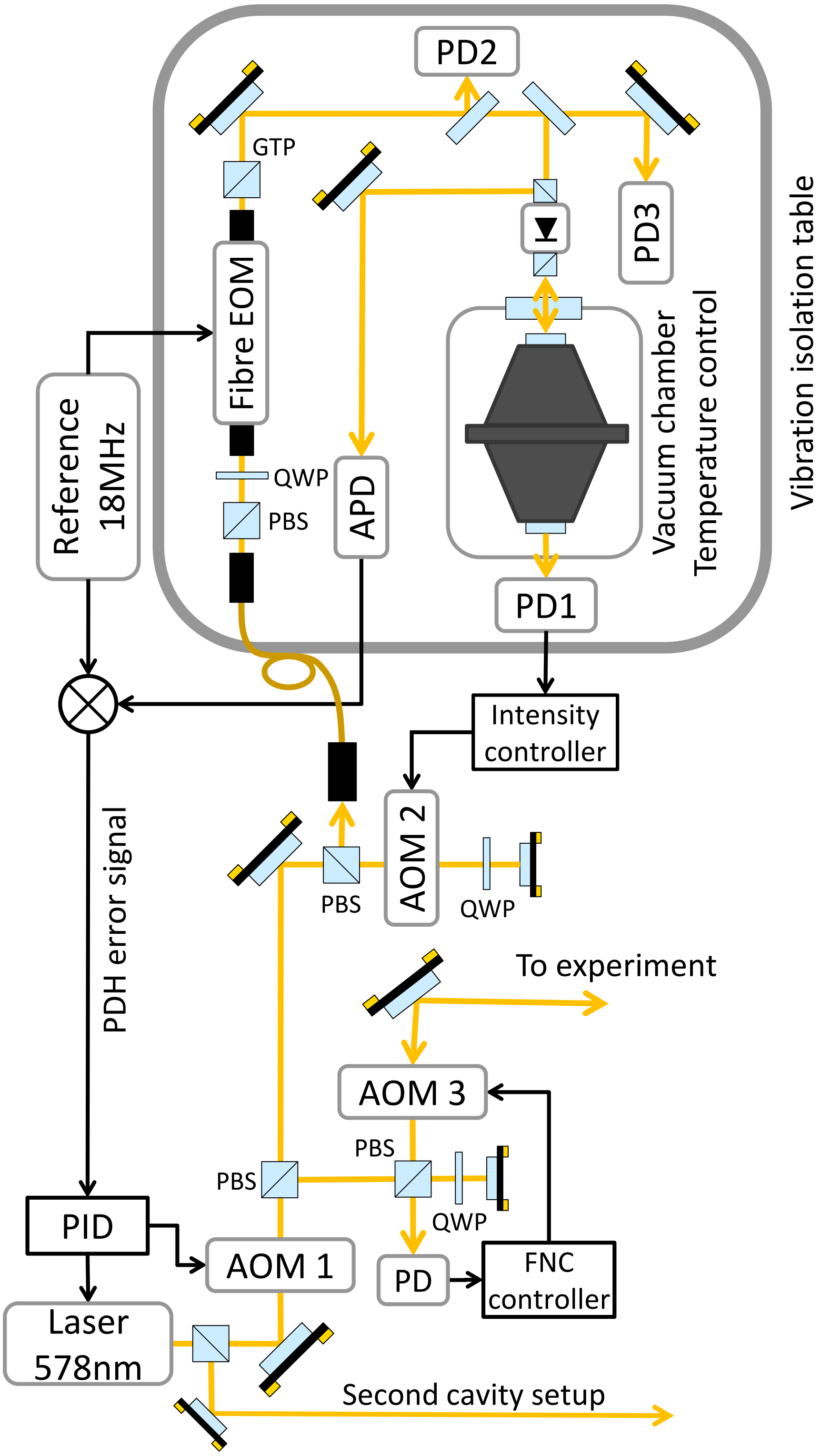

Figure 3.6.: Clock-laser setup. The graphic shows a simplified version of our clock-laser setup using a PDH lock for stabilization. As source we use a 579 nm SHG laser. The fast branch of the regulating electronics (PID) is fed to AOM1 for linewidth narrowing, the slow branch to the piezo of the laser for compensation of slow drifts. The fiber link onto the vibration-isolation table is power stabilized via AOM2 by measuring the cavity transmission (PD1). This AOM simultaneously covers the frequency span between cavity and atomic resonance. To generate the error signal we phase modulate the beam using a fiber EOM and detect the reflected light with a low-noise avalanche photo diode (APD). The all ULE cavity is located inside a vacuum chamber and thermally isolated using two heat shields. The outer one is actively temperature regulated. Further photo diodes can be used for monitoring the power in front of the cavity (PD2) and for the detection of RAM (PD3). The fiber link to the science cell is phase stabilized (FNC) using AOM3. PBS: polarizing beam splitter. QWP: quater wave plate. GTP: Glan-Taylor prism. Graphic was taken from [Pon17].

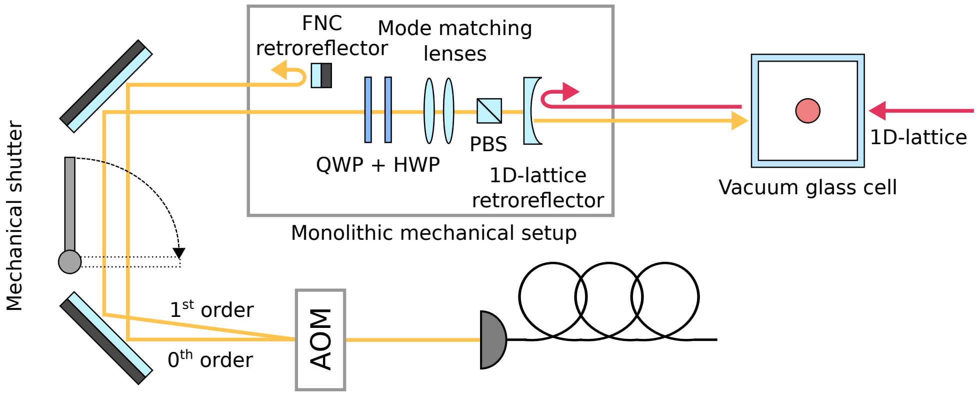

Figure 3.7.: FNC setup for the clock laser. The graphic shows the beam path of the clock laser on the experimental table. We use the zeroth mode of the AOM for retroreflecting light to the FNC setup and the first mode for atom illumination. In addition, the AOM is used for frequency sweeps which can be used for a rapid adiabatic passage. Retroreflector and 1D-lattice mirror are located on top of a rigid aluminum block minimizing relative motion to suppress Dopper shift in the lattice. Furthermore, the mechanical setup holds beam shaping optics to compensate the plan-concave mirror of the lattice and polarization optics for adjusting the beam polarization with respect to the quantization axis. Graphic was taken from [Hun16].

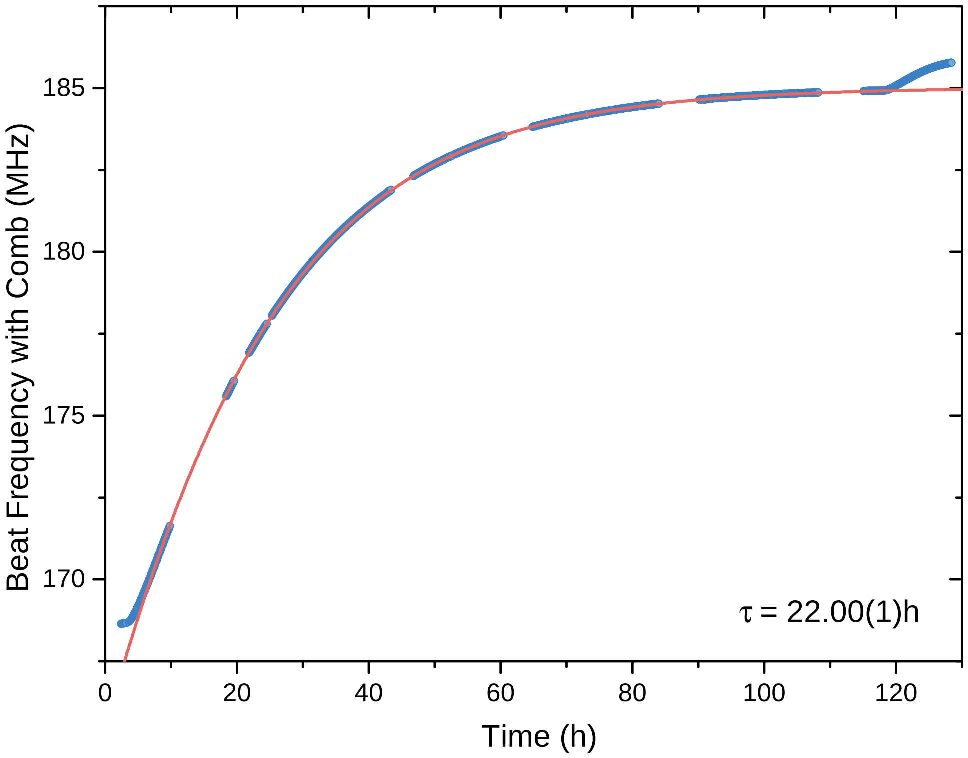

Figure 3.8.: Frequency evolution of the ULE cavity between two temperature steps. The plot shows exemplary the change of clock-laser frequency after changing the set value of the temperature regulation. The frequency change is measured by observing the beat note with a frequency comb. The behavior can be well approximated by an exponential time dependence (solid red line) with a time constant $\tau = 22\,\mathrm{h}$. The deviations at the beginning and end of the measurement indicate a previous and a subsequent temperature step.

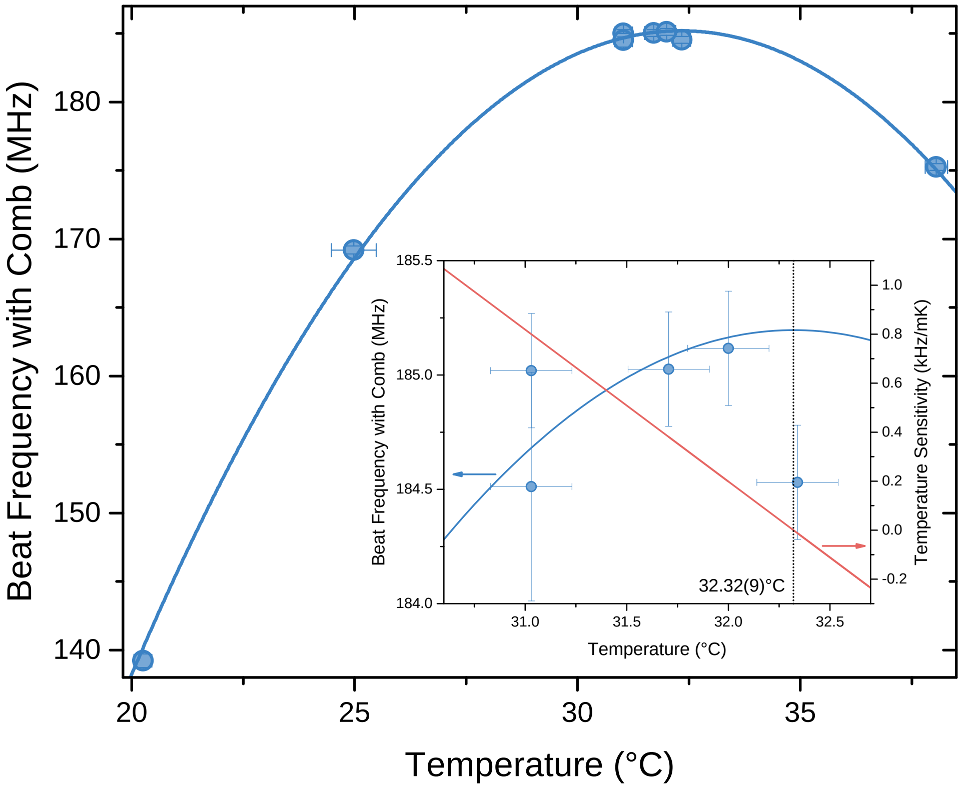

Figure 3.9.: Measuring the CTE zero crossing. The plot shows the relative frequency change for different temperatures. Data points were estimated by extrapolation of an exponential law $T(t)$ due to the long equilibration time on the order of days. The solid line indicates a parabola fit as expected from Eq. (3.3). We measured the CTE zero crossing to lie at $32.32(9)$ °C. The inset shows a zoom onto the central data points. The red solid line is the derivative of the fit and shows the frequency sensitivity of the cavity setup. The data set is not compensated for a linear drift.

Measurement of laser linewidth

In addition to the long-term stability it is also the short-term stability of the laser that eventually limits the effective resolution that can be reached during spectroscopy. For this purpose we set up an additional PDH lock using a similar ULE-cavity setup. Although the laser source is identical, light is picked up right before the regulating AOM (cf. Fig. 3.6) to realize an independently locked beam path. The second setup only uses a fast feedback, because the piezo of the laser is already referenced to the original cavity. Both stabilized laser beams are overlapped onto a photo diode to measure the beat. Its width can be used to estimate the linewidth, because the measured width is the sum of each individual widths assuming Lorentzian shapes. The result can be seen in Fig. 3.10.

Fig. 3.10a shows a single sweep $(2\,\mathrm{s})$ using a spectrum analyzer[13] with a FWHM $= 0.835(3)\,\mathrm{Hz}$. Thus we can assume that the laser linewidth lies well within a $1\,\mathrm{Hz}$ range on short time scales. However, as indicated in Fig. 3.10b the beat note is afflicted by low-frequency shaking of the peak. The plot shows narrow features which, when averaged over $30\,\mathrm{s}$, lead to an effective broadening with FWHM $= 4.45(4)\,\mathrm{Hz}$. Since we regulate the power using the cavity transmis-

---

[13] R&S FSV referenced to GPS

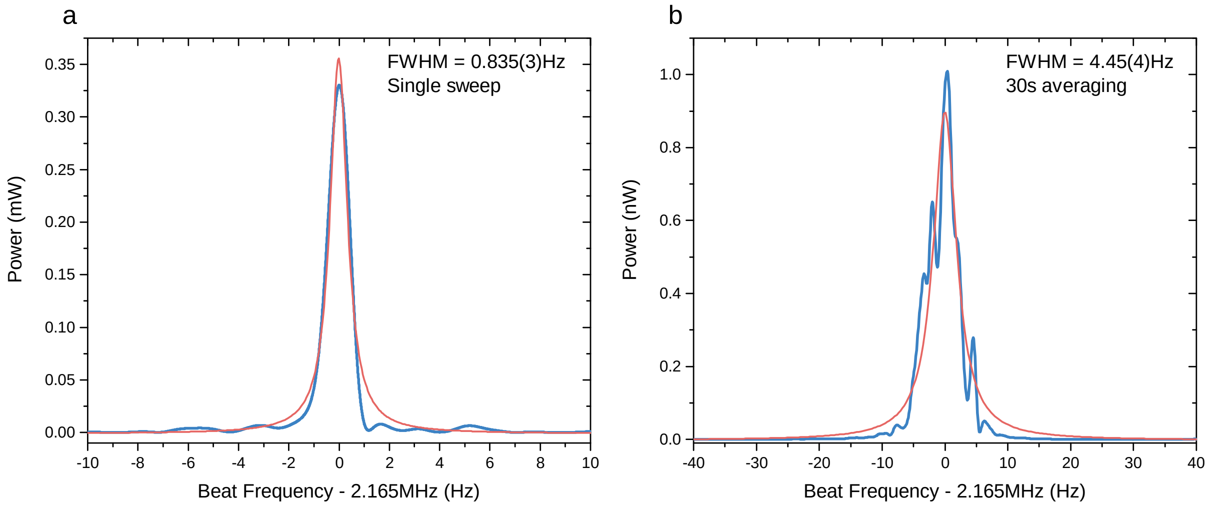

Figure 3.10.: Clock-laser linewidth. Both figures show the beat frequency between two independent clock-laser setups recorded with a spectrum analyzer (RBW $= 1\,\mathrm{Hz}$, VBW $= 1\,\mathrm{Hz}$, sweep time $1.9\,\mathrm{s}$). **(a)** shows a single sweep. The red solid line indicates a Lorentzian fit with FWHM $= 0.835(3)\,\mathrm{Hz}$. **(b)** shows a spectrum after $30\,\mathrm{s}$ averaging. Low-frequency noise of the carrier is visible leading to a broadened linewidth of FWHM $= 4.45(4)\,\mathrm{Hz}$. Linear frequency drifts were compensated during this measurement.

sion it is assumed that intra-cavity fluctuation are not significant. One possible reason can be found in persisting RAM. Although we applied passive countermeasures to reduce this effect an active feedback loop is still in preparation. We additionally observed the beat setup to be highly sensitive to vibration and pressure changes. Since the stability of this detector basically needs to reach interferometric standards a phase stabilization might solve this issue.

Observing long-term frequency drifts

To specify the long-term stability of our clock-laser setup we used the atomic transition as reference. Since we logged the applied drift compensation and recorded all changes to the resonance position it is possible to deduce in retrospect drifts of the clock laser assuming that the atomic transition is constant and the deviations of all involved RF references are negligible. The results are shown in Fig. 3.11. The data is based on spectroscopic measurements during nine days.

Regarding Fig. 3.11a the linear drift of the cavity can be very well described with a respective fit (solid line). This behavior is usually connected to the material aging. The slope with $0.314(1)\,\mathrm{Hz\,s^{-1}}$ shows a rather large value, which is a factor of four to ten larger as values in the literature [Aln08, Häf15, Bia16]. Although this still might be connected to the aging, because this parameter can not be specified by the supply, it can suggest a defective compensation scheme. Fig. 3.11 illustrates the residual drifts, which have to be compensated regularly. The deviations range from very stable measurements, e.g. day two, seven or eight, up to a maximum of about $46\,\mathrm{mHz\,s^{-1}}$ during day five and six.

The residuals cover a range of about $4\,\mathrm{kHz}$. Mapping this value onto the temperature sensitivity based on the current temperature set value, we can estimate the temperature stability during the nine days to be better than $54\,\mathrm{mK}$, if we consider only the optical resonator as source for these deviations. The nominal stability of the regulation electronics is stated as $2\,\mathrm{mK}$. This might

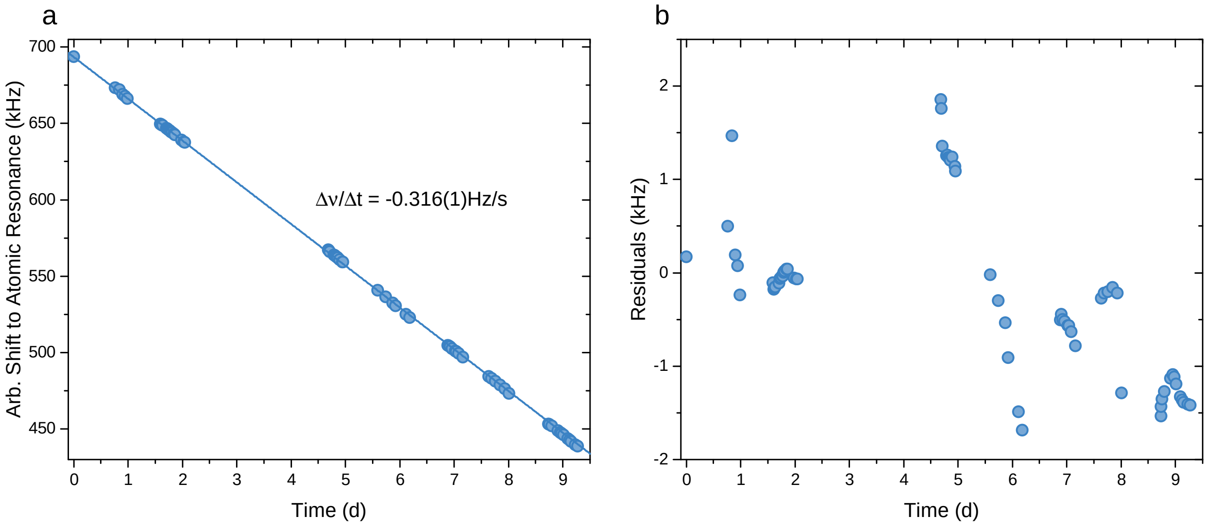

Figure 3.11.: Long-term drift of the ULE cavity. **(a)** shows the drift of the ULE reference cavity via measurement of the atomic transition with ultracold ^{173}Yb. The behavior can be very well approximated using a linear function with slope $\Delta\nu/\Delta t = -0.316(1)\,\mathrm{Hz\,s^{-1}}$. **(b)** shows the residuals of the fit indicating maximal drift deviations around $46\,\mathrm{mHz\,s^{-1}}$ (day five and six).

suggest that the full circuitry has a significantly lower performance compared to the bare control chip. Alternatively, cavity coatings can show a large temperature sensitivity [Aln08]. Drifts would then be caused by malfunctioning power regulation.

3.3. Clock spectroscopy in a 3D magic lattice

Although the final part of this chapter will present coherent control of a two-spin mixture, the spin-polarized gas can be used to characterize the optical lattice and our ability to address the atomic transition. For this purpose we initially prepared a spin mixture with mostly one component ($m_F = +5/2$) being populated using resonant, optical pumping. Due to evaporation low occupied spin states get eliminated and a spin-polarized DFG generated. We estimate the sample to have about 5% of residual occupation. To transfer the atoms into the 3D-optical lattice we ramp up their intensity within $100\,\mathrm{ms}$ while the optical dipole trap were still switched on. Afterwards the dipole trap was switched off to avoid a shift and broadening of the clock transition. The lattice depths were set to $47\,E_\mathrm{r}$ (1D) and $33\,E_\mathrm{r}$ (2D). We applied rectangular shaped clock pulses using linear polarized light (π-polarization). After interrogation by the clock laser we used band mapping with $1\,\mathrm{ms}$ ramp time and imaged both ground and excited states after TOF via absorption imaging and the repumper scheme. In case of the two-component mixture we adapted the pumping durations in a way that all components but two remain after evaporation ($m_F = 5/2, m'_F = -5/2$).

3.3.1. Exciting inter-band transitions in an optical lattice

Atoms subject to a periodic potential can not move freely in position-space but are bound to the momentum-space of the underlying lattices, which quantize the possible motional states. Since our applied lattice depths are rather deep, the energy differences between different bands lie in the tens of kHz regime, which is easily resolvable with our spectroscopic resolution. Furthermore, the bands show very small curvature and thus Doppler widths. The Rabi frequencies change for inter band transition due to the difference of the respective Franck-Condon factors [Con26]. Sideband transitions can for example be used for techniques like sideband cooling [Ham98]. However, here we only use them as a tool to probe the purity of our state preparation and as reference for the lattice calibration.

We prepared about 35000 atoms at a temperature of $26(1)\%\,T_\mathrm{F}$. The atoms were illuminated with $578\,\mathrm{nm}$ light for $220\,\mu\mathrm{s}$ at a power of $5\,\mathrm{mW}$, which corresponds to a π-pulse for the carrier transition and the frequency of the clock laser was changed between each experimental cycle. The resulting spectrum can be seen in Fig. 3.12.

The graph shows two distinct spectral features corresponding to the carrier and first blue sideband transition. The second blue sideband transition is not visible anymore due to an insufficient SNR and the reduced Rabi frequency. The frequency distance between the carrier and first blue sideband is about $23.8(2)\,\mathrm{kHz}$. Calculating the corresponding lattice depth results in $43\,E_\mathrm{r}$, which deviates from our estimation according to amplitude-modulation spectroscopy ($47\,E_\mathrm{r}$). Since lattice calibration and spectroscopy measurement were conducted during different weeks it can be the case that missalignment of the lattice beams lead to this effect. This circumstance needs to be taken into account during the next lattice calibration. Still, the lattice depth is sufficient for all following spectroscopic measurements.

At the position of the first red sideband no excitation is visible. This is a very reassuring result, because one of the main goals of the new dipole trap setup was the reduction of final trap frequencies to suppress higher band occupation: For an idealized 3D lattice model the amount of atoms (spin polarized) which can be transferred into the lowest band of the lattice can be estimated using [Ruu04, Viv04, Bla07]

$$N_\text{lowest band} = \frac{1}{6}\left(\frac{E_\mathrm{r}}{\bar{\omega}}\right)^3 , \tag{3.4}$$

with average trap frequency $\bar{\omega} = 36\,\mathrm{Hz}$ of the dipole trap and a Fermi energy of $E_\mathrm{F} \approx h \times 1.99\,\mathrm{kHz}$. Compared to our previous setup we could increase the amount of atoms in the lowest lying band from 1800 to 27000 atoms. The latter value is in reasonable agreement with our observation considering that we prepared a spin-polarized DFG with 35000 atoms.

The green bars in Fig. 3.12 indicate the Rabi frequencies normalized to the carrier transition. The Franck-Condon factor for the transition between lowest and first excited band for an harmonic oscillator suggests a reduction of the coupling strength by 62%. Comparing this with the peak values from Lorentzian fits, which show a ratio of 64%, we find very good agreement with this estimation.

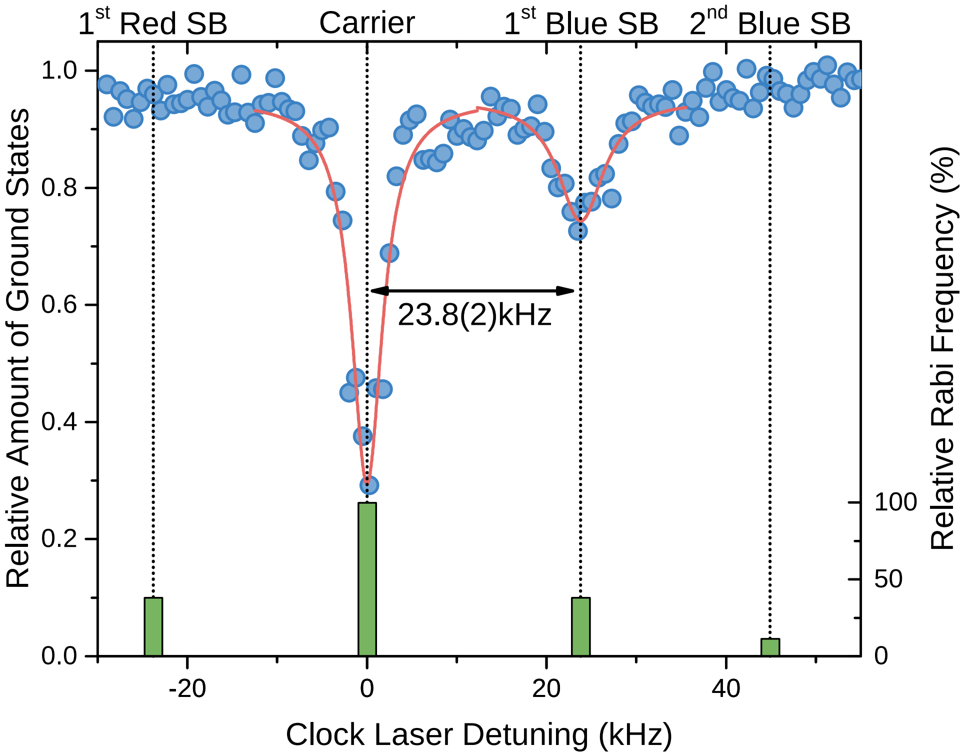

Figure 3.12.: Sideband-covering clock spectroscopy with spin-polarized ^{173}Yb. The plot shows the spectrum of spin-polarized ^{173}Yb using the clock transition with 35000 atoms at $26\% \, T_\mathrm{F}$. The amount of ground-state atoms was normalized to the total atom count. The lattice was set to $43 \, E_\mathrm{r}$ (1D, according to sideband spacing) and $33 \, E_\mathrm{r}$ (2D). The pulse area was adjusted to $1 \times \pi$ at the carrier and the pulse duration was kept constant during the full scan. Three transitions can be identified as carrier, first and second blue sideband. The sidebands show a reduced Rabi frequency in good accordance to the Franck-Condon factor. No excitation of the first red sideband can be observed indicating only population of the lowest lattice band.

3.3.2. High-resolution spectroscopy of a spin-polarized Fermi gas

For testing our clock-laser setup using the atomic transition we continued spectroscopy sequences on a spin-polarized, ultracold gas. Due to the different cooling stages our sequences typically last about $50 \, \mathrm{s}$, which is a lot longer compared to typical atomic-clock experiments with sub-second cycles. Data was taken on different days with sample sizes from 15000 to 30000 atoms and temperatures from $20\% \, T_\mathrm{F}$ to $25\% \, T_\mathrm{F}$. Due to the large scatter of particle numbers these results highly profit from the repumper scheme to increase the SNR. Differently to the previous paragraph, we reduced the span of the spectra to only show the carrier transition for better frequency resolution. The pulse area was kept at $1 \times \pi$ for maximum excitation. The theoretical resolution limit is given by the Fourier limit of a rectangular shaped pulse and can be increased by decreasing the power. Note that the Rabi frequency, and thus the interrogation time, scales with the root of beam power/intensity. The result for five different Rabi frequencies is shown in Fig. 3.13.

The first four spectra were fitted using a Sinc^2 shape with the indicated FWHM sizes. The measurements show excitation ratios between 81% and 92%. Although the higher order maxima are perturbed they can partly still be identified. From the respective pulse durations of $1.65\,\mathrm{ms}$, $3.5\,\mathrm{ms}$, $7.66\,\mathrm{ms}$ and $18.1\,\mathrm{ms}$ the Fourier limits can be calculated [Boy07] to be $539.4\,\mathrm{Hz}$, $254.3\,\mathrm{Hz}$, $116.2\,\mathrm{Hz}$ and $49.2\,\mathrm{Hz}$. The values are in very good agreement with the fit results. Only 3.13a differs more than 10%. This width might be underestimated: The position of the first side peak to the left shows a discrepancy between data-peak position and fit-peak position. Another indicator that these plots show a bandwidth limited behavior are the clean spectral features. In Fig. 3.13e this is not the case anymore. Here the resolution was set to $33.6\,\mathrm{Hz}$ with a pulse duration of $26.5\,\mathrm{ms}$. Due to the large scatter of data points proper fitting is not possible. The width can roughly be estimated to be $50\,\mathrm{Hz}$. Although the Fourier limited resolution was reduced, the actual measurement result stays unchanged with respect to Fig. 3.13d. Low frequency noise leads to broadening of the spectral feature by causing a multi-peak structure similar to Fig. 3.10b.

Attempts to reach even higher resolutions showed spectra disturbed by low-frequency noise. These were not smoothly broadened but rather indicated multi-peak features similar to observations at the two-clock-laser beat note. Thus we estimate possible noise sources to lie in the mHz to hertz regime. We identified two possible reasons for this effect: First, we used a polarizer right in front of the lattice mirror to clean the polarization and also to reduce the clock-laser power using the lambda plates mounted right in front of it (cp. Fig. 3.7). At very low powers, $950\,\mathrm{nW}$ for Fig. 3.13d, the polarizer tends to produce strong intensity gradients across the beam, because we need to set it to maximum extinction. This is unfavorable, because all atoms need to be illuminated homogeneously to ensure equal Rabi frequencies throughout the sample. Fluctuations of the beam position can then lead to dephasing and a diminished excitation ratio. Second, although the FNC electronics works with an automatic-gain circuit, with power levels below $1\,\mu\mathrm{W}$ its capabilities are very limited. If the lock is not properly functioning it can shift and broaden the laser frequency, which severely disturbs the measurement. We are currently working on an improved setup, where the FNC does not have to be switched during an experimental cycle. It additionally relies on a digital version of the FNC electronics. Differently to the current controller the digital version can apply true phase modulation, which will prevent a possible frequency walk off.

3.3.3. Spectroscopy of a two-component Fermi gas

Contrary to the previous chapter a two-component Fermi gas can cause doubly occupied sites for suitable lattice parameters, because the Pauli exclusion principle is canceled between the spin states. In this way two-particle states can build up, which rely on electronic and spin degrees of freedom. Furthermore, these states are subject to atomic interaction and are thus an ideal candidate to simulate quantum many-body physics. A clock transition can now be used to visualize these effects by spectrally identifying the interaction induced frequency shifts.

Solving the full many-body system quickly becomes a difficult numerical problem. For deep lattices, where tunneling is mainly suppressed, regarding each lattice well individually is a valid approximation and greatly simplifies the model to a two-body problem. The involved states are ground state $|g\rangle = {}^1S_0$, excited state $|e\rangle = {}^3P_0$, spin up $|\uparrow\rangle = |m_F = +5/2\rangle$ and spin down $|\downarrow\rangle = |m_F = -5/2\rangle$. Due to the Pauli principle the interaction basis of the respective Hilbert

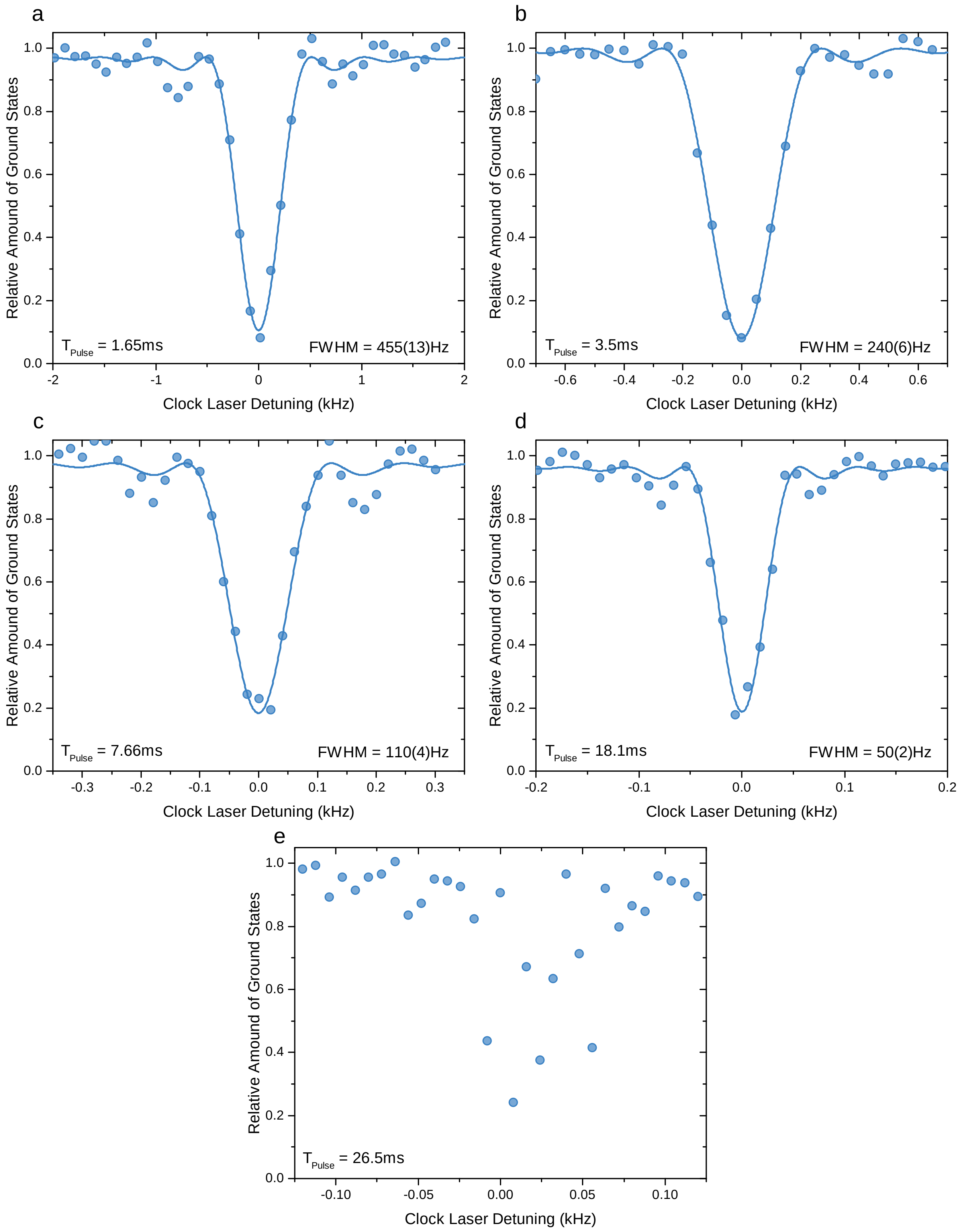

Figure 3.13.: High-resolution spectroscopy of spin-polarized ^{173}Yb. Plot (**a**) to (**e**) show high resolution spectra using the clock transition and ultracold gases of ^{173}Yb. The pulse area was kept constant at $1 \times \pi$ (maximum excitation ratio). The Rabi frequency and thus the resolution limit was stepwise reduced by decreasing the beam power and increasing the interrogation time. Solid lines indicate fits using a Sinc^2 function. Up to a 50 Hz resolution the peaks show a Fourier limited behavior. Further increase of the resolution leads to broadening of the peak due to low-frequency noise (**e**). Each graph is produced via a single experimental run.

space has only six elements:

$$|gg\rangle\,|{\uparrow\downarrow}\rangle^{-}\,,\ |eg\rangle^{+}\,|{\uparrow\downarrow}\rangle^{-}\,,\ |eg\rangle^{-}\,|{\uparrow\uparrow}\rangle\,,\ |eg\rangle^{-}\,|{\uparrow\downarrow}\rangle^{+}\,,\ |eg\rangle^{-}\,|{\downarrow\downarrow}\rangle\,,\ |ee\rangle\,|{\uparrow\downarrow}\rangle^{-}\,, \tag{3.5}$$

with $+$ and $-$ indicating the symmetric or antisymmetric superposition respectively:

$$|eg\rangle^{\pm}\,|{\uparrow\downarrow}\rangle^{\mp} = \frac{1}{\sqrt{2}}\left(|eg\rangle \pm |ge\rangle\right) \otimes \frac{1}{\sqrt{2}}\left(|{\uparrow\downarrow}\rangle \mp |{\downarrow\uparrow}\rangle\right).$$

The CG coefficients of spin-up and spin-down states have the same magnitude but opposite sign. It turns out that the matrix elements for the states $|eg\rangle^{-}\,|{\downarrow\downarrow}\rangle$ and $|eg\rangle^{-}\,|{\uparrow\uparrow}\rangle$ vanish for excitation with π-polarized light. For clarity, these states will be omitted in the following. The two-atom Hamiltonian based on atomic interaction and differential Zeeman shift then reads [Sca15]

$$\hat{\mathcal{H}}_{\text{int, Z}} = \begin{pmatrix} U_{gg} & 0 & 0 & 0 \\ 0 & U_{eg^+} & E_{\text{Z}} & 0 \\ 0 & E_{\text{Z}} & U_{eg^-} & 0 \\ 0 & 0 & 0 & U_{ee} \end{pmatrix}. \tag{3.6}$$

Here, U describes the respective atomic interaction (cp. Eq. (4.5)) and E_{Z} the energy connected to the differential Zeeman splitting. Note that the magnetic field acts on the off diagonal elements, because only the eigenstates of the Zeeman Hamiltonian contribute. The basis of the Zeeman Hamiltonian, which energy scale is dominated by an external magnetic field, consists of two different states. These can be written as superposition of basis elements from Eq. (3.5):

$$\begin{aligned} |e\uparrow g\downarrow\rangle - |g\downarrow e\uparrow\rangle &= |eg\rangle^{-}\,|{\uparrow\downarrow}\rangle^{+} + |eg\rangle^{+}\,|{\uparrow\downarrow}\rangle^{-}\,, \\ |e\downarrow g\uparrow\rangle - |g\uparrow e\downarrow\rangle &= |eg\rangle^{-}\,|{\uparrow\downarrow}\rangle^{+} - |eg\rangle^{+}\,|{\uparrow\downarrow}\rangle^{-}\,. \end{aligned}$$

The left side of both equations indicates that either one atom is in the spin-up or the spin-down state, but not in a superposition, which explains the dependence on an external magnetic field. Eq. (3.6) can be diagonalized with energies

$$E_{\pm} = V \pm \sqrt{V_{\text{ex}}^2 + E_{\text{Z}}^2}, \tag{3.7}$$

with $V = (U_{eg^+} + U_{eg^-})/2$ and $V_{\text{ex}} = (U_{eg^+} - U_{eg^-})/2$. It is especially the last equation, which demonstrates the effects of the exchange interaction. Due to the coupling between $|eg\rangle^{+}\,|{\uparrow\downarrow}\rangle^{-}$ and $|eg\rangle^{-}\,|{\uparrow\downarrow}\rangle^{+}$ caused by a magnetic field the energies get shifted. According to Eq. (3.7) the interaction energies can be determined with an experimental sequence that measures $E_{\pm}(B)$. This can be done by using high-resolution spectroscopy.

In the absence of a magnetic field the Hamiltonian for atom-laser (L) interaction with π-polarized light can be written as

$$\hat{\mathcal{H}}_{\text{L},\pi} = \sqrt{2}\,\frac{\hbar\Omega}{2}\left(|eg\rangle^{-}\,|{\uparrow\downarrow}\rangle^{+}\,\langle gg|\,\langle{\uparrow\downarrow}|^{-} - |ee\rangle\,|{\uparrow\downarrow}\rangle^{-}\,\langle eg|^{-}\,\langle{\uparrow\downarrow}|^{+} + \text{h.c.}\right), \tag{3.8}$$

with Rabi frequency Ω. It is apparent that only two transitions are allowed. The ground state can be coupled to the antisymmetric $|eg\rangle^{-}$ state, and this one can only be coupled to the doubly excited $|ee\rangle$ state. Furthermore, the Rabi frequency is enhanced by a factor of $\sqrt{2}$ compared to the single-particle states. The doubly excited state is subject to strong inelastic collisions, which leads to loss of these particles. Due to our detection method, i.e. normalizing to the sum of ground and excited states, this feature does not occur in our spectrum. Hence, in addition to the excitation of singly occupied lattice sites one more peak is expected.

The Hamiltonian describing atom-laser interaction can be extended for the case of an external magnetic field. The eigen states corresponding to the energies from Eq. (3.7) can be written as

$$\begin{aligned} |+\rangle &= c_1(E_\mathrm{Z})\,|eg\rangle^+\,|\uparrow\downarrow\rangle^- + c_2(E_\mathrm{Z})\,|eg\rangle^-\,|\uparrow\downarrow\rangle^+ \,, \\ |-\rangle &= c_1(E_\mathrm{Z})\,|eg\rangle^-\,|\uparrow\downarrow\rangle^+ - c_2(E_\mathrm{Z})\,|eg\rangle^+\,|\uparrow\downarrow\rangle^- \,, \end{aligned}$$

with

$$\begin{aligned} c_1(E_\mathrm{Z}) &= \frac{V_\mathrm{ex} + \sqrt{V_\mathrm{ex}^2 + E_\mathrm{Z}^2}}{\sqrt{2V_\mathrm{ex}^2 + 2E_\mathrm{Z}^2 + 2V_\mathrm{ex}\sqrt{V_\mathrm{ex}^2 + E_\mathrm{Z}^2}}}, \\ c_2(E_\mathrm{Z}) &= \frac{E_\mathrm{Z}}{\sqrt{2V_\mathrm{ex}^2 + 2E_\mathrm{Z}^2 + 2V_\mathrm{ex}\sqrt{V_\mathrm{ex}^2 + E_\mathrm{Z}^2}}}. \end{aligned}$$

Plugging in the new eigen states the Hamiltonian in Eq. (3.8) reads:

$$\hat{\mathcal{H}}_{\mathrm{L},\pi,\mathrm{Z}} = \sqrt{2}\,c_2(\Delta_\mathrm{Z})\,\frac{\hbar\Omega}{2}\,|+\rangle\,\langle gg|\,\langle\uparrow\downarrow|^- + \sqrt{2}\,c_1(\Delta_\mathrm{Z})\,\frac{\hbar\Omega}{2}\,|-\rangle\,\langle gg|\,\langle\uparrow\downarrow|^- \,. \tag{3.9}$$

As can be seen, due to the magnetic coupling two transitions are possible originating from the ground state $|gg\rangle$. This includes excitation of the $|+\rangle$ state, which becomes $|eg\rangle^+\,|\uparrow\downarrow\rangle^-$ in the limit of a vanishing magnetic field. Furthermore, the Rabi frequencies get reduced by the mixing coefficients $c_{1,2}$. Two limiting cases can be considered. For a vanishing magnetic field Eq. (3.9) reduces to Eq. (3.8) and $c_1 = 1$, $c_2 = 0$. In the opposite limit $E_\mathrm{Z} \gg V_\mathrm{ex}$ the Rabi frequencies get reduced to the level of single atoms and $c_{1,2} \approx 1/\sqrt{2}$.

For experimentally probing the interaction between two Yb atoms we prepared a two-component spin mixture as described above with about 30000 atoms at $25\%\,T_\mathrm{F}$. We estimated that our preparation method involving resonant pumping produces an occupation imbalance of about 2%. The atoms were illuminated for $2\,\mathrm{ms}$ ($\Delta\nu_\mathrm{FWHM} = 445\,\mathrm{Hz}$) with a power of $52\,\mu\mathrm{W}$ and π-polarization. We changed the clock-laser frequency between every experimental cycle and measured the normalized amount of ground states. We applied an external magnetic field with $B = 11.6\,\mathrm{G}$. This has two reasons: 1. In this way the quantization axis for spectroscopy is defined. 2. The Zeeman shift removes the degeneracy of singly occupied lattice sites. This splitting can be used as a reference in the spectrum. The result can be seen in Fig. 3.15.

The graphic shows three distinct features. The outer peaks are connected to singly occupied lattice sites. The total spacing of $6.48\,\mathrm{kHz}$ was used to determine the magnetic field strength by using the magnetic sensitivity $m_\mathrm{F} \times 112\,\mathrm{Hz}\,\mathrm{G}^{-1}$. Comparing both peak sizes the bias seems to be a lot larger than the 2% expectation. In other experimental runs we observed these peaks to also be shifted the other way round. We thus attribute this finding to fluctuations of the relative excitation fraction.

The central peak is connected to the $|-\rangle$ state. Since the mixing for our parameters is very small it is mainly proportional to the $|eg\rangle^{-}\,|\uparrow\downarrow\rangle^{+}$ state. The central feature indicates an excitation fraction of 12%. This value can be used to estimate the amount of double occupancy in the lattice, but it needs to be corrected for two reasons: 1. The applied clock-pulse duration causes maximum excitation on singly occupied lattice sites. However, the Rabi frequency of doubly occupied sites needs to be modified by a factor $\sqrt{2}\,c_1$. Taken into account the actual values for E_{Z} and V_{ex} [Sca14, Cap14] the reduction caused by c_1 is only about 2%. For comparison Fig. 3.14 illustrates the dependence of c_1 on the Zeeman shift. The change in Rabi frequency by a factor 1.39 causes an excitation underestimation of about 31%. 2. Only half of the atoms from doubly occupied sites get excited according to the Hamiltonian. Thus we can estimate about 29% of the atoms to be paired in two-body states. Comparing this with a numeric simulation[14], which calculates the lattice occupation based on the confining potential caused by dipole trap and optical lattice, yields a value of 29.9% in very good agreement to the experimental value. Alternatively, an occupation estimation can be done using the peaks caused by singly occupied sites. However, their amount sums up to about 80%, which leaves 20% of the atoms on doubly occupied sides contrary to the estimation using the central peak. The cause of this discrepancy is unclear. Analysis of Rabi oscillations with doubly occupied sites might give more detailed insights on the underestimation of the central peak.

The frequency position of the central peak is very important, because it is directly connected to the interaction energies U_{eg^+} and U_{eg^-}. Considering Eq. (3.7) the values for V and V_{ex} can be determined by measuring the magnetic-field dependence. Although this has not been done during the course of this thesis, similar measurements were conducted in Munich and Florence [Sca14, Cap14]. The determined resonance position of $|-\rangle$ at $-200\,\mathrm{Hz}$ is in good agreement with their findings. Eventually these results allowed to deduce the lattice independent scattering lengths of both two-particle states:

$$a_{eg^-} = 219.5\,a_0,\ a_{eg^+} \approx 2169\,a_0,$$

with Bohr radius a_0. The large difference between both scattering lengths possibly allows to analyze a large part of the KLM phase diagram [Gor10].

Conclusion

This chapter presented our results regarding spectroscopy using the $^1S_0 \Leftrightarrow ^3P_0$ clock transition of ^{173}Yb. To exploit its features two prerequisites are essential: The use of a magic lattice and a narrow linewidth laser. We successfully implemented both of these at our experimental apparatus. The lattice laser operates at the magic wavelength of $759\,\mathrm{nm}$ and by reaching lattice depths up to $47\,E_{\mathrm{r}}$ the clock spectroscopy can be carried out in the Lamb-Dicke regime. The clock laser is stabilized to an all ULE cavity for long term stability and linewidth reduction. We observe a sufficiently-narrow FWHM linewidth of $1\,\mathrm{Hz}$ using the beat note with a second, independent clock laser. Low frequency noise leads to broadening of the linewdith. The beatnote shows a FWHM linewidth of $5\,\mathrm{Hz}$ after averaging for $30\,\mathrm{s}$.

---

[14] Parameters used: combined trapping frequencies from dipole trap and lattice beams $\omega_{\mathrm{x}} = 2\pi \times (24 + 51)\mathrm{Hz}$, $\omega_{\mathrm{y}} = 2\pi \times (70 + 51)\mathrm{Hz}$, $\omega_{\mathrm{z}} = 2\pi \times (27 + 55)\mathrm{Hz}$. $U = 1.54\,E_{\mathrm{r}}$

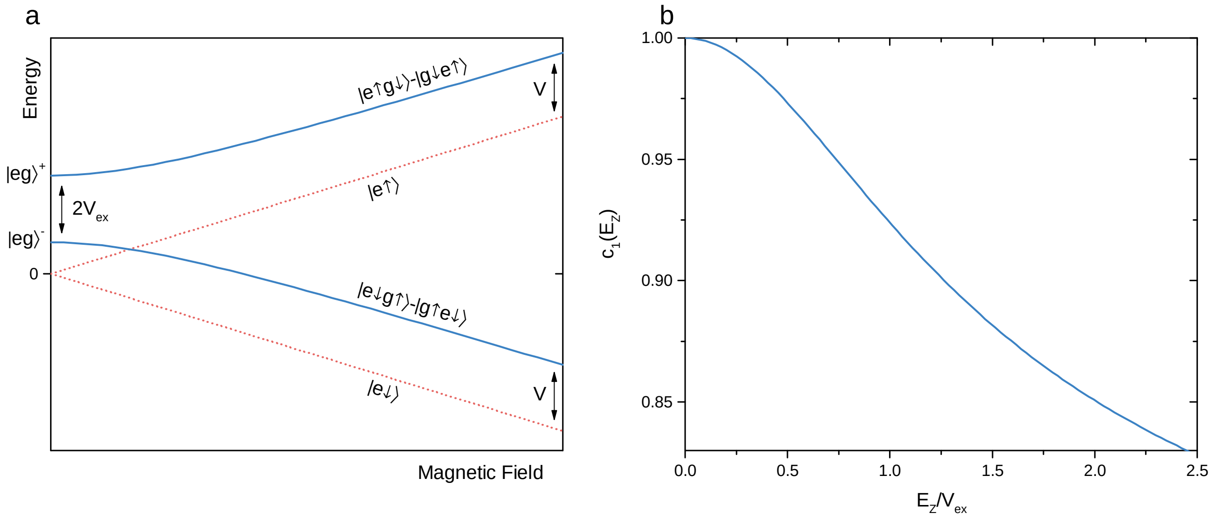

Figure 3.14.: Two-component state mixing by an external magnetic field. **(a)** The graphic illustrates the energy of singly and doubly occupied lattice sites subject to an external magnetic field. The red dotted lines indicate single particles with spin-up and spin-down showing a linearly increasing energy splitting according to the differential Zeeman shift. For $B = 0$ the two-particle states can be prepared only in a symmetric and antisymmetric superposition caused by the Pauli principle. The exchange interaction leads to an energy splitting of $2V_{\text{ex}} = U_{eg^+} - U_{eg^-}$. Applying a magnetic fields mixes these states. In the limit of $E_{\text{Z}} \gg V_{\text{ex}}$ the superposition decomposes into individual, polarized states. **(b)** The plot shows the mixing coefficient c_1 depending on the Zeeman energy. For a significant reduction of c_1 the Zeeman energy needs to be on the order of the exchange energy V_{ex}. For our parameters only a mixing of 2% is expected.

We demonstrated spectra of a spin-polarized DFG with a Fourier limited resolution of $50\,\text{Hz}$ and 80% excitation fraction. Possible technical limitations are inhomogeneities of the clock-laser beam and the FNC electronics at powers below $1\,\mu\text{W}$. Furthermore, we observed inter-band transitions in the optical lattice. These confirmed that the reduction of the mean trapping frequency of our new optical dipole trap setup could significantly increase the efficiency of loading into the lowest band. We showed first measurements concerning spectroscopy of a two-spin mixture. Doubly occupied lattice sites are subject to atomic interaction. In case of Yb the SU($\mathcal{N}$) symmetry leads to spin-exchange, i.e. the energy difference between U_{eg^+} and U_{eg^-}, resulting in a B-field depending clock shift.

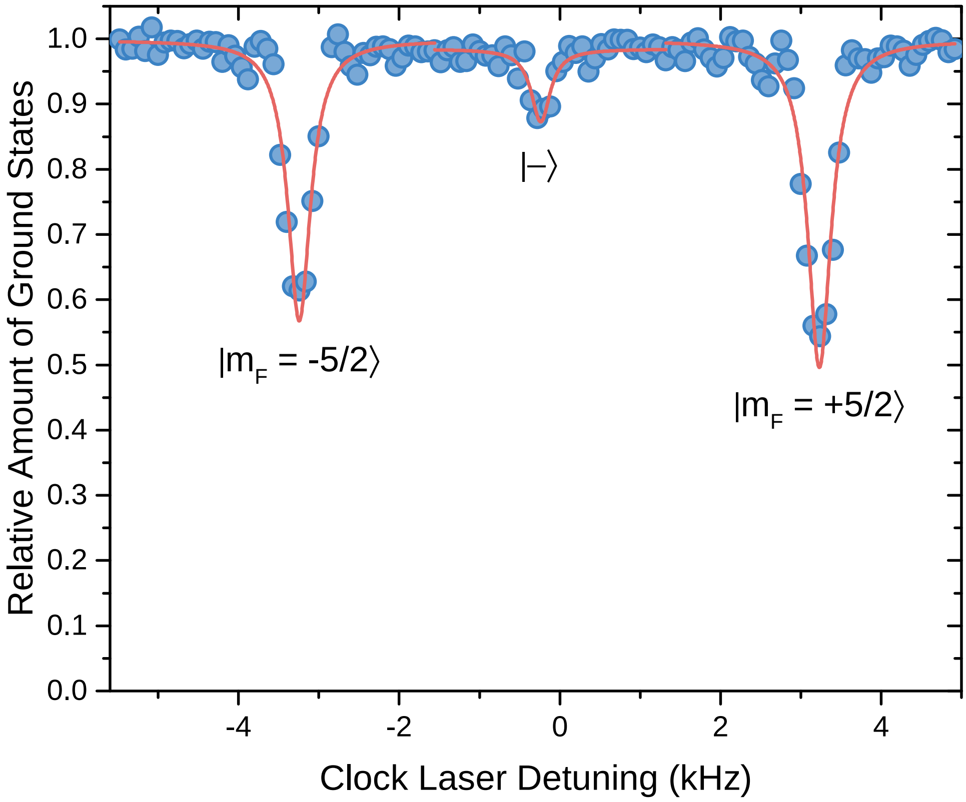

Figure 3.15.: Spectroscopy of a two-component DFG. The plot shows the excitation of a $m_F = +5/2$ and $m_F = -5/2$ spin mixture using π-polarized light ($2\,\mathrm{ms}$). To split the signals from singly occupied sites an external magnetic field was applied with $11.6\,\mathrm{G}$. These are indicated by the large peaks on the left and right. The central peak is connected to the two-particle state $|-\rangle$. Its size can be used to estimate the amount of atoms in double occupied sites to be 30%. The position is depending on the magnetic field and can be used to determine the values for U_{eg+} and U_{eg-}. See the main text for further explanations. The solid lines indicate local Lorentzian fits.

4. Realizing Dissipative Systems with ^{173}Yb

Ultracold gas experiments profit from strong isolation between gas ensemble and its environment. Therefore experiments with repeatable conditions and a high degree of control can be conducted. However, this isolation can only be regarded as an idealization to the actual situation and a complete description has to include coupling to the environmental bath [Die08]. These open quantum systems are highly interesting, because of their impact on decoherence phenomena in quantum information protocols [Nie10] and the possibility of emerging topological phases [Die11, Sta14].

Some of these effects arise due to an environmental coupling mediated by particle dissipation. Although often connected to the increase of entropy and decoherence, particle loss can be a source of strong correlations [FF12] and the quantum-Zeno-effect [Ita90]. Ultracold atoms constitute a convenient toolbox to engineer such dissipative systems, where atom loss can be introduced using strong, inelastic interactions. Pioneering work has been carried out using molecules of bosonic ^{87}Rb [Sya08] and theoretical description based on a Tonks-Girardeau gas [GR09]. Similar experiments could also be carried out using fermionic-hetero-nuclear molecules to demonstrate quantum Zeno dynamics [Yan13, Zhu14]. Other approaches use an electron beam pointed onto a BEC to initiate losses [Bar13b].

Exploiting the inelastic interaction between excited states, ^{173}Yb in an optical lattice constitutes a good candidate to study loss dynamics. These inelastic interactions can be initiated by excitation of the meta-stable state and controlled via the tunneling rate. The latter one can conveniently be adjusted by changing the lattice depth. Although the Zeno regime is not easily reachable due to intrinsic parameters of ^{173}Yb, this isotope is a good starting point to analyze loss dynamics, where the on-site loss rate and interaction are comparable. Future experiments involving ^{171}Yb can possible circumvent this restriction.

The chapter is divided into two parts. The first one describes our preparation method during which we apply a rapid adiabatic passage (RAP) for exciting the $^3P_0$ state. The second one shows how we experimentally realized a Fermi-Hubbard-model (FHM) in which we induce losses via inelastic, two-body collisions and how we analyzed the data using a two-body loss model. Measurements were carried out by B. Hundt, T. Ponath and the author. Data analysis was performed by B. Hundt.

4.1. State preparation using RAP

As a complementary approach to Rabi oscillations, i.e. using a π pulse for maximal state transfer, between the ground state $|g\rangle = {}^1S_0$ and the excited state $|e\rangle = {}^3P_0$, we used RAP as

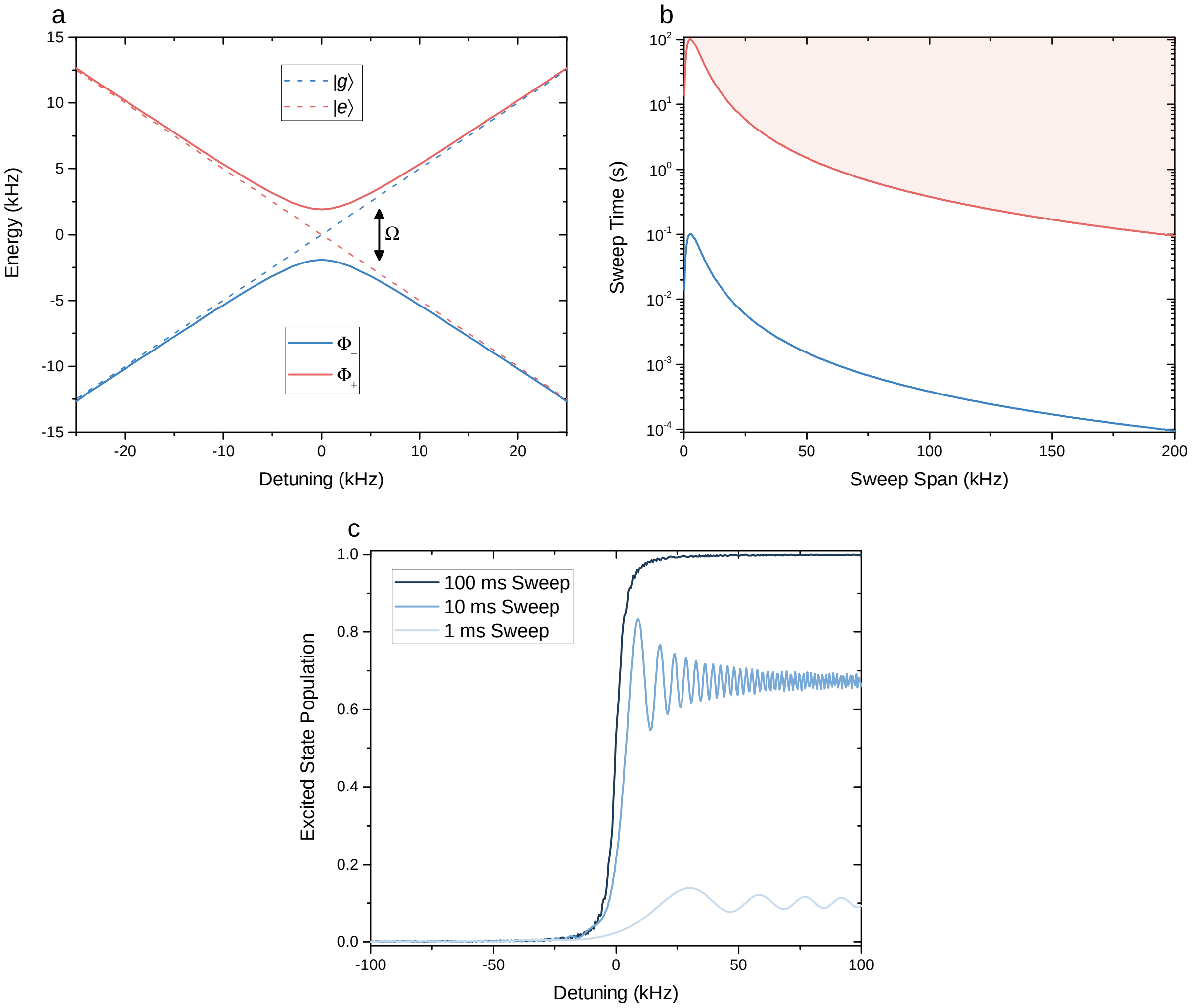

Figure 4.1.: Principle mechanism of RAP. **(a)** The graphic shows the energy spectrum according to Eq. (4.2). Bare states are shown in dashed lines with a crossing at resonance position $\Delta = 0$. The dressed states have an avoided crossing at $\Delta = 0$ with an energy difference of $\Omega = 3.8\,\mathrm{kHz}$ **(b)** The necessary sweep duration is demonstrated for $\Omega = 3.8\,\mathrm{kHz}$. The *blue* curve shows Eq. (4.4) in case of equality and the *red* curve an area for an inequality greater than 1000. **(c)** The plot shows population transfer using RAP for different sweep durations. The initial ground state, which is equal to Φ_- for large detunings, can only be transferred effectively for slow sweeps. Otherwise the dressed states mix and oscillations occur. Images **(a)** and **(c)** are taken from [Hun16].

a robust method for coherent state preparation. Contrary to Rabi oscillations RAP relies on a frequency sweep covering the atomic resonance with a large initial and final detuning. Hence, the exact frequency of the excitation laser is less critical and small drifts can be neglected. For typical parameters we merely shift the clock laser few times a week. Additionally, the frequency sweep can cover the Zeeman splitting of m_F states and as such provides a tool for the excitation of multiple spin states simultaneously.

4.1.1. Principle mechanism of RAP

RAP can be exemplary understood as a state transfer in a two-level picture with ground $|g\rangle$ and excited state $|e\rangle$. Here, the Hamiltonian can be written as [Sho90]

$$\hat{H}(t) = \frac{\hbar}{2}\begin{pmatrix} \Delta(t) & \Omega(t) \\ \Omega(t)^* & -\Delta(t) \end{pmatrix}, \tag{4.1}$$

with the detuning $\Delta(t) = \omega_0 - \omega(t)^1$, the atomic resonance frequency ω_0 and the Rabi frequency $\Omega(t)$. Solving this Hamiltonian gives the eigenvalues

$$E_\pm = \pm\frac{\hbar}{2}\sqrt{\Delta(t)^2 + \Omega(t)^2}$$

and eigenvectors

$$\begin{aligned} \Phi_+ = &\ \sin\Theta(t)\,|g\rangle + \cos\Theta(t)\,|e\rangle\,, \\ \Phi_- = &\ \cos\Theta(t)\,|g\rangle - \sin\Theta(t)\,|e\rangle\,, \end{aligned} \tag{4.2}$$

with $\Theta(t) = \frac{1}{2}\arctan\left(\Omega(t)/\Delta(t)\right)$. This situation is shown in Fig. 4.1a, where the dressed states $\Phi_\pm$ show an avoided crossing due to the coupling Ω in contrast to the bare atomic states $|g\rangle$ and $|e\rangle$. If the initial state is purely one of the dressed states and the frequency sweep in Δ is done adiabatically, the states in Eq. (4.2) do not mix with each other. This condition is fulfilled if the coupling between Φ_+ and Φ_- is small compared to their eigenfrequencies $E_\pm/\hbar$. An estimation is possible using [Vit01]

$$\frac{1}{2}|\dot{\Omega}\Delta - \Omega\dot{\Delta}| \ll (\Omega^2 + \Delta^2)^{\frac{3}{2}}, \tag{4.3}$$

where for our experimental procedures Ω is usually constant and $\ddot{\Delta} = 0$. In this case Eq. (4.3) can be rewritten to

$$T \gg \frac{\Omega\Delta}{(\Omega^2 + \Delta^2)^{\frac{3}{2}}}. \tag{4.4}$$

This equation is illustrated in Fig. 4.1b. The red area indicates the parameter space where Eq. (4.3) is fulfilled by a factor of 1000.

The Hamiltonian in Eq. (4.1) can also be used to calculate the time evolution of the system. Fig. 4.1c shows a simulation of the excitation population for a sweep span of $200\,\mathrm{kHz}$ and a coupling strength $\Omega = 3.8\,\mathrm{kHz}$ for different sweep durations. As can be seen, for a population transfer close to $100\,\%$ about $100\,\mathrm{ms}$ of sweep duration are needed. Comparing this with Fig. 4.1b, these values corresponds to an inequality of 1000 in Eq. (4.3).

4.1.2. Experimental sequence

After producing a degenerate gas of ^{173}Yb according to the method described in Chap. 2 the magic lattice is ramped up. The intensity for 2D and 1D lattice are sequentially increased to prevent tunneling in the 2D plane. The 1D lattice depth is set to $50\,E_\mathrm{r}$ for suppression

---

[1] Δ will be considered as real only

of excitation to higher lattice bands. Subsequently, the crossed dipole trap is switched of to eliminate the shift and broadening of the clock transition due to the AC-Stark shift.

We apply a linear frequency sweep covering the clock transition for RAP using a modulated[2] AOM. Clock-laser light is initially switched on at a detuning of $-50\,\mathrm{kHz}$. For the following measurements we set the sweep span to $100\,\mathrm{kHz}$ and the sweep time to $20\,\mathrm{ms}$. In terms of Eq. (4.4) the inequality is well satisfied (factor ≈ 50). During the experiment we apply a small magnetic field of $3\,\mathrm{G}$ in the vertical direction to have a well defined quantization axis. The amount of ground and excited state atoms is measured afterwards using absorption imaging according to Sec. 2.3.

4.1.3. RAP characterization

Single component gas

We first analyzed the RAP using a spin polarized gas. Therefore, we prepared ^{173}Yb in a single state $m_F = +5/2$ according to Sec. 2.2. Using the sequence of the previous section and a coupling strength $\Omega = 3.8\,\mathrm{kHz}$ we measured the excitation stepwise in $1\,\mathrm{ms}$ and averaged for five sequences. To reduce the particle number the dipole-trap depth was reduced slightly before superimposing the optical lattice. The results can be found in Fig. 4.2.

The RAP for two different amounts of atoms shows very good excitation efficiencies. Furthermore, the data points can be resembled quite well using the numerical time evolution for Eq. (4.1) and above mentioned parameters. Regarding the total atom number, no significant particle loss is observed during excitation.

In Fig. 4.2b a slight step regarding excited atoms is visible at $\approx 25\,\mathrm{kHz}$. It can easily be overseen for the ground-state atom number due to the large errors. This value corresponds reasonable well with the 1D-lattice band spacing at $50\,E_\mathrm{r}$. We therefore attribute this step to an inter-band excitation in addition to the internal-state change. This transition is expected to be at $-26\,\mathrm{kHz}$ with respect to the atomic resonance. Such inter-band transition can also be seen in case of the multi-component RAP in Fig. 4.3.

Six component gas

We analyzed the RAP for a six component gas of ^{173}Yb in a very similar way. While the RAP procedure stayed the same, no pumping was applied before evaporative cooling to produce an equally distributed spin mixture. Due to the larger amount of atoms compared to a single-spin sample we repeated the measurement for four different initial atom numbers. The measurement is four times averaged and can be found in Fig. 4.3.

Regarding the RAP efficiency for the lowest particle number the transfer works significantly worse than for a single-component gas. It is apparent that some thousand ground state atoms persist after the sequence. In contrast to the single spin sample the CG coefficients differ between the m_F states. They play an important role, because the Rabi frequency is directly influenced. Thus, we expected to observe a reduced transfer probability. Addressing the clock transition using linearly polarized light the CG coefficients can be calculated to be 0.845, 0.507, 0.169, -0.169, -0.507, -0.845 for $m_F = 5/2$ to $m_F = -5/2$ respectively. For a sample only

---

[2] Rohde & Schwarz SMB

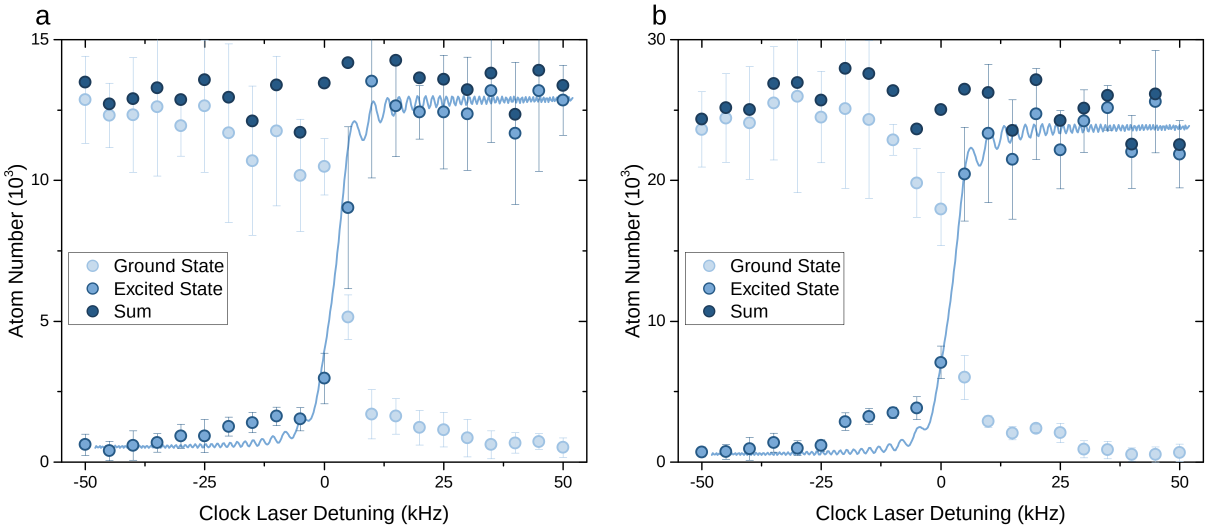

Figure 4.2.: RAP characterization with spin polarized ^{173}Yb. Both graphs show a time resolved RAP for different initial ground state atom number **(a)** and **(b)**. We measured ground and excited state atoms every $1\,\mathrm{ms}$ with a coupling strength of $\Omega = 3.8\,\mathrm{kHz}$. The excitation efficiency is very high in both cases and good resemblance with numerical time evolution (solid blue line) can be observed. The preparation works without significant particle loss during the sequence.

consisting of singly occupied sites each atom is affected individually and only the magnitude of the CG coefficient plays a role. Using our RAP parameters the transfer probability can be estimated to be 99%, 81%, 16% for $|m_F| = 5/2$, $|m_F| = 3/2$, $|m_F| = 1/2$ respectively. For equally distributed spin states this results in an effective transfer of 65%. Since we actually measured an efficiency of more than 80% we assume that other reasons relax Eq. (4.3).

For larger initial particle numbers we expect double occupancy to play a significant role. The results of an occupation simulation in the optical lattice can be seen in Fig. 4.4. The calculation assumes no tunneling ($J = 0$), zero temperature and includes our trapping frequencies[3], particle interaction strength ($U = 1.56\,E_\mathrm{r}$) and Pauli-exclusion principle. We compare this to our data in Fig. 4.3 by taking the first three ground-state data points together with the last three excited-state data points and assume the latter ones to only belong to singly occupied sites. In this way we experimentally have a measure for the existing double occupancy. The data shows good agreement with this idealized lattice model. We thus assume that the particle loss induced by RAP for large particle numbers is a result of inelastic collisions between excited state atoms on doubly occupied sites.

To confirm inelastic collisions between two excited-state atoms, we analyzed the possible excitation of an $|ee\rangle$ state using RAP. The Rabi frequencies according to the CG coefficients are not directly applicable to doubly occupied lattice sites. Instead, the two particle Hamiltonian needs to be solved. Skipping the actual calculation [Lem11, Tho14, Hun16], a two photon excitation is possible, but the coupling strength deviates strongly depending on the CG differences of the spin-state pair. The transfer probabilities for all spin-pair combinations can be seen in Tab. 4.1. Averaging these values for a sample with equal spin-pair distribution yields an effective transfer

---

[3] $\omega_\mathrm{x} = 2\pi(24 + 51)\mathrm{Hz}$, $\omega_\mathrm{y} = 2\pi(70 + 51)\mathrm{Hz}$, $\omega_\mathrm{z} = 2\pi(27 + 55)\mathrm{Hz}$

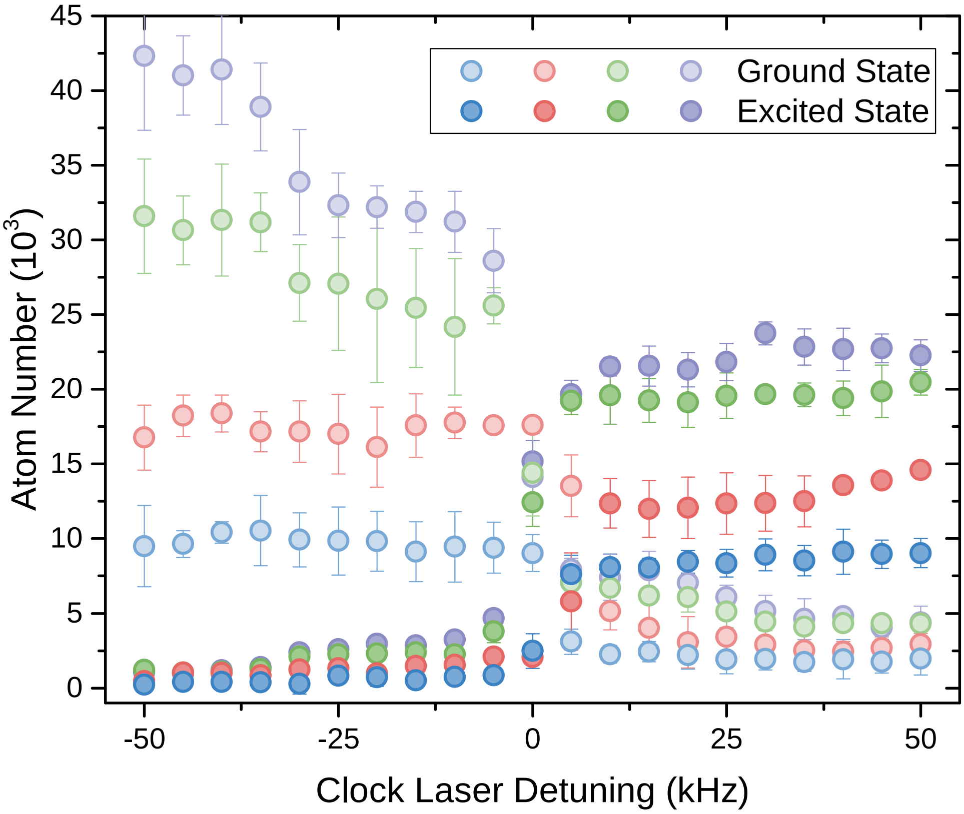

Figure 4.3.: RAP with a six-component mixture. The graphic illustrates a time-resolved RAP using a six component mixture of ^{173}Yb. $^1S_0$ atoms are shown in light and $^3P_0$ atoms in dark colors. The transfer efficiency as well as particle losses significantly depend on the initial amount of atoms. These can be attributed to differences in CG coefficients between single m_F states and inelastic collisions between excited state atoms. The excitations and losses at a detuning of 25 kHz can be attributed to initial higher-band population.

probability of 66%. Similar to the spin-polarized case, experimentally we observe a larger excitation ratio. Specifically, in case of a $m_F = 5/2$ and $m_F = 3/2$ mixture, we observed a ratio far above the predicted 15% using only the two-particle Hamiltonian. Apparently this idealized model can not reproduce the actual situation in the optical lattice.

Exciting the single-spin sample using RAP showed a slight amount of $^3P_0$ atoms about $-24\,\mathrm{kHz}$ shifted with respect to the clock transition. Such a behavior can also be seen in case of the six component mixture. Here, a slight increase of excited-state atoms around $-25\,\mathrm{kHz}$ is visible with a simultaneously dropping amount of ground-state atoms. As before, this fits well with the anticipated band gap of about $26\,\mathrm{kHz}$ for a lattice depth of $50\,E_\mathrm{r}$. Furthermore, the effect is depending on the amount of atoms as can be seen in Fig. 4.2 and more clearly in Fig. 4.3. Certainly, for transferring atoms into higher bands of the optical lattice the atoms need to occupy higher levels in the dipole trap, which is directly connected to the amount of particles. We attribute the additional particle loss to inelastic collisions between ground- and excited-state atoms, where the RAP excites the red sideband of a ground-state atom occupying the first band.

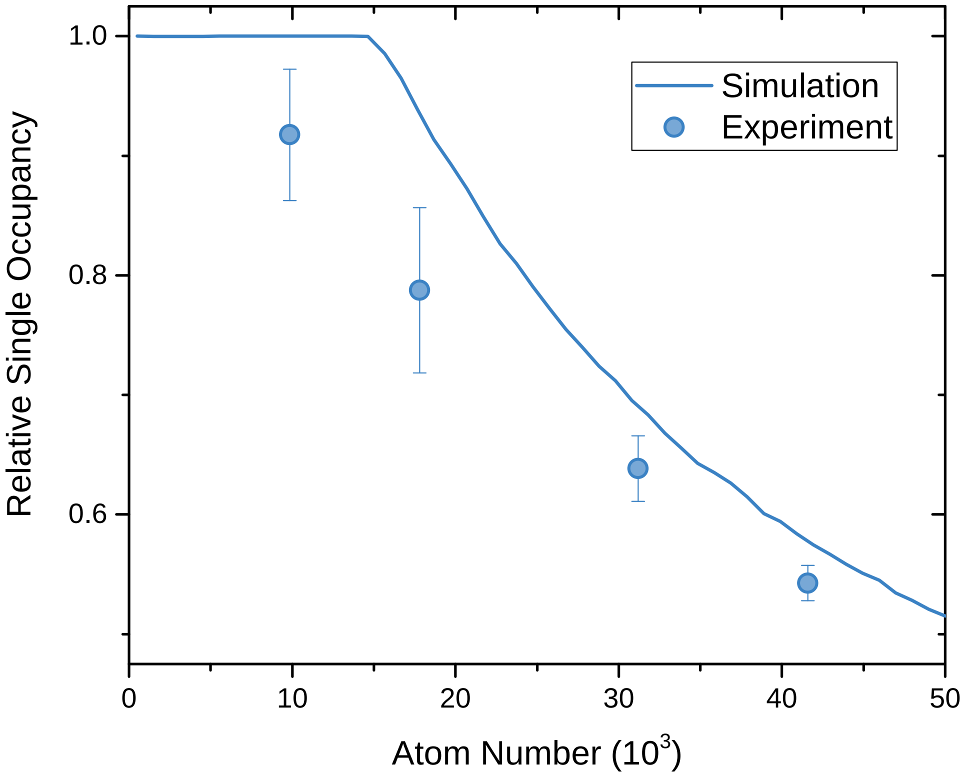

Figure 4.4.: Occupancy distribution in an optical lattice. The graphic shows the relative amount of singly occupied sites depending on the total atom number. The solid line uses an occupation simulation with no tunneling ($J = 0$). To experimentally measure lattice occupation the data from Fig. 4.3 was used. See main text for more details.

$\|m_F, m'_F\rangle$	Transition Probability	$\|m_F, m'_F\rangle$	Transition Probability
$\left\|\frac{5}{2}, \frac{3}{2}\right\rangle$	0.15	$\left\|\frac{3}{2}, -\frac{5}{2}\right\rangle$	0.99
$\left\|\frac{5}{2}, \frac{1}{2}\right\rangle$	0.77	$\left\|\frac{1}{2}, -\frac{1}{2}\right\rangle$	0.17
$\left\|\frac{5}{2}, -\frac{1}{2}\right\rangle$	0.99	$\left\|\frac{1}{2}, -\frac{3}{2}\right\rangle$	0.79
$\left\|\frac{5}{2}, -\frac{3}{2}\right\rangle$	0.99	$\left\|\frac{1}{2}, -\frac{5}{2}\right\rangle$	0.98
$\left\|\frac{5}{2}, -\frac{5}{2}\right\rangle$	0.98	$\left\|-\frac{1}{2}, -\frac{3}{2}\right\rangle$	0.18
$\left\|\frac{3}{2}, \frac{1}{2}\right\rangle$	0.17	$\left\|-\frac{1}{2}, -\frac{5}{2}\right\rangle$	0.80
$\left\|\frac{3}{2}, -\frac{1}{2}\right\rangle$	0.83	$\left\|-\frac{3}{2}, -\frac{5}{2}\right\rangle$	0.14
$\left\|\frac{3}{2}, -\frac{3}{2}\right\rangle$	0.99		

Table 4.1.: Excitation probability using RAP on doubly occupied sites. The table shows simulated excitation probabilities using RAP for linear polarized light. The transfer into the doubly excited state $|ee\rangle$ highly depends on the m_F quantum number. In principal, double excitation can be reached with any combination of spins. For RAP conditions see the main text.

Summary

This section showed how the $^3P_0$ state can efficiently be populated using RAP. Especially in the sense of laser stability this tool is helpful, because it covers a broad frequency span and is thus less sensitive to frequency drifts of the laser source. The same reasoning can be used for excitation in a non-magic lattice, where the clock transition is broadened. In addition, the technique allows to simultaneously excite spin mixtures which is hardly possible by using π-pulses.

Considering the preparation of spin mixtures, simulations on an ideal quantum system suggest to optimize the RAP parameters in the sense that Eq. (4.3) is fulfilled for all involved spin states. Depending on the demand of state purity, the preparation of large amount of atoms could be insufficient, because on these samples RAP has a lower efficiency. Specifically the effects of higher band and double occupancy might generally limit this method. Working with low atom numbers can circumvent these complications.

4.2. A dissipative 1D Fermi-Hubbard model

In the following section RAP will be used as a tool to populate the meta-stable state in ^{173}Yb. This will initiate the loss process and realize a dissipative FHM. First, the relevant parameters in an optical-lattice system are presented followed by a discussion of the applied loss model. Second, the preparation procedure and experimental findings are shown and analyzed using this model.

4.2.1. Two-body loss model

Our optical lattice system can be well described by the FHM [Alb03]. The most relevant parameters within are nearest neighbor tunneling J, on-site interaction U and the two-body loss rate Γ. Where J depends only on properties of the lattice, U and Γ are influenced by atomic properties. They can be calculated using [Jak05, Yan13]

$$U = \frac{4\pi\hbar^2 a}{m}\int |w_0(\mathbf{r})|^4 \,\mathrm{d}\mathbf{r} \text{ and} \tag{4.5}$$

$$\Gamma = \beta\int |w_0(\mathbf{r})|^4 \,\mathrm{d}\mathbf{r}. \tag{4.6}$$

w_0 denotes Wannier functions and m the mass of Yb. Since we use inelastic collisions between two excited states to induce losses into the lattice system, Eq. (4.5) and Eq. (4.6) need to be evaluated for the respective s-wave scattering length $a_{ee} \approx 306.2\,a_0$ and the on-site loss rate $\beta_{ee} = 2.2 \times 10^{-11}\,\mathrm{cm}^3\,\mathrm{s}^{-1}$ [Sca14]. Comparing both equations, it is apparent that the interaction parameter and the loss coefficient scale equally with the wave-function overlap and thus with the lattice depth. J, U and Γ have been calculated according to our lattice parameters and the results can be seen in Fig. 4.5a.

To actually observe dissipation in our experiment we measure the particle loss after each experimental cycle. Since the above mentioned Hubbard parameters U, J and Γ influence each other, the loss rate Γ might not be accessible as a measure for these dynamics. Instead, it is helpful to use an effective loss rate Γ_{eff}, which can be calculated using an effective master equation in the limit of $\hbar\Gamma \gg J$ [GR09]:

$$\Gamma_{\text{eff}} = \frac{4J^2}{\hbar^2\Gamma}\frac{1}{1+\left(\frac{2U}{\hbar\Gamma}\right)^2}. \tag{4.7}$$

The actual values for our lattice parameters are illustrated in Fig. 4.5b. Two limits of this equation can be identified. If $U \gg \Gamma$, Eq. (4.7) can be approximated by

$$\Gamma^U_{\text{eff}} = \frac{J^2}{\hbar U}\frac{\hbar\Gamma}{U}. \tag{4.8}$$

In this regime the system is in a Mott-insulator-like phase where tunneling is dominated by super-exchange processes with an amplitude J^2/U [Lew07]. Thus, the effective loss rate is diminished for larger on-site interaction. In the opposite limit of $\Gamma \gg U$, Eq. (4.7) can be approximated by

$$\Gamma^\Gamma_{\text{eff}} = \frac{4J^2}{\hbar^2\Gamma}. \tag{4.9}$$

In this regime the effective loss rate gets diminished for larger Γ and can be described by Zeno-like dynamics [Mis77, Ita90]. The Zeno effect can be understood as particle losses being projections onto new quantum states. These constitute continuous measurements onto the system which counter-intuitively lead to suppression of losses. The parameters for Yb result in a ratio $\hbar\Gamma_{ee}/U_{ee} = 0.29$, which indicates that Mott-Insulator behavior dominates our system. Eq. (4.7) is illustrated in Fig. 4.6. Comparing Eq. (4.8) and Eq. (4.9) shows that both processes can not be distinguished via modifying the lattice depth. Instead, measures need to be found which can alter U and J individually.

The relevant loss channel involves inelastic collisions of two excited-state atoms. To model the time evolution of the total atom number N a rate equation (cp. App. B) depending on Γ_{eff} can be applied [GR09]:

$$\frac{\mathrm{d}N}{\mathrm{d}t} = -\frac{\mathcal{N}-1}{\mathcal{N}}\frac{\kappa}{N_0}N^2. \tag{4.10}$$

N_0 is the initial atom number, $\mathcal{N}$ the amount of spins and κ the loss coefficient according to

$$\kappa = 4q\,\Gamma_{\text{eff}}\,g^{(2)}\,\eta_0. \tag{4.11}$$

q is the co-ordination number and describes the number of neighboring sites. For a 1D lattice $q = 2$. η_0 is the initial lattice filling with $\eta = 1$ for single occupation. $g^{(2)}$ is the nearest-neighbor correlation function, which describes if two-body losses are suppressed or enhanced based on spin correlation. In case of spin $1/2$ particles it can be calculated via [Bau10]

$$g^{(2)} = \frac{\langle \hat{n}_i\hat{n}_j - 4\hat{S}_i\hat{S}_j\rangle}{\langle \hat{n}_i\rangle^2}$$

with atom number n_i and spin operator $\hat{S}_i$ at lattice site i. The essential cases are:

- $g^{(2)} = 2$, if the system constitutes an ideal antiferromagnet, i.e. alternation between spin-up and spin-down

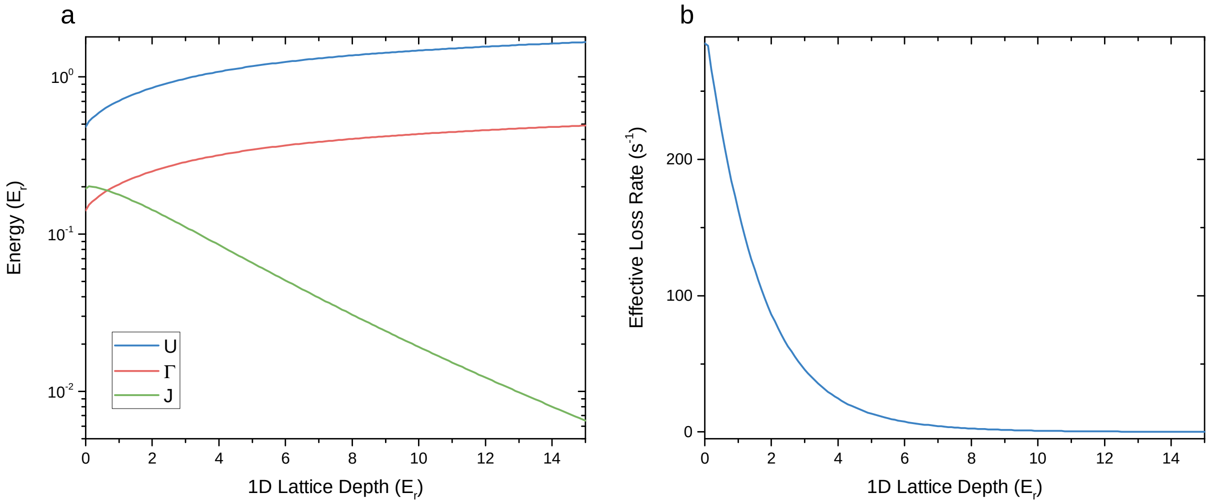

Figure 4.5.: Calculated 1D lattice parameters. **(a)** and **(b)** show numerical results for the on-site interaction U, on-site loss rate Γ, tunneling J and effective loss rate Γ_{eff} depending on the 1D lattice depth. The calculation is based on the actual Wannier integrals with a lattice wavelength of $759\,\text{nm}$.

- $g^{(2)} = 1$, if the system is in a Mott-insulator sate, i.e. no correlation exist: $\langle \hat{n}_i \hat{n}_j \rangle = \langle \hat{n}_i \rangle^2$, $\langle \hat{S}_i \hat{S}_j \rangle = 0$
- $g^{(2)} = 0$, if the system has ferromagnetic order, i.e. all spins point into the same direction

For systems with a larger spin manifold the situation is different though. In case of no correlation, the chance of Pauli blocking by the next neighbor is diminished. Thus, the correlation function is > 1. The actual factor can be calculated using [Tai12]

$$\frac{g^{(2)}_{\mathcal{N}}}{g^{(2)}_{\mathcal{N}=1}} = 2\,\frac{\mathcal{N}-1}{\mathcal{N}}.$$

For a time-independent correlation function Eq. (4.10) can be solved analytically with

$$N(t) = \frac{N_0}{1+\kappa' t}, \quad \kappa' = \frac{\mathcal{N}-1}{\mathcal{N}}\,\kappa \tag{4.12}$$

Usually, $g^{(2)}$ can not be considered constant. In this way, loss measurements can be regarded as a tool to analyze the changing correlations in a dissipative system.

4.2.2. Experimental sequence

The experimental sequence starts with production of a degenerate Fermi gas of ^{173}Yb. We typically reach temperatures $\leq 0.25\,T_{\text{F}}$ for a polarized gas, $\mathcal{N} = 2$ and $\mathcal{N} = 6$ spin-component mixtures. RAP is applied to excite the $^3P_0$ state. Details can be found in Sec. 4.1.2. Our initial particle number is around 18000 atoms as a compromise between low double occupancy and good signal strength. For our typical lattice depths (1D lattice $50\,E_{\text{r}}$, 2D lattice $18.8\,E_{\text{r}}$) we

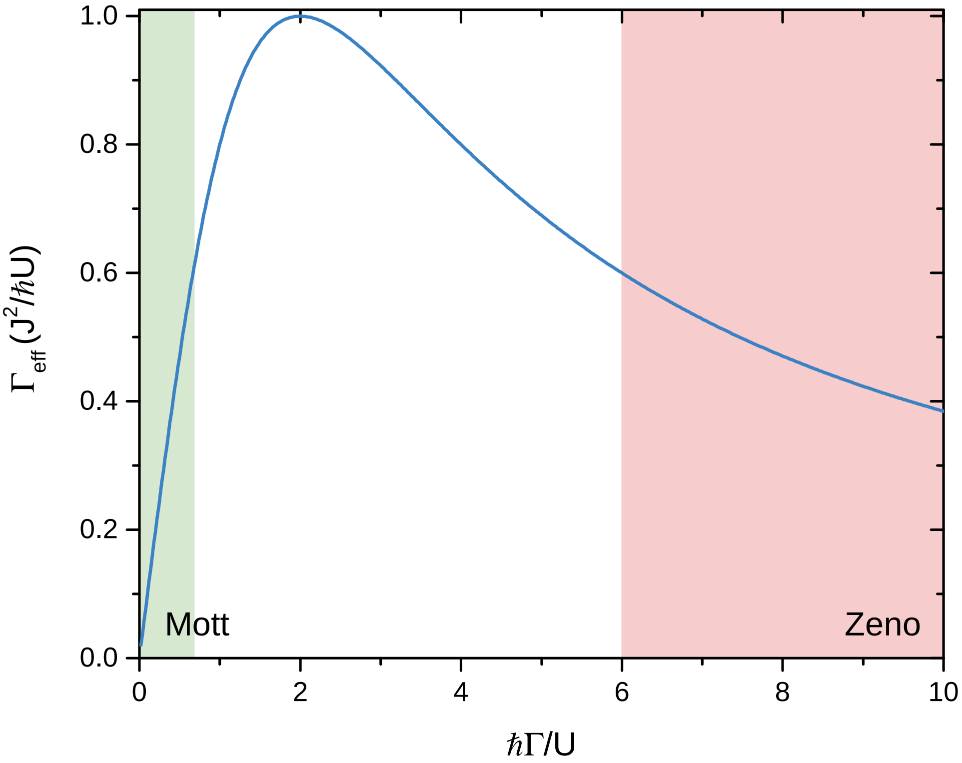

Figure 4.6.: Effective loss rate Γ_{eff}. The graphic shows the two regimes of Mott-like and Zeno-like behavior in a lattice system depending on Γ/U. The Mott regime is dominated by super-exchange tunneling scaling with J^2/U, whereas the Zeno regime can be characterized with a suppression according to J^2/Γ. To reach the far right of the plot, U and Γ need to be tuned individually.

expect to have about 20% doubly occupied sites.

The losses are initiated by reducing the 1D-lattice depth to different levels within $300\,\mu\text{s}$. Such a short time interval ensures negligible loss dynamics during the intensity ramp and further reduces excitation into higher lattice bands. The 2D-lattice depth is kept unchanged to suppress tunneling into the perpendicular plane[4] and to keep enough confinement against gravity. A deep 2D lattice further increases the losses due to compression of the Wannier functions.

Eventually, the 3D lattice is switched off exponentially. ${}^1S_0$ and ${}^3P_0$ states are counted for each experimental cycle simultaneously after TOF of $13\,\text{ms}$. For details on the repumping procedure used during imaging, see Sec. 2.3.

4.2.3. Analysis of loss dynamics

Spin polarized gas

We first analyzed the relevant time scales working with a spin-polarized gas ($m_F = 5/2$). The sample was prepared in a $50\,E_\text{r}$ deep 1D lattice and atom lifetime with and without RAP was observed. The results can be seen in Fig. 4.7.

---

[4] Equivalent 1D tunneling $J_{\text{1D}} = 7\,\text{mHz}$

To measure the lifetime $N(t)$ exponential decay or growth functions were applied with:

$$\begin{aligned} \text{Decay:} \quad & N(t) = N_0 \exp(-\gamma\, t), \\ \text{Growth:} \quad & N(t) = N_0\, (1 - \exp(-\gamma\, t)). \end{aligned} \tag{4.13}$$

N_0 indicates the initial or final atom number. The fit results are as follows:

$$\begin{aligned} \gamma_g &= 0.054(7)\,\mathrm{s}^{-1}, \\ \gamma_e^{\mathrm{RAP}} &= 0.226(4)\,\mathrm{s}^{-1}, \\ \gamma_g^{\mathrm{RAP}} &= 0.41(3)\,\mathrm{s}^{-1}. \end{aligned} \tag{4.14}$$

The bare lifetime of ground state atoms without using RAP shows a large value of $1/\gamma_g = 18.5\,\mathrm{s}$. Estimating the residual off-resonant scattering rate with the lattice beams yields $14.3\,\mathrm{s}$ as a lower bound. Although this is reasonable close, the extended lifetime can be attributed to the strong confinement of the deep lattice.

Considering the situation after $^3P_0$ preparation the data shows several characteristics. First, the lifetime of the excited state with $1/\gamma_e^{\mathrm{RAP}} = 4.4\,\mathrm{s}$ indicates a strong reduction compared to the natural lifetime of the $^3P_0$ state with $\geq 17\,\mathrm{s}$ [Xu11]. This deviation is probably caused by the influence of the optical lattice mixing internal states and thus altering the lifetime. Second, due to the deep lattice the excited atoms are not lost after decay. Instead, the $^1S_0$ population increases. And third, the sum of ground and excited states after RAP indicates an additional particle loss when compared with ground-state atoms without RAP. We attribute this enhancement to inelastic collisions between ground and excited states, because Pauli blocking is suppressed.

The just mentioned processes can be combined in a pair of coupled rate equations to model the time evolution of ground N_g and excited N_e atoms:

$$\begin{aligned} \frac{\mathrm{d}N_e}{\mathrm{d}t} &= -\gamma_g\, N_e - \gamma_e\, N_e - \gamma_{eg}\, N_e N_g, \\ \frac{\mathrm{d}N_g}{\mathrm{d}t} &= -\gamma_g\, N_g + \gamma_e\, N_e - \gamma_{eg}\, N_e N_g. \end{aligned} \tag{4.15}$$

Excited state atoms are lost due to spontaneous decay γ_e and additionally single particle decay γ_g according to Eq. (4.14). Losses due to inelastic collisions are modeled by γ_{eg}. Analogously, the ground-state atoms are affected by γ_g and they can be populated via the decay of excited-state atoms (γ_e). This model assumes equal γ_g for ground and excited states and neglects excitations into higher bands of the optical lattice (Lamb-Dicke regime). The results can be found in Fig. 4.8. The fit results are as follows:

$$\begin{aligned} \gamma_g &= 0.054\,\mathrm{s}^{-1}, \\ \gamma_e &= 0.156\,\mathrm{s}^{-1}, \\ \gamma_{eg} &= 0.0045\,\mathrm{s}^{-1}. \end{aligned} \tag{4.16}$$

The model is in very good agreement with the data points and additionally can reach a better approximation compared to a simple exponential fit [Hun16]. The fit results indicate that a single-particle loss model underestimates the lifetime of the excited-state atoms. Instead, also

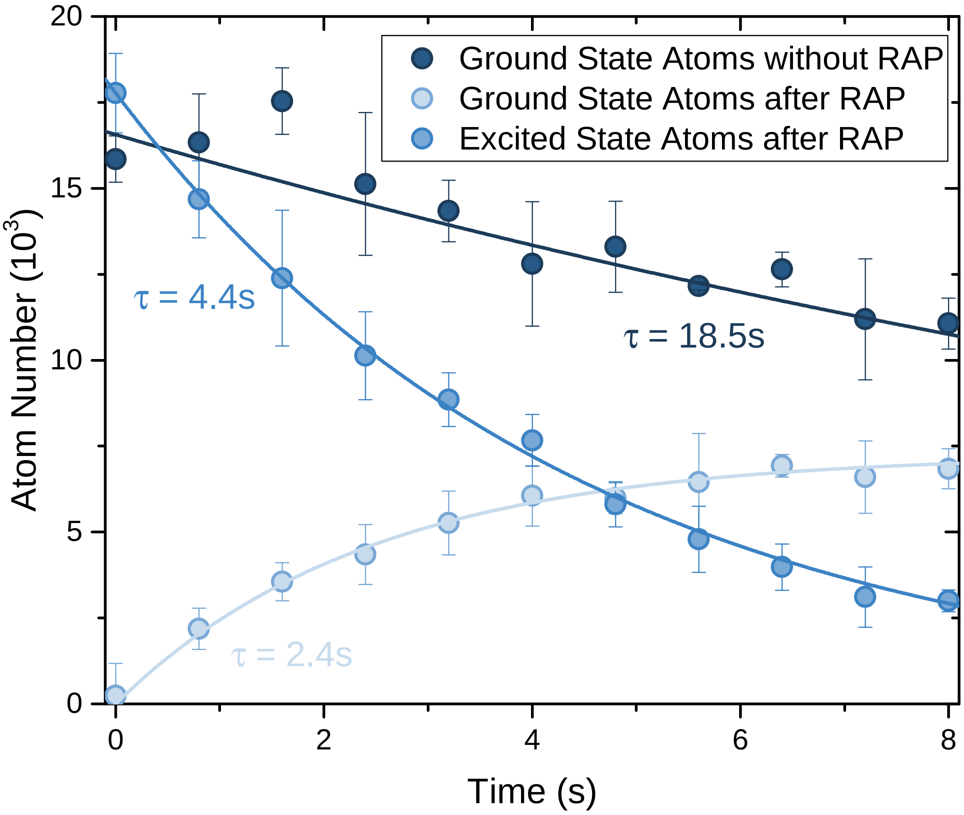

Figure 4.7.: Spin-polarized ^{173}Yb in a deep lattice. The graph shows the lifetime of excited state atoms for a spin-polarized gas in a $50\,E_\mathrm{r}$ deep 1D lattice. The rising amount of ground-state atoms indicates radiative decay of the excited states. The lifetime of the meta-stable state is strongly reduced compared to the natural lifetime due to the influence of the lattice. The amount of atoms after RAP is counted simultaneously for each sequence using a repumping scheme. As comparison, the lifetime of ground-state atoms is also measured showing a value, which is comparable to off-resonant scattering with the lattice beams.

two-body losses play a significant role even for a spin-polarized gas. Thus, the given analysis is important for estimating an upper bound of these loss rates.

Multi-spin gas

We used the same preparation method for analyzing the multi-spin samples outlined in Sec. 4.2.2. The measurements were carried out with one, two- and six-spin components. The shallow 1D-lattice depths for loss dynamics were set to $3\,E_\mathrm{r}$, $5\,E_\mathrm{r}$, $6\,E_\mathrm{r}$, $8\,E_\mathrm{r}$, $11\,E_\mathrm{r}$ and $14\,E_\mathrm{r}$. The results for all spin compositions and lattice depths can be found in Fig. 4.9.

Considering the figures qualitatively it is apparent that for depths of $3\,E_\mathrm{r}$ to $8\,E_\mathrm{r}$ the particle numbers show fast, initial decays. These are suppressed in case of a polarized gas and for lattice depths of $11\,E_\mathrm{r}$ and $14\,E_\mathrm{r}$. In case of the spin-polarized gas this effect can be attributed to the Pauli principle, which leads to a reduction of inelastic collisions. For both deep lattice depths J is already strongly suppressed, which slows down any dynamics. This can be well observed in Fig. 4.9f, where all spin compositions show a similar behavior. Specifically, the lifetime of the excited state for the spin-polarized gas is comparable to the case with a $50\,E_\mathrm{r}$ deep lattice, i.e.

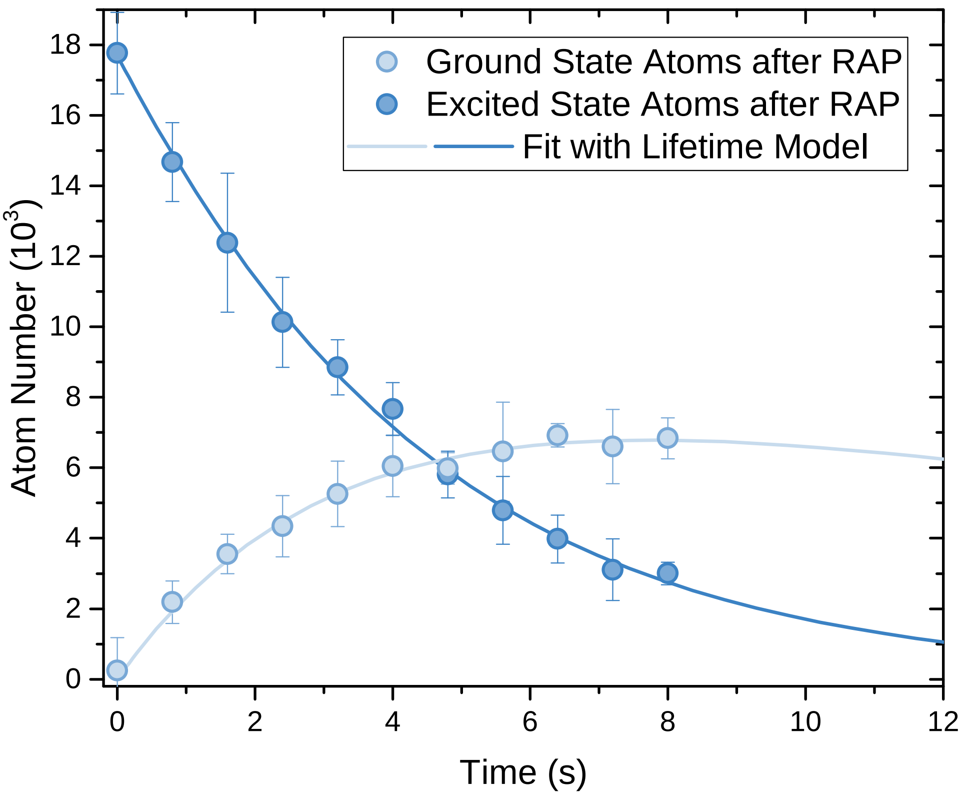

Figure 4.8.: Lifetime model for a spin-polarized gas. The graph shows a spin-polarized gas after preparation using RAP in a $50\,E_\mathrm{r}$ deep lattice. The data is the same as in Fig. 4.7, but solid lines indicate a fit with Eq. (4.15) contrary to an uncoupled, exponential approximation. The model is in very good agreement with the data. Fit results can be found in Eq. (4.16).

the timescale of radiative decay is reached. In all other cases, a fit with Eq. (4.13) yields larger values compared to the case of a single-spin component in a $50\,E_\mathrm{r}$ deep lattice. Thus, two-body collisions play a role and we use the respective model from Eq. (4.10) in the following.

For a quantitative description we determine the time evolution according to Eq. (4.12) to find the corresponding loss coefficients κ. We fitted both appearing timescales individually. Exemplary, Fig. 4.10 indicates the fitting procedure for a two-component gas and a 1D-lattice depth of $6\,E_\mathrm{r}$. The results for κ are shown in Fig. 4.11 for all measured lattice depths.

Fig. 4.11a to 4.11c illustrate the behavior for the initial decay. Apparent are the significant lower values when working with a spin polarized gas as can be expected for fermions affected by the Pauli principle. In case of two and six components we observe a strong increase of the loss coefficient. According to Eq. (4.11), κ is connected to the effective loss rate Γ_eff, the correlation function $g^{(2)}$ and the initial filling fraction η_0. We can calculate Γ_eff according to our lattice parameters with Eq. (4.7) and thus expect a J^2 scaling. Regarding the correlation function as constant and our initial system as uncorrelated, we set $g^{(2)}$ to 1 and $5/3$ in the case of two and six spins respectively (cf. Sec. 4.2.1). In this way, measurement of κ can be used to extract the density as the only free fit parameter. The results are shown as solid lines in Fig. 4.11b and

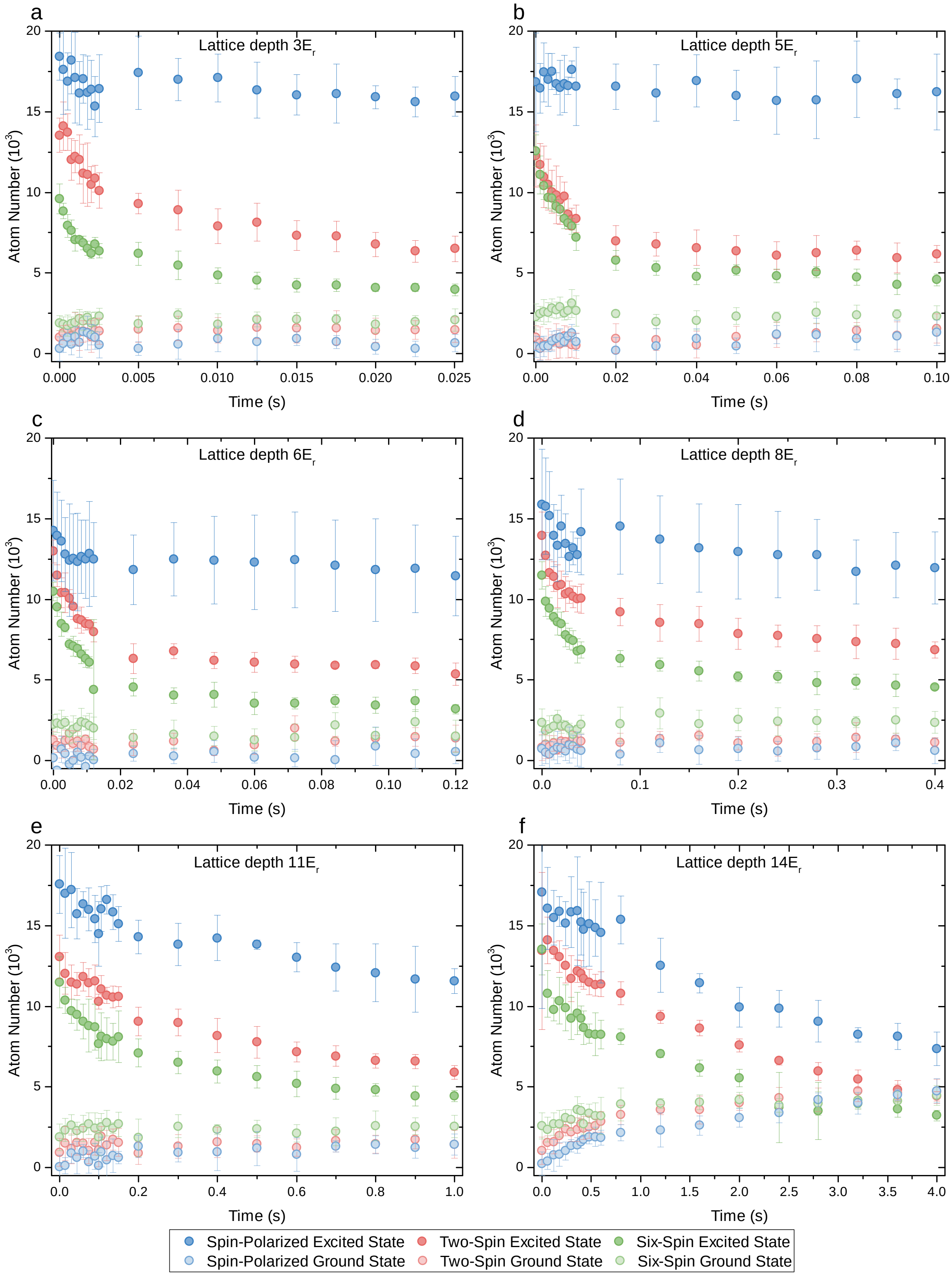

Figure 4.9.: Atom-loss dynamics for different 1D-lattice depths. The graphs show the atom-number evolution depending on the spin composition for different settings of the 1D lattice: **(a)** $3\,E_\mathrm{r}$, **(b)** $5\,E_\mathrm{r}$, **(c)** $6\,E_\mathrm{r}$, **(d)** $8\,E_\mathrm{r}$, **(e)** $11\,E_\mathrm{r}$, **(f)** $14\,E_\mathrm{r}$. A strong initial decay for two- and six-spin components is visible, which gets suppressed for higher 1D-lattice depths.

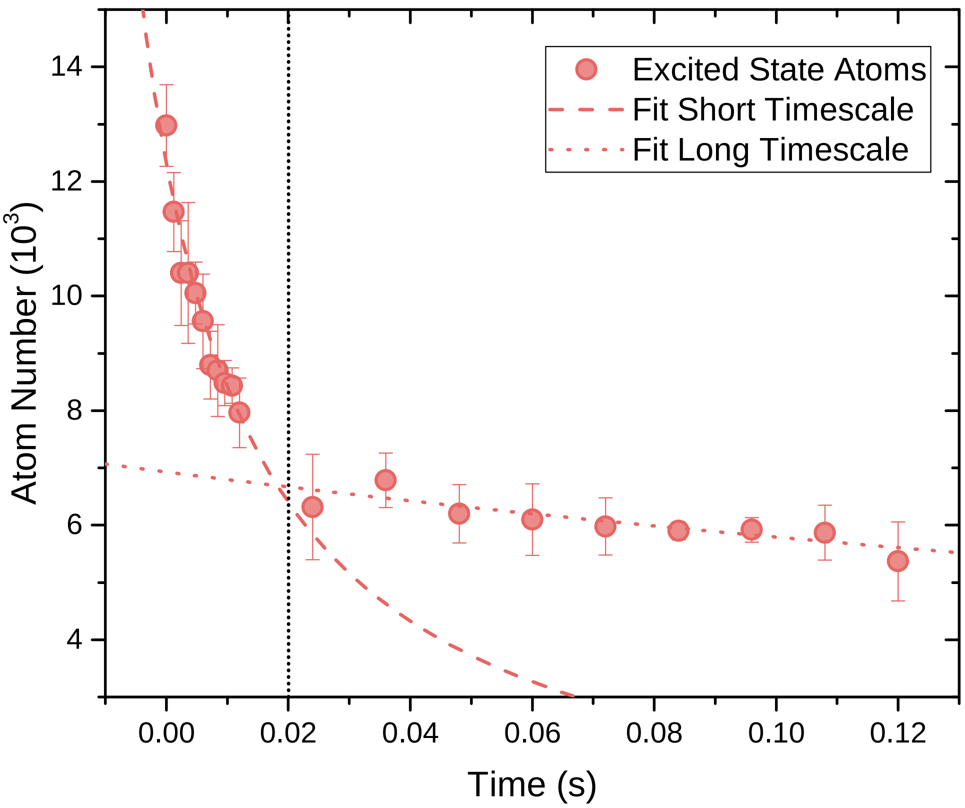

.

Figure 4.10.: Atom-loss dynamics for a two-component mixture at $6\,E_\mathrm{r}$. The graphic shows exemplary fits to different parts of the measurements. The black dotted line divides the fast, initial and the slow, secondary time scale. This procedure is applied to the data in Fig. 4.9.

4.11c. The corresponding densities are

$$\mathcal{N} = 2: \;\; \eta_0 = 85\% \pm 3\%,$$
$$\mathcal{N} = 6: \;\; \eta_0 = 42\% \pm 3\%.$$

The densities confirm that our preparation using RAP works quite good in case of two spins, because we almost reach single occupancy throughout the lattice. However, in case of six spins the resulting η_0 indicates a reduced loss rate due to unoccupied lattice sites. From analysis of the RAP we know that the preparation with six components tends to have a lower excitation efficiency and thus the system is left with more ground-state atoms. Hereby, the possibility of collisions between excited-state atoms is reduced.

Considering the second, slower decaying parts in Fig. 4.9 the respective values for κ can be found in Fig. 4.11d to 4.11f. All plots show strongly reduced loss rates with only a slight increase for a very shallow lattice. Four possible reasons can lead to this behavior:

1. The losses generate a highly correlated state in which entanglement prohibits any further decay and the system becomes stationary [FF12]

2. The atom loss leads to a significant dilution of the lattice system resulting in unoccupied sites. Hence, collisions can only occur after several tunneling events. However, the magnitude of loss coefficient and tunneling frequency indicate, that this effect should not play a significant role

3. The harmonic confinement of the optical lattice can lead to localization of atoms due to the energy offset [Sch08]. This can be analyzed by using even less particles to ensure lattice filling only in the lowest shell

4. Preparation using RAP produces left over ground-state atoms. With their large, elastic interaction strength they can lead to a tunneling blockade. To reduce the amount of unexcited atoms and to rule out this effect the efficiency of RAP has to be increased or the ground-state atoms might be removed from the system using resonant light.

A clear differentiation between these effects is not possible at this point but needs further analysis of these processes. The two-body loss model is certainly only a first approximation of all involved effects and we hope to get more insight into the theoretical background via a collaboration with L. Freystatzky [Fre17].

Conclusion

This chapter demonstrated how we experimentally realized a Fermi-Hubbard model. We used RAP to excite the meta-stable $^3P_0$ state of ^{173}Yb to induce dissipative dynamics via inelastic collisions. Two different timescales appear and they were analyzed for various lattice depths and spin configurations. We applied a two-body loss model to characterize these timescales and to point out the differences between the spin compositions. While usage of a polarized gas leads to strong suppression of the losses, we came to the conclusion that our state preparation in case of six components leaves unoccupied lattice sites. Although this idealized model certainly gave insight into our dissipative system, it is surely limited in clear answers on what processes dominate the slower, second timescale. We identified possible reasons, e.g. a highly correlated state or thinning of the sample, which might lead to a loss suppression. However, these will definitely profit from a more comprehensive, theoretical description.
Although ^{173}Yb appears to be a good candidate to study dissipative systems its parameters eventually enforce Mott-like behavior, because $\hbar\Gamma_{ee}/U_{ee} \approx 0.29$. To really reach a regime which is dominated by Zeno dynamics the ratio between Γ_{ee} and U_{ee} has to be changed. The loss rate Γ_{ee} of the other fermionic isotope ^{171}Yb is about a factor of two larger and thus comparable to the one of ^{173}Yb [Lud11]. But, the s-wave scattering length a_{ee} is not yet known. In case of a small value the ratio between interaction and losses could be significantly changed leading to a system far in the Zeno regime (cf. Fig. 4.6).

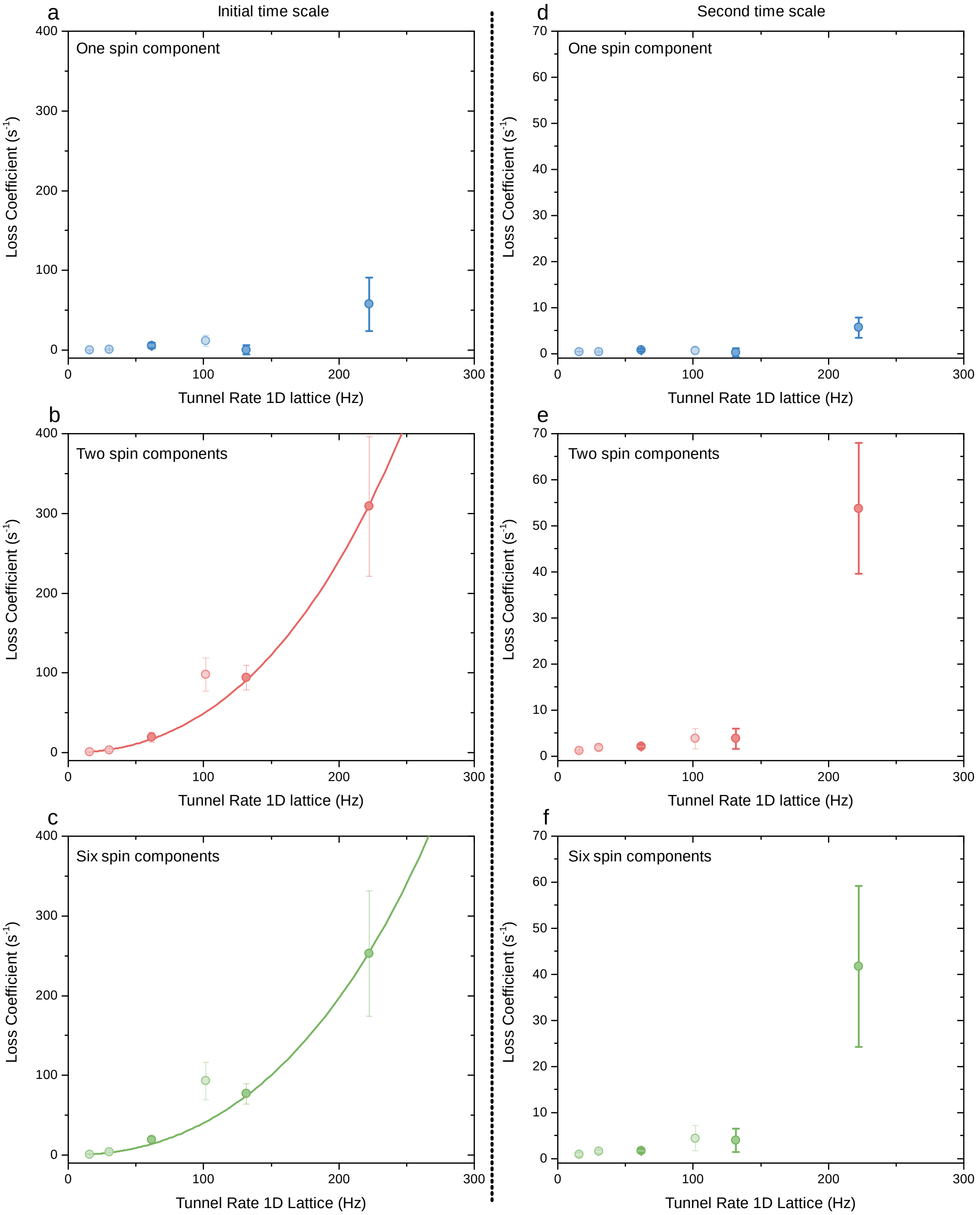

Figure 4.11.: Loss coefficient κ for one-, two- and six-spin component mixtures. The graphs show the fit results using Eq. (4.12) for two appearing timescales. Figures **(a)** to **(c)** correspond to the fast, initial decay and figures **(d)** to **(e)** to the slower, second timescale. The colors indicate one (blue), two (red) and six (green) components. Light-color data points are not included in the fitting procedure; in case of $6\,E_\mathrm{r}$ due to technical problems during the time of measurement, in case of $11\,E_\mathrm{r}$ and $14\,E\mathrm{r}$ due to strong suppression of tunneling. Solid lines show fits to Eq. (4.11) with η_0 as only fit parameter. Only figure **(b)** and **(c)** include these, because two-body losses are dominant in this case.

5. Towards the Realization of the 1D Kondo-Lattice-Model

The two previous chapters showed, how a magic, optical lattice can be used to perform ultra-narrow spectroscopy and to probe dissipative systems. Characteristic for such a lattice is the equal polarizabilty of the $^1S_0$ and $^3P_0$ state. These system can be well described by Fermi-Hubbard models, which are one of the key ingredients to understand present quantum-gas experiments involving optical lattices [Blo08, Ess10]. Although they could expand our knowledge significantly, their application to real materials, which behavior rely on the interplay between internal (spin) and external (orbital) degrees of freedom, can be limited. The Kondo-lattice-model (KLM) includes such interactions and constitutes a promising candidate to explain novel effects in heavy fermion materials, spin liquids or valence-bond-solids [Don77, Rea89, Her09, Isa15]. A crucial component in the KLM is given by two spin species, of which one is mobile and the other one localized [FF10b]. Such a system is governed by the tunneling J and the exchange energy V_{ex} [Gor10]. Yb constitutes a prime candidate for the experimental realization of such a model system. With its meta stable $^3P_0$ state it offers a second spin species, which can be localized in a state-dependent lattice, whereas the ground state $^1S_0$ is able to tunnel between lattice sites due to the different AC-stark polarizabilies. In addition, the SU(N) symmetry allows for an exchange interaction wherever a ground state atom tunnels to an occupied site. We planned an optical lattice at $660\,\mathrm{nm}$ for experimentally realizing the KLM. At this wavelength the polarizability ratio is $\alpha_{^3P_0}/\alpha_{^1S_0} \approx 5.5$.
The following chapter describes our laser setup for producing a state-dependent, optical lattice. First, the setup itself is explained and characterized. Second, we show first measurements using modulation-spectroscopy with ultra-cold ^{173}Yb. The laser system was planned by A. Skottke and the author. The laser was setup by A. Skotte. Implementation at the main experiment and the measurements were carried out by B. Hundt, B. Santra and A. Skottke. Further detailed information concerning this chapter can be found in [Sko16].

5.1. A state-dependent, optical lattice at $\lambda = 660\,\mathrm{nm}$

One of the crucial design considerations of a state-dependent lattice is the wavelength of the laser source. Geometric arguments might play a role, if for instance two lattices are supposed to be commensurate, but more importantly the difference in the AC-Stark polarizability of the involved states defines the characteristic dynamics of the system. In the previous chapter it was shown how inelastic collisions between two excited atoms can lead to large losses. Consequently, one has to choose the excited-state atoms to be the localized species. In this case, the choice of wavelength is basically given by the electronic structure, which determines the polar-

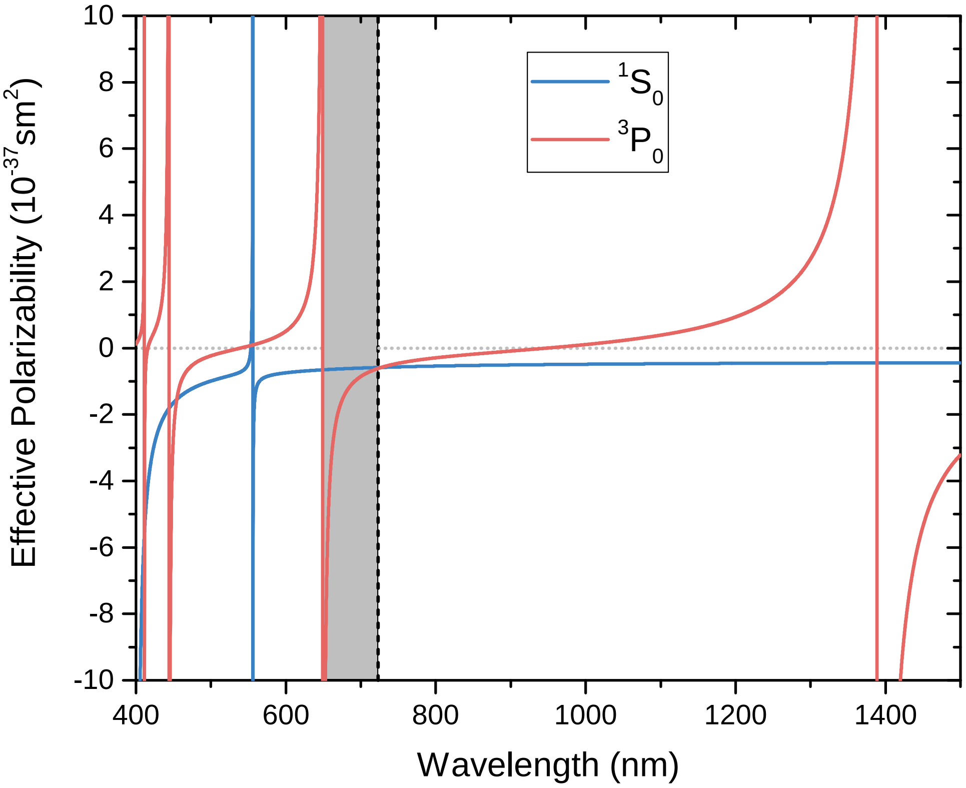

Figure 5.1.: Polarizability of the $^1S_0$ and $^3P_0$ state. The graphic shows the effective polarizability $\alpha/(2\epsilon_0 c)$ depending on wavelength of ground and lowest lying meta-stable state of Yb. The values have been calculated according to the most prominent known transitions. The approximation shows good results close to atomic resonances but otherwise can deviate significantly, e.g. the magic wavelength lies at $727\,\mathrm{nm}$ instead of the measured value of $759\,\mathrm{nm}$. See App. A for calculation details.

izability α. As can be seen in Fig. 5.1, three regions are of interest: The wavelength regions next to $^3P_0 \Leftrightarrow {}^3D_1$(6s6d) $(444\,\mathrm{nm})$, $^3P_0 \Leftrightarrow {}^3S_1$(6s7s) $(649\,\mathrm{nm})$ and $^3P_0 \Leftrightarrow {}^3D_1$(6s5d) $(1388\,\mathrm{nm})$. The first option involves a single-mode laser source close to $444\,\mathrm{nm}$ with high output power, which is quite difficult to obtain. The option in the infrared is principally possible from the point of laser availability (telecom range). However, one has to keep in mind that due to the larger lattice spacing tunneling will be strongly suppressed such that experiment durations increase. For comparison Fig. 5.2a indicates how the tunneling paramter J depends on the choice of laser wavelength. We therefore decided to get a laser source close to $649\,\mathrm{nm}$. We found a commercial Diode-Pumped-Solid-State[1] source to be the best compromise between ratio of polarizabilities, scattering rate and output power. The laser can provide $500\,\mathrm{mW}$ at $660\,\mathrm{nm}$. The polarizability difference between ground- and excited-state atoms has a lattice-depth independent value of $\alpha_{^3P_0}/\alpha_{^1S_0} \approx 5.5$. However, the tunneling parameter J depends non linearly on the lattice depth. The actual values are shown in Fig. 5.2b. For instance, at a lattice depth of $5\,E_\mathrm{r}$ for ground-state atoms, the depth for excited-state atoms is $27.5\,E_\mathrm{r}$ and the tunneling rates differ by two orders of magnitude. In eventual experimental sequences one has to find a

---

[1] COBOLT Flamenco

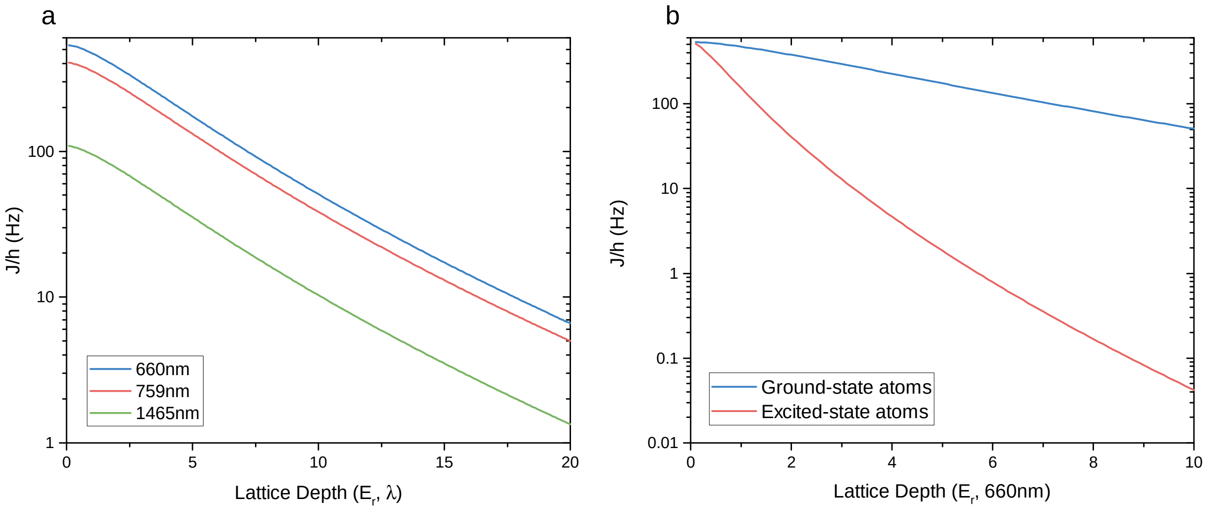

Figure 5.2.: Tunneling J depending on lattice wavelength and electronic states. Both graphs were generated using a 1D band-structure calculation and deducing J via the Wannier-function overlap. **(a)** shows how the tunneling depends on the lattice-laser wavelength. The x-axis depends on the indicated wavelengths. **(b)** shows how the tunneling depends on the electronic state of Yb in a lattice with wavelength $\lambda = 660\,\mathrm{nm}$. The x-axis gives the lattice depth for the ground-state atoms. The difference in J is highly non linear. At a lattice depth of $5\,E_\mathrm{r}$ the tunneling rates differ by two orders of magnitude.

compromise between tunneling of ground-state atoms, localization of excited-state atoms and off-resonant scattering by the lattice beam.

5.1.1. The laser setup

The laser setup is kept as compact as possible to ensure high stability. A sketch can be found in Fig. 5.3. Since the beam is superimposed with the 1D magic lattice, only a single branch is lead to the experiment. The light can be switched on and off via an $80\,\mathrm{MHz}$ AOM. Furthermore, the AOM is used for intensity-stabilization, -ramps and -modulation. These applications are necessary to produce a lattice of certain depth, smoothly load the atoms from the dipole trap into the lattice and analyze the lattice structure via amplitude-modulation-spectroscopy. The intensity regulation is capable of suppressing intensity noise by $\approx 15\,\mathrm{dB}$ and has a bandwidth of about $100\,\mathrm{kHz}$. We set up an additional shutter to have an alternative way of blocking the light. To analyze the longitudinal mode of the laser light is sent to an optical cavity, which length can be scanned, and a wavelength meter. They help to verify single-mode operation and to measure the wavelength. The fiber link to the main experiment is equipped with manual polarization control, which can be used to optimize power transmission at a polarizing cube (polarization cleaning) inside the telescope.

Atoms located in an optical lattice can be manipulated deliberately via modulation of the intensity or the frequency of the laser. However, any significant amount of power in these respective noise types can cause unwanted excitations to higher bands or, in general, heating of the system.

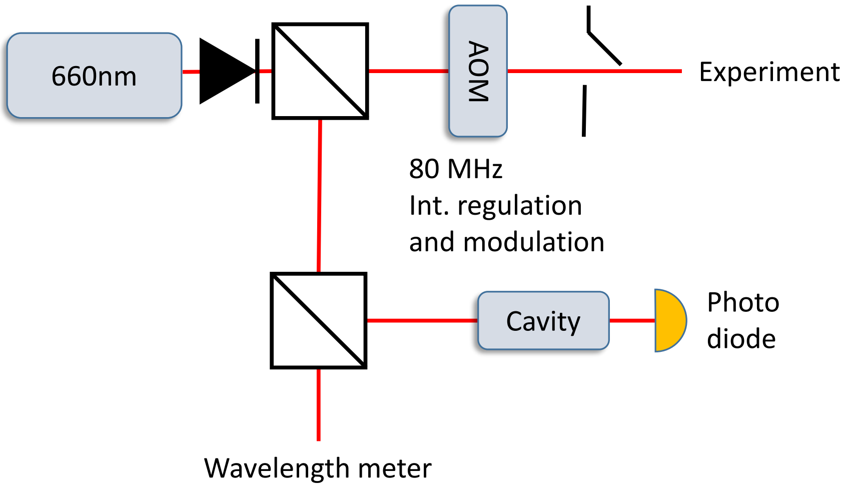

Figure 5.3.: Laser system for the state-dependent lattice. The picture shows a simplified version of the laser setup for $\lambda = 660\,\mathrm{nm}$. We secured the laser against back reflection with an optical isolator. The intensity can be stabilized, switched, ramped and modulated via the same AOM. An additional shutter can be used for blocking the beam. The setup holds a Fabry-Pérot cavity with photo diode for monitoring single-mode operation and a fiber link to a wavelength meter for determining the frequency.

The probability of such excitations is connected to the spectral power density

$$S_\epsilon(\omega) = \frac{2}{\pi} \int_0^\infty \mathrm{d}\tau \, \cos\omega\tau \, \langle \epsilon(t)\, \epsilon(t+\tau) \rangle$$

and can be calculated as an excitation rate in case of intensity noise with

$$\frac{\langle \dot{E} \rangle}{\langle E \rangle} = \frac{\pi}{2}\, \omega_{\mathrm{tr}}^2 \, S_\epsilon(2\,\omega_{\mathrm{tr}}). \tag{5.1}$$

Here, ω_{tr}, ϵ and E denote the trap frequency, the fractional fluctuation and the energy respectively [Sav97, Jáu01]. Although we did not evaluate Eq. (5.1), the formulas can give an estimate about which frequency range is relevant for us. As we know the maximum lattice depth for our laser parameters to be $458\,E_\mathrm{r}$ (cp. with Sec. 5.1.3), we need to regard frequencies up to $217\,\mathrm{kHz}$. Alternatively, we compared the noise spectrum of the new laser to the ones we had already used. We measured the amplitude noise by detecting light on a commercial photo diode[2] and evaluated the signal using an Audio Analyzer[3]. The result is shown in Fig. 5.4. As references we used a MOPA[4] ($1064\,\mathrm{nm}$), a Ti:Sa[5], and an ECDL[6] ($780\,\mathrm{nm}$). In our research group, we successfully set up optical lattices using the MOPA and Ti:Sa systems. As shown, the $660\,\mathrm{nm}$ laser is partly as low-noise as the Ti:Sa and for all relevant frequencies at least $5\,\mathrm{dB}$ below the level of the MOPA system. We thus conclude that the intensity-noise characteristics are sufficiently well.

---

[2] Thorlabs PDA36A
[3] Rhode & Schwarz UPV
[4] Coherent Mephisto
[5] Coherent MBR
[6] TOPTICA DL PRO

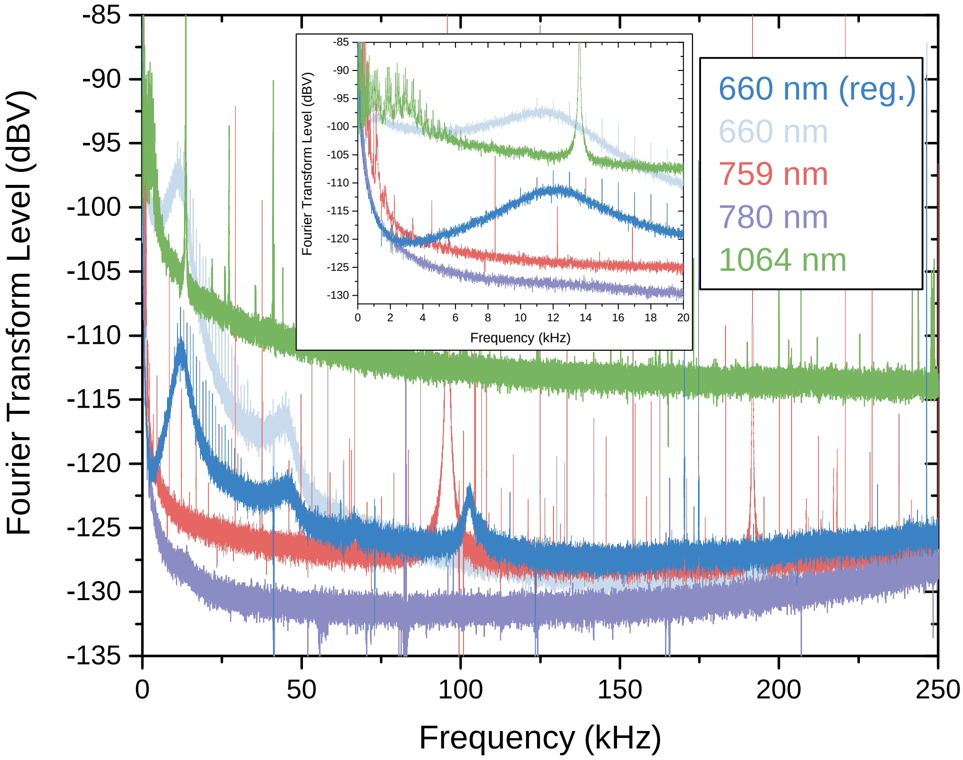

Figure 5.4.: Intensity stability of state-dependent-lattice laser. The plot depicts the noise amplitudes of four different laser source: A MOPA ($1064\,\mathrm{nm}$), a Ti:Sa ($759\,\mathrm{nm}$), a DPSS ($660\,\mathrm{nm}$, with and without intensity regulation) and an ECDL ($780\,\mathrm{nm}$). Light is sent to a photo diode and evaluated via an Audio Analyzer. The relevant frequency range extends to $217\,\mathrm{kHz}$. In this range the noise level of the $660\,\mathrm{nm}$ laser is below the level of the MOPA, with which we successfully build optical lattices. The noise level even reaches as low as a narrow-linewidth Ti:Sa system in large parts. The peak of the Ti:Sa at $90\,\mathrm{kHz}$ is caused by an internally used etalon. Further explanations can be found in the main text. The Graphic is taken from [Sko16].

The spectrum shows a narrow-linewidth comb structure around $25\,\mathrm{kHz}$ and two distinct peaks around $175\,\mathrm{kHz}$. According to the manufacturer, both can be attributed to electronic leakage of the power supply and the control unit. Three broader features are visible at $17\,\mathrm{kHz}$, $45\,\mathrm{kHz}$ and $105\,\mathrm{kHz}$.The first two are probably a result of laser-specific properties and the third one is a result of noise amplification due to the limited regulation-loop bandwidth of the regulation electronics (“servo bumps“).

In a similar way, frequency noise can lead to excitation in an optical lattice. To evaluate the frequency stability of our $660\,\mathrm{nm}$ laser we measured the beat signal with respect to a GPS-stabilized frequency comb. The result can be seen in Fig. 5.5. As an upper bound the stability can be estimated to be better than $205(4)\,\mathrm{kHz\,s^{-1}}$. Such a deviation corresponds to about $0.4\,\mathrm{mrad\,s^{-1}}$ of phase deviation at the position of the atoms[7]. This effect is negligible on typical experimental time scales in the lattice (up to few $100\,\mathrm{ms}$).

---

[7] Distance to retroreflector is $300\,\mathrm{mm}$.

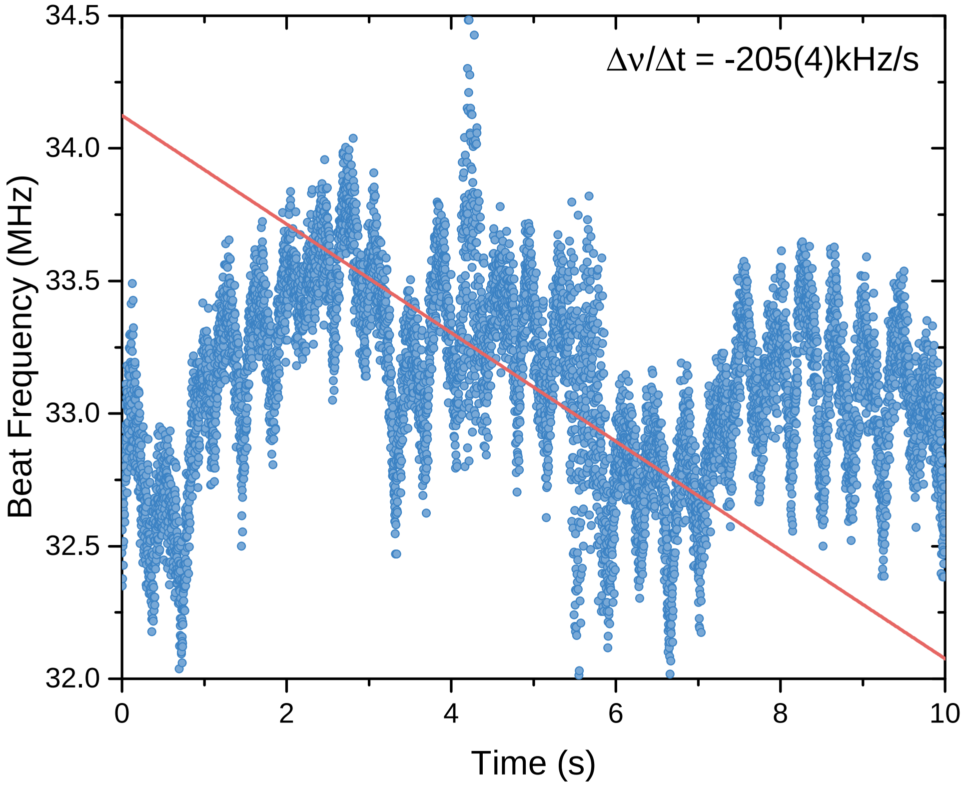

Figure 5.5.: Frequency stability of the state-dependent-lattice laser. The plot depicts the beat signal with respect to a GPS-stabilized frequency comb. Fast fluctuations are caused by the instabilites of the comb. A linear fit to the central part of the data points yields a slope of $205(4)\,\mathrm{kHz\,s^{-1}}$. This corresponds to $0.4\,\mathrm{mrad\,s^{-1}}$ phase deviation of the optical lattice at the position of the atoms, which can be neglected.

5.1.2. The telescope

One of the big advantages of optical lattices as opposed to solid-state materials is the defect-free geometry generated by interfering laser beams. However, this is actually only valid for plain waves. The best approximation of plain waves can be achieved near the waist of a Gaussian beam [Sve98]. But, the beam shaping optics need to be carefully picked and analyzed to prevent wavefront errors to disturb the lattice structure. Fortunately, the laser light is linked to the main experimental chamber via an optical fiber, which is used as a mode clean-up filter. The lenses are picked according to two boundary conditions: The size of the waist and the working distance. The first one is determined by forcing the waists of magic and state-dependent lattice to overlap. This is certainly preferable in case we want to switch between the lattices without realignment of the dipole traps. For a retro-reflected lattice the the wavefront curvature of both wavelengths needs to be equal on the surface of the mirror. This can be calculated via

$$\frac{w_{759}^2}{759\,\mathrm{nm}} = \frac{w_{660}^2}{660\,\mathrm{nm}} \Rightarrow w_{660} = 78\,\mathrm{\mu m}.$$

The second condition is merely given by the possible distance between the telescope and the position of the atoms due to other optical elements close to the science cell. In our case the working distance f_{wd} needs to be $62\,\mathrm{cm} \leq f_{\mathrm{wd}} \leq 77\,\mathrm{cm}$.

To circumvent the costs of a commercial objective we initially conducted numerical analysis of different optical designs using only commercially available lenses (singlets, doublets, aspheres). Although many configurations looked promising theoretically, we experienced strong deviations between theoretical and measured imaging quality [Sko16]. Eventually, we decided for a four lens design shown in Fig. 5.7. This amount of lenses was necessary because the aspheres with focal lengths $\leq 10\,\mathrm{mm}$ tend to have better imaging quality. To still reach our design goals a magnifying telescope with two lenses was required. The telescope additionally houses a PBS to define a distinct polarization axis. The fiber is connected to a commercial collimator[8]. The tube, which houses the polarizer and the lenses, is rigidly fastened to the coupler via a massive aluminum plate.

For the numerical analysis we used a commercial optical-design software[9]. The lenses and the PBS were modeled with their actual dimension[10] except for the asphere. This one was approximated via a perfect lens with effective focal length[11] EFL $= 7.9\,\mathrm{mm}$. One way to analyze the imaging quality is an evaluation of the optical path differences (OPD). An optical system can be characterized as diffraction limited if the OPD RMS error is smaller than $0.07\,\lambda$ [Smi07]. The results can be found in Fig. 5.6. The data is produced for the optical system in Fig. 5.7 with a waist of $78\,\mu\mathrm{m}$, a working distance of $67\,\mathrm{cm}$, the mode-field-diameter of the fiber is assumed to be $4\,\mu\mathrm{m}$ and the numerical aperture is estimated with NA $= 0.13$. To reach appropriate values for waist and working distance the collimation lens had to be slightly shifted away from its nominal position, i.e. $140\,\mu\mathrm{m}$ away from its focal length. The plots show that the system works diffraction limited even for coarse missalignment of $4°$ of the incoming beam. Furthermore, the numerical analysis confirms that the collimating asphere is the most sensitive part of the telescope with respect to misalignment, because the optical performance, waist and working distance greatly change for minor position deviations of this lens.

Analogous to Sec. 2.1.3, we evaluated the beam quality by measuring the transversal beam profiles along the optical axis using a CCD camera[12]. The measurement is shown in Fig. 5.8. As can be seen, the waist $w_0 \approx 78.5\,\mu\mathrm{m}$ and working distance $f_{\mathrm{wd}} \approx 66\,\mathrm{cm}$ of the beam lie within the design goals. Considering the beam quality, the fit to all data points has a value of $M^2 = 1.02$ (x-direction) and $M^2 = 1.005$ (y-direction) which is very close to the ideal case. However, the curve does not resemble the data points around the focus very well. Considering only the data points close to the center (red arrows) yields $M^2 = 1.25$ (x-direction) and $M^2 = 1.26$ (y-direction). In this case the center is certainly better approximated, but overall the beam divergence is overestimated. Apparently, the axial profile can not be well described by applying a M^2 model. The deviations from an ideal Gaussian beam are probably caused by abberations, which can explain deformations and asymmetries around the focus. They can be modeld by using the geometric-phase delay caused by optical elements and calculate the Fresnel diffraction integral [Pu98, Lü01]. Additional measurements indicate that the collimating asphere significantly influences this behavior [Sko16].

---

[8] TOPTICA Fiber Dock

[9] Lambda Research OSLO

[10] Thorlabs TLVISLC1715, TLVISLA1509, TLVISLA1908; Qioptiq width $10\,\mathrm{mm}$, glass S-NBH51

[11] Actual data not available

[12] Data Ray Inc., WinCamD-LCM

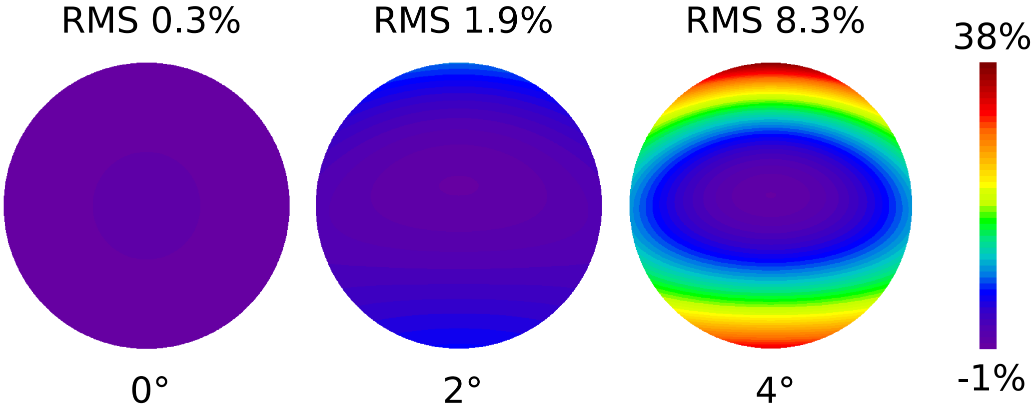

Figure 5.6.: Numerically simulated OPD errors. The graphic shows the deviations of optical-path-differences at the position of the waist with respect to the nominal imaging plane across the aperture of the optical system. The three areas correspond to different beam angles incident on the first lens of the telescope. Since the errors are bound by about 8%, the system can be regarded diffraction limited. This is even true for strong angle misalignment up to $4°$. All units are given in multiples of $\lambda = 660\,\mathrm{nm}$. More details can be found in the main text.

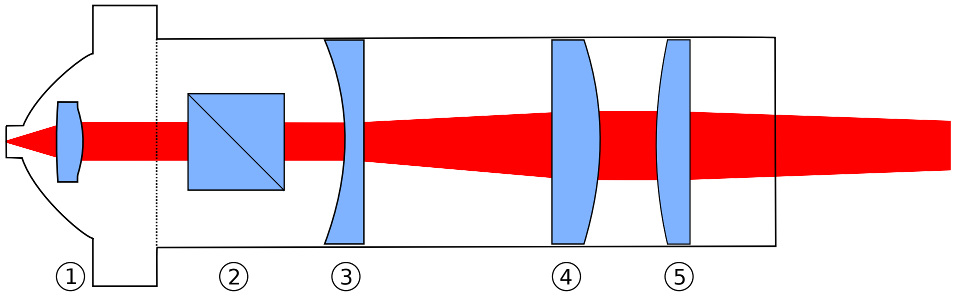

Figure 5.7.: Telescope for the state-dependent lattice. The sketch shows the optical assembly for producing the state-dependent lattice. The following components are used: **1.** Aspheric lens with effective focal length $f = 7.9\,\mathrm{mm}$ at $\lambda = 660\,\mathrm{nm}$ **2.** Polarizing, thin-film beam splitter, rotatable **3.** Plano-concave lens $f = -50\,\mathrm{mm}$ **4.** Plano-convex lens $f = 100\,\mathrm{mm}$ **5.** Plano-convex lens $f = 500\,\mathrm{mm}$. The first lens is mounted in a rigid fiber-collimator with adjustable position along the optical axis. All other components are manually adjusted inside a tube system and fixed via retaining rings. The whole telescope is mounted on top of a translation stage and can be shifted along the optical axis. The graphic is taken from [Sko16].

Despite minor deviations from an ideal gaussian mode we decided the optical performance to be sufficient for our purposes. Already implemented telescopes, like the ones for the 1D- and 2D-magic lattice [Pet14, Hun16], showed similar errors and were successfully utilized to produce optical lattices.

5.1.3. Implementation at the main apparatus

Realization of the state-dependent lattice involved a change of the main mirrors close to the science cell, because these were initially planned to only work with a lattice wavelength of

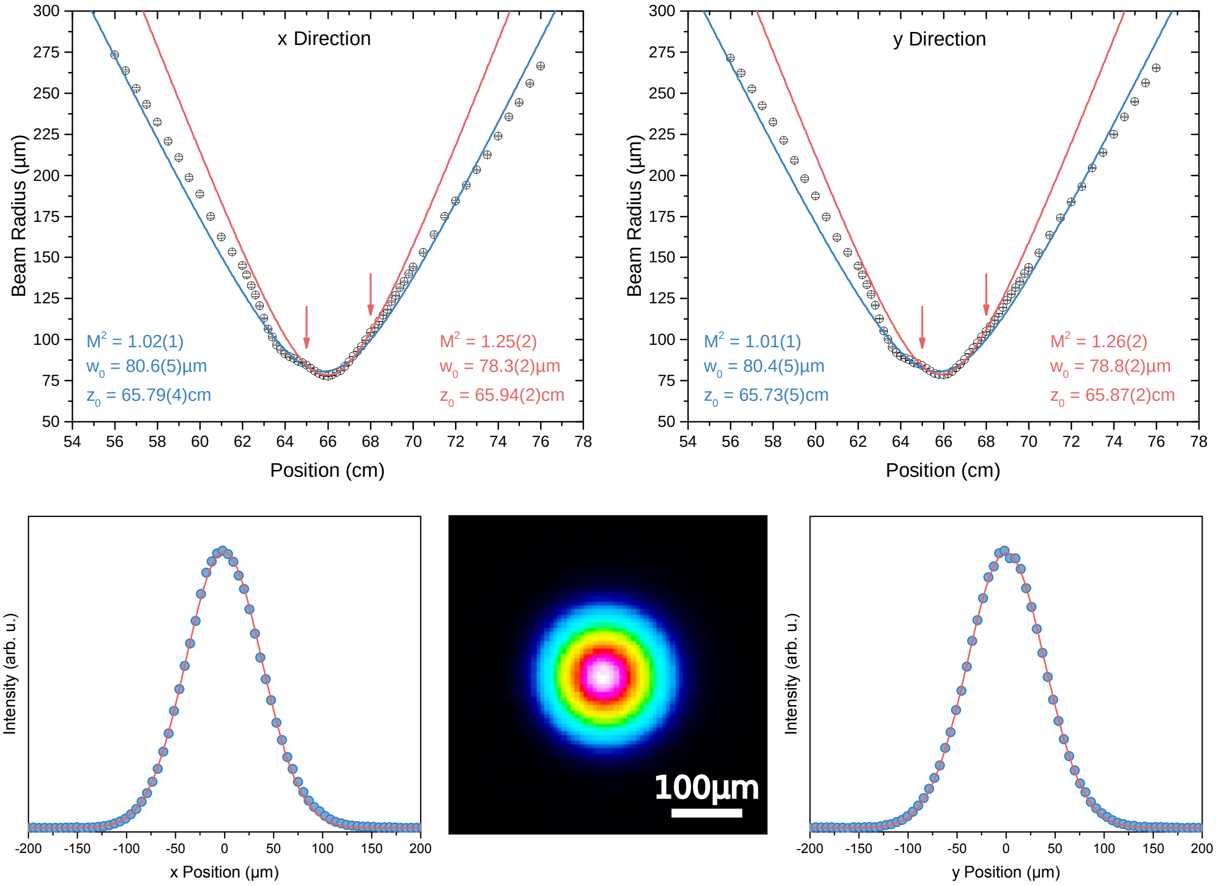

Figure 5.8.: M^2 **measurement and beam profile of state-dependent lattice. Top:** The two graphs show the beam radius measured along the optical axis in x- and y-direction. Both data sets are approximated using Eq. (2.4). The blue results correspond to all visible data points, whereas the red results correspond to the data points within the two red arrows. Both blue approximations show M^2 values very close to the ideal value of $M^2 = 1$. However, deviations are clearly visible and are probably caused by abberations of the collimating lens. The red curves approximate the waist better but overestimate the beam divergence. The measured waist of $w_0 \approx 78.5\,\mathrm{\mu m}$ is very close to the design goal of $78\,\mathrm{\mu m}$ and the working distance of $f_{\mathrm{wd}} \approx 66\,\mathrm{cm}$ lies within the design range. **Bottom:** The central image shows exemplary one of the CCD images taken for the graphs above at the position $66\,\mathrm{cm}$. The graphs on the left and the right show cross sections along the horizontal (x) and vertical (y) axis through the center of the beam profile. The graphic is taken from [Sko16].

$759\,\mathrm{nm}$. Most of our laser beams pass these mirrors simultaneously, thus they need high quality coatings to ensure good reflective and transmittive properties and a high surface quality. All of the surfaces have been produced using Ion-Beam-Sputtering (IBS), the substrates are made from Fuzed Silica and have an elliptical shape to yield a $25\,\mathrm{mm}$ aperture at an angle of $45°$. The two mirrors closest to the science cell are additionally $0°30'$ wedged to suppress etaloning effects along one of the imaging axes. A sketch of the setup can be found in Fig. 5.9.

Behind the first mirror after the telescope we positioned a photo diode for the intensity regulation. The electronic signal is connected to the PID controller, which regulates the AOM in the laser setup. The lattice wavelengths are superimposed via an unadjustable, dichroic mirror. Each beam has two additional mirror holders such that they can be aligned individ-

	HR	**HT**
①	660	759
②	660, 759	532, 1064
③	532, 578, 660, 759, 1064	399, 556
④	578, 660, 759	532, 1064
⑤	660, 759	578

Table 5.1.: Overview of the new mirror coatings. The table shows the current front-surface properties, HR (highly reflective) and HT (highly transmittive), of the newly implemented mirrors needed for the state-dependent lattice. All rear surfaces are anti-reflex coated respectively. All units are given in nm.

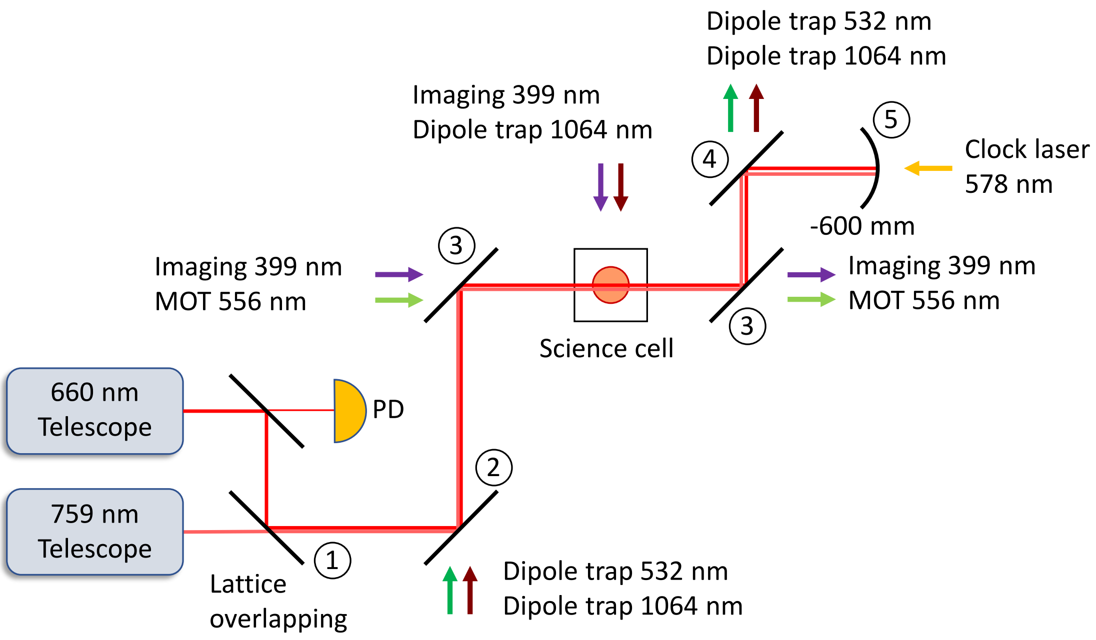

Figure 5.9.: Mirror setup for the state-dependent lattice. The sketch shows a simplified version of our setup close to the science cell. 660 nm light is picked up with a photo diode for intensity regulation. Both lattice wavelengths are superimposed using a non-adjustable, dichroic mirror. All mirrors carry IBS coatings according to Tab. 5.1.3. Omitted are mirrors for aligning both lattice beams individually.

ually, although both lattices are retro-reflected via the same concave mirror (radius of curvature $-600\,\mathrm{mm}$). The coatings of the new mirros are summarized in Tab. 5.1.3.

5.1.4. Lattice parameters

Maximum lattice depths

At the position of the atoms we measured a maximum power of $320\,\mathrm{mW}$. Combining this value with the waist of the beam ($w_{660} = 78\,\mu\mathrm{m}$) the maximum lattice depths and scattering rates for the $^1S_0$ (g) and $^3P_0$ (e) state can be calculated according to Eq. (2.2) and Eq. (2.3):

$$\Gamma^g_{\text{max}} = 1.7 \times 10^{-2}\,\mathrm{s}^{-1}, \Gamma^e_{\text{max}} = 8.1 \times 10^{-1}\,\mathrm{s}^{-1}, V_0^g = 49\,E_{\mathrm{r}}, V_0^e = 267\,E_{\mathrm{r}}.$$

These numbers have been calculated with respect to the most significant transitions $^1S_0 \Leftrightarrow {}^1P_1$ and $^3P_0 \Leftrightarrow {}^3S_0$.

The maximum scattering rate for the e-state corresponds to one event every $1.2\,\mathrm{s}$. This duration is still bigger than typical experiments in the optical lattice (few $100\,\mathrm{ms}$), but not by far. Possible experimental sequences will not use the full laser power permanently. This is only necessary during the phase of state preparation, where $578\,\mathrm{nm}$ light is applied. Here, a deep lattice can suppress excitation due to the momentum transfer of photons (Lamb-Dicke-Regime). Afterwards, the lattice intensity will be reduced to a few E_{r} for the ground-state atoms to initiate dynamics. This results in lattice depths of $10\,E_{\mathrm{r}}$ to $25\,E_{\mathrm{r}}$ for the excited state atoms, which is about a magnitude lower than the maximum depth. Hence, heating effects caused by off-resonant scattering should only play a marginal role.

State preparation of $^3P_0$

In presence of the state-dependent lattice, the difference in polarizability of ground- and excited-state atoms simultaneously leads to an AC-Stark shift which varies between different lattice sites. Using and modifying Eq. (2.1) the frequency broadening can be calculated with:

$$\Delta f = -\frac{1}{h}\frac{1}{2\epsilon_0 c}\Delta\alpha_{eg}\Delta I. \tag{5.2}$$

Here, $\Delta\alpha_{eg} = \Re(\alpha_e) - \Re(\alpha_g) = -1.53 \times 10^{-38}\,\mathrm{m}^2\,\mathrm{C}^2\,\mathrm{J}^{-1}$ and ΔI is the intensity variation along the lattice. Regarding the maximum lattice depth with $320\,\mathrm{mW}$, a waist of $w_{660} = 78\,\mu\mathrm{m}$ and a transversal, magic lattice[13], the dependence between frequency shift and radial position in the lattice can be calculated. The result is shown in Fig. 5.10. Typically a polarized Fermi gas inhabits about 50000 atoms, which occupy about 19 lattice sites in the radial direction. In this case the broadening amounts to $16\,\mathrm{kHz}$.

Excited states can possibly be produced using π-pulses. This makes it necessary to match the excitation beam profile with the lattice beam geometrically to fit the spacial varying Rabi frequency. However, this can only be carried out approximately, because the Rabi frequency across the clock-laser beam scales with $\Omega \propto \sqrt{I}$ and the effective Rabi frequency in the lattice scales with $\Omega_{\text{eff}} = \sqrt{\Omega^2 + \Delta^2}$. From Eq. (5.2) it is apparent that the detuning Δ scales with the intensity I. In addition, if the clock-laser beam radius is similar to the one of the lattice, the sensitivity due to misalignment will increase significantly. A more convenient way is to employ a RAP as demonstrated in Chap. 4. Although each atom is slightly shifted in resonance, the RAP condition can be applied on each atom individually. The sweep speed is mainly limited by the Rabi-frequency and thus has to be set according to the beam power. The sweep range needs to cover the resonance frequencies of all atoms sufficiently. For a Rabi-frequency of $\Omega = 2\pi \times 3.8\,\mathrm{kHz}$ this would be fulfilled with a span of $150\,\mathrm{kHz}$ and a sweep time of $30\,\mathrm{ms}$.

---

[13] Using a triangular 2D lattice with a wavelength $759\,\mathrm{nm}$ the distance between two wells is $506\,\mathrm{nm}$.

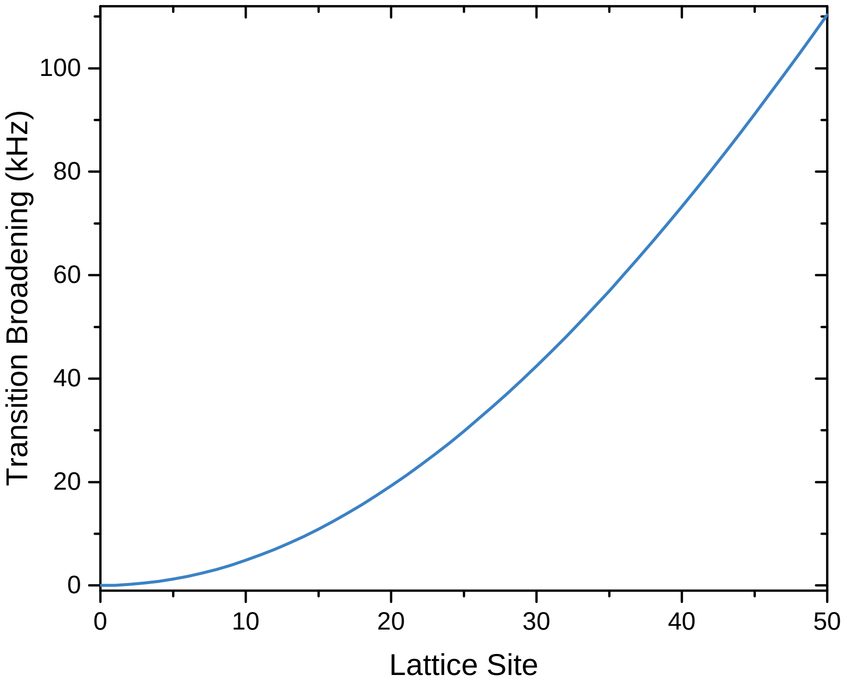

Figure 5.10.: Broadening of the $^1S_0 \Leftrightarrow {}^3P_0$ transition in a state-dependent lattice. The graph shows the transition broadening due to the differential AC-Stark shift in the state-dependent lattice at $660\,\mathrm{nm}$ as a function of the lattice site radially away from the waist. The calculation assumes a laser power of $320\,\mathrm{mW}$ and a waist of $78\,\mu\mathrm{m}$ for the state-dependent lattice. The lattice consists of a 1D state-dependent lattice ($660\,\mathrm{nm}$) and a perpendicular 2D magic lattice ($759\,\mathrm{nm}$) with triangular geometry. For a spin-polarized Fermi gas with 50000 atoms the broadening amounts to about $16\,\mathrm{kHz}$.

5.2. Ultracold ^{173}Yb in a state-dependent lattice

In the second part of this chapter measurements involving the state-dependent lattice and ultracold atoms are presented. Although it is planned to eventually realize the KLM with this setup, due to time restrictions only first results can be demonstrated.
As illustrated in Fig. 5.9 the implementation of the state-selective lattice made a change of the central mirrors close to the science cell necessary. Fortunately, the IR2 beam was not affected by this restriction and it could be used as a fix-point for alignment. The other beams were first coarsely realigned with optical apertures. The final adjustment of the state-selective lattice was carried out in a similar manner to the magic lattice. By blocking the retroreflecting mirror and switching the laser on for $10\,\mathrm{ms}$ at a low power center-of-mass oscillations of the DFG could be induced. Alignment was optimized after elimination of these oscillations.
As explained in Chap. 2 the experimental sequence started with cooling a thermal gas of ^{173}Yb to quantum degeneracy using the bicolor dipole trap. No pumping was applied which produces a balanced, six-component spin mixture. The DFG had about 75000 atoms at a temperature of $26\%\,T_{\mathrm{F}}$ determined by a fugacity fit.

5.2.1. Visualization of the first Brillouin zone

As a first indication of successful transfer of a DFG into the state-dependent lattice the shape of TOF images can be analyzed. Due to the Fermi statistics the atoms occupy states up to the Fermi energy. An efficient way of measuring the lattice occupation is the band-mapping technique already presented in Sec. 3.1, where it was used for the characterization of the magic lattice. In this way the quasi momenta can be mapped onto real momenta.

Loading atoms into the $660\,\mathrm{nm}$ lattice was carried out similar to the case of the magic lattice. While the dipole traps were still switched on, we ramped up the lattice intensity in $100\,\mathrm{ms}$. The 2D lattice beams were deactivated. We did not switch off the dipole trap afterwards to keep the harmonic confinement against gravity. The lattice power was then ramped down exponentially within $2\,\mathrm{ms}$ and absorption imaging followed after a TOF of $20\,\mathrm{ms}$. The result can be found in Fig. 5.11.

The graphic shows a typical image resulting from a 1D-optical lattice. For an ideal 1D lattice the Brillouin has a rectangular shape. This is precisely what we observe. In the direction of the lattice beam sharp edges are visible, where in the perpendicular direction a smoother distribution can be seen. This is expected, because perpendicular to the 1D lattice only the harmonic confinement of lattice and dipole trap beams contribute. In Sec. 3.3.1 we analyzed the possible population of the first excited band and showed that for a spin-polarized gas with 35000 no such excitation was visible. For the parameters of this image there are only 12500 atoms per spin component. Using a shorter wavelength, i.e. $660\,\mathrm{nm}$ instead of $759\,\mathrm{nm}$, should even increase the possible atom number in the lowest lying band by a factor of ≈ 1.5 (cp. Eq. (3.4)) assuming the same trap frequency $\bar{\omega}$. This means that no occupation of the second Brillouin zone should be visible in Fig. 5.11, which is confirmed by the image.

5.2.2. Calibration of the lattice

The lattice-dynamics describing parameters U, J and Γ depend on the lattice depth via the Wannier functions. Hence, for generating repeatable experimental conditions the lattice setup has to be properly calibrated. Sec. 3.1 described how amplitude modulation of the beam intensity can be used to determine the lattice depth by comparing the measured resonances to band structure calculations. Different to the calibration of the magic lattice, we did not identify the band gap at deep lattice depths but instead analyzed the band structure momentum resolved in the range $< 10\,E_\mathrm{r}$.

The experimental sequence starts as described in the paragraph above. Before commencing band mapping however, the lattice depth was sinusoidally modulated for $1\,\mathrm{ms}$. We typically use a modulation depth of 5% to 15% depending on the observed signal strength. An exemplary absorption image during a modulation sequence can be seen in Fig. 5.12. Here, the excitation into the second excited band is visible. The first Brillouin zone shows a distinct peak in the center caused by generated holes close by.

The band structure was measured by changing the modulation frequency by $500\,\mathrm{Hz}$ for every experimental cycle and determine the relative position of the excitation peaks. The range of the frequency sweep is based on the expected lattice depth. Since the TOF was known the quasi

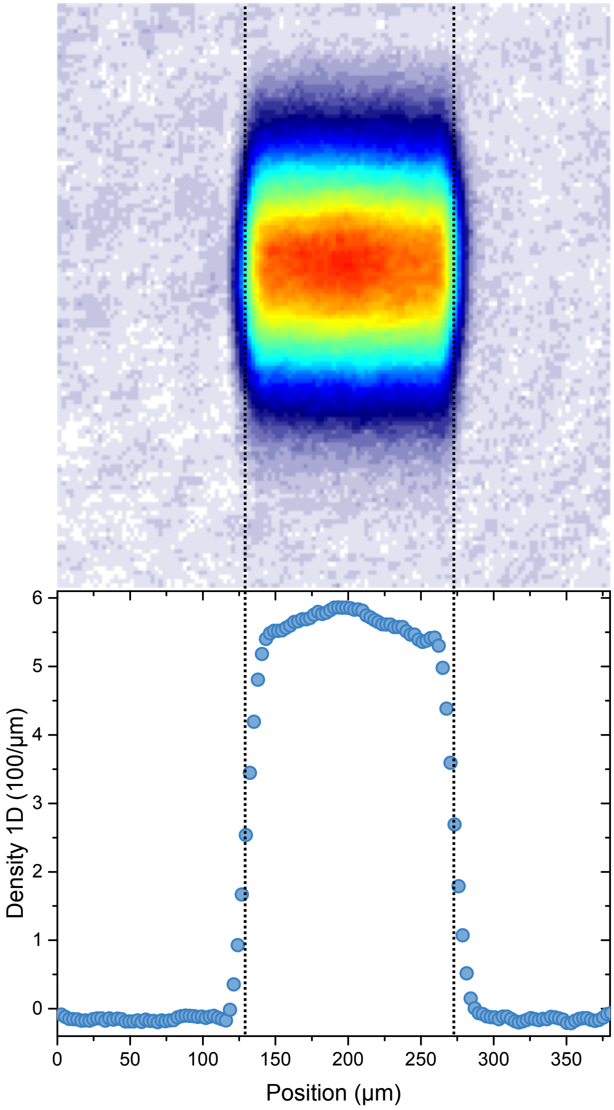

Figure 5.11.: Bandmapping of the first Brillouin zone in the state-dependent lattice. The image shows the absorption image of a six-component DFG with 75000 atoms after 20 ms TOF and 2 ms band-mapping duration. The shape shows the typical rectangular form of the first Brillouin zone in a 1D lattice. No population of higher Brillouin zones is visible. The image was averaged using 22 experimental cycles.

momenta q_{L} can be calculated using

$$q_{\mathrm{L}} = \frac{p}{\hbar k_{\mathrm{L}}} - \Delta n, \; p = \frac{m \cdot x}{\mathrm{TOF}},$$

with real momentum p, lattice wavenumber k_{L}, band index $\Delta n = 2$, mass m and position x. The measured correspondence between quasi momenta and modulation frequency for two lattice depths is shown in Fig. 5.13. The graphic also indicates the fit results using a 1D-band-structure calculation (solid blue lines). Note that values for $q_{\mathrm{L}} \leq 0.3$ and $q_{\mathrm{L}} \geq 0.8$ are omitted, because in this regime the excitation method tends to deviate from the ideal curve [Hei11].

The data can be well approximated by the respective band calculation confirming the presence

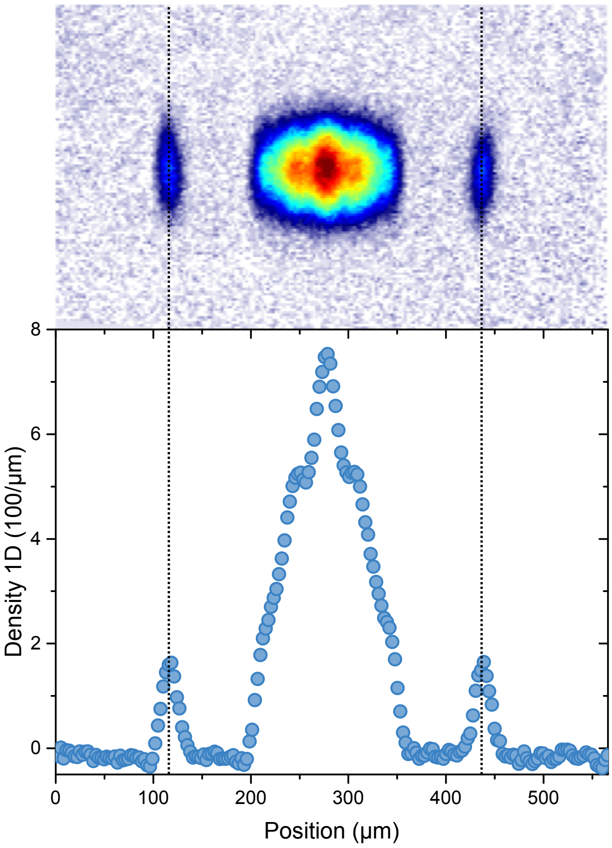

Figure 5.12.: Band excitation in the 660 nm lattice using amplitude modulation. The picture shows a six-component DFG with 75000 atoms in the state-dependent lattice. The intensity was amplitude modulated with 15.5 kHz for 1 ms. The absorption image is taken after band mapping (2 ms) and a TOF of 20 ms. The excitation peaks in the third Brillouin zone are clearly visible. Simultaneously, the first Brillouin zone shows distinct dips caused by hole excitation. We measured a lattice depth of $4.3\,E_\mathrm{r}$.

of an underlying lattice structure. The fits result in lattices depths of $4.3(2)\,E_\mathrm{r}$ and $7.91(1)\,E_\mathrm{r}$. However, these values deviate significantly from a depth estimation based on the measured beam power. The corresponding beam powers for 5.13a and 5.13b were $74\,\mathrm{mW}$ and $109\,\mathrm{mW}$ respectively, which should result in lattice depths of $11\,E_\mathrm{r}$ and $17\,E_\mathrm{r}$. Furthermore, we could not observe a band gap between the first and second excited band, which should definitely be visible based on the frequency step size. Both effects indicate that the lattice geometry deviates severely from the ideal case. One possible reason is the repulsive interaction of fermionic ^{173}Yb, which can lead to an effective lattice depth reduction [Hei11]. With an actual scattering length of $a = 199\,a_0$ however, a deviation to this extent is very unlikely. More probable seems a faulty beam adjustment, which can explain the strong reduction of observed lattice depth and the closing of the band gap [Sko16].

These first measurements show that the lattice setup is principally working, but control over the lattice depth needs to be improved. We are currently working on optimizing this part of the setup by repeating the adjustment of the laser beam and the calibration using a spin-polarized DFG.

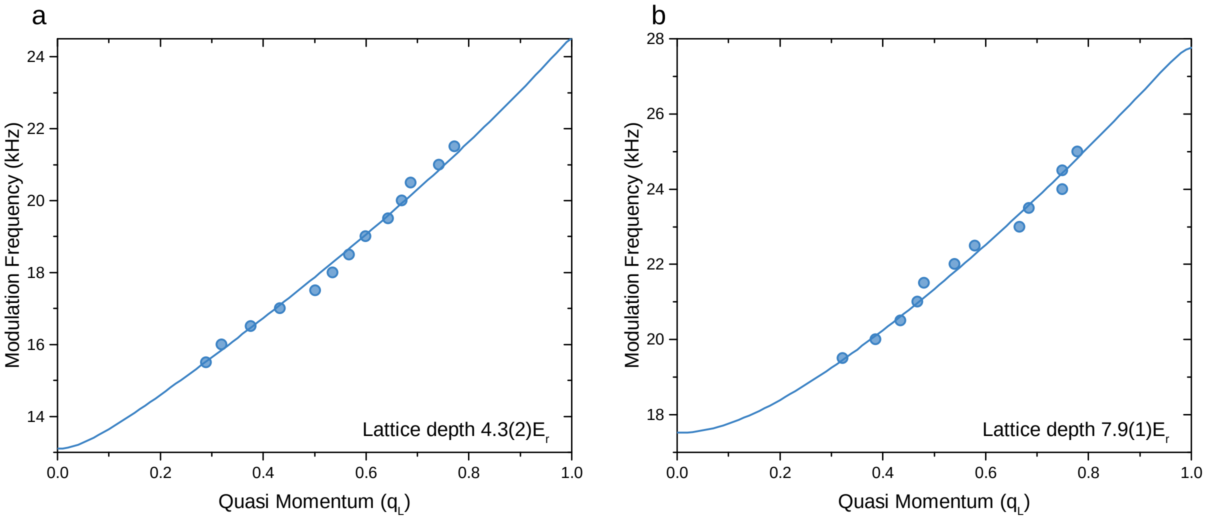

Figure 5.13.: Calibration of the state-dependent lattice. Both plots show the results of a momentum-resolved band spectroscopy with a six-component DFG in the state dependent lattice. For different amplitude-modulation frequencies the quasi momenta q_L are measured using band mapping. The data is compared with a 1D-band-structure calculation (solid, blue lines) to estimate the lattice depth. The data points can be well approximated using the ideal curves. However, the resulting values of $4.3\,E_\mathrm{r}$ and $7.9\,E_\mathrm{r}$ deviate strongly from our expectation based on actual power measurements.

Conclusion

This chapter presented a newly implemented laser setup at a wavelength of $660\,\mathrm{nm}$ for the realization of a state-dependent, optical lattice. At this wavelength the polarization ratio between ground state ${}^1S_0$ and excited state ${}^3P_0$ is about a factor of five. In terms of the recoil energy the output power enables us to reach maximal lattice depths of $49\,E_\mathrm{r}$ for the ground state and $267\,E_\mathrm{r}$ for the excited state. The ratio is large enough to localize the excited states while simultaneously allow ground states to tunnel. This attribute plays an important role in mixed systems, i.e. ground and excited states, because inelastic collisions between excited states need to be suppressed. These kind of samples will be present when simulating the KLM.

After successful calibration of the lattice two more characteristics are necessary to be analyzed. First, a lifetime measurement using an ultracold quantum gas can be used to confirm our estimation concerning parametric heating due to noise of the laser. The comparison to other laser sources, which are well established for producing optical lattices, suggests that the noise level of the state-dependent laser should be suitable for our applications. However, the ultimate prove can only be given by a measurement involving Yb atoms and analysis of the lattice induced heating. Second, efficient excitation of the clock state has to be shown. Estimating the transition broadening due to the AC-Stark shift of the state-dependent lattice, an excitation scheme which relies on a power-broadened π-pulse seems to be unrealistic given a maximum output power of $300\,\mathrm{mW}$. More feasible seems the technique of RAP demonstrated in the previous chapter. Excitation using a frequency sweep should enable us to produce mixtures between ground and meta-stable states. Furthermore, doubly occupied sites, which are spectroscopically shifted due to the exchange interaction, can also be addressed simultaneously.

Outlook

This thesis presented a versatile apparatus for producing ultracold quantum gases with the main focus on the fermionic isotope ^{173}Yb. Using resonant pumping and an OSG scheme, DFGs with arbitrary spin mixtures from one- to six-spin components can be produced and analyzed. For investigation of the Hubbard model beyond alkali metals the Yb quantum gas can be loaded into a 3D triangular optical lattice, where we can choose between a magic ($759\,\mathrm{nm}$) and a state-dependent ($660\,\mathrm{nm}$) lattice. Utilizing an ultra-narrow linewidth clock-laser, we coherently control the lowest lying meta-stable state $^3P_0$. Exploiting this tool we investigate two different many-body systems: 1. Due to the interplay of orbital and spin degree of freedom, an excited two-atom state is either an orbital symmetric spin singlet state $|eg\rangle^+ |{\uparrow\downarrow}\rangle^-$ or orbital antisymmetric spin triplet state $|eg\rangle^- |{\uparrow\downarrow}\rangle^+$ due to the Pauli principle. In this way a new spin-exchange interaction $V_{\text{ex}} = 1/2\,(U_{eg^+} - U_{eg^-})$ emerges, which plays an important role in connection with the KLM. 2. The inelastic collisional properties of the meta-stable state allow us to experimentally realize a dissipative Fermi-Hubbard model. Analyzing the decay dynamics with a two-body loss model we find a fast initial and a slower secondary decay, which we attribute to the emergence of many-body correlations.

One of the next important steps will be the simultaneous cooling of two Yb isotopes. We already demonstrated the MOT capabilities for the most prominent isotopes ^{171}Yb, ^{173}Yb, ^{174}Yb and are currently implementing a variable lock scheme for sequentially loading the 2D MOT into a two-isotope 3D MOT. This process will be essential for creating degenerate gases of ^{171}Yb, because its s-wave scattering length prevents evaporative cooling by itself. Sympathetic cooling schemes with other Yb isotopes could already be demonstrated to be successful [Tai10], where ^{174}Yb seems to be the most feasible cooling partner due to its abundance and best MOT performance. Furthermore, a two-isotope MOT opens up the intriguing research field of ultracold isotope mixtures with possible bose-fermi (^{171}Yb/^{174}Yb or ^{173}Yb/^{174}Yb) and fermi-fermi (^{171}Yb/^{173}Yb) statistics.

One of the future research interests will be to further analyze dissipative systems by continuing loss measurements similar to Chap. 4 and getting a better understanding of the underlying many-body processes. Investigation will concentrate on the preparation of the initial sample and the dependence between losses and spin composition. As was pointed out, preparing the system using RAP results in atoms being left in the ground state. These could possibly reduce tunneling by atomic interaction and hence losses of the excited-state atoms. To rule out any effects caused by the ground-state atoms the preparation method needs to become more efficient. This can possibly be achieved by optimizing the RAP parameters or by elimination of the ground-state atoms via application of a resonant light pulse. The conducted measurements are limited to the cases of two- and six-component mixtures so far. It would be very insightful to investigate, if and how the observed dynamics depend on the type of spin composition and if this causes any change in the $g^{(2)}$ function.

Furthermore, it will be especially interesting to see, if the atom properties of the ^{171}Yb isotope can shift the system towards a loss dominated regime, which is characterized by Zeno-like behavior. As pointed out in Chap. 4 due to the properties of the excited ^{173}Yb state the system dynamics are dominated by atomic interaction, i.e. Mott-insulator behavior. This can be changed by shifting the ratio between the excited-state loss rate Γ_{ee} and Hubbard interaction U_{ee}. The values for Γ_{ee} of ^{171}Yb and ^{173}Yb are of the same order [Lud11], but the s-wave scattering length of ^{171}Yb($^3P_0$) is still unknown. In case of a small scattering length a situation with $\Gamma_{ee} \gg U_{ee}$ could be created, which would enable us to conduct experiments within the Zeno regime (cp. Fig. 4.6). The intermediate regime, where atomic interactions and losses are balanced, is also highly interesting, because it holds the transition between Mott- and Zeno-insulator. It will be fascinating to see, whether this quantum-phase transition can be observed by combining Yb isotopes with measures to tune the atomic interaction, e.g. orbital Feshbach resonances [Höf15, Pag15].

The second topic will address the application of the state-dependent lattice (Chap. 5) for the experimental realization of the KLM. The lattice-laser wavelength is chosen in a way, that ground-state atoms are mobile, while the excited-state atoms are localized simultaneously. In this way inelastic collisions between two excited-state atoms can be suppressed. This model especially exploits the properties of alkaline-earth-like elements by including spin and orbital degrees of freedom and the spin-exchange interaction. Its Hamiltonian can be written in the limit of $U_{gg} = 0$ and $J_e = 0$ as [Gor10]:

$$\hat{\mathcal{H}}_{\text{KLM}} = -\sum_{\langle j,i\rangle m} J_g(c^\dagger_{igm}c_{jgm} + \text{h.c.}) + V_{\text{ex}} \sum_{j,m,m'} c^\dagger_{jgm}c^\dagger_{jem'}c_{jgm'}c_{jem},$$

with ground-state tunneling J_g, the state index $\alpha = \{g, e\}$, the spin index m and creation operator $c^\dagger_{j\alpha m}$ for a state $|\alpha m\rangle$ at site j. Since this description relies on a vanishing ground-state interaction, the ^{171}Yb isotope would be the ideal candidate for simulating this model. ^{173}Yb on the other hand could be used to investigate an extended KLM, which also includes atomic interaction between ground states. Especially the parameter regime between vanishing and large ground-state interaction is highly interesting, because complex quantum phases can be expected, e.g. Kondo- to Mott-insulator transition [Gor10]. Weather the access to this regime can be engineered by interaction-tuning tools, e.g. optical [The04] or orbital Feshbach resonances, will be an exciting challenge.

Depending on the ratio between V_{ex} and J_g two limiting cases can be distinguished. If $|V_{\text{ex}}| \ll J_g$ the ground-state atoms can mediate long-range Ruderman-Kittel-Kasuya-Yosida (RKKY) interaction between localized atoms. In the opposite case $|V_{\text{ex}}| \gg J_g$ the system is dominated by Kondo singlets and favors a heavy-Fermi-liquid. We hope to get a better understanding of these regimes and connected quantum phases by exploiting the tunability of J_g and V_{ex} given by the optical lattice. Particularly the parameter range with comparable RKKY interaction and Kondo effect holds many open questions concerning its phases and phase transitions [Col07, Geg08].

The 1D KLM was theoretically investigated in detail [FF10b], but it lacks any experimental realization to date. Analysis of its phase diagram shows that the emerging phases, i.e. ferromagnetic and paramagnetic, can be reached by changing the filling factor between ground- and excited-state atoms. State preparation using RAP should enable us to use the fraction of excited-state atoms as a tuning knob to experimentally probe the respective phase diagram. Another fascinating question is how the behavior changes when the dimensionality of the system is changed. We have the possibility to also investigate the 2D and 3D KLM, where still many open questions persist, e.g. the paramagnetic and ferromagnetic phases reverse going from 1D to 2D [FF10a].

The key energy scales for the respective phases of the KLM are $k_{\mathrm{B}}T \leq V_{\mathrm{ex}}^2/J_g$ in case of RKKY interaction and $k_{\mathrm{B}}T \leq J_g \exp(-J_g/|V_{\mathrm{ex}}|)$ for the Kondo regime [Gor10]. These can be higher as the superexchange energy J^2/U, which is necessary for magnetic ordering in the Hubbard model [Dua03, Ess10]. Choosing $J_g \lesssim |V_{\mathrm{ex}}|$, for example by means of an optical lattice, energies as high as $|V_{\mathrm{ex}}|$ might suffice to observe the respective phases of the KLM. The exchange energy for ^{171}Yb is not yet determined. Measurements involving a thermal gas of ^{171}Yb in an optical lattice could determine one of the two-particle scattering lengths to be $a_{eg}^{-} \approx -25\, a_0$ [Lem11], which is on the order of the ground-state interaction. It will be highly interesting, whether different regimes of the KLM can be reached with the fermionic Yb isotopes. Additionally, these interactions can be tuned using confinement-induced resonances [Zha16].

In conclusion, ultracold Yb gases constitute a versatile instrument for future investigation of the Fermi-Hubbard and the Kondo-lattice model. Its valuable properties, e.g. an ultra-narrow clock transition, the emergence of spin-exchange interaction or SU($\mathcal{N}$) symmetry, enable novel approaches and lead to new insights beyond well-understood model systems. These properties can be exploited to realize systems with intriguing quantum phenomena like synthetic dimensions, e.g. chiral edge states [Man15], or topological order, e.g. in chiral spin liquids [Her09]. Furthermore, orbital Feshbach resonances can be used for efficient interaction tuning leading to novel phases of Fermi superfluids with exotic order parameters [Zha15]. Yb quantum simulators are ideal tools to study strongly-correlated lattice systems and they constitute an essential approach to understand complex, many-body phenomena in condensed-matter physics.

A. Calculation of $^1S_0$ and $^3P_0$ Polarizabilities

The polarizability of the energetically lowest-lying states $^1S_0$ and $^3P_0$ can be calculated using [Gri00]

$$U_{\text{dip}} = \frac{3\pi c^2 \Gamma}{2\omega_0^2} I \times \sum_j \frac{c_j^2}{\Delta_j},$$

with c speed of light, Γ decay rate, ω_0 resonance frequency, I intensity, c_j^2 line strength, Δ_j detuning. The atomic transitions used for calculating the graph in Fig. 5.1 are shown in Tab. A.1.

Configuration	E^a (cm^{-1})	J	Γ (s^{-1})	τ (s)	Branching Ratio
			$^1S_0$		
$(6s6s)\,^1S_0$	0	0			
$(6s6p)\,^3P_1$	17992.007	1	1.145×10^6	$8.730 \times 10^{-7\,b}$	1
$(6s6p)\,^1P_1$	25068.222	1	1.830×10^8	$5.464 \times 10^{-9\,c}$	1^d
$(7/2, 5/2)\, j = 1$	28857.014	1	6.849×10^7	$1.46 \times 10^{-8\,e}$	1
$(6s7p)\,^1P_1$	40563.97	1	8.696×10^7	$9.2 \times 10^{-9\,e}$	0.80^e
$(6s8p)\,^1P_1$	44017.60	1	1.512×10^7	$4.3 \times 10^{-8\,e}$	0.65^e
$(4f^{13}5d6s^2)$	37414.59	1	$1.18 \times 10^{7\,f}$		
			$^3P_0$		
$(6s6p)\,^3P_0$	17288.439	0			
$(6s5d)\,^3D_1$	24489.102	1	1.679×10^6	$3.80 \times 10^{-7\,g}$	0.638^d
$(6s7s)\,^3S_1$	32694.692	1	9.420×10^6	$1.38 \times 10^{-8\,b}$	0.130^d
$(6s6d)\,^3D_1$	39808.72	1	2.598×10^7	$2.240 \times 10^{-8\,b}$	0.58^e
$(6s8s)\,^3S_1$	41615.04	1	3.971×10^6	$3.4 \times 10^{-8\,e}$	0.135^e
$(6s7d)\,^3D_1$	44311.38	1	1.474×10^7	$3.8 \times 10^{-8\,e}$	0.56^e
$(6p^2)\,^3P_1$	43805.69	1	2.333×10^7	$1.5 \times 10^{-8\,e}$	0.35^e

Table A.1.: Atomic transitions used for calculating the polarizability for the states $^1S_0$ and $^3P_0$. The following symbols are used: E energy of atomic transition, J total angular momentum, Γ decay rate, τ lifetime. The values are taken from: *a* [Kra16], *b* [Bla94], *c* [Tak04], *d* [Por99], *e* [Bar07], *f* [Mor00], *g* [Bow96].

B. Two-Body-Loss Rate Equation

To describe the loss dynamics in a dissipative system with $\mathcal{N}$ spins it is instructive to first write down the rate equation for one spin component m. In the following we assume equal spin distribution $N_m = N_{m'}$. We then obtain:

$$\frac{\mathrm{d}N_m}{\mathrm{d}t} \propto -N_m \sum_{m' \neq m} N_{m'} = -(\mathcal{N}-1)N_m^2, \tag{B.1}$$

with m in the range of $1\,..\,\mathcal{N}$. The total amount of atoms can be written as

$$N_{\text{tot}} = \sum_{m'} N_{m'} = \mathcal{N} N_m, \tag{B.2}$$

Substituting Eq. (B.2) into Eq. (B.1) results in

$$\frac{1}{\mathcal{N}} \frac{\mathrm{d}N_{\text{tot}}}{\mathrm{d}t} \propto -\frac{\mathcal{N}-1}{\mathcal{N}^2} N_{\text{tot}}^2. \tag{B.3}$$

The loss coefficient κ is proportional to the total density η, where we define a component density by

$$\eta = \mathcal{N} \eta_m.$$

This dependence transfers to the loss coefficient with

$$\kappa = \mathcal{N} \kappa_m.$$

Thus, Eq. (B.3) can be written as

$$\frac{\mathrm{d}N_{\text{tot}}}{\mathrm{d}t} = -\frac{\mathcal{N}-1}{\mathcal{N}} \frac{\kappa}{N_0} N_{\text{tot}}^2 = -(\mathcal{N}-1) \frac{\kappa_m}{N_0} N_{\text{tot}}^2,$$

with initial particle number N_0.

Bibliography

[Abe16] B. Abeln, Design, Implementation and Characterization of a new Laser System for Mixtures of Ytterbium Quantum Gases, Master thesis, University of Hamburg, Hamburg (2016).

[Aik12] K. Aikawa, A. Frisch, M. Mark, S. Baier, A. Rietzler, R. Grimm, and F. Ferlaino. Bose-Einstein Condensation of Erbium. *Physical Review Letters* **108**, 210401 (2012).

[Alb03] A. Albus, F. Illuminati, and J. Eisert. Mixtures of bosonic and fermionic atoms in optical lattices. *Physical Review A* **68**, 023606 (2003).

[Aln08] J. Alnis, A. Matveev, N. Kolachevsky, T. Udem, and T. W. Hänsch. Subhertz linewidth diode lasers by stabilization to vibrationally and thermally compensated ultralow-expansion glass Fabry-Pérot cavities. *Physical Review A* **77**, 053809 (2008).

[And95] M. H. Anderson, J. R. Ensher, M. R. Matthews, C. E. Wieman, and E. A. Cornell. Observation of Bose-Einstein Condensation in a Dilute Atomic Vapor. *Science* **269**, 198 (1995).

[App09] J. Appel, A. MacRae, and A. I. Lvovsky. A versatile digital GHz phase lock for external cavity diode lasers. *Measurement Science and Technology* **20**, 055302 (2009).

[Aud97] G. Audi, O. Bersillon, J. Blachot, and A. H. Wapstra. The NUBASE evaluation of nuclear and decay properties. *Nuclear Physics A* **624**, 1 (1997).

[Bai12] S. Baier, An optical dipole trap for Erbium with tunable geometry, Master thesis, University of Innsbruck, Innsbruck (2012).

[Bak09] W. S. Bakr, J. I. Gillen, A. Peng, S. Fölling, and M. Greiner. A quantum gas microscope for detecting single atoms in a Hubbard-regime optical lattice. *Nature* **462**, 74 (2009).

[Bal10] L. Balents. Spin liquids in frustrated magnets. *Nature* **464**, 199 (2010).

[Bar57] J. Bardeen, L. N. Cooper, and J. R. Schrieffer. Microscopic Theory of Superconductivity. *Physical Review* **106**, 162 (1957).

[Bar07] Z. Barber, Ytterbium Optical Lattice Clock, Ph.D. thesis, University of Colorado, Boulder (2007).

[Bar08] Z. W. Barber, J. E. Stalnaker, N. D. Lemke, N. Poli, C. W. Oates, T. M. Fortier, S. A. Diddams, L. Hollberg, C. W. Hoyt, A. V. Taichenachev, and V. I. Yudin. Optical Lattice Induced Light Shifts in an Yb Atomic Clock. *Physical Review Letters* **100**, 103002 (2008).

[Bar13a] C.-E. Bardyn, M. A. Baranov, C. V. Kraus, E. Rico, A. İmamoğlu, P. Zoller, and S. Diehl. Topology by dissipation. *New Journal of Physics* **15**, 085001 (2013).

[Bar13b] G. Barontini, R. Labouvie, F. Stubenrauch, A. Vogler, V. Guarrera, and H. Ott. Controlling the Dynamics of an Open Many-Body Quantum System with Localized Dissipation. *Physical Review Letters* **110**, 035302 (2013).

[Bau10] S. K. Baur and E. J. Mueller. Two-body recombination in a quantum-mechanical lattice gas: Entropy generation and probing of short-range magnetic correlations. *Physical Review A* **82**, 023626 (2010).

[Bec08] C. Becker, Multi component Bose-Einstein Condensates, Ph.D. thesis, University of Hamburg, Hamburg (2008).

[Bec10] C. Becker, P. Soltan-Panahi, J. Kronjäger, S. Dörscher, K. Bongs, and K. Sengstock. Ultracold quantum gases in triangular optical lattices. *New Journal of Physics* **12**, 065025 (2010).

[Ber00] G. Berden, R. Peeters, and G. Meijer. Cavity ring-down spectroscopy: Experimental schemes and applications. *International Reviews in Physical Chemistry* **19**, 565 (2000).

[Bia16] W. Bian, Y. Huang, H. Guan, P. Liu, L. Ma, and K. Gao. 1 Hz linewidth Ti:Sapphire laser as local oscillator for $^{40}Ca^{+}$ optical clocks. *Review of Scientific Instruments* **87**, 063121 (2016).

[Bjo83] G. C. Bjorklund, M. D. Levenson, W. Lenth, and C. Ortiz. Frequency modulation (FM) spectroscopy. *Applied Physics B* **32**, 145 (1983).

[Bla94] K. B. Blagoev and V. A. Komarovskii. Lifetimes of Levels of Neutral and Singly Ionized Lanthanide Atoms. *Atomic Data and Nuclear Data Tables* **56**, 1 (1994).

[Bla01] E. D. Black. An introduction to Pound–Drever–Hall laser frequency stabilization. *American Journal of Physics* **69**, 79 (2001).

[Bla07] P. B. Blakie, A. Bezett, and P. Buonsante. Degenerate Fermi gas in a combined harmonic-lattice potential. *Physical Review A* **75**, 063609 (2007).

[Blo05] I. Bloch. Ultracold quantum gases in optical lattices. *Nature Physics* **1**, 23 (2005).

[Blo08] I. Bloch, J. Dalibard, and W. Zwerger. Many-body physics with ultracold gases. *Reviews of Modern Physics* **80**, 885 (2008).

[Blo14] B. J. Bloom, T. L. Nicholson, J. R. Williams, S. L. Campbell, M. Bishof, X. Zhang, W. Zhang, S. L. Bromley, and J. Ye. An optical lattice clock with accuracy and stability at the 10^{-18} level. *Nature* **506**, 71 (2014).

[Bol16] M. Boll, T. A. Hilker, G. Salomon, A. Omran, J. Nespolo, L. Pollet, I. Bloch, and C. Gross. Spin- and density-resolved microscopy of antiferromagnetic correlations in Fermi-Hubbard chains. *Science* **353**, 1257 (2016).

[Bow96] C. J. Bowers, D. Budker, E. D. Commins, D. DeMille, S. J. Freedman, A.-T. Nguyen, S.-Q. Shang, and M. Zolotorev. Experimental investigation of excited-state lifetimes in atomic ytterbium. *Physical Review A* **53**, 3103 (1996).

[Bow99] C. J. Bowers, D. Budker, S. J. Freedman, G. Gwinner, J. E. Stalnaker, and D. DeMille. Experimental investigation of the $6s^2\ {}^1S_0 \rightarrow 5d6s\ {}^3D_{1,2}$ forbidden transitions in atomic ytterbium. *Physical Review A* **59**, 3513 (1999).

[Boy07] M. M. Boyd, High Precision Spectroscopy of Strontium in an Optical Lattice: Towards a New Standard for Frequency and Time, Ph.D. thesis, University of Colorado, Boulder (2007).

[Brz02] T. M. Brzozowski, M. Maczynska, M. Zawada, J. Zachorowski, and W. Gawlik. Time-of-flight measurement of the temperature of cold atoms for short trap-probe beam distances. *Journal of Optics B: Quantum and Semiclassical Optics* **4**, 62 (2002).

[Cap14] G. Cappellini, M. Mancini, G. Pagano, P. Lombardi, L. Livi, M. Siciliani de Cumis, P. Cancio, M. Pizzocaro, D. Calonico, F. Levi, C. Sias, J. Catani, M. Inguscio, and L. Fallani. Direct Observation of Coherent Interorbital Spin-Exchange Dynamics. *Physical Review Letters* **113**(12), 120402 (2014).

[Cat98] F. S. Cataliotti, E. A. Cornell, C. Fort, M. Inguscio, F. Marin, M. Prevedelli, L. Ricci, and G. M. Tino. Magneto-optical trapping of Fermionic potassium atoms. *Physical Review A* **57**, 1136 (1998).

[Caz09] M. A. Cazalilla, A. F. Ho, and M. Ueda. Ultracold gases of ytterbium: ferromagnetism and Mott states in an SU(6) Fermi system. *New Journal of Physics* **11**, 103033 (2009).

[Caz14] M. A. Cazalilla and A. M. Rey. Ultracold Fermi gases with emergent SU(N) symmetry. *Reports on Progress in Physics* **77**, 124401 (2014).

[Che16] G. Chen, K. R. A. Hazzard, A. M. Rey, and M. Hermele. Synthetic-gauge-field stabilization of the chiral-spin-liquid phase. *Physical Review A* **93**, 061601 (2016).

[Chi10] C. Chin, R. Grimm, P. Julienne, and E. Tiesinga. Feshbach resonances in ultracold gases. *Reviews of Modern Physics* **82**, 1225 (2010).

[Cho12] J. W. Cho, H.-g. Lee, S. Lee, J. Ahn, W.-K. Lee, D.-H. Yu, S. K. Lee, and C. Y. Park. Optical repumping of triplet-P states enhances magneto-optical trapping of ytterbium atoms. *Physical Review A* **85**, 035401 (2012).

[Col06] P. Coleman. Heavy Fermions: electrons at the edge of magnetism (2006). ArXiv: cond-mat/0612006.

[Col07] P. Coleman. Handbook of Magnetism and Advanced Magnetic Materials Vol. 1. Wiley (2007).

[Col14] Y. Colombe, D. H. Slichter, A. C. Wilson, D. Leibfried, and D. J. Wineland. Single-mode optical fiber for high-power, low-loss UV transmission. *Optics Express* **22**, 19783 (2014).

[Con26] E. Condon. A Theory of Intensity Distribution in Band Systems. *Physical Review* **28**, 1182 (1926).

[Coo56] L. N. Cooper. Bound Electron Pairs in a Degenerate Fermi Gas. *Physical Review* **104**, 1189 (1956).

[Dal08] A. J. Daley, M. M. Boyd, J. Ye, and P. Zoller. Quantum Computing with Alkaline-Earth-Metal Atoms. *Physical Review Letters* **101**, 170504 (2008).

[Dal11] J. Dalibard, F. Gerbier, G. Juzeliūnas, and P. Öhberg. Colloquium: Artificial gauge potentials for neutral atoms. *Reviews of Modern Physics* **83**, 1523 (2011).

[Das05] D. Das, S. Barthwal, A. Banerjee, and V. Natarajan. Absolute frequency measurements in Yb with 0.08ppb uncertainty: Isotope shifts and hyperfine structure in the 399nm $^1S_0 \rightarrow {}^1P_1$ line. *Physical Review A* **72**, 032506 (2005).

[Dav95] K. B. Davis, M. O. Mewes, M. R. Andrews, N. J. van Druten, D. S. Durfee, D. M. Kurn, and W. Ketterle. Bose-Einstein Condensation in a Gas of Sodium Atoms. *Physical Review Letters* **75**, 3969 (1995).

[dE09] Y. N. M. de Escobar, P. G. Mickelson, M. Yan, B. J. DeSalvo, S. B. Nagel, and T. C. Killian. Bose-Einstein Condensation of ^{84}Sr. *Physical Review Letters* **103**, 200402 (2009).

[Deb12] P. Debye. Zur Theorie der spezifischen Wärmen. *Annalen der Physik* **344**, 789 (1912).

[DeM99] B. DeMarco and D. S. Jin. Onset of Fermi Degeneracy in a Trapped Atomic Gas. *Science* **285**, 1703 (1999).

[DeM01a] B. DeMarco, Quantum Behavior of an Atomic Fermi Gas, Ph.D. thesis, University of Colorado, Boulder (2001).

[DeM01b] B. DeMarco, S. B. Papp, and D. S. Jin. Pauli Blocking of Collisions in a Quantum Degenerate Atomic Fermi Gas. *Physical Review Letters* **86**, 5409 (2001).

[Dem15] W. Demtröder. Laser Spectroscopy 2: Experimental Techniques. Springer, Heidelberg, 5th edition (2015), ISBN 978-3-662-44641-6.

[DeS10] B. J. DeSalvo, M. Yan, P. G. Mickelson, Y. N. Martinez de Escobar, and T. C. Killian. Degenerate Fermi Gas of ^{87}Sr. *Physical Review Letters* **105**, 030402 (2010).

[Die08] S. Diehl, A. Micheli, A. Kantian, B. Kraus, H. P. Büchler, and P. Zoller. Quantum states and phases in driven open quantum systems with cold atoms. *Nature Physics* **4**, 878 (2008).

[Die11] S. Diehl, E. Rico, M. A. Baranov, and P. Zoller. Topology by dissipation in atomic quantum wires. *Nature Physics* **7**, 971 (2011).

[Din99] T. P. Dinneen, K. R. Vogel, E. Arimondo, J. L. Hall, and A. Gallagher. Cold collisions of Sr*-Sr in a magneto-optical trap. *Physical Review A* **59**, 1216 (1999).

[Don77] S. Doniach. The Kondo lattice and weak antiferromagnetism. *Physica B+C* **91**, 231 (1977).

[Dör13a] S. Dörscher, Creation of ytterbium quantum gases with a compact 2D-/3D-MOT setup, Ph.D. thesis, Universität Hamburg, Hamburg (2013).

[Dör13b] S. Dörscher, A. Thobe, B. Hundt, A. Kochanke, R. Le Targat, P. Windpassinger, C. Becker, and K. Sengstock. Creation of quantum-degenerate gases of ytterbium in a compact 2D-/3D-magneto-optical trap setup. *Review of Scientific Instruments* **84**, 043109 (2013).

[Dre83] R. W. P. Drever, J. L. Hall, F. V. Kowalski, J. Hough, G. M. Ford, A. J. Munley, and H. Ward. Laser phase and frequency stabilization using an optical resonator. *Applied Physics B* **31**, 97 (1983).

[Dua03] L.-M. Duan, E. Demler, and M. D. Lukin. Controlling Spin Exchange Interactions of Ultracold Atoms in Optical Lattices. *Physical Review Letters* **91**, 090402 (2003).

[Ein05] A. Einstein. Über einen die Erzeugung und Verwandlung des Lichtes betreffenden heuristischen Gesichtspunkt. *Annalen der Physik* **322**, 132 (1905).

[Erh04] M. Erhard, Experimente mit mehrkomponentigen Bose-Einstein-Kondensaten, Ph.D. thesis, University of Hamburg, Hamburg (2004).

[Esc03] J. Eschner, G. Morigi, F. Schmidt-Kaler, and R. Blatt. Laser cooling of trapped ions. *Journal of the Optical Society of America B* **20**, 1003 (2003).

[Ess10] T. Esslinger. Fermi-Hubbard Physics with Atoms in an Optical Lattice. *Annual Review of Condensed Matter Physics* **1**, 129 (2010).

[Fey82] R. P. Feynman. Simulating physics with computers. *International Journal of Theoretical Physics* **21**, 467 (1982).

[FF10a] M. Foss-Feig, M. Hermele, V. Gurarie, and A. M. Rey. Heavy fermions in an optical lattice. *Physical Review A* **82**, 053624 (2010).

[FF10b] M. Foss-Feig, M. Hermele, and A. M. Rey. Probing the Kondo lattice model with alkaline-earth-metal atoms. *Physical Review A* **81**, 051603 (2010).

[FF12] M. Foss-Feig, A. J. Daley, J. K. Thompson, and A. M. Rey. Steady-State Many-Body Entanglement of Hot Reactive Fermions. *Physical Review Letters* **109**, 230501 (2012).

[Flä16] N. Fläschner, B. S. Rem, M. Tarnowski, D. Vogel, D.-S. Lühmann, K. Sengstock, and C. Weitenberg. Experimental reconstruction of the Berry curvature in a Floquet Bloch band. *Science* **352**, 1091 (2016).

[Föl07] S. Fölling, S. Trotzky, P. Cheinet, M. Feld, R. Saers, A. Widera, T. Müller, and I. Bloch. Direct observation of second-order atom tunnelling. *Nature* **448**, 1029 (2007).

[Fre17] L. Freystatzky, In preparation, Bachelor thesis, University of Hamburg, Hamburg (2017).

[Fuk07] T. Fukuhara, Y. Takasu, M. Kumakura, and Y. Takahashi. Degenerate Fermi Gases of Ytterbium. *Physical Review Letters* **98**, 030401 (2007).

[Fuk09] T. Fukuhara, S. Sugawa, M. Sugimoto, S. Taie, and Y. Takahashi. Mott insulator of ultracold alkaline-earth-metal-like atoms. *Physical Review A* **79**, 041604 (2009).

[Gad09] B. Gadway, D. Pertot, R. Reimann, M. G. Cohen, and D. Schneble. Analysis of Kapitza-Dirac diffraction patterns beyond the Raman-Nath regime. *Optics Express* **17**, 19173 (2009).

[Gaë09] A. Gaëtan, Y. Miroshnychenko, T. Wilk, A. Chotia, M. Viteau, D. Comparat, P. Pillet, A. Browaeys, and P. Grangier. Observation of collective excitation of two individual atoms in the Rydberg blockade regime. *Nature Physics* **5**, 115 (2009).

[Geg08] P. Gegenwart, Q. Si, and F. Steglich. Quantum criticality in heavy-fermion metals. *Nature Physics* **4**, 186 (2008).

[Geo14] I. M. Georgescu, S. Ashhab, and F. Nori. Quantum simulation. *Reviews of Modern Physics* **86**(1), 153 (2014).

[Ger22] W. Gerlach and O. Stern. Der experimentelle Nachweis der Richtungsquantelung im Magnetfeld. *Zeitschrift für Physik* **9**, 349 (1922).

[Ger10] F. Gerbier and J. Dalibard. Gauge fields for ultracold atoms in optical superlattices. *New Journal of Physics* **12**, 033007 (2010).

[Gio08] S. Giorgini, L. P. Pitaevskii, and S. Stringari. Theory of ultracold atomic Fermi gases. *Reviews of Modern Physics* **80**, 1215 (2008).

[Gor09] A. V. Gorshkov, A. M. Rey, A. J. Daley, M. M. Boyd, J. Ye, P. Zoller, and M. D. Lukin. Alkaline-Earth-Metal Atoms as Few-Qubit Quantum Registers. *Physical Review Letters* **102**, 110503 (2009).

[Gor10] A. V. Gorshkov, M. Hermele, V. Gurarie, C. Xu, P. S. Julienne, J. Ye, P. Zoller, E. Demler, M. D. Lukin, and A. M. Rey. Two-orbital SU(N) magnetism with ultracold alkaline-earth atoms. *Nature Physics* **6**, 289 (2010).

[GR09] J. J. García-Ripoll, S. Dürr, N. Syassen, D. M. Bauer, M. Lettner, G. Rempe, and J. I. Cirac. Dissipation-induced hard-core boson gas in an optical lattice. *New Journal of Physics* **11**, 013053 (2009).

[Gre01] M. Greiner, I. Bloch, O. Mandel, T. W. Hänsch, and T. Esslinger. Exploring Phase Coherence in a 2D Lattice of Bose-Einstein Condensates. *Physical Review Letters* **87**, 160405 (2001).

[Gre02] M. Greiner, O. Mandel, T. Esslinger, T. W. Hänsch, and I. Bloch. Quantum phase transition from a superfluid to a Mott insulator in a gas of ultracold atoms. *Nature* **415**, 39 (2002).

[Gre08] M. Greiner and S. Fölling. Condensed-matter physics: Optical lattices. *Nature* **453**, 736 (2008).

[Gre13] D. Greif, T. Uehlinger, G. Jotzu, L. Tarruell, and T. Esslinger. Short-Range Quantum Magnetism of Ultracold Fermions in an Optical Lattice. *Science* **340**, 1307 (2013).

[Gri00] R. Grimm, M. Weidemüller, and Y. B. Ovchinnikov, Optical Dipole Traps for Neutral Atoms, in Advances In Atomic, Molecular, and Optical Physics, volume 42, editor Benjamin Bederson and Herbert Walther, pp. 95–170, Academic Press (2000), ISBN 1049-250X.

[Gri05a] A. Griesmaier, J. Werner, S. Hensler, J. Stuhler, and T. Pfau. Bose-Einstein Condensation of Chromium. *Physical Review Letters* **94**, 160401 (2005).

[Gri05b] A. Griessner, A. J. Daley, D. Jaksch, and P. Zoller. Fault-tolerant dissipative preparation of atomic quantum registers with fermions. *Physical Review A* **72**, 032332 (2005).

[Häf15] S. Häfner, Ultra-Stabile Lasersysteme für Weltraum- und Bodenanwendungen, Ph.D. thesis, University of Hanover, Hannover (2015).

[Hal12] P. Halder, C.-Y. Yang, and A. Hemmerich. Alternative route to Bose-Einstein condensation of two-electron atoms. *Physical Review A* **85**, 031603 (2012).

[Ham98] S. E. Hamann, D. L. Haycock, G. Klose, P. H. Pax, I. H. Deutsch, and P. S. Jessen. Resolved-Sideband Raman Cooling to the Ground State of an Optical Lattice. *Physical Review Letters* **80**, 4149 (1998).

[Har89] D. C. Harris and M. D. Bertolucci. Symmetry and Spectroscopy. Dover Publications (1989), ISBN 978-0-486-66144-5.

[Hay16] W. M. Haynes. CRC Handbook of Chemistry and Physics. CRC Press, 97th edition (2016), ISBN 978-1-4987-5428-6.

[Hei11] J. Heinze, S. Götze, J. S. Krauser, B. Hundt, N. Fläschner, D.-S. Lühmann, C. Becker, and K. Sengstock. Multiband Spectroscopy of Ultracold Fermions: Observation of Reduced Tunneling in Attractive Bose-Fermi Mixtures. *Physical Review Letters* **107**, 135303 (2011).

[Her09] M. Hermele, V. Gurarie, and A. M. Rey. Mott Insulators of Ultracold Fermionic Alkaline Earth Atoms: Underconstrained Magnetism and Chiral Spin Liquid. *Physical Review Letters* **103**, 135301 (2009).

[Her11] M. Hermele and V. Gurarie. Topological liquids and valence cluster states in two-dimensional SU(N) magnets. *Physical Review B* **84**, 174441 (2011).

[Hil17] L. Hilbig, Simulation for optimization of a 2-dimensional magneto-optical trap with ytterbium, Bachelor thesis, University of Hamburg, Hamburg (2017).

[Hin13] N. Hinkley, J. A. Sherman, N. B. Phillips, M. Schioppo, N. D. Lemke, K. Beloy, M. Pizzocaro, C. W. Oates, and A. D. Ludlow. An Atomic Clock with 10^{-18} Instability. *Science* **341**, 1215 (2013).

[Höf15] M. Höfer, L. Riegger, F. Scazza, C. Hofrichter, D. R. Fernandes, M. M. Parish, J. Levinsen, I. Bloch, and S. Fölling. Observation of an Orbital Interaction-Induced Feshbach Resonance in ^{173}Yb. *Physical Review Letters* **115**, 265302 (2015).

[Hol00] M. J. Holland, B. DeMarco, and D. S. Jin. Evaporative cooling of a two-component degenerate Fermi gas. *Physical Review A* **61**, 053610 (2000).

[Hon99] K. Honda, Y. Takahashi, T. Kuwamoto, M. Fujimoto, K. Toyoda, K. Ishikawa, and T. Yabuzaki. Magneto-optical trapping of Yb atoms and a limit on the branching ratio of the $^1P_1$ state. *Physical Review A* **59**, R934 (1999).

[Hon02] K. Honda, Y. Takasu, T. Kuwamoto, M. Kumakura, Y. Takahashi, and T. Yabuzaki. Optical dipole force trapping of a fermion-boson mixture of ytterbium isotopes. *Physical Review A* **66**, 021401 (2002).

[Hun16] B. Hundt, Optical Potentials for the Realization of Dissipative Fermi-Hubbard Models with Ultracold Ytterbium Atoms, Ph.D. thesis, University of Hamburg, Hamburg (2016).

[Isa15] L. Isaev and A. M. Rey. Heavy-Fermion Valence-Bond Liquids in Ultracold Atoms: Cooperation of the Kondo Effect and Geometric Frustration. *Physical Review Letters* **115**, 165302 (2015).

[Ita90] W. M. Itano, D. J. Heinzen, J. J. Bollinger, and D. J. Wineland. Quantum Zeno effect. *Physical Review A* **41**, 2295 (1990).

[Jak98] D. Jaksch, C. Bruder, J. I. Cirac, C. W. Gardiner, and P. Zoller. Cold Bosonic Atoms in Optical Lattices. *Physical Review Letters* **81**, 3108 (1998).

[Jak05] D. Jaksch and P. Zoller. The cold atom Hubbard toolbox. *Annals of Physics* **315**, 52 (2005).

[Jáu01] R. Jáuregui, N. Poli, G. Roati, and G. Modugno. Anharmonic parametric excitation in optical lattices. *Physical Review A* **64**, 033403 (2001).

[Jo12] G.-B. Jo, J. Guzman, C. K. Thomas, P. Hosur, A. Vishwanath, and D. M. Stamper-Kurn. Ultracold Atoms in a Tunable Optical Kagome Lattice. *Physical Review Letters* **108**, 045305 (2012).

[Joh98] T. F. Johnston. Beam propagation (M^2) measurement made as easy as it gets: the four-cuts method. *Applied Optics* **37**, 4840 (1998).

[Jör08] R. Jördens, N. Strohmaier, K. Günter, H. Moritz, and T. Esslinger. A Mott insulator of fermionic atoms in an optical lattice. *Nature* **455**, 204 (2008).

[Jot14] G. Jotzu, M. Messer, R. Desbuquois, M. Lebrat, T. Uehlinger, D. Greif, and T. Esslinger. Experimental realization of the topological Haldane model with ultracold fermions. *Nature* **515**, 237 (2014).

[Kaw15] A. Kawasaki, B. Braverman, Q. Yu, and V. Vuletic. Two-color magneto-optical trap with small magnetic field for ytterbium. *Journal of Physics B: Atomic, Molecular and Optical Physics* **48**, 155302 (2015).

[Ket08] W. Ketterle and M. W. Zwierlein. Making, probing and understanding ultracold Fermi gases (2008). ArXiv:0801.2500.

[Kit08] M. Kitagawa, K. Enomoto, K. Kasa, Y. Takahashi, R. Ciuryło, P. Naidon, and P. S. Julienne. Two-color photoassociation spectroscopy of ytterbium atoms and the precise determinations of s-wave scattering lengths. *Physical Review A* **77**, 012719 (2008).

[Kle97] K. F. Klein, P. Schließmann, E. Smolka, G. Hillrichs, M. Belz, W. J. O. Boyle, and K. T. V. Grattan. UV-stabilized silica-based fibre for applications around 200nm wavelength. *Sensors and Actuators B: Chemical* **39**, 305 (1997).

[Koe87] J. M. V. A. Koelman, H. T. C. Stoof, B. J. Verhaar, and J. T. M. Walraven. Spin-polarized deuterium in magnetic traps. *Physical Review Letters* **59**, 676 (1987).

[Köh05] M. Köhl, H. Moritz, T. Stöferle, K. Günter, and T. Esslinger. Fermionic Atoms in a Three Dimensional Optical Lattice: Observing Fermi Surfaces, Dynamics, and Interactions. *Physical Review Letters* **94**, 080403 (2005).

[Kol06] C. Kollath, A. Iucci, I. P. McCulloch, and T. Giamarchi. Modulation spectroscopy with ultracold fermions in an optical lattice. *Physical Review A* **74**, 041604 (2006).

[Kol16] S. Kolkowitz, I. Pikovski, N. Langellier, M. D. Lukin, R. L. Walsworth, and J. Ye. Gravitational wave detection with optical lattice atomic clocks. *Physical Review D* **94**(12), 124043 (2016).

[Kra09] S. Kraft, F. Vogt, O. Appel, F. Riehle, and U. Sterr. Bose-Einstein Condensation of Alkaline Earth Atoms: ^{40}Ca. *Physical Review Letters* **103**, 130401 (2009).

[Kra16] A. Kramida, Y. Ralchenko, J. Reader, and N. A. T. (2015), NIST Atomic Spectra Database (ver. 5.3) (2016).

[Lee06] P. A. Lee, N. Nagaosa, and X.-G. Wen. Doping a Mott insulator: Physics of high-temperature superconductivity. *Reviews of Modern Physics* **78**, 17 (2006).

[Lee15] J. Lee, J. H. Lee, J. Noh, and J. Mun. Core-shell magneto-optical trap for alkaline-earth-metal-like atoms. *Physical Review A* **91**, 053405 (2015).

[Lei03] D. Leibfried, R. Blatt, C. Monroe, and D. Wineland. Quantum dynamics of single trapped ions. *Reviews of Modern Physics* **75**, 281 (2003).

[Lem11] N. D. Lemke, J. von Stecher, J. A. Sherman, A. M. Rey, C. W. Oates, and A. D. Ludlow. *p*-Wave Cold Collisions in an Optical Lattice Clock. *Physical Review Letters* **107**, 103902 (2011).

[Let95] V. S. Letokhov, M. A. Ol'shanii, and Y. B. Ovchinnikov. Laser cooling of atoms: a review. *Quantum and Semiclassical Optics: Journal of the European Optical Society Part B* **7**, 5 (1995).

[Lew07] M. Lewenstein, A. Sanpera, V. Ahufinger, B. Damski, A. Sen(De), and U. Sen. Ultracold atomic gases in optical lattices: mimicking condensed matter physics and beyond. *Advances in Physics* **56**, 243 (2007).

[Li12] L. Li, F. Liu, C. Wang, and L. Chen. Measurement and control of residual amplitude modulation in optical phase modulation. *Review of Scientific Instruments* **83**, 043111 (2012).

[Lin09] Y.-J. Lin, R. L. Compton, K. Jiménez-García, J. V. Porto, and I. B. Spielman. Synthetic magnetic fields for ultracold neutral atoms. *Nature* **462**(7273), 628 (2009).

[Liu04] W. V. Liu, F. Wilczek, and P. Zoller. Spin-dependent Hubbard model and a quantum phase transition in cold atoms. *Physical Review A* **70**, 033603 (2004).

[Lü01] B. Lü and X. Ji. Focal shift in Gaussian beams focused by a spherically aberrated bifocal lens. *Optics Communications* **189**, 47 (2001).

[Lu11] M. Lu, N. Q. Burdick, S. H. Youn, and B. L. Lev. Strongly Dipolar Bose-Einstein Condensate of Dysprosium. *Physical Review Letters* **107**, 190401 (2011).

[Lud07] A. D. Ludlow, X. Huang, M. Notcutt, T. Zanon-Willette, S. M. Foreman, M. M. Boyd, S. Blatt, and J. Ye. Compact, thermal-noise-limited optical cavity for diode laser stabilization at 10^{-15}. *Optics Letters* **32**, 641 (2007).

[Lud11] A. D. Ludlow, N. D. Lemke, J. A. Sherman, C. W. Oates, G. Quéméner, J. von Stecher, and A. M. Rey. Cold-collision-shift cancellation and inelastic scattering in a Yb optical lattice clock. *Physical Review A* **84**, 052724 (2011).

[Luo10] X. Luo, P. Chen, and Y. Wang. Power content M^2-values smaller than one. *Applied Physics B* **98**, 181 (2010).

[Ma94] L.-S. Ma, P. Jungner, J. Ye, and J. L. Hall. Delivering the same optical frequency at two places: accuratecancellation of phase noise introduced by an optical fiber or other time-varyingpath. *Optics Letters* **19**, 1777 (1994).

[Man15] M. Mancini, G. Pagano, G. Cappellini, L. Livi, M. Rider, J. Catani, C. Sias, P. Zoller, M. Inguscio, M. Dalmonte, and L. Fallani. Observation of chiral edge states with neutral fermions in synthetic Hall ribbons. *Science* **349**, 1510 (2015).

[Mar93] L. Marcassa, V. Bagnato, Y. Wang, C. Tsao, J. Weiner, O. Dulieu, Y. B. Band, and P. S. Julienne. Collisional loss rate in a magneto-optical trap for sodium atoms: Light-intensity dependence. *Physical Review A* **47**, R4563 (1993).

[Mat98] N. D. Mathur, F. M. Grosche, S. R. Julian, I. R. Walker, D. M. Freye, R. K. W. Haselwimmer, and G. G. Lonzarich. Magnetically mediated superconductivity in heavy fermion compounds. *Nature* **394**, 39 (1998).

[Maz16] A. Mazurenko, C. S. Chiu, G. Ji, M. F. Parsons, M. Kanász-Nagy, R. Schmidt, F. Grusdt, E. Demler, D. Greif, and M. Greiner. Experimental realization of a long-range antiferromagnet in the Hubbard model with ultracold atoms (2016). ArXiv: 1612.08436.

[Mes81] A. Messiah. Quantum Mechanics (Volume II). North Holland Publishing, 12th edition (1981).

[Met99] H. J. Metcalf. Laser Cooling and Trapping. Springer (1999), ISBN 978-1-4612-1470-0.

[Mis77] B. Misra and E. C. G. Sudarshan. The Zeno's paradox in quantum theory. *Journal of Mathematical Physics* **18**, 756 (1977).

[Mon90] C. Monroe, W. Swann, H. Robinson, and C. Wieman. Very cold trapped atoms in a vapor cell. *Physical Review Letters* **65**, 1571 (1990).

[Mor00] D. C. Morton. Atomic Data for Resonance Absorption Lines. II. Wavelengths Longward of the Lyman Limit for Heavy Elements. *The Astrophysical Journal Supplement Series* **130**, 403 (2000).

[Mor03] H. Moritz, T. Stöferle, M. Köhl, and T. Esslinger. Exciting Collective Oscillations in a Trapped 1D Gas. *Physical Review Letters* **91**, 250402 (2003).

[Muk03] T. Mukaiyama, H. Katori, T. Ido, Y. Li, and M. Kuwata-Gonokami. Recoil-Limited Laser Cooling of ^{87}Sr Atoms near the Fermi Temperature. *Physical Review Letters* **90**, 113002 (2003).

[Nak15] M. Nakagawa and N. Kawakami. Laser-Induced Kondo Effect in Ultracold Alkaline-Earth Fermions. *Physical Review Letters* **115**, 165303 (2015).

[Nie10] M. A. Nielsen and I. L. Chuang. Quantum computation and quantum information. Cambridge Univ. Press, Cambridge, 10th edition (2010), ISBN 9786612967290.

[Not05] M. Notcutt, L.-S. Ma, J. Ye, and J. L. Hall. Simple and compact 1-Hz laser system via an improved mounting configuration of a reference cavity. *Optics Letters* **30**, 1815 (2005).

[Öls12] M. Ölschläger, G. Wirth, T. Kock, and A. Hemmerich. Topologically Induced Avoided Band Crossing in an Optical Checkerboard Lattice. *Physical Review Letters* **108**, 075302 (2012).

[Öls13] M. Ölschläger, T. Kock, G. Wirth, A. Ewerbeck, C. M. Smith, and A. Hemmerich. Interaction-induced chiral $p_\mathrm{x} \pm ip_\mathrm{y}$ superfluid order of bosons in an optical lattice. *New Journal of Physics* **15**, 083041 (2013).

[Pag14] G. Pagano, Many-body physics with Ytterbium Fermi gases in optical lattices: from one-dimensional systems to orbital magnetism, Ph.D. thesis, Scuola normale superiore Pisa, Pisa (2014).

[Pag15] G. Pagano, M. Mancini, G. Cappellini, L. Livi, C. Sias, J. Catani, M. Inguscio, and L. Fallani. Strongly Interacting Gas of Two-Electron Fermions at an Orbital Feshbach Resonance. *Physical Review Letters* **115**, 265301 (2015).

[Pan09] K. Pandey, A. K. Singh, P. V. K. Kumar, M. V. Suryanarayana, and V. Natarajan. Isotope shifts and hyperfine structure in the 555.8nm $^1\mathrm{S}_0 \rightarrow {}^3\mathrm{P}_1$ line of Yb. *Physical Review A* **80**, 022518 (2009).

[Par13] C. Y. Park, D.-H. Yu, W.-K. Lee, S. E. Park, E. B. Kim, S. K. Lee, J. W. Cho, T. H. Yoon, J. Mun, S. J. Park, T. Y. Kwon, and S.-B. Lee. Absolute frequency measurement of $^1\mathrm{S}_0$ (F = 1/2) $\rightarrow$ $^3\mathrm{P}_0$ (F = 1/2) transition of ^{171}Yb atoms in a one-dimensional optical lattice at KRISS. *Metrologia* **50**, 119 (2013).

[Par16] M. F. Parsons, A. Mazurenko, C. S. Chiu, G. Ji, D. Greif, and M. Greiner. Site-resolved measurement of the spin-correlation function in the Fermi-Hubbard model. *Science* **353**, 1253 (2016).

[Pet14] N. Petersen, Aufbau und Charakterisierung eines optischen Dreiecksgitters für Ytterbium, Master thesis, University of Hamburg, Hamburg (2014).

[Pla01] M. Planck. Über das Gesetz der Energieverteilung im Normalspectrum. *Annalen der Physik* **309**, 553 (1901).

[Pon17] T. Ponath, In preparation, Ph.D. thesis, University of Hamburg, Hamburg (2017).

[Por99] S. G. Porsev, Y. G. Rakhlina, and M. G. Kozlov. Electric-dipole amplitudes, lifetimes, and polarizabilities of the low-lying levels of atomic ytterbium. *Physical Review A* **60**(4), 2781 (1999).

[Pre16] A. Prehn, M. Ibrügger, R. Glöckner, G. Rempe, and M. Zeppenfeld. Optoelectrical Cooling of Polar Molecules to Submillikelvin Temperatures. *Physical Review Letters* **116**, 063005 (2016).

[Pri83] D. E. Pritchard. Cooling Neutral Atoms in a Magnetic Trap for Precision Spectroscopy. *Physical Review Letters* **51**, 1336 (1983).

[Pu98] J. Pu and H. Zhang. Intensity distribution of Gaussian beams focused by a lens with spherical aberration. *Optics Communications* **151**, 331 (1998).

[Ran14] M. Randeria and E. Taylor. Crossover from Bardeen-Cooper-Schrieffer to Bose-Einstein Condensation and the Unitary Fermi Gas. *Annual Review of Condensed Matter Physics* **5**, 209 (2014).

[Rap04] U. D. Rapol, A. Krishna, A. Wasan, and V. Natarajan. Laser cooling and trapping of Yb from a thermal source. *The European Physical Journal D - Atomic, Molecular, Optical and Plasma Physics* **29**, 409 (2004).

[Rap07] Á. Rapp, G. Zaránd, C. Honerkamp, and W. Hofstetter. Color Superfluidity and "Baryon" Formation in Ultracold Fermions. *Physical Review Letters* **98**, 160405 (2007).

[Rea89] N. Read and S. Sachdev. Valence-bond and spin-Peierls ground states of low-dimensional quantum antiferromagnets. *Physical Review Letters* **62**, 1694 (1989).

[Reg04] C. A. Regal, M. Greiner, and D. S. Jin. Observation of Resonance Condensation of Fermionic Atom Pairs. *Physical Review Letters* **92**, 040403 (2004).

[Rem92] G. Rempe, R. Lalezari, R. J. Thompson, and H. J. Kimble. Measurement of ultralow losses in an optical interferometer. *Optics Letters* **17**, 363 (1992).

[Ruf94] J. A. Ruff and A. E. Siegman. Measurement of beam quality degradation due to spherical aberration in a simple lens. *Optical and Quantum Electronics* **26**, 629 (1994).

[Rüt10] T. Rützel, Conceptual Design and Setup of a Highly Stable Laser for Precision Measurements on Ultracol Quantum Gases, Diploma thesis, University of Hamburg, Hamburg (2010).

[Ruu04] V. Ruuska and P. Törmä. Quantum transport of non-interacting Fermi gas in an optical lattice combined with harmonic trapping. *New Journal of Physics* **6**, 59 (2004).

[Sal91] B. E. A. Saleh and M. C. Teich. Fundamentals of Photonics. Wiley (1991), ISBN 978-0-471-35832-9.

[Sav97] T. A. Savard, K. M. O'Hara, and J. E. Thomas. Laser-noise-induced heating in far-off resonance optical traps. *Physical Review A* **56**, R1095 (1997).

[Sca14] F. Scazza, C. Hofrichter, M. Höfer, P. C. De Groot, I. Bloch, and S. Fölling. Observation of two-orbital spin-exchange interactions with ultracold SU(N)-symmetric fermions. *Nature Physics* **10**, 779 (2014).

[Sca15] F. Scazza, Probing SU(N)-symmetric orbital interactions with ytterbium Fermi gases in optical lattices, Ph.D. thesis, LMU München, München (2015).

[Sch08] U. Schneider, L. Hackermüller, S. Will, T. Best, I. Bloch, T. A. Costi, R. W. Helmes, D. Rasch, and A. Rosch. Metallic and Insulating Phases of Repulsively Interacting Fermions in a 3D Optical Lattice. *Science* **322**, 1520 (2008).

[Ses89] D. Sesko, T. Walker, C. Monroe, A. Gallagher, and C. Wieman. Collisional losses from a light-force atom trap. *Physical Review Letters* **63**, 961 (1989).

[Sha97] L. Shampine and M. Reichelt. The MATLAB ODE Suite. *SIAM Journal on Scientific Computing* **18**, 1 (1997).

[She10] J. F. Sherson, C. Weitenberg, M. Endres, M. Cheneau, I. Bloch, and S. Kuhr. Single-atom-resolved fluorescence imaging of an atomic Mott insulator. *Nature* **467**, 68 (2010).

[Shi09] K. Shibata, S. Kato, A. Yamaguchi, S. Uetake, and Y. Takahashi. A scalable quantum computer with ultranarrow optical transition of ultracold neutral atoms in an optical lattice. *Applied Physics B* **97**, 753 (2009).

[Sho90] B. W. Shore. The theory of coherent atomic excitation. Wiley, New York (1990), ISBN 978-0-471-52417-5.

[Sie86] A. E. Siegman. Lasers. Univ. Science Books, Mill Valley, Calif. (1986), ISBN 978-0-935702-11-8.

[Sig91] M. Sigrist and K. Ueda. Phenomenological theory of unconventional superconductivity. *Reviews of Modern Physics* **63**, 239 (1991).

[Sko16] A. Skottke, Aufbau eines zustandsabhängigen Gitters für die Realisierung des 1D-Kondo-Gitter-Modells mit ultrakalten Ytterbium-Atomen, Master thesis, University of Hamburg, Hamburg (2016).

[Sle92] T. Sleator, T. Pfau, V. Balykin, O. Carnal, and J. Mlynek. Experimental demonstration of the optical Stern-Gerlach effect. *Physical Review Letters* **68**, 1996 (1992).

[Smi07] W. J. Smith. Modern Optical Engineering. McGraw-Hill Education, New York, 4th edition (2007), ISBN 978-0-07-147687-4.

[Sob14] T. Sobottke, Design und Realisierung eines hochauflösenden Detektionssystems für Ytterbium-Quantengase, Bachelor thesis, University of Hamburg, Hamburg (2014).

[SP11] P. Soltan-Panahi, J. Struck, P. Hauke, A. Bick, W. Plenkers, G. Meineke, C. Becker, P. Windpassinger, M. Lewenstein, and K. Sengstock. Multi-component quantum gases in spin-dependent hexagonal lattices. *Nature Physics* **7**, 434 (2011).

[Sta14] K. Stannigel, P. Hauke, D. Marcos, M. Hafezi, S. Diehl, M. Dalmonte, and P. Zoller. Constrained Dynamics via the Zeno Effect in Quantum Simulation: Implementing Non-Abelian Lattice Gauge Theories with Cold Atoms. *Physical Review Letters* **112**, 120406 (2014).

[Ste09] S. Stellmer, M. K. Tey, B. Huang, R. Grimm, and F. Schreck. Bose-Einstein Condensation of Strontium. *Physical Review Letters* **103**(20), 200401 (2009).

[Ste11] S. Stellmer, R. Grimm, and F. Schreck. Detection and manipulation of nuclear spin states in fermionic strontium. *Physical Review A* **84**, 043611 (2011).

[Ste13] D. A. Steck, Rubidium 85 D Line Data (2013).

[Sto06] H. Stoehr, F. Mensing, J. Helmcke, and U. Sterr. Diode laser with 1 Hz linewidth. *Optics Letters* **31**, 736 (2006).

[Str11] J. Struck, C. Ölschläger, R. L. Targat, P. Soltan-Panahi, A. Eckardt, M. Lewenstein, P. Windpassinger, and K. Sengstock. Quantum Simulation of Frustrated Classical Magnetism in Triangular Optical Lattices. *Science* **333**, 996 (2011).

[Str12] J. Struck, C. Ölschläger, M. Weinberg, P. Hauke, J. Simonet, A. Eckardt, M. Lewenstein, K. Sengstock, and P. Windpassinger. Tunable Gauge Potential for Neutral and Spinless Particles in Driven Optical Lattices. *Physical Review Letters* **108**, 225304 (2012).

[Stu15] B. K. Stuhl, H.-I. Lu, L. M. Aycock, D. Genkina, and I. B. Spielman. Visualizing edge states with an atomic Bose gas in the quantum Hall regime. *Science* **349**, 1514 (2015).

[Sug11] S. Sugawa, R. Yamazaki, S. Taie, and Y. Takahashi. Bose-Einstein condensate in gases of rare atomic species. *Physical Review A* **84**, 011610 (2011).

[Sve98] O. Svelto. Principles of Lasers. Springer, 4. edition (1998).

[Sya08] N. Syassen, D. M. Bauer, M. Lettner, T. Volz, D. Dietze, J. J. García-Ripoll, J. I. Cirac, G. Rempe, and S. Dürr. Strong Dissipation Inhibits Losses and Induces Correlations in Cold Molecular Gases. *Science* **320**, 1329 (2008).

[Tai10] S. Taie, Y. Takasu, S. Sugawa, R. Yamazaki, T. Tsujimoto, R. Murakami, and Y. Takahashi. Realization of a SU(2)×SU(6) System of Fermions in a Cold Atomic Gas. *Physical Review Letters* **105**, 190401 (2010).

[Tai12] S. Taie, R. Yamazaki, S. Sugawa, and Y. Takahashi. An SU(6) Mott insulator of an atomic Fermi gas realized by large-spin Pomeranchuk cooling. *Nature Physics* **8**, 825 (2012).

[Tai16] M. E. Tai, A. Lukin, M. Rispoli, R. Schittko, T. Menke, D. Borgnia, P. M. Preiss, F. Grusdt, A. M. Kaufman, and M. Greiner. Microscopy of the interacting Harper-Hofstadter model in the few-body limit (2016). ArXiv: 1612.05631.

[Tak03] Y. Takasu, K. Maki, K. Komori, T. Takano, K. Honda, M. Kumakura, T. Yabuzaki, and Y. Takahashi. Spin-Singlet Bose-Einstein Condensation of Two-Electron Atoms. *Physical Review Letters* **91**, 040404 (2003).

[Tak04] Y. Takasu, K. Komori, K. Honda, M. Kumakura, T. Yabuzaki, and Y. Takahashi. Photoassociation Spectroscopy of Laser-Cooled Ytterbium Atoms. *Physical Review Letters* **93**, 123202 (2004).

[Tak05] M. Takamoto, F.-L. Hong, R. Higashi, and H. Katori. An optical lattice clock. *Nature* **435**, 321 (2005).

[Tar15] M. R. Tarbutt. Magneto-optical trapping forces for atoms and molecules with complex level structures. *New Journal of Physics* **17**, 015007 (2015).

[The04] M. Theis, G. Thalhammer, K. Winkler, M. Hellwig, G. Ruff, R. Grimm, and J. H. Denschlag. Tuning the Scattering Length with an Optically Induced Feshbach Resonance. *Physical Review Letters* **93**, 123001 (2004).

[Tho82] D. J. Thouless, M. Kohmoto, M. P. Nightingale, and M. den Nijs. Quantized Hall Conductance in a Two-Dimensional Periodic Potential. *Physical Review Letters* **49**, 405 (1982).

[Tho14] A. Thobe, Ultracold Yb Gases with Control over Spin and Orbital Degrees of Freedom, Ph.D. thesis, University of Hamburg, Hamburg (2014).

[Toj06] S. Tojo, M. Kitagawa, K. Enomoto, Y. Kato, Y. Takasu, M. Kumakura, and Y. Takahashi. High-Resolution Photoassociation Spectroscopy of Ultracold Ytterbium Atoms by Using the Intercombination Transition. *Physical Review Letters* **96**, 153201 (2006).

[Tsu97] H. Tsunetsugu, M. Sigrist, and K. Ueda. The ground-state phase diagram of the one-dimensional Kondo lattice model. *Reviews of Modern Physics* **69**, 809 (1997).

[Una98] R. Unanyan, M. Fleischhauer, B. W. Shore, and K. Bergmann. Robust creation and phase-sensitive probing of superposition states via stimulated Raman adiabatic passage (STIRAP) with degenerate dark states. *Optics Communications* **155**, 144 (1998).

[Urb09] E. Urban, T. A. Johnson, T. Henage, L. Isenhower, D. D. Yavuz, T. G. Walker, and M. Saffman. Observation of Rydberg blockade between two atoms. *Nature Physics* **5**, 110 (2009).

[Vit01] N. V. Vitanov, T. Halfmann, B. W. Shore, and K. Bergmann. Laser-Induced Population Transfer by Adiabatic Passage Techniques. *Annual Review of Physical Chemistry* **52**, 763 (2001).

[Vit16] N. V. Vitanov, A. A. Rangelov, B. W. Shore, and K. Bergmann. Stimulated Raman adiabatic passage in physics, chemistry and beyond. *arXiv:1605.00224 [quant-ph]* (2016). ArXiv: 1605.00224.

[Viv04] L. Viverit, C. Menotti, T. Calarco, and A. Smerzi. Efficient and Robust Initialization of a Qubit Register with Fermionic Atoms. *Physical Review Letters* **93**, 110401 (2004).

[Wei11] C. Weitenberg, M. Endres, J. F. Sherson, M. Cheneau, P. Schauß, T. Fukuhara, I. Bloch, and S. Kuhr. Single-spin addressing in an atomic Mott insulator. *Nature* **471**, 319 (2011).

[Wen13] A. N. Wenz, G. Zürn, S. Murmann, I. Brouzos, T. Lompe, and S. Jochim. From Few to Many: Observing the Formation of a Fermi Sea One Atom at a Time. *Science* **342**, 457 (2013).

[Wie95] C. Wieman, G. Flowers, and S. Gilbert. Inexpensive laser cooling and trapping experiment for undergraduate laboratories. *American Journal of Physics* **63**, 317 (1995).

[Win98] D. J. Wineland, C. Monroe, W. M. Itano, D. Leibfried, B. E. King, and D. M. Meekhof. Experimental Issues in Coherent Quantum-State Manipulation of Trapped Atomic Ions. *J. Res. Natl. Inst. Stand. Technol.* **103**, 259 (1998).

[Xu11] C.-Y. Xu, S.-M. Hu, J. Singh, K. Bailey, Z.-T. Lu, P. Mueller, T. P. O'Connor, and U. Welp. Optical Excitation and Decay Dynamics of Ytterbium Atoms Embedded in a Solid Neon Matrix. *Physical Review Letters* **107**, 093001 (2011).

[Xu12] Z. Xu, X. Zhang, K. Huang, and X. Lu. A digital optical phase-locked loop for diode lasers based on field programmable gate array. *Review of Scientific Instruments* **83**, 093104 (2012).

[Yan13] B. Yan, S. A. Moses, B. Gadway, J. P. Covey, K. R. A. Hazzard, A. M. Rey, D. S. Jin, and J. Ye. Observation of dipolar spin-exchange interactions with lattice-confined polar molecules. *Nature* **501**, 521 (2013).

[Zha14] W. Zhang, M. J. Martin, C. Benko, J. L. Hall, J. Ye, C. Hagemann, T. Legero, U. Sterr, F. Riehle, G. D. Cole, and M. Aspelmeyer. Reduction of residual amplitude modulation to 10^{-6} for frequency modulation and laser stabilization. *Optics Letters* **39**, 1980 (2014).

[Zha15] R. Zhang, Y. Cheng, H. Zhai, and P. Zhang. Orbital Feshbach Resonance in Alkali-Earth Atoms. *Physical Review Letters* **115**, 135301 (2015).

[Zha16] R. Zhang, D. Zhang, Y. Cheng, W. Chen, P. Zhang, and H. Zhai. Kondo effect in alkaline-earth-metal atomic gases with confinement-induced resonances. *Physical Review A* **93**, 043601 (2016).

[Zho16] Y. Zhong, Y. Liu, and H.-G. Luo. Simulating heavy fermion physics in optical lattice: Periodic Anderson model with harmonic trapping potential (2016). ArXiv: 1610.04372.

[Zhu14] B. Zhu, B. Gadway, M. Foss-Feig, J. Schachenmayer, M. L. Wall, K. R. A. Hazzard, B. Yan, S. A. Moses, J. P. Covey, D. S. Jin, J. Ye, M. Holland, and A. M. Rey. Suppressing the Loss of Ultracold Molecules Via the Continuous Quantum Zeno Effect. *Physical Review Letters* **112**, 070404 (2014).

[Zim11] B. Zimmermann, T. Müller, J. Meineke, T. Esslinger, and H. Moritz. High-resolution imaging of ultracold fermions in microscopically tailored optical potentials. *New Journal of Physics* **13**, 043007 (2011).

[Zwi04] M. W. Zwierlein, C. A. Stan, C. H. Schunck, S. M. F. Raupach, A. J. Kerman, and W. Ketterle. Condensation of Pairs of Fermionic Atoms near a Feshbach Resonance. *Physical Review Letters* **92**, 120403 (2004).

Danksagung

Die vorliegende Arbeit hätte ohne die Mithilfe von vielen Personen nicht entstehen können. In den vergangenen Jahren konnte ich auf einen unterstützenden Kreis von Freunden zurück greifen und habe Neue in dieser Arbeitsgruppe finden dürfen. Ich bedanke mich ganz herzlich bei der AG Sengstock für das immense, vorhandene Know-How und das freundschaftliche Arbeitsklima. Einige der Personen möchte ich speziell nennen:

Ich danke Klaus Sengstock für die Möglichkeit an einem so spannenden Experiment etwas über Quantengase zu lernen. Trotz der vielen Hochs und Tiefs bleiben am Ende nur die vielen faszinierenden Eindrücke aus der Quantenwelt. Außerdem vielen Dank für die gute Ausstattung der "Gruppenkasse" und deinen sechsten Sinn bei der Mitarbeiterauswahl, welcher diese Gruppe maßgeblich prägt.
Großer Dank gilt Christoph Becker, der dieses Projekt mit seinem umfassenden Wissen stets voran bringt. Deine Tür steht für uns immer offen und auf jede Frage hast du eine Antwort parat. Vielen Dank auch für die Korrekturen dieser Arbeit. Ich muss noch viel über strukturiertes und klares Formulieren lernen.
Bastian Hundt und Thomas Ponath haben mich den Großteil meiner Promotion begleitet. Vielen Dank für unsere gemeinsamen Jahre im "Keller". Man könnte sich keine besseren Lab-Buddys wünschen. Ich erwarte auch weiterhin lange, philosophische Exkurse über Banalitäten des Lebens.
Ich bedanke mich außerdem bei unseren Vorgängern Sören Dörscher und Alexander Thobe. Eure Planung, Aufbauarbeiten und Messungen haben den Grundstein für diese Arbeit gelegt. Das Wissen, welches ihr weitergereicht habt, habe ich sehr zu schätzen gelernt. Danke auch an Bodhaditya Santra für die Hilfe am Ende dieser Promotion.
Dieses Experiment beschäftigte neben den Doktoranden eine Vielzahl Diplomanden, Bacheloranden und Masteranden. Dabei bedanke ich mich für das Übernehmen anspruchsvoller Aufgaben bei Niels Petersen, Torben Sobottke Lukas Heinze und Lars Hilbig. Großer Dank gilt außerdem Anna Skottke und Benjamin Abeln. Teile dieser Arbeit konnten nur mit eurer Hilfe entstehen und mit euch zu arbeiten hat besonders viel Spass gemacht.
Ich bedanke mich bei Janina Dahms für die außerordentlich Betreuung des Yb Teams. Wie du uns Besserwisser aushälst ist mir nicht klar. Daher vielen Dank für deine Geduld.
Danke Reinhard Mielck und Ralf Lühr für eure Weisheiten im Bereich Feinmechanik, Kabelkonfektionierung und Haustechnik.
Ich bedanke mich außerdem bei weiteren Mitarbeitern des ILP und ZOQ: Dieter Barlösius, für schwierige Beschichtungen, Wolfram Kalb-Rottmann, für Hilfe bei Computerproblemen, Ellen Gloy und Nadja Wardenburg, für ihre Organisation aus dem "Office".
Vielen Dank geht auch an Andreas Hemmerich für die Übernahme des Zweitgutachtens.
Ich bedanke mich bei meinen Freunden für ihre ansteckende gute Laune und entschuldige mich für die "Abwesenheit" der letzten Monate. Haltet mich weiterhin auf Trab!
Schließlich bedanke ich mich bei meiner Familie Rosa, Waldemar und Katrin. Eure Unterstützung bedeutet mir viel.

Erratum

Eq. (3.3)**:**
Relative length extension is anti-proportional to the relative change in frequency. The equation needs to be modified with a minus sign:

$$\frac{\Delta L(t)}{L_0} = -\frac{\Delta\nu(t)}{\nu_0} = -\alpha_{\mathrm{CTE}} \times (\Delta T)^2(t).$$

Fig. 1.1:
The singlet and triplet states carry $S = 0$ and $S = 1$ respectively. Hence, they have a multiplicity of $2\,S + 1$, i.e. 1 and 3 respectively.

Fig. 2.12:
The aspect ratio of the image got changed to 2:1, thus the atomic clouds seem to have an elliptic shape.

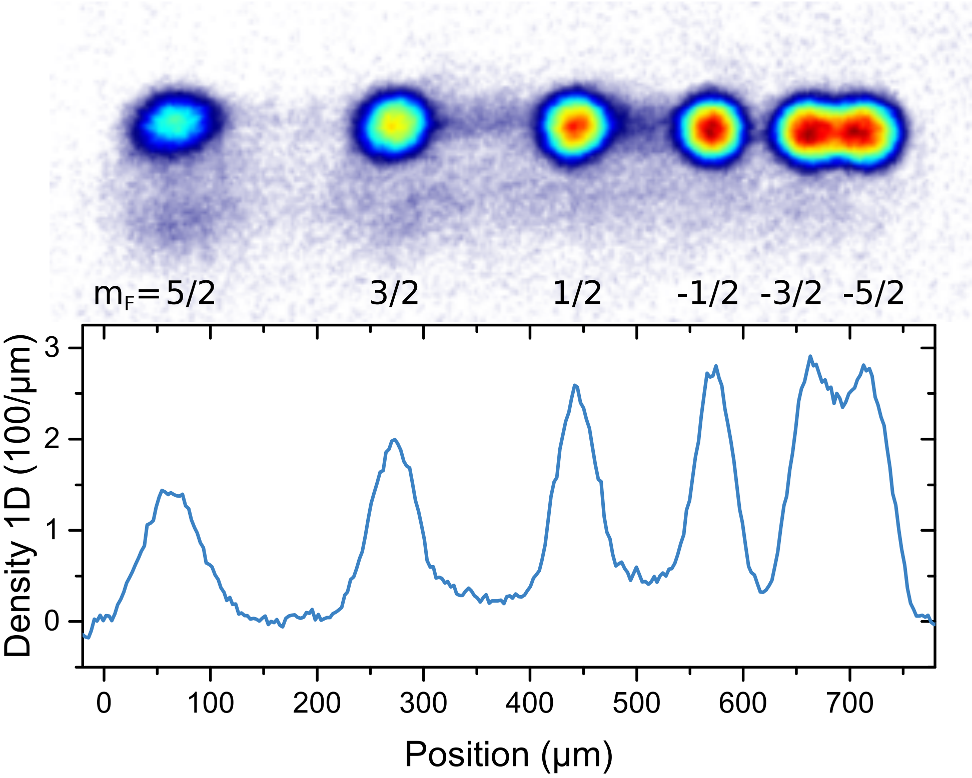

Fig. 3.15:
Considering the sum of ground and excited state atoms, it is apparent that on the resonances of singly occupied lattice sites the total atom number was overestimated.

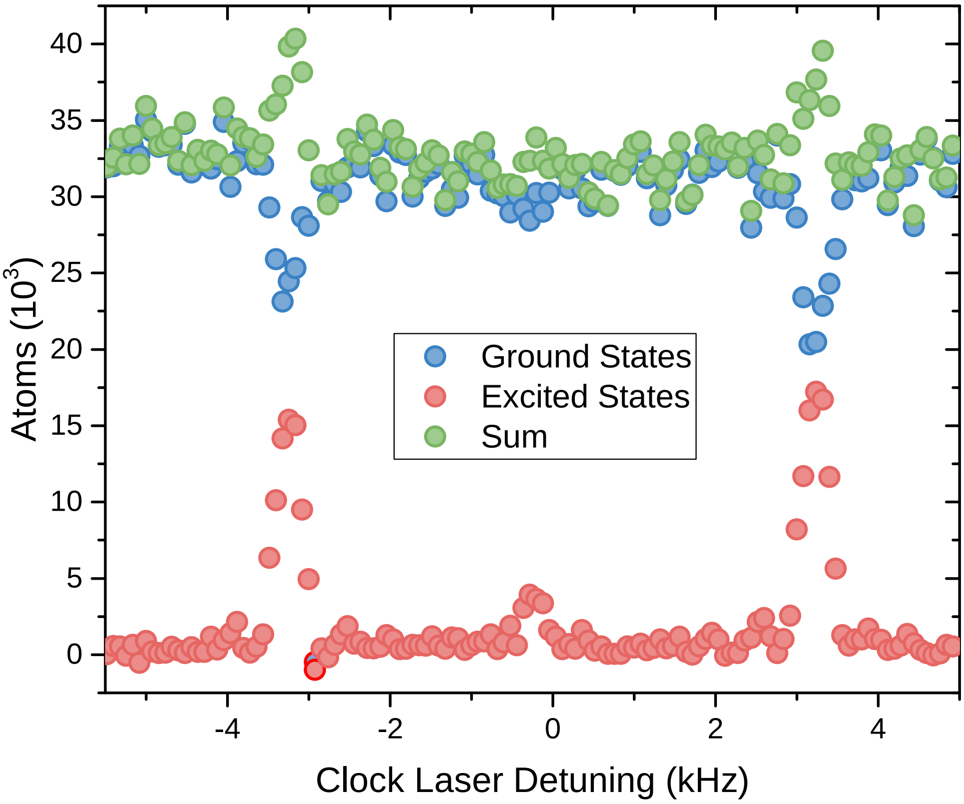

The number of ground state atoms indicate that the amount of excited state atoms is to high. Considering the numbers for ground state atoms the estimation of doubly occupied sites seems to fit. The central peak is supposed to represent about 30% of atoms (see main text for explanation), the singly occupied lattice sites cover roughly 66%. Why the repump scheme did not work during this sequence is not understood.